Structure-property relations in pnictides and chalcogenides of Eu^{2+}

Dissertation

zur Erlangung des Doktorgrades
der Naturwissenschaften (Dr. rer. nat.)
der Fakultät für Chemie und Pharmazie
der Universität Regensburg

vorgelegt von

Dipl.-Chem. Igor Plokhikh
aus Kursk / Russische Föderation

Regensburg, August 2020

The practical work was performed from October 2017 to April 2020 at the Institute of Inorganic Chemistry at the University of Regensburg in the working group of Prof. Dr. Arno Pfitzner.

This thesis was supervised by Prof. Dr. Arno Pfitzner
Submission of the doctoral application: 14.07.2020
Date of the oral examination: 14.08.2020
Examination committee:
Chairman: Prof. Dr. Frank-Michael Matysik
1st reviewer: Prof. Dr. Arno Pfitzner
2nd reviewer: Prof. Dr. Richard Weihrich
Further examiner: Prof. Dr. Patrick Nürnberger

Declaration

I, Igor Plokhikh, declare that this thesis titled, '*Structure-property relations in pnictides and chalcogenides of* Eu^{2+}', and the work presented in it are my own under the supervision of Prof. Dr. Arno Pfitzner and I did not use any unnamed sources or aid. This work has not been submitted at any other University, and I am aware of § 25 Abs. 5 and its legal consequences.

Regensburg, July 2020

Abstract

In this thesis, the structure-properties relations in pnictides and chalcogenides of divalent Eu were elaborated. Interest to its compounds was due to the high magnetic moment of Eu^{2+} cations, owing to a half-filled 4*f* shell. It was expected to induce unusual magnetic states and to have a substantial impact on the physics of the matrixes, in which it is nested. The highly-localized nature of the 4*f* electrons precludes substantial direct magnetic exchange or superexchange, but interactions through the conducting frameworks can be sizable and lead to non-trivial magnetic states. The crystallographic similarity of Eu^{2+} and Sr^{2+} was a tool for predicting the new materials. The synthetic work resulted in the preparation of more than ten new compounds, including rare fluorides belonging to the 1111 structure type and the first magnetic tetrel-free clathrate $EuNi_2P_4$. Crystallographic and synthetic work were accompanied by physical properties measurements – temperature-dependent magnetization, heat capacity, and resistivity. Neutron powder diffraction was instrumental for establishing the natures of the low-temperature magnetically ordered phases despite the strong neutron absorption of natural Eu.

Abstrakt

In dieser Arbeit wurden die Struktur-Eigenschaften-Beziehungen in Pnictiden und Chalkogeniden von zweiwertigem Eu ausgearbeitet. Das Interesse an seinen Verbindungen wurde durch das hohe magnetische Moment der Eu^{2+}-Kationen aufgrund der halbgefüllten 4*f*-Schale vorgegeben. Es wird erwartet, dass es ungewöhnliche magnetische Zustände induziert und einen wesentlichen Einfluss auf die physikalischen Eigenschaften seiner Umgebung hat. Die stark lokalisierte Natur der 4*f*-Elektronen schließt einen wesentlichen direkten magnetischen Austausch oder Superaustausch aus, aber Wechselwirkungen durch die leitenden Gerüste können beträchtlich sein und zu nicht trivialen magnetischen Zuständen führen. Die kristallographische Ähnlichkeit von Eu^{2+} und Sr^{2+} ist ein Werkzeug zur Vorhersage der neuen Materialien. Die Synthesearbeit führte zur Herstellung von mehr als zehn neuen Verbindungen, darunter seltene Fluoride des 1111 Strukturtyps und das erste magnetische tetrelfreie Clathrat $EuNi_2P_4$. Kristallographische und synthetische Arbeiten werden von der Bestimmung physikalischer Eigenschaften begleitet - temperaturabhängige Magnetisierung, Wärmekapazität und spezifischer Widerstand. Neutronenbeugung an kristallinen Pulvern war maßgeblich für die Ermittlung der Natur der magnetisch geordneten Niedertemperaturphasen trotz der starken Neutronenabsorption von natürlichem Eu.

Acknowledgment

This word could not be possible or would not be as exciting without the support of my colleagues. A substantial part of this work has been done by other contributors, which are reflected as co-authors in the published papers.

1. Prof. Dr. Arno Pfirtzner for the supervision of the work in Regensburg, providing the laboratory space and materials as well as for valuable discussions and support at all stages of the work.
2. My colleagues from the Lomonosov Moscow State University in Russia, Prof Andrei Shevelkov, Dr. Dmitri Charkin, and Prof. Alexey Kuznetsov for full and comprehensive support with my whole work, including valuable discussion and providing new ideas. Above all, I am thankful for computational work performed with the equipment of the shared research facilities of the HPC resources at the Lomonosov Moscow State University.
3. My colleagues from Augsburg Dr. Nazir Khan and Dr. Alexander Tsirlin for performing different physical properties measurements, handling the data, and discussion of the results.
4. Neutron diffraction beamtime has been provided by the ISIS Neutron and Muon Source (Oxford, UK) and by the Heinz Maier-Leibnitz Zentrum FRM-II (Garching, Germany). I would like to thank Dr. Dmitry D. Khalyavin, the beamline scientist at the WISH diffractometer at the ISIS, and Dr. Anatoliy Senyshyn, the beamline scientist at the SPODI diffractometer at the FRM-II, for support at all stages of my neutron diffraction experiments – from the preparation of the proposals to data collection and analysis. I also would like to thank other staff of the ISIS and FRM-II for the smooth handling of my experimental and bureaucratic issues.
5. I thank the group of co-workers from the University of Münster, Dr. Lukas Heletta, Dr. Steffen Klenner, and Prof. Rainer Pöttgen for performing magnetic and ^{151}Eu Mössbauer measurements.
6. The work has been financially supported by the BAYHOST and DAAD foundations *via* the doctoral scholarships. I am thankful to the staff of the corresponding foundations: Mrs. Katrin Döppe (BAYHOST) and Mrs. Elena Schmid (DAAD). In particular, I am grateful to Mr. Nikolas Djukić (BAYHOST), who entrusted me to introduce the BAYHOST foundation at the conference held in Skoltech.

7. I am thankful to all my colleagues from the University of Regensburg. The special thank goes to Dr. Ria Mandal, Dr. Thomas Buchecker, and Mr. Christian Klimas for their patience during my first few months in the lab. Mrs. Bianca Frömel and Mrs. Katharina Trögl handled all my bureaucracy well. The PhD students Mr. Sebastian Fäth, Mr. Maximilian Obermeier, and Mr. Florian Buchecker taught how to teach the students. I acknowledge for the experimental and theoretical support as well as for the simple time being at the lab Mrs. Ulrike Schießl, Mr. Florian Truksa, Mrs. Elisabeth Bauer, Dr. Marc Schlosser, Mrs. Daniela Garcia, Mr. Ferdinand Gigl, Mrs. Heidi Paulus, Dr. Florian Pielnhofer Dr. Martina Andratschke, Dr. Claudia De Giorgi, Mrs. Freya von Krziwanek, Mr. Severin Bauer, Mr. Salil Bal, Mr. Christoph Meier, Mr. Thomas Rothenaigner, Mr. Maximilian Sehr.
8. The staff of the X-ray department of the Uni Regensburg, Dr. Michael Bodensteiner, Mrs. Sabine Stempfhuber, and Mrs. Birgit Hischa, are acknowledged for their support with single-crystal measurements and bureaucratic accompaniment of my experiments at the FRM II.
9. Prof. Dr. Alkwin Slenzcka for Raman measurement.

List of publications

1. D. O.Charkin A. V. Urmanov. I. V. **Plokhikh**, A. D. Korshunov, A. N. Kuznetsov, S. M. Kazakov. Synthesis and crystal structures of novel LaOAgS-type alkaline earth – zinc, manganese, and cadmium fluoride pnictides. *J Alloys Compd.* **2014**, *585*, 644 – 649.

2. D. O. Charkin, R. Demchyna, Yu. Prots, H. Borrmann, U. Burkhardt, U. Schwarz, W. Schnelle, **I.V. Plokhikh**, S. M. Kazakov, A. M. Abakumov, D. Batuk, V. Yu. Verchenko, A. A. Tsirlin, C. Curfs, Yu. Grin, A. V. Shevelkov. Two new arsenides, $Eu_7Cu_{44}As_{23}$ and $Sr_7Cu_{44}As_{23}$, with a new filled variety of the $BaHg_{11}$ structure. *Inorg. Chem.* **2014**, *53*, 11173 – 11184.

3. D. O. Charkin, **I. V. Plokhikh**, A. N. Kuznetsov, S. M. Kazakov. BaFAlSi and BaFAlGe: First transition metal-free LaOAgS-type fluoride tetrelides. *J. Alloys Compd.* **2015**, *627*, 451 – 454.

4. **I. V. Plokhikh**, D. O. Charkin, V. Yu. Verchenko, I. A. Ignatyev, S. M. Kazakov, A. V. Sobolev, I. A. Presniakov, A. A. Tsirlin, A. V. Shevelkov. Effect of transition metal substitution on the structure and properties of a clathrate-like compound $Eu_7Cu_{44}As_{23}$. *Materials* **2016**, *9*, 587.

5. **I. V. Plokhikh**, D. O. Charkin, V. Yu. Verchenko, A. N. Kuznetsov, S. M. Kazakov, A. A. Tsirlin, A. V. Shevelkov. Structural and thermodynamic stability of the "1111" structure type: a case study of EuFZnPn series. *Inorg. Chem.* **2016**, *55*, 12409 – 12418.

6. D. O. Charkin, **I. V. Plokhikh**, A. I. Zadoya, S. M. Kazakov, A. N. Zaloga, M. S. Kozin, W. Depmeier, O. I. Siidra. $[Pb_2F_2](SeO_4)$: a heavier analogue of grandreefite, the first layered fluoride selenate. *Phys. Chem. Miner.* **2018**, *45*, 69 – 76.

7. D. O. Charkin, **I. V. Plokhikh**, A. N. Zaloga, M. V. Lobanov, S. M. Kazakov. One disorder out of two orders: synthesis and crystal structures of cation-ordered $PbNaF_2NO_3$, anion-ordered Pb_2OFNO_3, and continuous disordered $(Pb, Na)_2(O,F)_{2-d}NO_3$ solid solution with Sillen-derived structures. *Solid State Sci.* **2017**, *71*, 111 – 116.

8. D. O. Charkin, **I. V. Plokhikh**, K. E. Gurianov, V. Yu. Verchenko, S. M. Kazakov. Investigation of the substitution at the anionic position BaT_2As_2 (T = Fe, Ni) superconductors. *Russ. J. Inorg. Chem.* **2017**, *62*, 1026 – 1031.

9. D. O. Charkin, **I. V. Plokhikh**, S. M. Kazakov, S. N. Kalmykov, V. S. Akinfiev, A. V. Gorbachev, M. Batuk, A. M. Abakumov, Y. A. Teterin, K. I. Maslakov, A. Yu. Teterin, K. E. Ivanov. Synthesis and structural characterization of a novel Sillen – Aurivillius bismuth oxyhalide, $PbBi_3VO_{7.5}Cl$, and its derivatives. *Solid State Sci.* **2018**, *75*, 27 – 33.

10. **I. V. Plokhikh**, D. O. Charkin, V. Yu. Verchenko, A. N. Kuznetsov, A. A. Tsirlin, S. M. Kazakov, A. V. Shevelkov. Synthesis, crystal structure and physical properties of europium – manganese fluoride pnictides, EuMnPnF (Pn = P, As, Sb). *J Solid State Chem.* **2018**, *258*, 682 – 690.

11. **I. V. Plokhikh**, D. O. Charkin, A. N. Kuznetsov, V. Yu. Verchenko, I. A. Ignatiev, S. M. Kazakov, A. A. Tsirlin, A. V. Shevelkov. New clathrate-like compound $Eu_7Cu_{44}Sb_{23-\delta}$: synthesis, crystal and electronic structure, and the effect of As-for-Sb substitution on the magnetic properties. *Intermetallics* **2018**, *98*, 1 – 10.

12. V. Novikov, K. Pilipenko, A. Matovnikov, N. Mitroshenkov, **I. Plokhikh**, A. Tyablikov, A. Shevelkov. Structure-related thermal properties of type-VII clathrates $SrNi_2P_4$ and $BaNi_2P_4$ at low temperature. *Phys. Status Solidi*, **2018**, *255*, 1800067.

13. D. O. Charkin, **I. V. Plokhikh**, A. I. Zadoya, A. N. Zaloga, W. Depmeier, O. I. Siidra. Structural, thermal, and IR studies of β-$[Nd_2O_2](CrO_4)$, an unexpected analog of a slag phase $[Ba_2F_2](S^{6+}O_3S^{2-})$. *Z. Kristallogr. – Cryst. Mat.* **2019**, *234*, 1 – 8.

14. D. O. Charkin, **I. V. Plokhikh**, A. I. Zadoya, P. L. Kuznetsova, S. M. Kazakov, O. I. Siidra. $CdBiO_2NO_3$, a new layered bismuth oxide nitrate. *Solid State Sci.* **2018**, *84*, 23 – 27.

15. K. A. Vinogradova, N. A. Shekhovtsov, A. S. Berezin, T. S. Sukhikh, V. P. Krivopalov, E. B. Nikolaenkova, **I. V. Plokhikh,** M. B. Bushuev. A near-infra-red emitting manganese (II) complex with a pyrimidine-based ligand. *Inorg. Chem. Commun.* **2019**, *100*, 11 – 15.

16. **I. V. Plokhikh,** A. N. Kuznetsov, D. O. Charkin, A. V. Shevelkov, A. Pfitzner. Layered compounds BaFMgPn (Pn = P, As, Sb, and Bi), transition-metal-free representatives of the 1111 structure type. *Inorg. Chem.* **2019**, *58*, 3435 – 3444.

17. D. O. Charkin, A. S. Karpov, S. M. Kazakov, **I. V. Plokhikh**, A. I. Zadoya, A. N. Kuznetsov, K. I. Maslakov, A. Y. Teterin, Y. A. Teterin, A. N. Zaloga, O. I. Siidra O.I. Synthesis, crystal structure, spectroscopic properties, and thermal behavior of rare-earth oxide selenates, $Ln_2O_2SeO_4$ (Ln = La, Pr, Nd): the new perspectives of solid-state double-exchange synthesis. *J Solid State Chem.* **2019**, *277*, 163 – 168.

18. **I. V. Plokhikh**, N. Khan, A. A. Tsirlin, A. N. Kuznetsov, D. O. Charkin, A. V. Shevelkov, A. Pfitzner. Synthesis, crystal and electronic structure of the Pt-rich phosphides $EuPt_3P$ and $EuPt_6P_2$. *Dalton Trans.* **2019**, *48*, 15272 – 15282.

19. V. V. Novikov, K. S. Pilipenko, A. V. Matovnikov, N. V. Mitroshenkov, B. I. Kornev, **I.V. Plokhikh**, A. S. Tyablikov, E. A. Zvereva, G. Raganyanm, A. V. Shevelkov. Low-temperature thermodynamic and magnetic properties of clathrate-like arsenide $Eu_7Cu_{44}As_{23}$. *J. Magnetism and Magnetic Mat.* **2020**, *498*, 166165.

20. D. O. Charkin, G. A. Akimov, **I. V. Plokhikh**, A. N. Zaloga, A. S. Borisov, S. Yu. Stefanovich, A. N. Kuznetsov, O. I. Siidra. $Bi_2O_2SO_4$, a new representative of the grandreefite structure type. *J Solid State Chem.* **2020**, *282*, 121124.

21. **I. V. Plokhikh**, N. Khan, A. A. Tsirlin, A. N. Kuznetsov, D. O. Charkin, A. V. Shevelkov, A. Pfitzner. $EuNi_2P_4$, the first magnetic unconventional clathrate prepared *via* a mechanochemically assisted route. *Inorg. Chem. Front.* **2020**, *7*, 1115 – 1126.

22. D. O. Charkin, A. S. Borisov, **I. V. Plokhikh**, S. Yu. Stefanovich, A. I. Zadoya, A. N. Zaloga, T. F. Semenova, Oleg I. Siidra. $Pb_6O_5(NO_3)_2$: a nonlinear optical oxynitrate structurally based on lead oxide framework. *Inorg. Chem.* **2020**, *59*, 3523 – 3526.

23. **I. V. Plokhikh**, A. A Tsirlin, L. Heletta, S. Klenner, D. O. Charkin, A. N. Kuznetsov, A. V Shevelkov, R. Pöttgen, A. Pfitzner. Synthesis, electronic structure and physical properties of two new layered compounds, EuFAgSe and $EuFAg_{1-\delta}Te$, featuring the active redox pair Eu^{2+}/Ag^{+}. *Dalton Trans.* ***2020***, *49*, 7426 – 7435.

24. V. V. Novikov, A. V. Matovnikov, N. V. Mitroshenkov. A. V. Morozov, K. S. Pilipenko, **I. V. Plokhikh**, A. Pfitzner, A. V. Shevelkov. Ferromagnetic phase transition and anomalies of thermodynamic characteristics of copper-deficient $EuCu_2P_2$ at low temperatures. *J Alloys Compd.* **2020**, 156150.

Resume

Personal data

Name	Igor
Surname	Plokhikh
Date of birth	15.07.1993
Place of birth	Kursk, Russian Federation
Parents	Irina Plokhikh and Vladimir Plokhikh

School education

09/2000 – 08/2004	Primary school, Lyceum No. 6, Kursk, Russia
09/2004 – 08/2011	Secondary school, Lyceum No. 6 Kursk, Russia

University Education

09/2011 – 08/2017	Lomonosov Moscow State University, Moscow
06/2017	Graduation, Diploma with Honour, Specialist in chemistry and lecturer in chemistry

Postgraduate Studies

From 10/2017	University of Regensburg, Department of Chemistry and Pharmacy, Institute of Inorganic Chemistry, Chair of Prof. Dr. Arno Pfitzner. Structured doctoral program ChemPharm. Supported by DAAD and BAYHOST.

Awards, talks, conferences, certification and mentoring

Conferences

1. XVIII International conference on crystal chemistry, X-ray diffraction and spectroscopic studies of minerals, 13 - 15 October 2014, Yekaterinburg. **Oral report** Synthesis, Structure and Properties of Two New Arsenides, $Eu_7Cu_{44}As_{23}$ and $Sr_7Cu_{44}As_{23}$, with a Filled Decoration Variety of the $BaHg_{11}$ Structure (in English).
2. VII National Crystal Chemical Conference, Suzdal, Russia, 17—21 June 2013. **Poster** Новые фторид-пниктиды ЩЗЭ – цинка, кадмия, марганца со структурой LaOAgS (in Russian).
3. VIII National Crystal Chemical Conference, Suzdal, Russia, 30 May – 3 June 2016. **Poster** Четверные фторид-пниктиды цинка, марганца и европия со структурой LaOAgS – синтез,кристаллическое строение и физические свойства (in Russian).
4. 24th Congress & General Assembly of the International Union of Crystallography, Hyderabad, India, 1 – 28 August 2017. **Poster** On the stability borders of the LaOAgS structure type.
5. 6th International Conference on Superconductivity and Magnetism, Antalaiy/Beldibi, Turkey, 29 April – 04 May 2018. **Poster**.
6. Joint Bavarian-RussianConference „Chemistry meetsBiomedicine". **Oral report** "Mission, expertise, and services of BAYHOST". Moscow, Russia, 19 – 21 September 2019.

Honors and awards

1 - 3. All-Russian Olympiads on chemistry, Arkhangelsk, Russia, 2009. **Winner**. Kazan, Russia, 2010. **Winner**. Arkhangelsk, Russia, 2011. **Winner**.
4,5. International Mendeleev Chemistry Olympiad, Baku, Azerbaijan, 2010. **Bronze medal**. Moscow, Russia, 2011. **Silver medal**.
6. 7th International Scientific Olympiad for students, Chemistry, August 16 – 19, 2014, Shiraz, Iran. **Bronze medal**.
7, 8. International conference for students and young scientists "Lomonosov", 2013, inorganic chemistry, students. **Prizewinner**.2016, inorganic chemistry, students. **Winner**.
9 – 12. Prizes of the President of the Russian Federation for support of talented youth in 2009, 2010, 2011, 2014.
13. Stipend of the Russian Federation Government, 2014/2015.
14. The O.V. Deripaska's prize for Lomonosov Moscow State University students, graduate students and young scientists 2015.

15. Prize of Academician Alexandra Vasilievna Novoselova for the year 2017.

16. G.A. Jeffrey Student Travel award for attending the XXIV Congress of the International Union of Crystallography in Hyderabad India.

17. BAYHOST doctoral scholarship 2017 – 2018.

18. DAAD scholarship 2018 – 2020.

19. Selected as participant in the 70th Lindau Nobel Laureate Meeting 2020 (postponed to 2021).

Seminars

1, 2. The 26th Ad Hoc Workshop on Jana2006 (structure analysis of powders). 5 - 6 October 2015, and 37th Ad Hoc Workschop on Jana 2006 (Magnetic structures) 14 -15 November 2019, Prague, Czech Republic.

3 - 5. XII school-conference "Actual problems of the inorganic chemistry", 9 - 11 November 2012, Zvenigorod, Russia. + Poster. XIII school-conference "Actual problems of the inorganic chemistry", 14 - 16 November 2014, Zvenigorod, Russia + Poster. XIV school-conference "Actual problems of the inorganic chemistry", 13 - 15 November 2015, Zvenigorod, Russia + Poster.

6, 7. International workshop "Applications of topological methods in materials science", International Scientific School "Combined Topological and DFT Methods for Prediction of New Materials II" 1 – 10 July 2016. Samara, Russia. + Oral report

8, 9. RACIRI Summer School 2016: Convergent Science and Technology for Society, Repino, Russia, August 21-28, 2016. + Poster, RACIRI Summer School 2018, Rugen Island, Germany, 25. August – 1. September 2018: From Basic Science and Applications to Technologies inspired by Nature + Poster.

10. MSU-IFW-ILTPE Joint Workshop "Synthesis, theoretical examination and experimental investigation of emergent materials", 14 – 16 June 2017, Moscow, Russia. + Poster

11. International Symposium "Diffraction Methods in Characterization of New Materials", 31May – 2 June, 2017, Moscow, Russia + Oral Report.

12. Laboratory seminar, Uni Augsburg, Center for Electronic Correlations and Magnetism, 6 December 2018, Invited talk (Alexandr Tsirlin).

13. HERCULES 2019 European school. Session A: physics and chemistry of condenced matter 17 March – 19 April 2019.

Table of Contents

1 Introduction and general overview

The growing electronic industry demands new highly-performing materials. Nowadays, even a small enhancement of a single material's characteristic can significantly increase the performance of the final product, which then increases profit. There are two approaches for material design: search for new compounds and modification of known ones. The advantage of the first approach is that one can yield breakthrough results, although this method lacks tangible concepts on structure-properties relations. This is partly due to the historical separation of classical inorganic chemistry and crystallography from solid-state physics. Previously, it was conventional to report only the crystal structure of a new compound, without mentioning at least some of its physical properties and prospects of the compound as a potential material. Because of this reason, many well-known compounds celebrate their re-discovery as "potential", "promising", "exciting," and so on materials. An illustrative example is probably $LiCoO_2$, which made its re-investigator win the Nobel Prize. Today solid-state chemistry and physics move towards their fusion. As the number of known solid inorganic compounds gets extensive with almost 200 000 unique entries in the Pearson's Crystal Database, the interest in the compounds and structures just for the sake of their existence deteriorates. This trend is expressed in credos of some journals (like JALCOM, **Figure 1.1**), which have been sheltering crystallography even 20 years ago, but now omit pure "synthesis & proves of existence" works.

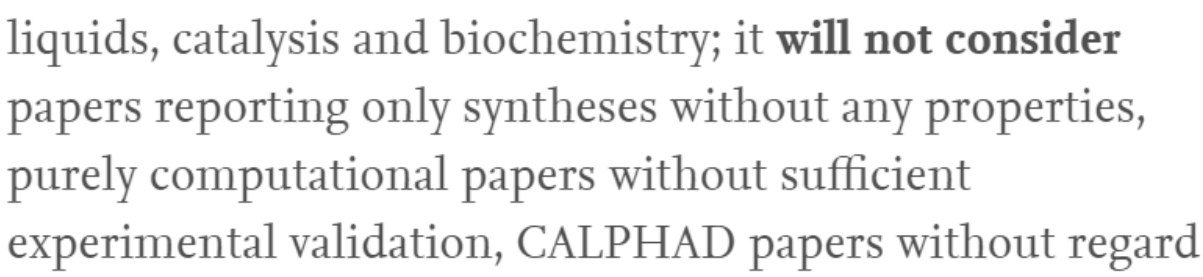
liquids, catalysis and biochemistry; it **will not consider** papers reporting only syntheses without any properties, purely computational papers without sufficient experimental validation, CALPHAD papers without regard

Figure 1.1 Quotation from the start page ("General Perspective") of the Journal of Alloys and Compounds.

A powerful tool for predicting new materials is crystallographic analysis, which is based on crystal-chemical analogies. For example, it is well known that a series of isostructural lanthanide-based compounds can be prepared by simple replacement of one lanthanide with another. However, Eu-based compounds quite frequently fall out of such series. Although Eu is located in the row of lanthanides, it often behaves structurally similar to alkaline-earth metals, since the oxidation state +2 is relatively stable, especially in pnictide

(P, As, Sb, Bi) or chalcogenide (S, Se, Te) environment. The Eu^{2+} cation is of about the same radius as Sr^{2+}. Each Eu^{2+} ($4f^7$) cation, bearing seven unpaired electrons, manifests a high magnetic moment, but has a low tendency to establish a long-range magnetic order due to the highly localized nature of 4*f* electrons. The situation can be changed drastically when Eu^{2+} is incorporated in metallic phases or adjoins with other magnetically active elements, *i.e.*, 3*d* metals. Many other practically important properties, driven by the crystal structure, can be expected, among which thermoelectric and magnetocaloric properties are of great importance for Eu. During my previous work, some patterns concerning the structure-property relationship in Eu-pnictides have been elucidated. It is worth mentioning that along with Eu, the oxidation state +2 is also stable but, to a lesser extent, for Yb. The size of the Yb^{2+} cation is in between Ca^{2+} and Sr^{2+}. Still, the formation of any Yb compounds has not been observed in the current study.

Previous work

The previous work at the Lomonosov Moscow State University has been majorly dedicated to two structure types – layered 1111 (ZrCuSiAs or LaOAgS) and the 3D clathrate-like compound $Eu_7Cu_{44}As_{23}$. The 1111-type group of materials has been extended by more than ten new fluorides, including those containing $[Eu_2F_2]^{2+}$ layers. It has been shown that the latter can be matched with $[T_2Pn_2]^{2-}$ layers, where *Pn* – P, As or Sb, and *T* – Zn and Mn only, but not any other transition metals.

The projection of the crystal structure of $Eu_7Cu_{44}As_{23}$ is provided in **Figure 1.2.** Besides the prototype, only $Sr_7Cu_{44}As_{23}$ crystallizes in the same structure type, and the antimonide $Eu_7Cu_{44}Sb_{23-\delta}$ adopts a slightly disordered and non-stoichiometric variant. It has been shown that in the predominantly ionic and hence insulating 1111 compounds, the magnetic ordering of an antiferromagnetic type is dominant. Contrary to that, the metallic Cu – As framework facilitates ferromagnetic-type RKKY interactions in $Eu_7Cu_{44}As_{23}$. Different variants of substitution can tune the strength of magnetic interactions.

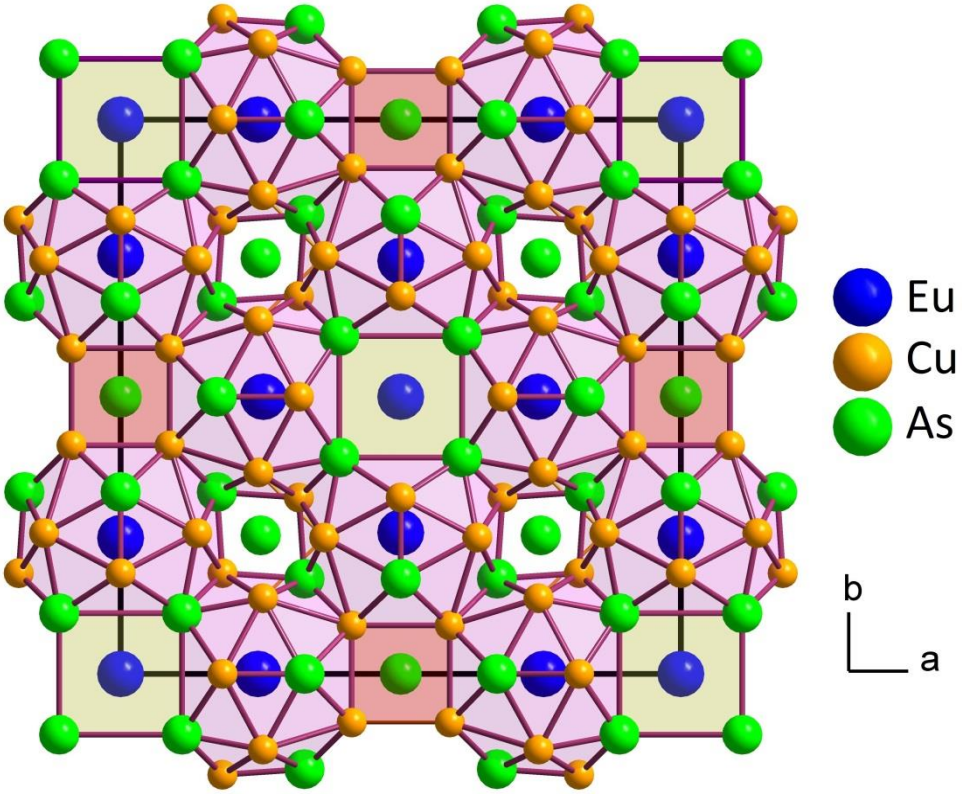

Figure 1.2 Projection of the crystal structure of $Eu_7Cu_{44}As_{23}$.

Justifications of techniques used

In contrast to in the previous work, where the main focus was on the crystallographic aspect of the investigated compounds, the current work is more focused on structure-properties relations. Evidently, it led to a more diverse range of characterization techniques. The classical solid-state synthesis is a major approach, with such variables as starting materials, temperature and time of annealing affecting the experiment. Yet, in some specific cases, it had to be decorated, for example, with additional mechanochemical treatment. X-ray crystallography is an essential part of the work, as it provides explicit information about both the internal structure of the material and the samples' quality, especially when combined with scanning electron microscopy techniques. For example, when it is impossible to produce a particular compound in a single-crystalline form, the structure factors can be reliably extracted using a full-profile diffraction pattern analysis, and the further refinement can be done with the Rietveld method especially when the starting model is available. The described method is quite often used for 1111-type compounds, which combine ionic and covalent fragments and thus makes difficult growth of single-crystal. Non-ambient diffraction studies are necessary for the elucidation of the lattice dynamics and phase transition behaviour. They were done in this work using both laboratory X-ray sources and

synchrotron (ESRF). The bulk physical properties (magnetization and heat capacity) were measured using conventional physical-properties measurement systems (PPMS) to perform a screening for low-temperature effects. The valence state of Eu in our compounds was also studied using ^{151}Eu Mössbauer spectroscopy. On top of various experimental studies, theoretical investigations of electronic structure and bonding were done, with the help of DFT (Density Functional Theory).

Finally, a substantial part of this work was neutron diffraction. The purpose was to elucidate the nature of magnetic transitions that take place in our materials. Neutron diffraction, which is a commonly used technique for characterization of the materials' crystal and magnetic structures, is somehow special when applied to Eu compounds. The major problem is a strong absorption of Eu when conventional wavelengths are used. The idea to perform the first neutron diffraction experiment came from the intention to understand the bulk magnetic properties of the EuMn*Pn*F (*Pn* = P, As, and Sb), prepared by me previously. While trying to identify the facilities and instruments where such experiments are possible, literature about this topic was analyzed, and specialists from respective instruments in different neutron sources around Europe were contacted. The most straightforward way is to use hot, *i.e.,* high-energetic, neutrons, to minimize absorption. The ILL facility in Grenoble, France, offers a unique instrument, the D4 diffractometer, which operates at 0.35 – 0.7 Å. Unfortunately, short wavelengths cause shrinking of conventional I *vs.* 2θ diffraction pattern to lower angles, which decreases the 2θ-resolution and precludes measuring the high-*d*-spacing reflections crucial for magnetic structures and complex atomic superstructures. Another option is to use a conventional wavelength for neutron powder diffractometers, but minimize the path of neutrons through the sample using double-walled vanadium cylinders. The diffractometer setup provides the same resolution independent from the size of a sample with the help of the long source-sample and sample-detector distances, and hence allows for preserving the diffracting volume. In this manner, we performed several experiments on the powder diffractometer SPODI at the Forschungs-Neutronenquelle Heinz Maier-Leibnitz Forschungsreaktor München II (FRM II), the only currently operating neutron source in Germany. As it is shown in the corresponding section, it is indeed possible to obtain data of reasonable quality, but at the cost of increased counting time. It was not the case for another highly-effective diffractometer WISH located at ISIS Neutron and Muon Source, Rutherford Appleton Laboratory of the Science and Technology Facilities Council, UK. A set of technological improvements, which included optimization of flux and detecting system made this diffractometer, according to the

opinion of the specialists in this field, the most effective in Europe. For example, in our work, WISH has allowed to unambiguously confirm the intrinsic nature of three low-temperature magnetic phase transitions in the newly-discovered clathrate $EuNi_2P_4$ as it is described below. Finally, the concept of magnetic crystallography widely implemented in JANA 2006 was of particular interest to me and was extensively used for refinements.

Summary of chapters

A chapter-by-chapter description of the primary motivation, results, and difficulties/limitations of the current work that were not fully reflected in the text of the chapters, is provided below.

The first group of compounds considered is Eu-analogs of the superconductors in the ternary Sr – Pt – P system, $SrPt_3P$, $SrPt_6P_2$, and $SrPt_{10}P_4$. The first compound of this group induces intensive discussions in the literature due to the unconventional mechanism of superconductivity observed therein. We succeeded in the preparation of two proposed compounds, $EuPt_3P$ and $EuPt_6P_2$, while the third one, $EuPt_{10}P_4$, cannot be prepared and probably does not exist. It is suggested that the difference in structural complexity is a reason for such behaviour. In contrast, the difference in magnetic properties is due to the difference in the separation of magnetic cations. Attempts to prepare analogs with Pd instead of Pt resulted in the preparation of single-crystals of new compound $Eu_2Pd_{15}P_4$, with a crystal structure reminiscent to that of $Y_2Pd_{14}B_5$ and ferromagnetic ordering below 7 K. Attempts to prepare Yb analogs – $YbPt_3P$, $YbPt_6P_2$ – were unsuccessful.

The second group of compounds is Eu containing clathrates, the analogs of $SrNi_2P_4$, $BaNi_2P_4$, and $BaCu_2P_4$, previously together with their transport properties reported by Prof. K. Kovnir. The very first experiments have shown that $EuCu_2P_4$ most likely does not exist ($EuCu_2P_2$ and elemental P form instead), while $EuNi_2P_4$ can be prepared by applying the same synthetic procedure as it has been described for $SrNi_2P_4$. Unfortunately, the Eu-samples always contain a substantial amount of another ternary phase $EuNi_2P_2$ and phosphorus as byproducts, contrary to the case of the Sr-compounds. In a personal discussion with Prof. Kirill Kovnir, he confirmed that his research group also struggled with the same problem without a successful solution. Several synthetic techniques have been attempted in the current work, including high-pressure synthesis and flux growth. The existence of the other more stable compounds in this ternary system has been proven to be a factor precluding the formation of the target phase in thermodynamic mode. It has appeared that an

additional mechanochemical input *via* ball-milling is necessary to prepare $EuNi_2P_4$ due to the sizable mismatch between Eu^{2+} cations and the Ni – P cages. This compound raised two questions about its functional properties and underlying physical characteristics. The first question concerns thermoelectric performance and the transport properties characteristics (Seebeck coefficient, electrical and thermal conductivity) that comprise the thermoelectric figure-of-merit. Though the material is metallic, it shows a relatively low thermal conductivity due to the rattling of the Eu^{2+} cations inside the oversized cages, which has been proven independently through heat capacity, the temperature dependence of atomic displacement parameters and Raman scattering.

Another point is that substitution of the non-magnetic Sr^{2+} cation with magnetic Eu^{2+} caused a substantial difference in the low-temperature behaviour of $EuNi_2P_4$, which features three magnetic phase transitions at ~ 2.5 K, ~ 6.1 K and ~ 11 K in zero fields along with several effects in isothermal magnetization sections. While only the first and the third effects are visible in resistivity and heat capacity data, the second one has the strongest manifestation in magnetic susceptibility data. Based on a set of constant-field and isothermal magnetization measurements, a low-temperature field *vs.* temperature phase diagram of $EuNi_2P_4$ was proposed and the phase boundaries of the antiferromagnetic phases were drawn. Altogether, these data have been published in Inorganic Chemistry Frontiers, while still leaving several additional questions on the low-temperature magnetic behaviour and lattice dynamics. As clarification using the dedicated local tools was necessary, a set of neutron diffraction experiments on the WISH diffractometer was performed. The diffraction patterns below 11 K featured additional magnetic reflections, which are different for different phase fields (below 2.5 K, between 2.5 K and 6.1 K and between 6.1 K and 11 K), confirming the intrinsic nature of these transitions.

The next focus is the 1111 structure type, which is also quite often designated as ZrCuSiAs or LaOAgS. One should comment here on discrepancies in the titles of this structure type. Both prototypes ZrCuSiAs and LaOAgS feature similar cell dimensions, space group (*P4/nmm*), and the Wyckoff sequence, but the bonding patterns are substantially different. While the second compound is truly layered (short distances within LaO and AgS fragments, and long between them), the first one is truly three-dimensional. The demarcation between these two structures is quite common among crystallographers and even implemented in the "Pearson's Crystal Data" database. Still, in the majority of publications, it is designated as ZrCuSiAs as earlier discovered or also 1111, according to the overall stoichiometry, for

the sake of simplicity among the physical community. Overall, this structure type hosts over two hundred representatives, most of which, however, feature oxygen-containing $[Ln_2O_2]^{2+}$ layers (*Ln* – lanthanide). The possibility of placement of fluorine-containing layers $[A_2F_2]^{2+}$ (*A* – alkali-earth cations, Eu^{2+} or Sr^{2+}) has been considered in my previous work and expanded further on in the current study. The existence of the EuF*TPn* materials (*T* = Zn and Mn, *Pn* = P, As, and Sb) suggested that EuFMg*Pn* materials could also be prepared. A more general question was if any of the supposedly isostructural *A*FMg*Pn* (*A* – not only Eu but also Ca, Sr or Ba) compounds are feasible. Apparently, only BaFMg*Pn* compounds were realized for all pnictogens – from phosphorus to bismuth, while the absence of the others has been corroborated computationally. The new compounds are a very rare case of transition-metal-free phases adopting the title structure type.

The new compounds EuFAgSe and $EuFAg_{1-\delta}Te$ were synthesized from the elements and EuF_3. It has appeared that their relatively low thermal stability allows only for a narrow temperature range of one-pot synthesis. As it has been shown by magnetic measurements and is in line with ionic representation, these compounds contain the rare red-ox pair Eu^{2+}/Ag^{+}. While trying to shed light on valence fluctuations in the $EuFAg_{1-\delta}Te$, Mössbauer spectroscopy has been implemented and provided evidence for a substantial $Eu^{2+}/Ag^{+} \leftrightarrow Eu^{3+}/Ag$ interplay.

Finally, when dealing with this structure type, I returned to the previously discovered by me compounds EuF*TPn* (*T* = Zn and Mn, *Pn* = P, As, and Sb) along with the EuFFeAs, which has been reported before by other authors. From the bulk magnetization measurements, they are very similar – antiferromagnets with T_Ns ~ 3 K. Still, on a microscopic scale, metallic EuFFeAs shows a very complex incommensurate ordering of Eu^{2+} magnetic moments, the semiconducting EuFZnAs, and EuFMnAs both exhibit a commensurate stripe order with the latter not depending on the magnetism of the transition metal cation (Zn^{2+} with $3d^{10}$ or Mn^{2+} with $3d^{5}$).

Studies showing success in neutron diffraction experiments were used as a basis to suggest that this technique can also be applied to other Eu-materials that have already been reported. $EuCu_4P_3$ similar to $EuNi_2P_4$, shows a set of three magnetic phase transitions. Unfortunately, similar to the previous experiment, neutrons were unable to distinguish between the nature of the magnetically ordered phases, and some additional measurements will be necessary.

The crystallographic background might seem relatively straightforward since analogies between Eu^{2+} and Sr^{2+} have been available for a long time now. Still, we should consider that solid-state studies are done both by scientists with a chemical and physical background. This study contains one inspiring example of a compound that has been overlooked both by chemists and physicists – the antiperovskite $EuPt_3P$. For the chemists, this compound does not spark interest, as its existence is so obvious given the $SrPt_3P$ phase, which adopts a straightforward antiperovskite crystal structure. On the other hand, other compounds from this series – MPt_3P (M = Ca, Sr, La, and Ce), as well as similar borides, induced such active discussions in the literature, but still did not result in the preparation of $EuPt_3P$. Results from this study have been reported in Dalton Transactions and have already attracted attention (in private communication) from the physicists working on the $SrPt_3P$ compound.

2 Synthesis, crystal and electronic structure of the Pt-rich phosphides $EuPt_3P$ and $EuPt_6P_2$

Abstract

Two new ternary Pt-rich phosphides, $EuPt_6P_2$ and $EuPt_3P$, have been prepared *via* two-step solid state reaction. Their crystal structures have been determined from powder XRD data. $EuPt_6P_2$ is isostructural to $SrPt_6P_2$ (cubic, *Pa*-3, a = 8.4603(1) Å); its crystal structure comprises corner-shared Pt_6P trigonal prisms hosting Eu^{2+} cations in the cuboctahedral voids of the framework. $EuPt_3P$ is isostructural to the $SrPt_3P$ anti-perovskite (*P4/nmm*, a = 5.7452(1) Å, c = 5.4212(1) Å). Magnetization measurements reveal magnetic response caused by the Eu^{2+} ($4f^7$)-cations. $EuPt_6P_2$ is paramagnetic exhibiting no phase transitions down to 1.8 K, whereas $EuPt_3P$ orders ferromagnetically below 19 K. Similar to $SrPt_6P_2$ and $SrPt_3P$, the new compounds are metallic with states near the Fermi level predominantly formed by 5*d* orbitals of Pt.

Introduction

Since the discovery of superconductivity at the beginning of the previous century, several large groups of superconducting materials were investigated extensively in order to elucidate the physical mechanism of this exciting phenomenon. In course of time, smaller groups of structurally or chemically related superconducting compounds arise unexpectedly, thus positioning new questions about the origin of superconductivity therein. A small family of Pt-rich compounds found in the Sr–Pt–P system is an illustrative example. It includes three compounds, $SrPt_3P$, $SrPt_6P_2$ and $SrPt_{10}P_4$, which were reported to become superconducting below 8.4 K, 0.6 K and 1.4 K, respectively [1 – 4]. Moreover, an unconventional mechanism of superconductivity in $SrPt_3P$ was highlighted by detailed physical studies [4]. Besides these phosphides, superconductivity was also reported for some other platinum compounds including SrPtAs [5], $SrPt_2Ge_2$ [6], $CaPtSi_3$ [7], $SrPtGe_3$ [8], $Ca_2Pt_3Si_5$ [9], and Li_2Pt_3B [10], while structural diversity can be illustrated by many representatives, particularly the incommensurate phase $Sr_2Pt_{8-x}As$ [11]. Extensive studies of the $SrPt_3P$ phosphide [12 – 14] revealed that the compound is a likely multi-band superconductor similar to $PrPt_4Ge_{12}$ [15]. Upon Ca substitution, the T_C of $SrPt_3P$ does not scale with the density of states at the Fermi level, thus further suggesting an unconventional mechanism of superconductivity in this compound [4]. The centrosymmetric crystal structure of $SrPt_3P$, as well as those of the related non-centrosymmetric $CePt_3Si$ [16] and

$CePt_3B$ [17], were found to be rather flexible towards substitution on the alkali-/rare-earth position. For instance, all APt_3P compounds (A = Sr, Ca, La [1] and Ce [18]) adopt a similar anti-perovskite tetragonal structure. However, while the representatives containing non-magnetic $A = Sr^{2+}$, Ca^{2+} and La^{3+} are superconductors, their magnetic Ce^{3+} ($4f^1$) containing analog $CePt_3P$ exhibits antiferromagnetic ordering and a Kondo effect without showing any traces of superconductivity [18]. The second compound in the Sr – Pt – P system, $SrPt_6P_2$, adopts a yet unique structure and, according to [2], does not tolerate substitution of Sr^{2+} by Ca^{2+} or Ba^{2+}. It is known that Eu^{2+} commonly behaves as a crystal chemical analog of Sr^{2+}, particularly in pnictides and chalcogenides, where Eu^{2+} is relatively stable against oxidation to Eu^{3+}. The very similar ionic radii of Eu^{2+} (1.25 Å for coordination number 8) and Sr^{2+} (1.26 Å) allow formation of isostructural compounds in cases requiring precise geometrical matching [19], as illustrated by many couples of pnictide and chalcogenide compounds [20 – 23]. This allows proposing the existence of the Eu^{2+}-based analogs, namely $EuPt_3P$, $EuPt_6P_2$ and $EuPt_{10}P_4$ of the respective Sr-derivatives, which, to the best of our knowledge, were not reported yet.

Besides crystal-chemical interest, the proposed compounds can be attractive from the physical point of view due to effects originating from size and magnetism of Eu. First of all, one might expect, since the Eu^{2+} cations bear a high magnetic moment ($4f^7$), a possibility of unusual magnetic phenomena originating from the coupling between the Eu^{2+} magnetic system and the metallic or even superconducting Pt–rich framework. Another point is that due to the slightly smaller atomic radius of Eu^{2+} compared to Sr^{2+}, one could also expect that the substitution of Sr^{2+} by Eu^{2+} would apply chemical pressure on the Pt–P framework, which is known to enhance superconductivity, for instance, in iron-based pnictide superconductors [24]. Finally, europium phosphides are also known to tolerate considerable amounts of Eu^{3+}, and some mixed-valence Eu^{2+}/Eu^{3+} compounds are known to exhibit rather complex magnetic behaviour [25], associated also with an abrupt valence change [26]. For example, it is worth noting that the Eu–Pt–P system contains the mixed-valent EuPtP where only a half of the Eu atoms (probably Eu^{2+}) can be substituted by Sr, so that SrPtP most likely does not exist [27]. It is also thinkable that the Eu–Pt–P ternary system can host compounds exhibiting coexistence of superconductivity and ferromagnetism, a phenomenon claimed for doped $EuFe_2As_2$ [28].

Herein, we report on the synthesis, crystal and electronic structures as well as magnetic properties of two new compounds in the Eu–Pt–P system. $EuPt_3P$ and $EuPt_6P_2$ are

isostructural to their strontium-based archetypes. Our attempts to prepare $EuPt_{10}P_4$ were so far unsuccessful.

Experimental section

Synthesis and primary characterization. Polycrystalline $EuPt_6P_2$ and $EuPt_3P$ were prepared *via* similar solid-state routes. The starting materials were granules of Eu (ChemPur, 99.9%), Pt pieces (99.99%), and PtP_2 powder obtained by annealing Pt and P (Sigma Aldrich, 99.9%) at 1073 K for 4 days. All operations were performed in an argon-filled glove-box (MBraun). Eu was chopped prior to the reaction. The mixtures (~0.5 g total) of the starting materials (50% excess of Eu-metal) were placed in silica-jacketed graphite crucibles, evacuated, and sealed. First, the samples were annealed at 1273 K for 2 days (heating rate 5 K/min). The brittle intermediate products were milled, pressed into pellets (6 mm diameter, 40 bar external pressure), sealed in graphite-lined silica tubes and annealed at 1173 K for 4 days. These operations were repeated until homogenous crystalline materials were produced.

The samples are stable in air for weeks. Their phase composition was checked using a STOE STADI P diffractometer (STOE & Cie, Darmstadt, Germany) equipped with a Dectris Mythen 1K detector with the Cu-$K\alpha_1$ radiation (λ = 1.5406 Å). $EuPt_6P_2$ and $EuPt_3P$ were found as the major phases. Elemental composition was confirmed using a Zeiss EVO MA 15 scanning electron microscope equipped with a Bruker Quantax EDX system with an X Flash Detector 630 M. According to DTA measurements, performed on a SETARAM TG-DTA 92 (silica container sealed in vacuum, 10 K/min heating rate), both compounds melt congruently at 1240±5 K ($EuPt_6P_2$) and 1225±5 K ($EuPt_3P$).

Crystal structure determination. Single crystals suitable for structure determination could not be produced during the synthesis. Therefore, crystal structures were refined from high-quality powder X-ray diffraction data, acquired at 293 K on a STOE STADI P diffractometer (STOE & Cie, Darmstadt, Germany) equipped with a Dectris Mythen 1K detector. Mo$K\alpha_1$ radiation (λ = 0.709300 Å) was utilized in order to increase the q-range of the data (d_{min} = 0.6 Å). A Rietveld refinement was performed in the JANA2006 [29] software using the crystal structures of $SrPt_3P$ and $SrPt_6P_2$ as starting models. The refinements proceeded in a straight-forward manner using standard mathematical apparatus (Pseudo-Voigt profile function; Legendre polynomials of up to 15th degree for background treatment) implemented in JANA2006. Only traces of impurities were found in the $EuPt_6P_2$ sample, while $EuPt_3P$ was found to contain ~ 4 mass % PtP_2. At the final stage, occupancies of all

atoms were checked and appeared to be equal to unity within 3σ, confirming the composition. Experimental details are collected in **Table 2.1**; the refined structural data are given in **Table 2.2** and selected interatomic distances in **Table 2.3**; final Rietveld refinement plots are presented in **Figure 2.1**.

Magnetic and heat capacity measurements. Magnetization was measured on pellets of polycrystalline $EuPt_6P_2$ and $EuPt_3P$ using a MPMS 3 SQUID from Quantum Design. The measurements were performed in the temperature range 1.8–380 K in applied fields up to 7 T. Heat capacity was measured with the relaxation method using Quantum Design PPMS in the temperature range 1.8–50 K in applied fields up to 10 T.

Table 2.1 Details of powder diffraction experiments for $EuPt_6P_2$ and $EuPt_3P$

	$EuPt_6P_2$	$EuPt_3P$
Space group	*Pa*-3 (*No.* 205)	*P4/nmm* (*No.* 129)
Z	4	2
Pearson symbol	*cP*36	*tP*10
Cell parameters		
a in Å	8.4603(1)	5.7452(1)
c in Å	= a	5.4212(1)
V in Å^3	605.56(1)	178.94(1)
$d_{calc.}$ in g/cm^3	15.19	14.26
2θ range in deg for $MoK_{\alpha 1}$	7 – 71	7 – 71
Data points/overall parameters	4262/28	4329/38
Reflections/structural parameters	465/8	261/11
R values (%):		
R_F	2.84	3.95
R_P	1.93	2.06
R_{wP}	2.59	2.92
χ^2	1.43	2.15

Table 2.2 Atomic coordinates and displacement parameters in the structures of $EuPt_6P_2$ and $EuPt_3P$.

Atom	Position	*x/a*	*y/b*	*z/c*	U_{iso} in Å^2
		$EuPt_6P_2$			
Pt	24*d* (*x; y; z*)	0.6560(1)	0.34235(8)	0.07815(8)	0.0055(2)
Eu	4*b* (½; 0; 0)	½	0	0	0.0072(5)
P	8*c* (*x; x; x*)	0.1956(6)	*x*	*x*	0.005(1)
		$EuPt_3P$			
Pt1	2*c* (0; ½; *z*)	0	½	0.1436(3)	0.0035(4)
Pt2	4*e* (¼; ¼; ½)	¼	¼	½	0.0055(2)
Eu	2*a* (0; 0; 0)	0	0	0	0.0045(5)
P	2*c* (0; ½; *z*)	0	½	0.262(2)	0.025(4)

Table 2.3 Selected interatomic distances *d* (in Å) for $EuPt_3P$ and $EuPt_6P_2$.

$EuPt_6P_2$		$EuPt_3P$	
d(Pt – Pt)	2.812(1) × 2	*d*(Pt1 – Pt2)	2.804(1) × 4
	2.827(1) × 2		
	2.816(1) × 2	*d*(Pt2 – Pt2)	2.8726(1) × 4
	3.337(1) × 2		
d(Pt – P)	2.306(5) ×3	*d*(Pt1 – P)	2.20(1)
	2.362(5) × 3	*d*(Pt2 – P)	2.408(6)
d(Pt – Eu)	3.2510(7)	*d*(Pt1 – Eu)	2.9761(5) × 4
	3.2687(8)	*d*(Pt2 – Eu)	3.3872(1) × 8
d(Eu – P)	3.480(5) × 6	*d*(Eu – P)	3.203(5) × 4

Electronic structure calculations were performed on the Density Functional Theory (DFT) level using the pseudopotential projector augmented wave method (PAW) as implemented in the Vienna *ab initio* Simulation Package (VASP) [30, 31]. A Monckhorst-Pack *k*-point mesh of 12×12×12 was employed, and the energy cutoff was set at 500 *eV* [32]. The PBE exchange-correlation functional of the GGA-type was used in the PAW-based calculations [33].

In order to account for the *f*-orbitals of Eu^{2+}, a special potential for europium, supplied with the VASP package, was used, which places the localized *f*-orbitals into the core. The use of this potential was validated by unconstrained structure optimization performed for the $EuPt_3P$ compound (the same computational conditions were used). The optimized unit cell metrics were: a= 5.7590 Å, c= 5.4619 Å, V=181.15 $Å^3$, which is in a very good agreement with experimental values (see **Table 2.1**) and there is only *ca.* 1.23% difference in cell volume. The convergence of the total energy with respect to the *k*-point sets was checked. Experimental unit cell parameters and coordinates of atomic positions were taken as starting points for calculations, with atomic coordinates relaxed while retaining cell metrics. Atomic charges in the direct-space analysis were calculated according to Bader's QTAIM approach [34, 35]. The electron localization function (ELF) was calculated by the internal VASP routine according to [36].

Results and discussion

Synthesis. Our first attempts to prepare $EuPt_3P$ and $EuPt_6P_2$ from the elements resulted in samples with high impurity content. Essentially better results were achieved using PtP_2 as a precursor akin to the synthesis of the Sr compounds [1]. Due to the high volatility of Eu-metal at elevated temperatures, a 50 % excess had to be applied in order to prepare samples of acceptable quality. According to DTA measurements, both compounds melt between 1173 K and 1273 K, thus we can assume that the preliminary treatment at 1273 K leads to the formation of melts, while the consequent annealing below the solidification points drives the system toward equilibria and crystallization. The same synthetic procedure was applied upon targeting $EuPt_{10}P_4$ but resulted in a complex mixture of $EuPt_3P$, $EuPt_6P_2$ and other unidentified phases. Thus, the Eu–Pt–P ternary system is likely to contain some more compounds whose nature remains to be established.

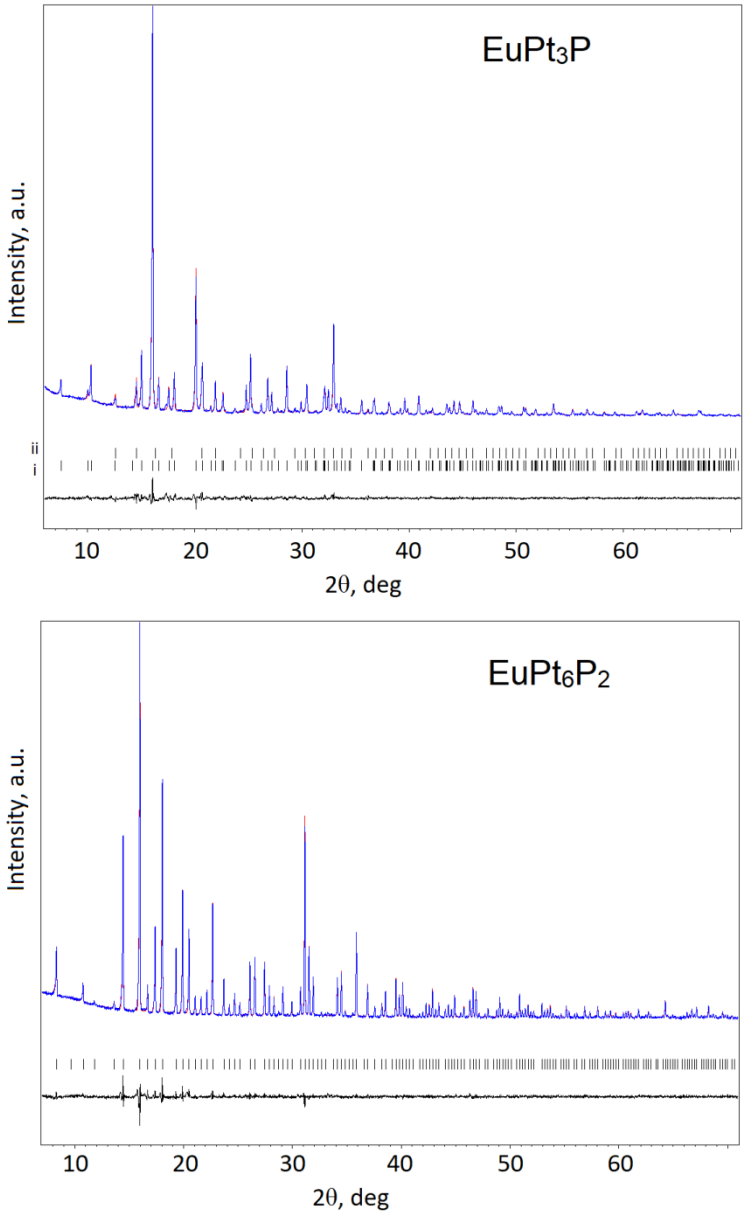

Figure 2.1 Experimental (blue), calculated (red), difference (black) and positions of peaks (black) – Rietveld plots for $EuPt_3P$ and $EuPt_6P_2$. In the $EuPt_3P$ sample, an impurity of PtP_2 (ii) has been included into refinement.

Crystal structures. General projections and polyhedral description of the $EuPt_3P$ and $EuPt_6P_2$ crystal structures are presented in **Figures 2.2** and **2.3**, respectively. $EuPt_3P$ is isostructural to APt_3P (*A* = Ca, Sr, La and Ce) and exhibits a tetragonal-distorted anti-perovskite type ABX_3 crystal structure, where *A* = Eu (large ion), *B* = P (small ion), and *X* = Pt. The tetragonal distortion is most pronounced in the asymmetric coordination of P atoms whose coordination spheres can be described as a square pyramid formed by the Pt atoms (one axial at 2.20 Å and four basal at 2.41 Å; **Figure 2.2**). These distances are quite similar to the lengths of the Pt – P contacts reported in the other structures (2.36 Å in EuPtP [27],

2.20 Å and 2.43 Å in $SrPt_3P$ [1], 2.21 Å in Ce_2Pt_8P [37] and $DyPt_8P_2$ [38]). Considering the very distant sixth Pt atom separated by 3.23 Å, we may expand the coordination of P to a strongly distorted octahedron, only to show the topology of the anti-perovskite structure. The framework formed by the PPt_5 moieties is additionally stabilized by a short Pt2 – Pt2 contact of 2.87 Å (compare to 2.77 Å in metallic platinum), while the Pt1 atom, only weakly bonded to the P atoms, forms rather short bonds (2.80 Å) to four Pt2 atoms.

The Eu^{2+} valence is confirmed by the magnetic data. These ions fill the distorted cuboctahedral voids in the Pt_3P framework formed by 4 Pt1 at 2.98 Å and 8 Pt2 at 3.38 Å. The four P atoms at 3.20 Å form a distorted tetrahedron around Eu^{2+} completing the coordination number of Eu^{2+} to 16. It is worth noting that the Pt1 – Eu distance of 2.98 Å is among the shortest found in the literature (compare, for example, with 3.08 Å in $Eu_2Pt_7MP_3$ (M = Al, Mg, Fe, Zn and Mn) [39] and EuPtP [27] or 3.06 Å in EuPtGa [40]) and essentially smaller than the sum of the metal radii of Eu and Pt (3.20 Å). This may indicate a pronounced attraction (most likely electrostatic, see below) between Eu and Pt1. The same peculiarity is also observed in the crystal structure of $SrPt_3P$ with the shortest Sr – Pt distance of 2.99 Å.

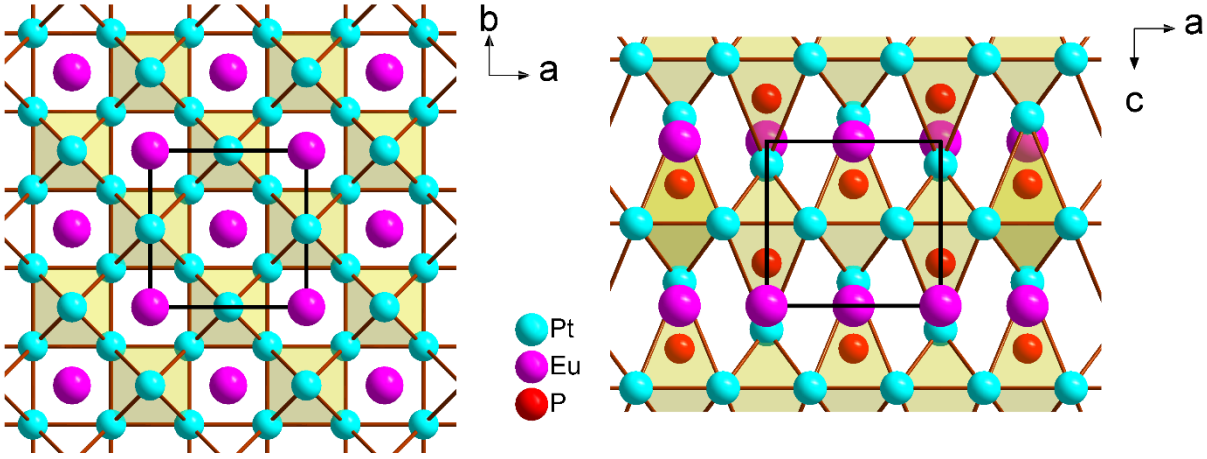

Figure 2.2 Projection of the $EuPt_3P$ crystal structure along the *c*-direction and *a*-direction. The coordination of phosphorus is shown as distorted octahedral to underline the relationship to and the distortion of the parent anti-perovskite structure type.

A peculiar trend in the cell dimensions within the APt_3P series (*A* = Ca, Eu and Sr) is worth mentioning. While the increase of the cell volume (175.6 $Å^3$ for *A* = Ca, 178.9 $Å^3$ for *A* = Eu and 181.7 $Å^3$ for *A* = Sr) and the *a* cell parameter (5.667 Å for *A* = Ca, 5.745 Å for *A* = Eu and 5.809 Å for *A* = Sr) are consistent with the increased radius of the *A* cation, the *c* cell parameter shows an opposite trend (5.4687 **in %** for *A* = Ca, 5.421 Å for *A* = Eu and 5.383

Å for *A* = Sr). As follows from **Figure 2.2**, the square grid of the Eu^{2+} cations located at the shortest distance of 4.06 Å forms the *ab*-plane, while the shortest Eu – Eu distances in the *ac*-plane are equal to the *c* parameter, *i.e.*, 5.42 Å. As a larger *A*-cation in the Eu position, Sr^{2+} will lead to an increase in the *a* parameter and an elongation of the *A*–Pt and *A*–P distances. This would result in an under-bonding of the P and Pt1 atoms, which is in turn compensated by the shortening of the P–Pt2 and Pt1–Pt2 distances yielding the decrease in the *c* parameter as observed experimentally.

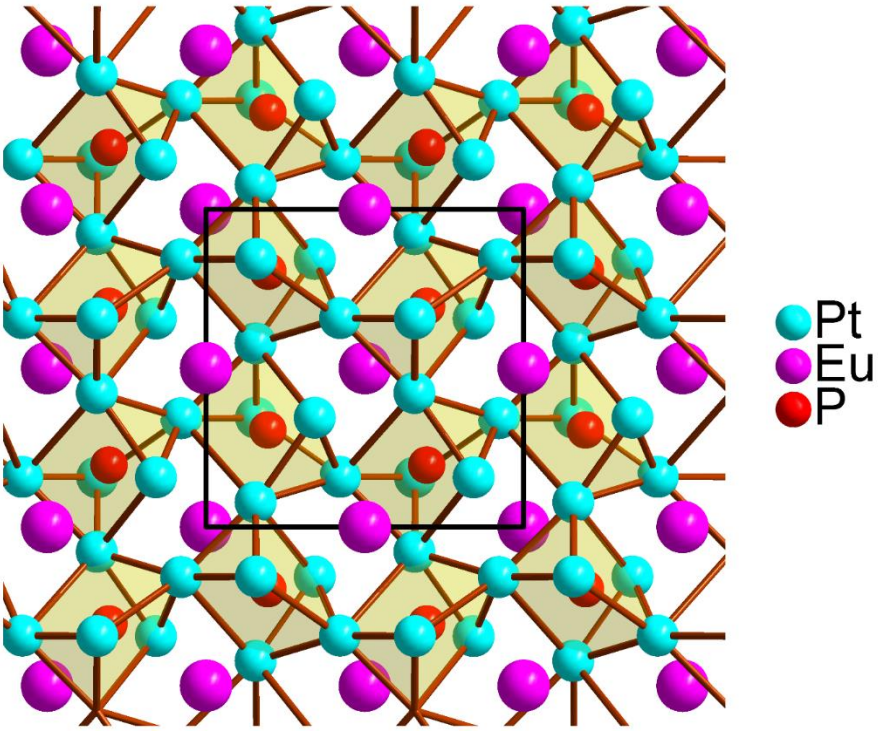

Figure 2.3 Projection of the $EuPt_6P_2$ cubic crystal structure.

Though the composition of $EuPt_6P_2$ is characterized by the same Pt:P ratio as $EuPt_3P$, their crystal structures (**Figure 2.3**) are entirely different. $EuPt_6P_2$ is comprised by three symmetrically independent positions of Pt, Eu, and P, respectively. Each P atom is surrounded by 6 Pt atoms separated by 2.31 – 2.36 Å and forming a slightly distorted trigonal prism. These corner-shared Pt_6P prisms form a framework accommodating the Eu^{2+} cations. The latter are coordinated by 12 Pt atoms at 3.25 – 3.27 Å, which is just slightly above the sum of the metal radii (3.20 Å), and 6 P atoms located at slightly longer distances of 3.48 Å (**Figure 2.3**). $EuPt_6P_2$ is a second representative of the $SrPt_6P_2$ crystal structure type. Its cubic cell parameter is slightly lower than that of the archetype, as expected from the ionic radii of Sr^{2+} and Eu^{2+}.

As discussed in [2], the closest structurally-related compound is $Sn(SeO_3)_2$ (≡ SnO_6Se_2, space group *Pa*-3) [74], which can be interpreted as a framework of essentially off-centered SeO_6 trigonal prisms. More distant relationships can be traced to some polymorphic forms of alkaline-earth nitrates, $A(NO_3)_2$ (*A* = Ca, Sr, Ba) [42].

Electronic structure. Calculated total and projected DOS for $EuPt_3P$ and $EuPt_6P_2$ are shown in **Figure 2.4**. As seen from the plots, dominant contributions near the Fermi level are provided by Pt 5*d* states, which is quite common for Pt-rich intermetallics. Both compounds are metallic according to the calculations. Phosphorus *p*-states are mixed with platinum *d*-states at the Fermi level, indicating possible covalent bonding. Main contributions from Eu^{2+} *d*-states are above the Fermi level. Band structures (**Figure 2.5**) for both compounds confirm metallic properties and show no indications for prominent low-dimensionality of the compounds.

Calculated QTAIM charges are: -0.71 (Pt1), -0.22 (Pt2), +1.35 (Eu), -0.19 (P) for $EuPt_3P$, and -0.28 (Pt), +1.40 (Eu), +0.15 (P). Based on these calculations, one can conclude that both compounds are intermetallic in their nature and should not be considered as phosphides, the atomic charges of phosphorus being closer to zero than to -3. In $EuPt_6P_2$, the charges are even positive. Topological analysis of the ELF reveals covalent Pt – P pairwise interactions (marked 1 in **Figures 2.6** and **2.7**) at relatively high localization values. Scanning down to *ca.* 0.3 values (typical for Pt – Pt covalent interactions [43]) of the localization parameter also reveals a covalence between Pt atoms (marked 2). The absence of bonding attractors between Eu and other atoms indicates predominantly ionic interactions of the *A*-cation.

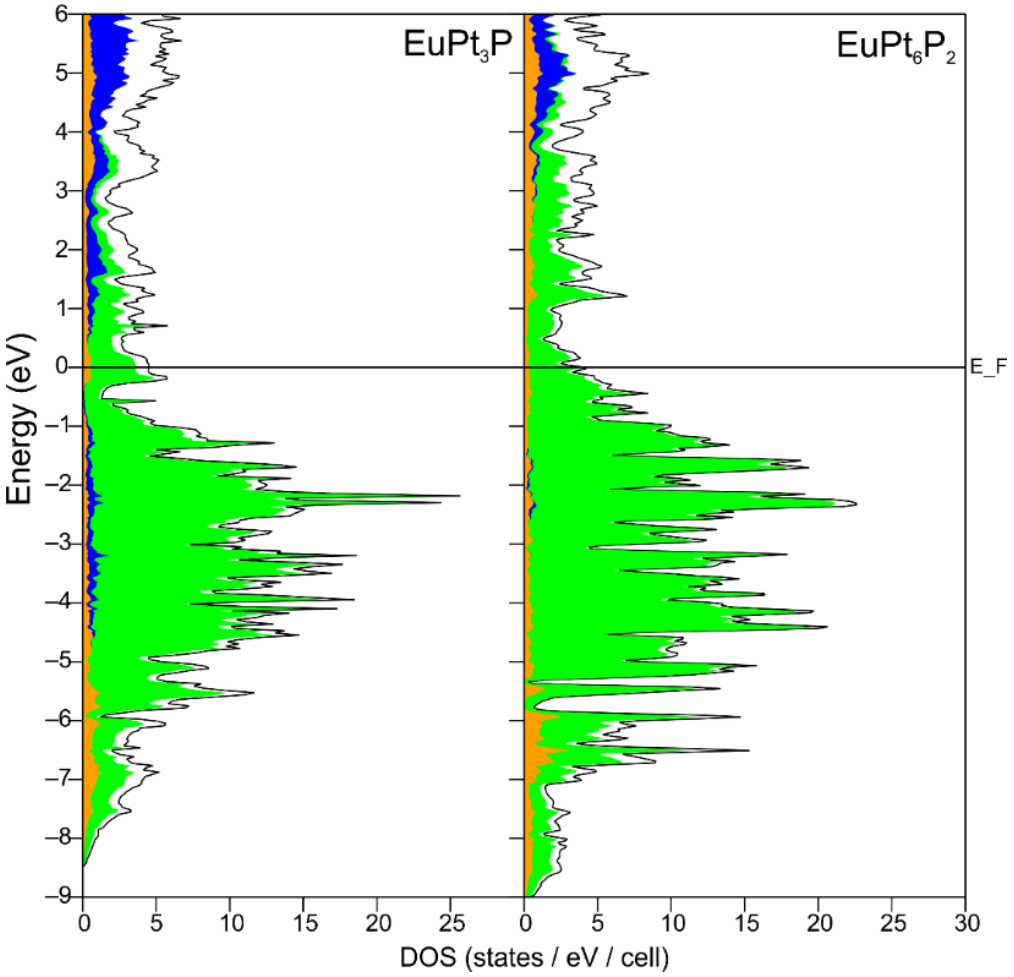

Figure 2.4 Total (TDOS) and projected (PDOS) densities of states near the Fermi level for $EuPt_3P$ (left) and $EuPt_6P_2$ (right). Green shading denotes platinum states, blue – europium, and orange – phosphorus.

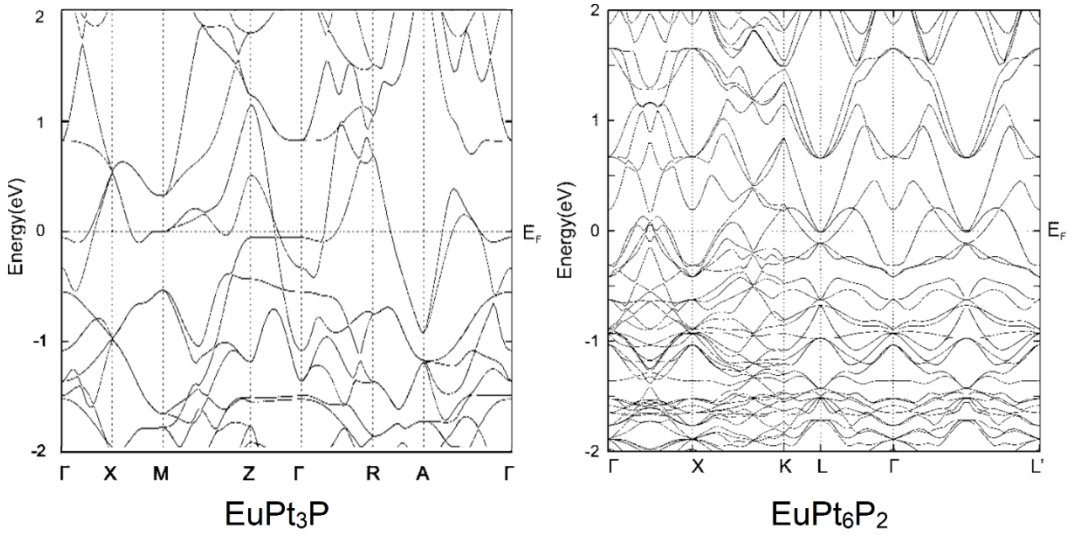

Figure 2.5 Band structures near the Fermi level for $EuPt_3P$ (left) and $EuPt_6P_2$ (right).

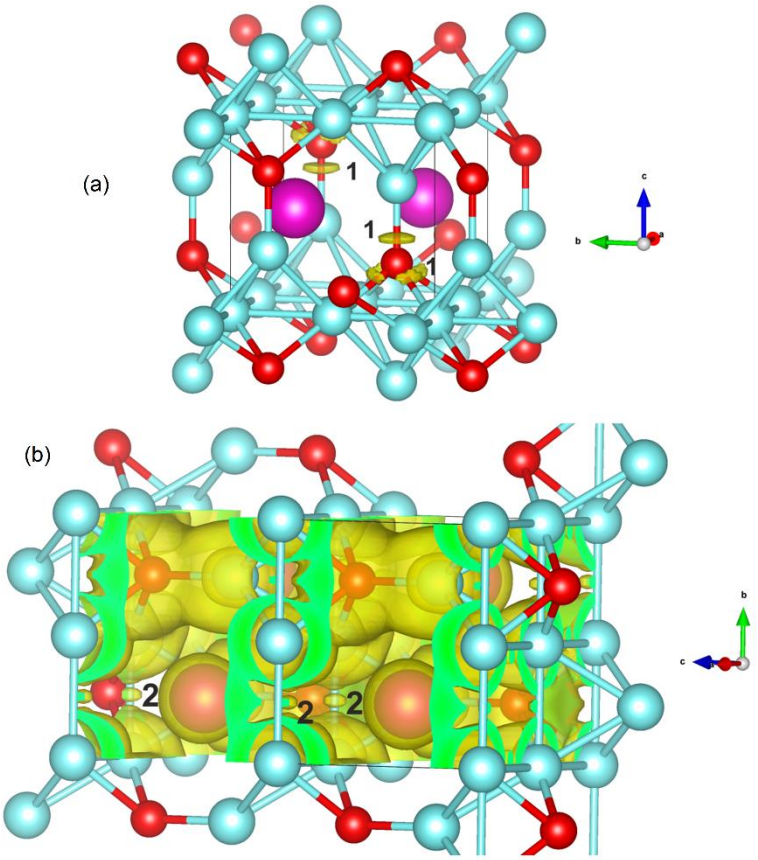

Figure 2.6 ELF isosurfaces (η = 0.74 – (a); η = 0.31 – (b)) for $EuPt_3P$. **1** – Pt – P bonding localization domains, **2** – Pt – Pt – bonding localization domains. Pt atoms are drawn in cyan, P atoms are red, Eu atoms are magenta, ELF isosurfaces are yellow.

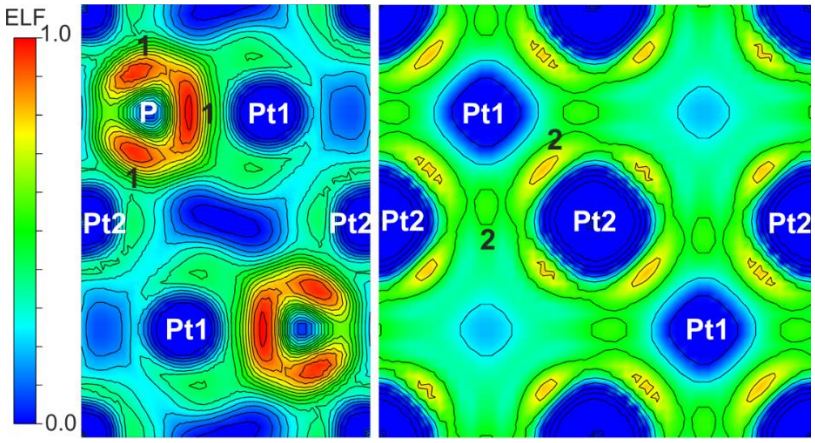

Figure 2.7 ELF sections passing through the Pt – P (left) and Pt – Pt (right) bonds for $EuPt_3P$. **1** – Pt – P bonding localization domains, **2** – Pt – Pt – bonding localization domains.

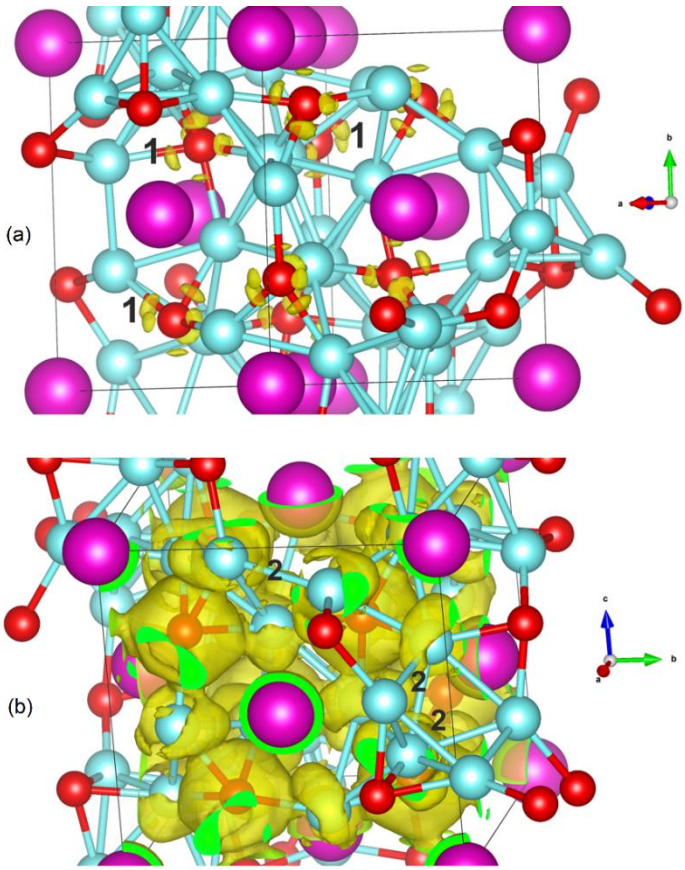

Figure 2.8 ELF isosurfaces (η=0.74 – (a); η=0.34 – (b)) for $EuPt_6P_2$. The Pt atoms are drawn in cyan, P atoms are red, Eu atoms are magenta, ELF isosurfaces are yellow. **1** – Pt –P bonding localization domains, **2** – Pt – Pt – bonding localization domains.

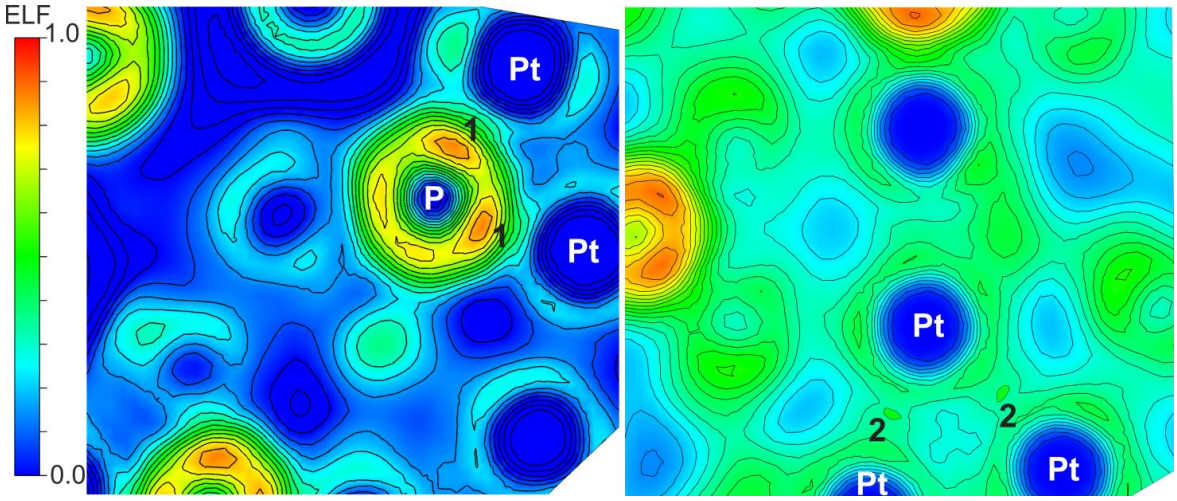

Figure 2.9 ELF sections passing through the Pt – P and Pt – Pt bonds for $EuPt_6P_2$. **1** – Pt – P bonding localization domains, **2** – Pt – Pt – bonding localization domains.

The ELF topology (**Figures 2.8** and **2.9**) of $EuPt_6P_2$ features similar Pt – P localization domains at high (η = 0.74) values of the localization parameter, indicating a similar kind of Pt – P covalency as in the case of $EuPt_3P$. The main difference between the two cases is the presence of two Pt positions with noticeable difference in atomic charges in $EuPt_3P$, while in the case of $EuPt_6P_2$ the negative charge is uniformly distributed between all Pt atoms. Another point of difference is that, although Pt – P bonds in $EuPt_6P_2$ are essentially two-center, as well as in $EuPt_3P$, there appears to be a degree of asymmetry about how the respective attractors are situated in $EuPt_6P_2$ (the lines connecting Pt and P atoms do not go through their centers), which might be a possible indication of small contribution from a third center, but this deviation is not sufficient to consider significant multi-center nature of these bonds.

At lower η values, we also observe localization domains that correspond, most likely, to the Pt – Pt interactions, although in this case they are somewhat obscured in the 3D plots by the domains corresponding to the Pt lone pairs and can be seen more clearly using the ELF sections (**Figure 2.9**). This represents rather typical problem for the *d*-metal based compounds with non-metals, where strong covalent bonds can be seen at relatively high (*ca.* 0.7 - 0.8) values of the localization parameter, while metal-metal bonds for transition metals appear at much lower η values, where they are easily masked by other features of isosurfaces.

Magnetic and heat capacity measurements. Magnetic susceptibility for $EuPt_3P$ is shown in **Figure 2.10**. Above 30 K, the sample behaves as a Curie-Weiss paramagnet with the positive (ferromagnetic) Curie-Weiss temperature θ_{CW} = 19.2 K and the effective moment μ_{eff} = 7.54 μ_B. In low fields, the susceptibility increases abruptly around 19 K indicating an onset of ferromagnetic order confirmed by the strongly non-linear magnetization curves measured below this temperature (**Figure 2.11**). At 1.8 K and 7 T, the magnetization reaches the value of M_s = 6.66 μ_B/f.u. Both M_s and μ_{eff} show a similar 5 % reduction compared to the theoretical values of, respectively, 7.0 μ_B/f.u. and 7.94 μ_B for Eu^{2+}. We ascribe this reduction to the presence of the non-magnetic PtP_2 impurity [44].

A Fisher's heat capacity d(χT)/dT plot (in SI) yields the transition temperature of T_C = 19.0 K. The onset of ferromagnetic order below this temperature is in excellent agreement with both the sign and the value of the Curie-Weiss temperature θ_{CW} = 19.2 K that should be equal to T_C in a simple three-dimensional ferromagnet. It is then particularly unexpected that the second transition is revealed by the low-field susceptibility around 5.5 K. To confirm the intrinsic nature of this transition, we measured the heat capacity (C_p) of $EuPt_3P$ and observed two λ-type anomalies indeed, as shown in **Figure 2.12.** Both anomalies are second-order in nature, as shown by the absence of latent heat. They are strongly field-dependent and significantly broaden already at 0.5 T, as typical for ferromagnets.

The area under the C_p/T curve yields the entropy S. By approximating the lattice contribution below 20 K with $C_p \sim T^3$, we single out the magnetic contribution and estimate the magnetic entropy of S_{mag} = 15.8 J/(mol·K), which is > 90% of the theoretical value $S_{mag} = R \cdot \ln(2s+1)$ = 17.3 J/(mol·K) for Eu^{2+} with $S = {}^7/_2$. The entropy contained in the 5.5 K anomaly is small but significant, whereas the susceptibility measured at 0.01 T increases by 15 % between 7 and 4 K. We conclude that the bulk sample is ferromagnetically ordered below 19 K, but a small part of it orders below 5.5 K only. This "residual" ferromagnetic ordering is probably unrelated to any crystalline impurity phase, as 5 – 10 % of such an impurity should be visible in XRD, but rather originates from the poorly crystalline phase, or represents an intrinsic effect. Spectroscopic probes would be useful to address the nature of the 5.5 K transition, but these are beyond the scope of our present work. The magnetic behaviour of $EuPt_6P_2$ is more simple and conventional (**Figure 2.13**). The sample is paramagnetic down to 1.8 K, the lowest temperature of our measurement. Above 50 K the curve can be approximated by the Curie-Weiss law with μ_{eff} = 8.13 μ_B and θ_{CW} = 3.1 K. The paramagnetic effective magnetic moment, as well as the saturation moment of M_S = 7.18 μ_B, are both consistent with the presence of Eu^{2+}, though slightly above the theoretical values of 7.94 μ_B and 7 μ_B respectively. The positive Curie-Weiss temperature and a slight deviation of the 1.8 K magnetization curve from the Brillouin function for Eu^{2+} indicate a possible ferromagnetic ordering below 1.8 K.

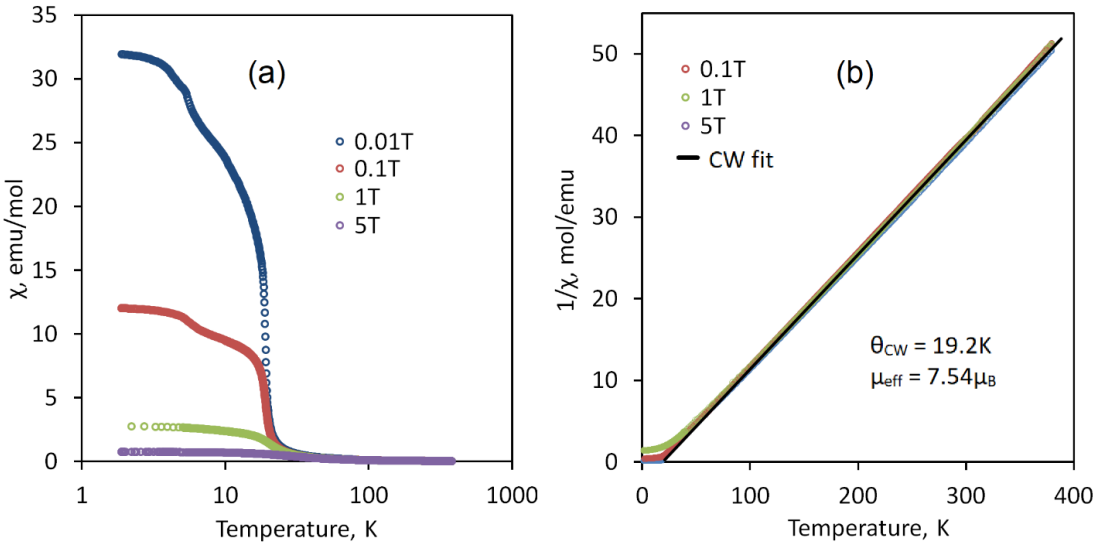

Figure 2.10 (a) Magnetic susceptibility *vs.* temperature plot for $EuPt_3P$ in 0.01, 0.1, 1 and 5 T fields. The temperature is plotted in logarithmic scale. (b) Curie-Weiss fit of the inverse magnetic susceptibility.

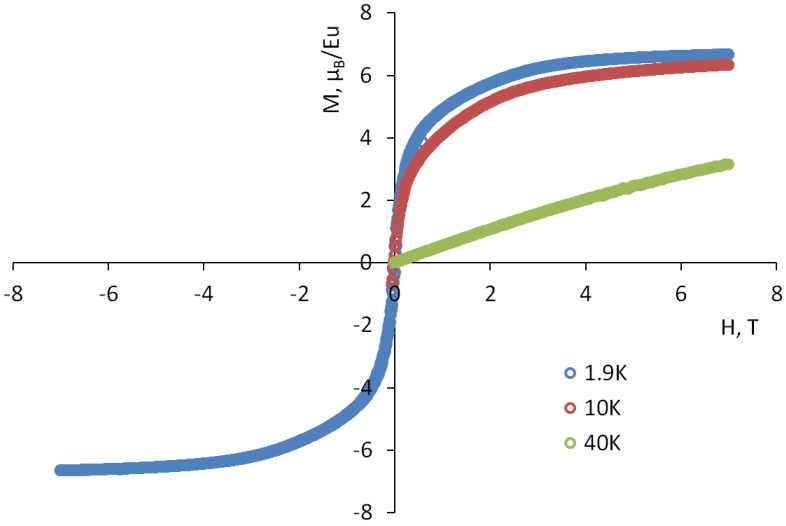

Figure 2.11 Magnetization curve taken at 1.9 K, 10 K (both in ferromagnetic state) and 40 K (in paramagnetic state) for EuP_3P.

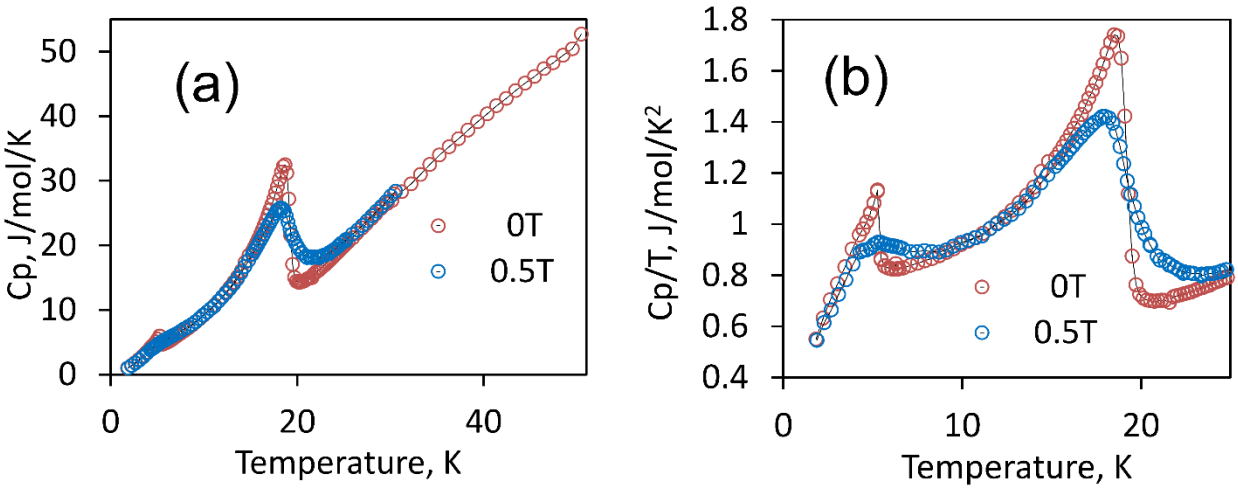

Figure 2.12 Heat capacity *vs.* temperature plot for $EuPt_3P$ (a) and *Cp/T vs. T* (b).

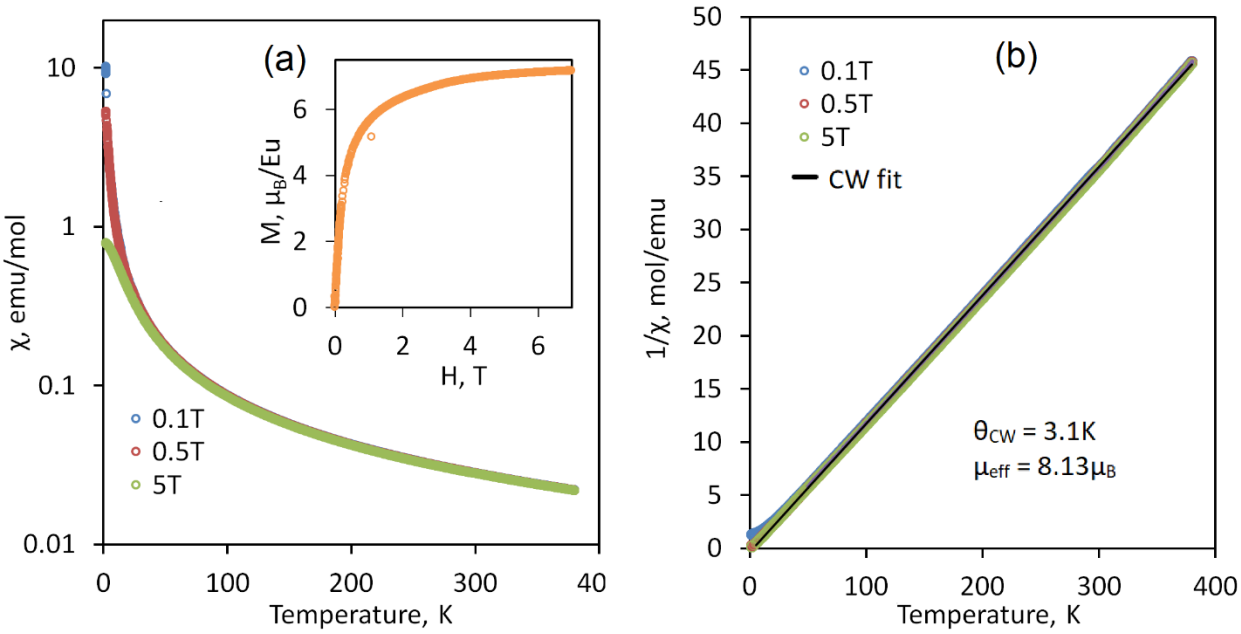

Figure 2.13 (a) Temperature dependence of the magnetic susceptibility for $EuPt_6P_2$ measured at fields of 0.01, 0.5 and 5 T. Note that the 0.01 and 0.5 T curves almost coincide. The magnetization curve measured at 1.8 K (in paramagnetic state) is shown as insert. (b) Curie-Weiss fit of the inverse magnetic susceptibility.

General overview and structure-property relationships. Among the three conjectured europium-based analogs of the Pt-rich compounds in the Sr–Pt–P ternary system, only two ($EuPt_6P_2$ and $EuPt_3P$) were found to exist, while $EuPt_{10}P_4$ could not be synthesized yet. In contrast to the mixed-valence EuPtP, the structures of the new compounds contain Eu atoms coordinated by Pt nearest neighbors, whereas P atoms reside in slightly longer distances. It is possible that such a "metallic" coordination mode stabilizes Eu^{2+} against Eu^{3+}. $EuPt_3P$ adopts the simplest (distorted anti-perovskite type) atomic arrangement, where the

Pt_3P framework can also accommodate some other cations (Sr^{2+}, Ca^{2+}, La^{3+} and Ce^{3+}) along with Eu^{2+}. In contrast, $SrPt_6P_2$ adopts a unique structure type, whereas Ca- and Ba-based analogs do not exist. The formation of $EuPt_6P_2$ can thus be considered a case of precise geometrical matching. The complex structure of $SrPt_{10}P_4$ is likely to be intolerant to any interventions. An "inverse" case of similar sensitivity has been observed for a Eu-based intermetallic, $Eu_7Cu_{44}Sb_{23-\delta}$, where only a small part of Eu^{2+} could be substituted by Sr^{2+} [45].

According to magnetic measurements and QTAIM charge calculations, $EuPt_3P$ and $EuPt_6P_2$ can be described as containing Eu^{2+} cations placed in the negatively charged Pt-rich conducting framework. The charge transfer from Eu to the frameworks is almost complete. The Pt – P framework is formed *via* covalent Pt – P and Pt – Pt bonding as shown by electron localization function analysis. A short Pt1 – Eu interatomic distance of 2.98 Å is a manifestation of Coulombic attraction between substantially negatively charged Pt1 (- 0.71 *e*) and positively charged Eu (+1.35 *e*), rather than covalence. Both compounds exhibit high density of states at the Fermi level, which likely facilitates magnetic interactions between the Eu^{2+} ions. The Curie-Weiss temperatures are positive in both cases. The magnetic sublattice in $EuPt_6P_2$ is roughly twice less dense as compared to that in $EuPt_3P$; the closest Eu – Eu distance in $EuPt_6P_2$ is 5.98 Å against 4.05 Å in $EuPt_3P$. Both values are quite high and hinder any direct magnetic exchange, thus making the RKKY-type interactions mediated by the metallic Pt-rich conducting framework the driving force of cooperative magnetism. Compared to $EuPt_3P$, larger interatomic separations weaken magnetic interactions in $EuPt_6P_2$, which does not show magnetic order down to at least 1.8 K.

Superconductivity is apparently suppressed upon introducing Eu atoms into the structure. Internal magnetic fields induced by ferromagnetically interacting Eu^{2+} centers are likely too high and thus detrimental for superconductivity. The estimated critical temperature and critical field for $SrPt_3P$ are 8.4 K and 5.7 T (at 0 K) respectively [1]; for $SrPt_6P_2$, the critical temperature is 0.6 K, while the critical field is estimated to be below 0.01 T. Apparently, it is found experimentally that the magnetic fields induced by the Eu^{2+} cations lead to the breakdown of superconductivity.

Conclusion

Our systematic study of the Eu-analogs of Pt-based superconductors in the Sr – Pt – P system revealed the existence of two new ternary platinum-europium phosphides, $EuPt_3P$ and $EuPt_6P_2$, isostructural with the previously reported APt_3P (*A* = Ca, Sr, La and Ce) and $SrPt_6P_2$. The new compounds were prepared *via* a high-temperature solid-state reaction. Their crystal and electronic structures as well as physical properties are reported. $EuPt_6P_2$ features a cubic structure comprised by the distorted vertex-sharing PPt_6 trigonal prisms, the voids between filled by the Eu^{2+} cations. $EuPt_3P$ is a tetragonally distorted anti-perovskite with a remarkably short Pt - Eu distance of 2.98 Å. According to electron localization function analysis, both Pt – P frameworks are formed by the covalent bonds, whereas interactions between the frameworks and Eu^{2+} are ionic. Magnetic response of both compounds is predominantly determined by the presence of Eu^{2+} ($4f^7$) with no indication of superconductivity down to 1.8 K. $EuPt_6P_2$ is paramagnetic down to 1.8 K, while $EuPt_3P$ becomes ferromagnetic below 19 K.

This chapter has been published in a peer-reviewed journal *Dalton Transactions* of the publisher Royal Society of Chemistry (DOI 10.1039/C9DT02845E). The crystal structures of the title compounds are deposited in ICSD under the reference numbers 1892355 and 1892328.

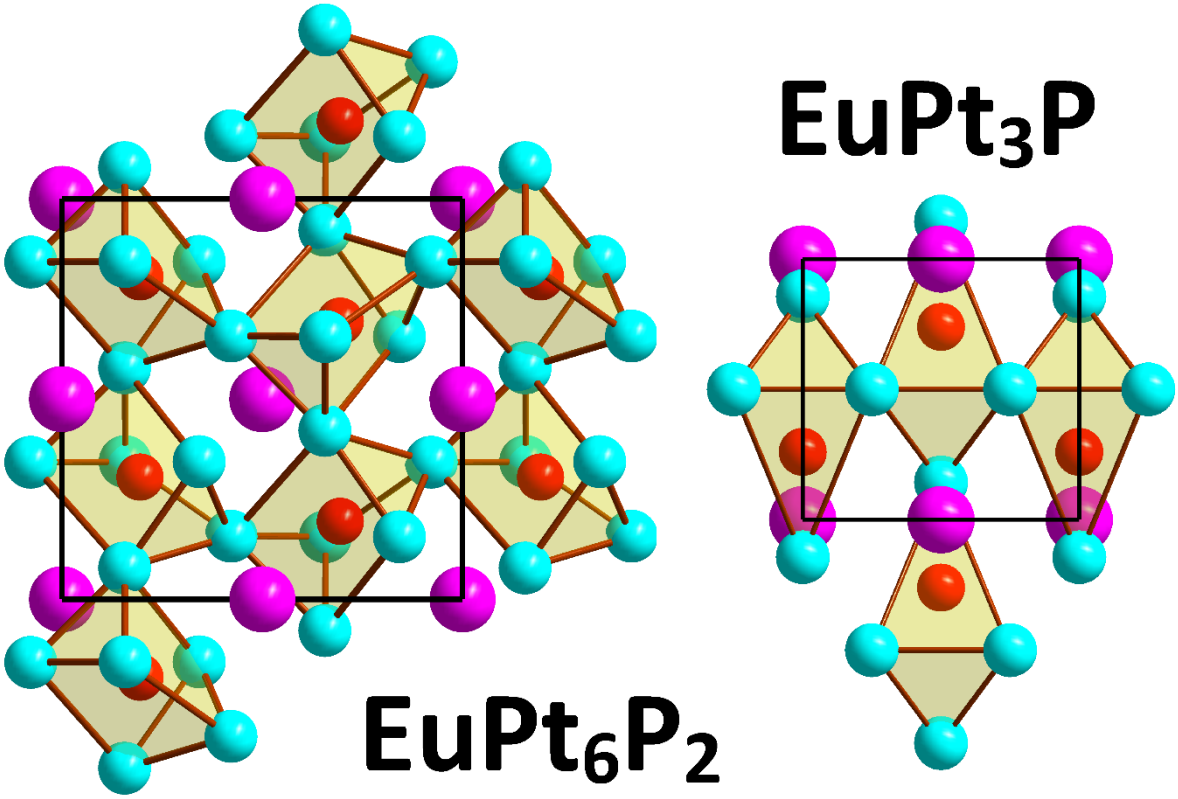

Figure 2.TOC Graphical abstract of the paper entitled "Synthesis, crystal and electronic structure of the Pt-rich phosphides $EuPt_3P$ and $EuPt_6P_2$".

Several other people also contributed to this work

- Dr. Nazir Khan and Dr. Alexander A. Tsirlin performed physical properties measurements, low-temperature synchrotron diffraction, discussed the results and improved the manuscript.
- Dr. Alexey N. Kuznetsov and Dr. Dmitri O. Charkin performed DFT calculations, supported with discussion of crystallographic part and improved the manuscript.
- Prof. Andrei V. Shevelkov and Prof. Arno Pfitzner contributed to discussion of the work, provided the lab space and equipment for work and improved the manuscript.
- Igor V. Plokhikh performed synthesis of the target compounds, designed computations and measurements and wrote the draft of the paper.

Addendum

During the attempts to prepare Pd analogs of the compounds belonging to Eu – Pt – P system, crystals of a new compound, $Eu_2Pd_{15}P_4$, were obtained. It crystallizes in tetragonal body-centered unit cell ($I4_1/amd$) with the parameters a = 8.9102(4) Å, c = 17.4025(9) Å, V = 1381.6(1) Å^3 at 293 K. Its crystal structure resembles that of $Y_2Pd_{15}B_5$. The structure of the compound features double trigonal prisms P_2Pd_{10} connected through the corners and disordered Pd bridges. The resulted framework Pd – P accommodates Eu^{2+} cations in cuboctahedral voids. Magnetic susceptibility and heat capacity measurements reveal a phase transition into ferromagnetic state at 7 K due to ordering of the Eu^{2+} magnetic moments.

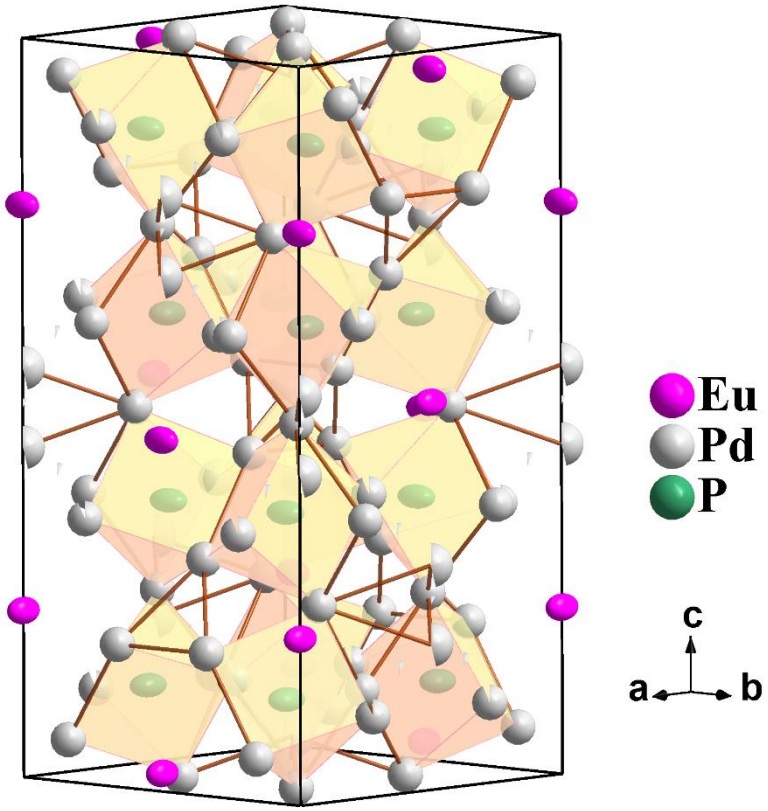

Figure 2.A1 Crystal structure of the $Eu_2Pd_{15}P_4$. Thermal ellipsoids are drawn at 95 % probability level and the defect sites are shown.

Supporting information

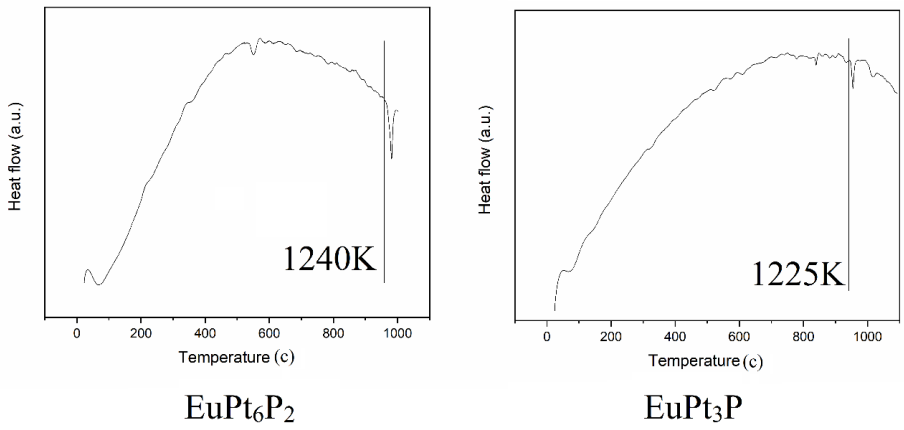

Figure 2.S1 DTA curves for $EuPt_6P_2$ and $EuPt_3P$.

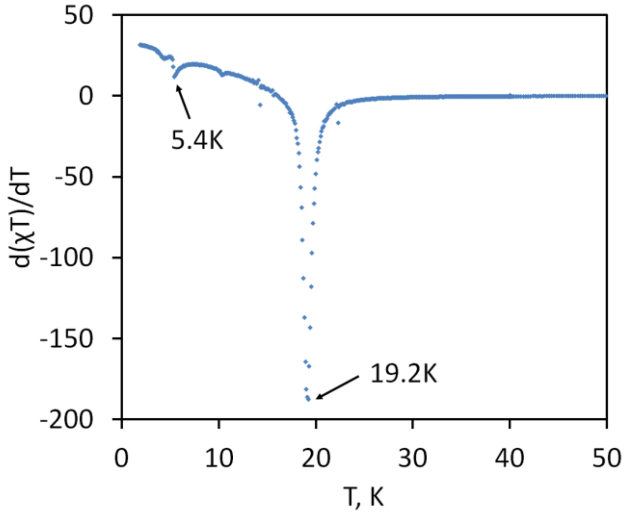

Figure 2.S2 Fisher's heat capacity d(χT)/dT plot for $EuPt_3P$.

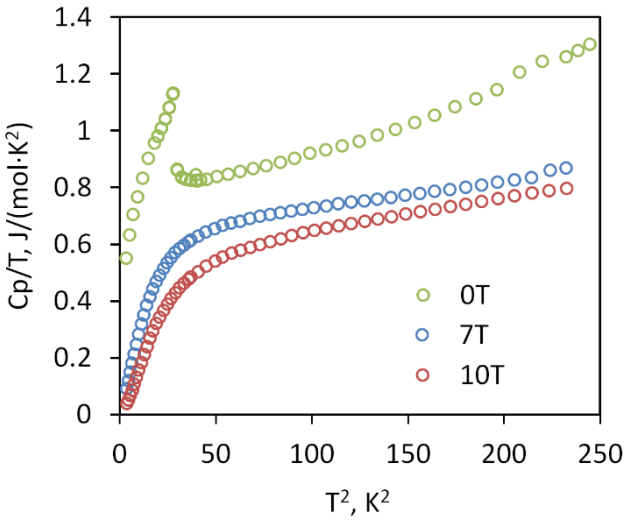

Figure 2.S3 Cp/T *vs.* T^2 plot for $EuPt_3P$ in 0, 7 and 10T fields.

References

[1] T. Takayama, K. Kuwano, D. Hirai, Y. Katsura, A. Yamamoto, H. Takagi. Strong coupling superconductivity at 8.4 K in an antiperovskite phosphide $SrPt_3P$. *Phys. Rev. Lett.* **2012**, *108*, 237001.

[2] B. Lv, B. I. Jawdat, Z. Wu, M. Sorolla, M. Gooch, K. Zhao, L. Deng, Y. Y. Xue, B. Lorenz, A. M. Guloy, C. W. Chu. Synthesis, structure, and superconductivity in the new-structure-type compound: $SrPt_6P_2$. *Inorg. Chem.* **2015**, 54, 1049.

[3] B. Lv, B. I. Jawdat, Z. Wu, S. Li, C.-W. Chu. Superconductivity in the ternary compound $SrPt_{10}P_4$ with complex new structure. *Phys. Rev. Materials* **2017**, *1*, 064801

[4] B. I. Jawdat. A study of superconductivity in a series of strontium platinum phosphides, PhD thesis, University of Houston, **2015**.

[5] Y. Nishikubo, K. Kudo, M. Nohara. Superconductivity in the honeycomb-lattice pnictide SrPtAs. *J. Phys. Soc. Jpn.* **2011**, *80*, 055002.

[6]. H. C. Ku, I. A. Chen, C. H. Huang. C. W. Chen, Y. B. You, M .F. Tai, Y. Y. Hsu. New superconductor $SrPt_2Ge_2$ with T_C = 10.2 K. *Physica C: Superconductivity* **2013**, *493*, 93 – 95.

[7] G. Eguchi, D. C. Peets, M. Kriener, Y. Maeno, E. Nishibori, Y. Kumazawa, K. Banno, S. Maki, H. Sawa. Crystallographic and superconducting properties of the fully gapped noncentrosymmetric 5*d*-electron superconductors $CaMSi_3$ (M = Ir, Pt). *Phys. Rev. B* **2011**, *83*, 024512.

[8] K. Miliyanchuk, F. Kneidinger, C. Blaas-Schenner, D. Reith, R. Podloucky, P. Rogl, T. Khan, L. Salamakha, G. Hilscher, H. Michor. Platinum metal silicides and germanides: superconductivity in non-centrosymmetric intermetallics. *J. Phys.: Conf. Ser.* **2011**, *273*, 012078

[9] T. Takeuchi, H. Muranaka, R. Settai, T. D. Matsuda, E. Yamamoto, Y. Haga, Y. Onuki. Superconductivity in a ternary silicide $Ca_2Pt_3Si_5$. *J. Phys. Soc. Jpn.* **2009**, *78*, 085001.

[10] U. Eibenstein, W. Jung. Li_2Pd_3B and Li_2Pt_3B: ternary lithium borides of palladium and platinum with boron in octahedral coordination. *J. Solid State Chem.* **1997**, *133*, 21 – 24.

[11] E. Martino, A. Arakcheeva, G. Autès, A. Pisoni, M. D. Bachmann, K. A. Modic, T. Helm, O. V. Yazyev, P. J. W. Moll, L. Forró, S. Katrych, S. $Sr_2Pt_{8-x}As$: a layered incommensurately modulated metal with saturated resistivity. *IUCrJ* **2018**, *5*, 470 – 477.

[12] T. Shiroka, M. Pikulski, N. D. Zhigadlo, B. Batlogg, J. Mesot, H.-R. Ot. Pairing of weakly correlated electrons in the platinum-based centrosymmetric superconductor $SrPt_3P$. *Phys. Rev. B* **2015**, *91*, 245143.

[13] D. A. Zocco, S. Krannich, R. Heid, K.-P. Bohnen, T. Wolf; T. Forrest, A. Bosak, F. Weber. Lattice dynamical properties of superconducting $SrPt_3P$ studied *via* inelastic x-ray scattering and density functional perturbation theory. *Phys. Rev. B* **2015**, *92*, 220504.

[14] R. Khasanov, A. Amato, P. K. Biswas, H. Luetkens, N. D. Zhigadlo, B. Batlogg. $SrPt_3P$: A two-band single-gap superconductor. *Phys. Rev. B* **2014**, *90*, 140507.

[15] Y. Nakamura, H. Okazaki, R. Yoshida, T. Wakita, H. Takeya, K. Hirata, M. Hirai, Y. Muraoka, T. Yokoya. Superconducting characteristics of filled skutterudites $LaPt_4Ge_{12}$ and $PrPt_4Ge_{12}$: ^{73}Ge-NQR/NMR studies. *J. Phys. Soc. Jpn.* **2010**, *79*, 063702.

[16] K. V. Samokhin, E. S. Zijlstra, S. K. Bose. $CePt_3Si$: An unconventional superconductor without inversion center. *Phys. Rev. B* **2004**, *69*, 094514.

[17] S. Süllow, G. J. Nieuwenhuys, A. A. Menovsky, J. A. Mydosh. Unusual magnetic behavior of $CePt_3B$. *Physica B: Cond. Mat.* **1994**, *199*, 644-646.

[18] J. Chen, Z. Wang, S. Zheng, C. Feng, J. Dai, Z. Xu. Antiferromagnetic Kondo lattice compound $CePt_3P$. *Sci. Rep.* **2017**, *7*, 41853.

[19] R. D. Shannon. Revised effective ionic radii and systematic studies of interatomic distances in halides and chalcogenides. *Acta Cryst. A* **1976**, 32, 751 – 767.

[20] D. O. Charkin, R. Demchyna, Yu. Prots, H. Borrmann, U. Burkhardt, U. Schwarz, W. Schnelle, I. V. Plokhikh, S. M. Kazakov, A. M. Abakumov, D. Batuk, V. Yu. Verchenko, A. A. Tsirlin, C. Curfs, Yu. Grin, A. V. Shevelkov. Two new arsenides, $Eu_7Cu_{44}As_{23}$ and $Sr_7Cu_{44}As_{23}$, with a new filled variety of the $BaHg_{11}$ structure. *Inorg. Chem.* **2017**, *53*, 11173 – 11184.

[21] N.-T. Suen, L. Huang, J. K. Meyers, S. Bobev. An unusual triple-decker variant of the tetragonal $BaAl_4$-structure type: synthesis, structural characterization, and chemical bonding of $Sr_3Cd_8Ge_4$ and $Eu_3Cd_8Ge_4$. *Inorg. Chem.* **2018**, *57*, 833 – 842.

[22] R. Zhang, M.-Y. Pan, M. Zhu, X.-T. Tao, S.-Q. Xia. Experimental and theoretical studies on the crystal structure of ternary copper arsenides $A_2Cu_3As_3$ (A = Sr, Eu). *Eur. J. Inorg. Chem.* **2016**, *23*, 3774 – 3780.

[23] E. Motomitsu, H. Yanagi, T. Kamiya, M. Hirano, H. Hosono. Synthesis, structure and physical properties of layered semiconductors *M*CuF*Ch* (*M* = Sr, Eu, *Ch* = S, Se). *J. Solid State Chem.* **2006**, *179*, 1668 – 1673.

[24] S. Jiang, H. Xing, G. Xuan, C. Wang, Z. Ren, C. Feng, J. Dai, Z. Xu, G. Cao. Superconductivity up to 30 K in the vicinity of the quantum critical point in $BaFe_2(As_{1-x}P_x)_2$. *J. Physics: Cond. Mat.* **2009**, *21*, 1 – 5.

[25] D. O. Charkin, A. V. Urmanov, S. M. Kazakov, D. Batuk, A. M. Abakumov, S. Knoner, E. Gati, B. Wolf, M. Lang, A. V. Shevelkov, G. Van Tendeloo, E. V. Antipov. Synthesis, crystal

structure, transport, and magnetic properties of novel ternary copper phosphides, $A_2Cu_6P_5$ (A = Sr, Eu) and $EuCu_4P_3$. *Inorg. Chem.* **2012**, *51*, 8948 – 8955.

[26] M. Radzieowski, F. Stegemannm, T. Block, J. Stahl, D. Johrendt, O. Janka. Abrupt europium valence change in $Eu_2Pt_6Al_{15}$ around 45 K. *J. Am. Chem. Soc.* **2018**, *140*, 8950 – 8957.

[27] Z. Ren, Q. Tao, S. Jiang, C. Feng, C. Wang, J. Dai, G. Cao, Z. Xu, Z. Superconductivity induced by phosphorus doping and its coexistence with ferromagnetism in $EuFe_2(As_{0.7}P_{0.3})_2$. *Phys. Rev. Lett.* **2009**, *102*, 137002.

[28] N. Lossau, H. Kierspel, J. Langen, W. Schlabitz, D. Wohlleben, A. Mewis, Ch. Sauer, EuPtP: a new mixed valent europium-system. *Z. Phys. B: Condens. Matter* **1989**, *74*, 227 – 232.

[29] V. Petříček, M. Dušek, L. Palatinus. Crystallographic computing system JANA2006: general features. *Z. Kristallogr.* **2014**, *229*, 345 – 352.

[30] G. Kresse, J. Furthmüller. Vienna Ab initio simulation package (VASP), v.5.3, http://www.vasp.at/.

[31] G. Kresse, D. Joubert. From ultrasoft pseudopotentials to the projector augmented-wave method. *Phys. Rev. B* **1999**, *59*, 1758 – 1775.

[32] H. J. Monckhorst, J. D Pack. Special points for Brillouin-zone integrations. *Phys. Rev. B* **1976**, *13*, 5188.

[33] J. P. Perdew, K. Burke, M. Ernzerhof. Generalized gradient approximation made simple. *Phys. Rev. Lett.* **1996**, *77*, 3865 – 3868.

[34] R. F. W. Bader, Atoms in Molecules: a Quantum Theory, Oxford University Press, Oxford, **1990**.

[35] M. Yu, D. R. Trinkle. Accurate and efficient algorithm for Bader charge integration, J. Chem. Phys. **2011**, *134*, 064111.

[36] B. Silvi, A. Savin. Classification of chemical bonds based on topological analysis of electron localization functions. *Nature* **1994**, *371*, 683.

[37] P. S. Chizhov, Y. Prots, E. V. Antipov, Yu. Grin. Ce_2Pt_8P: a phosphido-platinide with covalently bonded framework polyanion. *Z. Anorg. Allg. Chem.* **2009**, *635*, 1863 – 1868.

[38] A. Imre, A. Mewis. Synthese und Kristallstrukturen von $DyPt_8P_2$ und $Mg_{10-x}Pt_9P_7$. *Z. Anorg. Allg. Chem.* **2008**, *634*, 77 – 81.

[39] C. Lux, G. Wenski, A. Mewis. $Eu_2Pt_7AlP_3$ und isotype Verbindungen: Eine neue Struktur aus $CaBe_2Ge_2$- und Cu_3Au-Einheiten. *Z. Naturforsch. B* **1991**, *46*, 1035 – 1038.

[40] A. E. Dwight. Crystal structure of EuCuGa and related compounds, *J. Less-Common Met.* **1987**, *127*, 175-178.

[41] G. Steinhauser, C. Luef, M. Wildner, G. Giester. Syntheses and crystal structures of $Pb(SeO_3)_2$ and two modifications of $Sn(SeO_3)_2$, *J. Alloys Compd.* **2006**, *419*, 45 – 49.

[42] H. Nowotny, G. Heger. Structure refinement of strontium nitrate, $Sr(NO_3)_2$, and barium nitrate, $Ba(NO_3)_2$, *Acta Crystallogr. C* **1983**, *39*, 952 – 956.

[43] A. Karpov, U. Wedig, R. E. Dinnebier, M. Jansen. Dibariumplatinide: $(Ba^{2+})_2Pt^{2-}\cdot 2e^-$ and its relation to the alkaline-earth-metal subnitrides. *Angew. Chem. Int. Ed.* **2005**, *117*, 780 – 783.

[44] A. Baghdadi, A. Finley, P. Russo, R. J. Arnott, A. Wold. Crystal growth and characterization of PtP_2, *J. Less-Common Met.* **1974**, *34,* 31 – 38.

[45] I. V. Plokhikh, D. O. Charkin, A. N. Kuznetsov, V. Yu. Verchenko, I. A. Ignatiev, S. M. Kazakov, A. A. Tsirlin, A. V. Shevelkov. New clathrate-like compound $Eu_7Cu_{44}Sb_{23-\delta}$: synthesis, crystal and electronic structure, and the effect of As-for-Sb substitution on the magnetic properties. *Intermetallics* **2018**, *98*, 1 – 10.

3 $EuNi_2P_4$, the first magnetic unconventional clathrate prepared *via* mechanochemically assisted route

Abstract

For the first time, a magnetic unconventional clathrate $EuNi_2P_4$ has been prepared from the elements *via* a combined mechanochemical and solid-state route. Its crystal and electronic structure, magnetic and transport properties as well as lattice dynamics were elucidated. It crystallizes in the orthorhombic space group *Fddd* (Z = 8) with unit cell parameters a = 5.1852(1) Å, b = 9.4834(1) Å, and c = 18.9893(2) Å, V = 933.78(1) Å^3 at room temperature. Its crystal structure can be described as a covalent Ni – P framework forming a twisted Kelvin cell with Eu^{2+} guest cations occupying the voids of this framework, which is supported by chemical bonding analysis based on the Electron Localization Function topology. Eu^{2+} guests sit inside the oversized cages with a coordination number of 24 and exhibit strong rattling, which manifests in both thermodynamic properties and Raman spectra. The compound is metallic and exhibits a rather low thermal conductivity of ~4 W/K/m at high temperature along with a positive Seebeck coefficient. The magnetism of $EuNi_2P_4$ is predetermined by Eu^{2+} ($4f^7$) with dominant antiferromagnetic interactions. According to the magnetic susceptibility, heat capacity and resistivity measurements, $EuNi_2P_4$ undergoes three phase transitions at ~2.5 K, 6.1 K and 11.3 K in zero magnetic field.

Introduction

Intermetallic clathrates, the crystal chemical analogues of gas-hydrates [1], are known since long time and have been actively studied during the last few decades mostly due to their promising thermoelectric performance as well as other attractive physical properties ensuring their applications as photovoltaic, superconducting, and Li-ion batteries materials [2 – 5]. They can be generally described as tetrahedra of host-matrix atoms forming frameworks, which accommodate guest atoms with high coordination numbers. Frameworks of the classical anionic intermetallic clathrates are comprised by tetrel (Si, Ge and Sn) atoms that tend to maintain rather rigid ideal tetrahedral coordination. Classical clathrates crystallize in a limited number of structure types (or their superstructures) and prefer several typical space groups or their subgroups. Contrary to that, the frameworks of unconventional clathrates formed by pnictogen atoms are much more flexible and sustain more pronounced distortions of the classical clathrate polyhedra, thus giving rise to a more

diverse crystallography [5 – 8]. Here, it is also worth mentioning that the presence of ions with high coordination numbers encapsulated into the frameworks leads to a wide range of so-called clathrate-like or clathrate-related compounds, as pointed out in a review [2] and exemplified by many compounds, including Eu containing examples [9].

An unconventional clathrate $SrNi_2P_4$ was recently reported [10] to be isostructural with the previously known $BaCu_2P_4$ [11] and has no analogs among gas hydrates, while $BaNi_2P_4$ adopts a different (and conventional) clathrate-VII structure type [12]. The crystal structure of $SrNi_2P_4$ and $BaCu_2P_4$ features 24-coordinated guest ions (Sr^{2+} and Ba^{2+}, respectively) occupying 24-vertex twisted Kelvin cells, thus filling the whole space. The Ba^{2+} ions in $BaNi_2P_4$ occupy a more symmetric truncated octahedron, *i.e.,* this compound crystallizes in a distorted sodalite structure type. $BaNi_2P_4$ undergoes a tetragonal-to-orthorhombic distortion at ~373K [12] upon cooling or heating.

It is known that, unlike Ca and Ba, Eu commonly behaves as the closest analog of Sr [9, 13 – 15]. Therefore, we deduced the existence of a new compound, $EuNi_2P_4$ supposedly isomorphous to $SrNi_2P_4$. The radius of Eu^{2+} is comparable with that of Sr^{2+} [16], and the pnictide (phosphorus) environment ensures the stability of Eu^{2+} against Eu^{3+}. Among the classical intermetallic tetrel clathrates, rare examples of the Eu^{2+} magnetic ion introduced into the clathrate frameworks are known from the literature [17, 18]. Despite a substantial spatial separation in the $Eu_8Ga_{16}Ge_{30}$ structure, Eu^{2+} magnetic centers interact ferromagnetically, yielding a material exhibiting a pronounced magnetocaloric effect [19]. The example of $Eu_xBa_{8-x}Cu_{16}P_{30}$ shows that magnetic Eu^{2+} can be introduced into a framework of tetrel-free clathrates [20], but to the best of our knowledge, and contrary to the classical intermetallic clathrates, no pure-Eu^{2+} *magnetic* unconventional clathrates were reported till now.

Following this motivation, we attempted to prepare $EuNi_2P_4$ by a solid-state reaction in order to explore how the size, mass, electronic structure, and magnetism of the new guest ion would affect the behaviour of the host matrix and the whole compound. First of all, Eu^{2+} is slightly smaller than Sr^{2+} (1.25 Å against 1.26 Å for the coordination number 8), which can cause a higher degree of mismatch between the guest ion and the framework that in turn renders this framework less stable. On the other hand, if it is indeed possible to incorporate Eu^{2+} into the title clathrate framework, a higher degree of mismatch should lead to more pronounced rattling. As rattling is believed to be responsible for

thesuppression of thermal conductivity (phonon-glass behaviour), improved thermoelectric performance may be expected.

Magnetism of Eu^{2+} may also be interesting in this setting. On the one hand, the clathrate framework keeps the magnetic ions far from each other with nearest-neighbor distances over 5 Å. On the other hand, metallic nature of this framework facilitates long-range RKKY interactions that change sign depending on the Eu – Eu distance and may lead to complex magnetic behaviour, which is indeed the case, as we show below. Last but not least, Eu^{2+}/Eu^{3+} valence fluctuations remain a possibility, as in EuPtP or $EuNi_2P_2$ [21, 22], and could further enrich the magnetic behaviour. It has also been proposed that the mixing of 4*f* states of the lanthanide ion with itinerant states near the Fermi level can improve thermoelectric performance [20].

In the current paper, we report a mechanochemical synthesis as well as structural and thermodynamic study of the first magnetic unconventional clathrate, $EuNi_2P_4$, and compare it with the Sr analogue [10, 23].

Experimental section

Synthesis and primary characterization. $EuNi_2P_4$ was prepared from the elements by a combined mechanochemical and solid-state route. All preparations were performed in an Ar-filled grove-box (MBraun, O_2 and H_2O less than 1ppm). Mixtures of metallic Ni (over 99.9%, purified from surface oxide in H_2 flow at 1073K), red phosphorus (over 99.5%, Chempur), and Eu (Novaelements, over 99.5% purity) were placed into silica tubes, flame-sealed under vacuum and annealed at 873K for 5 days. The as-prepared mixture was treated mechanochemically (600rpm, 3min milling + 5min cooling, 10 cycles) in a Pulverisette 7 ball-mill (Fritsch, Germany). The obtained powder was pressed into pellets 0.3 – 0.5 g each, flame-sealed in evacuated silica tubes and annealed at 1113K for 30 days. After that the sample was slowly cooled (0.1 K/min) to room temperature. Sample purity was checked using a STOE STADI P diffractometer (Mo-$K\alpha_1$ radiation, λ = 0.70930 Å, Ge (111) monochromator, Dectris Mythen 1K detector). Powdered samples were loaded in quartz capillaries of 0.3 mm diameter and spun during the measurements at 293 K. The WinXPOW software package from STOE & Cie was used for data collection and processing [24]. A new compound isostructural with $SrNi_2P_4$ was found to be present in the sample as a majority phase. It is a black powder with metallic luster when compacted, stable in air over weeks. Elemental composition was confirmed using a Zeiss EVO MA 15 scanning electron

microscope equipped with a Bruker Quantax EDX system with an X Flash Detector 630 M. Thermal behaviour was studied *via* DTA technique utilizing a SETARAM TG-DTA 92 analyzer. The sample was loaded in silica capillaries and subjected to 2 heating and cooling cycles. It was found to irreversibly decompose at ~1120 K (see SI).

Temperature-dependent crystal structure determination. High-resolution synchrotron powder diffraction data were collected at the ID22 beamline of the European Synchrotron Radiation Facility (ESRF) (λ = 0.35414 Å) in the 10 – 273 K temperature range. For synchrotron measurements, samples were loaded into thin-walled borosilicate glass capillaries with an external diameter of 0.3 mm, and spun during the measurement. The diffracted intensity was collected by 8 scintillation detectors each preceded by a Si(111) analyzer crystal. The powder X-ray diffraction data were processed in the JANA2006 software. The crystal structure of $SrNi_2P_4$ was used as a starting model. The refinement was performed in a straight-forward manner using the standard mathematical apparatus for the Rietveld refinement implemented in JANA2006 [25]. Atomic displacement parameters of the light atoms (Ni and P) were refined in an isotropic approximation, while Eu was treated in an anisotropic approximation. The details of the powder diffraction experiment are collected in SI, a projection of the unit cell is depicted in **Figure 3.1**, the Rietveld refinement plot at 273 K is provided in **Figure 3.2**, and selected interatomic distances are given in **Table 3.1.**

Table 3.1 Selected interatomic distances (in Å) in the structure of $EuNi_2P_4$ at different temperatures.

Distance	10K	50K	100K	150K	250	273
Ni – P × 2	2.204(2)	2.206(2)	2.205(2)	2.205(2)	2.208(1)	2.209(2)
Ni – P× 2	2.212(2)	2.209(2)	2.211(2)	2.219(1)	2.219(1)	2.216(1)
Ni – Ni × 2	2.7008(1)	2.7013(1)	2.7019(1)	2.7024(1)	2.7083(1)	2.7094(1)
P – P	2.226(2)	2.225(2)	2.228(2)	2.222(2)	2.233(2)	2.232(2)
P – P × 2	2.226(2)	2.231(2)	2.228(2)	2.231(2)	2.221(2)	2.228(2)
Eu – Ni × 4	3.4447(7)	3.4443(7)	3.4450(7)	3.4482(6)	3.4502(6)	3.4491(6)
Eu – Ni × 4	3.6543(7)	3.6551(7)	3.6551(7)	3.6533(6)	3.6601(6)	3.6627(6)
Eu – P × 4	3.101(1)	3.098(1)	3.100(1)	3.101(1)	3.106(1)	3.107(1)
Eu – P × 4	3.106(1)	3.111(1)	3.110(1)	3.107(1)	3.115(1)	3.117(1)
Eu – P × 4	3.594(1)	3.595(1)	3.594(1)	3.592(1)	3.599(1)	3.602(1)
Eu – P × 4	3.842(1)	3.841(1)	3.842(1)	3.848(1)	3.848(2)	3.846(1)
Eu – Eu (the nearest)	5.1738(1)	5.1742(1)	5.1749(1)	5.1761(1)	5.1840(1)	5.1852(1)

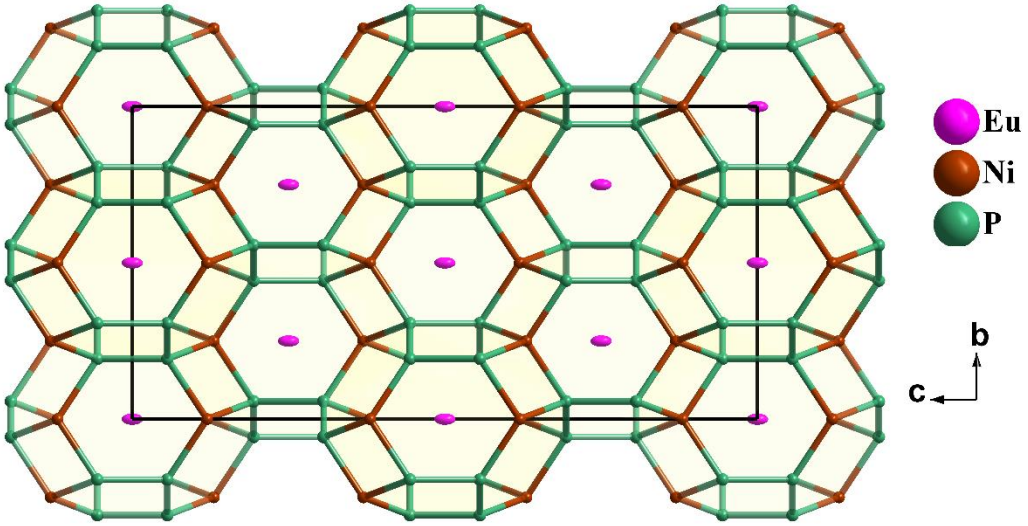

Figure 3.1 Projection of the $EuNi_2P_4$ unit cell along the *a*-direction in polyhedral representation. Cell edges are outlined in black. Thermal ellipsoids are drawn at 90 % probability level at 273 K.

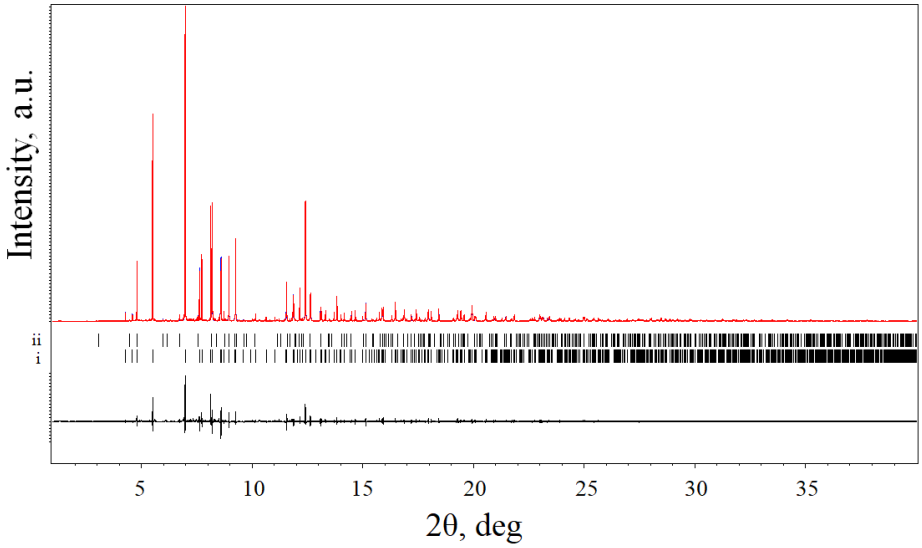

Figure 3.2 Synchrotron powder diffraction pattern of $EuNi_2P_4$ (phase i) at 273 K. A trace of $Eu_3(PO_4)_2$ impurity (phase ii), amounting ~1.6 weight %, is included into the refinement. The calculated line is shown in blue, experimental points are red, difference curve and positions of the reflections are black.

Magnetic, heat capacity, and thermoelectric properties measurements. The temperature and field dependence of the magnetization was measured using a Quantum Design SQUID-VSM magnetometer (MPMS 3). The specific heat was measured in a Quantum Design Physical Properties Measurement System (QD-PPMS 14 T) using the relaxation method. Temperature dependence of zero-field thermal conductivity, Seebeck coefficient, and

electrical resistivity were measured using the Thermal Transport Option (TTO) of the QD-PPMS. The sample was cut in a brick-like shape with the dimensions of 8.4 mm × 2.25 × 2.5 mm^2. The four-probe configuration was made by mounting four gold-plated copper leads to the sample using silver-filled epoxy. Data were collected in the continuous measurement mode by slowly sweeping the temperature from 300 K down to 2 K at the rate of 0.25 K/min. The Seebeck coefficient was found to be below 1 μV/K, which cannot be precisely measured using TTO setup.

Raman spectroscopy. Raman spectra were measured on a home-made Raman spectrometer equipped with a HeNe laser providing 35 mW at 632 nm and a CCD camera attached to a grating spectrograph with 350 mm focal length and 1800/mm grating for the signal detection. Find a detailed description of the setup in SI.

Electronic structure calculations and vibration spectra simulations. Density Functional Theory (DFT) based calculations were performed using the pseudopotential projector augmented wave method (PAW) as implemented in the Vienna *ab initio* Simulation Package (VASP) [26, 27]. A Monckhorst-Pack *k*-point mesh of 10 × 10 × 8 was employed, and the energy cutoff was set at 500 *eV* [28]. The PBE exchange-correlation functional of the GGA-type was used in the PAW-based calculations [29]. In order to account for the Eu^{2+} *f*-orbitals, a special potential for Eu^{2+}, supplied with the VASP package, was used, which puts localized *f*-orbitals into the core. The convergence of the total energy with respect to the *k*-point sets was checked. Atomic charges in the direct-space analysis were calculated according to Bader's QTAIM approach [30, 31]. The electron localization function (ELF) was calculated by the internal VASP routine according to [32]. A Raman spectrum for $EuNi_2P_4$ was simulated based on the Density Functional Perturbation Theory (also known as Linear Response Theory), with Raman frequencies obtained from VASP phonon calculations using the script from Fonari & Stauffer [33]

Results and discussion

Synthesis. According to literature [10, 23], samples of $SrNi_2P_4$ can be easily prepared from the elements by several subsequent annealing steps at 1123 K. Contrary to that, when a stoichiometric mixture of Eu, Ni, and P is subjected to the same synthetic procedure, the yield of the target crystalline phase of $EuNi_2P_4$ does not exceed 80 %, with all samples containing sizeable amounts of $EuNi_2P_2$ and phosphorus as by-products. Reducing the temperature to 973 K does not improve the sample quality, heating above 1123 K leads to

an irreversible decomposition observed by DTA measurements, whereas below 873 K reaction kinetics becomes too slow. Therefore, other methods (growth from salt melt, high-pressure synthesis, and mechanochemical activation) were tried. As only the mechanochemical route was successful, we will discuss only this procedure. The described synthetic procedure was checked to be scalable up to at least 3 g. Here, we also would like to mention that despite the existence of numerous compounds in the ternary Eu – Ni – P system ($EuNi_2P_2$ [22], $Eu_8Ni_{18}P_{11}$ [34], $Eu_9Ni_{26}P_{12}$ [35], $Eu_2Ni_7P_4$ [36], $EuNi_5P_3$ [37], $Eu_2Ni_{12}P_5$ [38], $Eu_2Ni_{12}P_7$ [39] and two modifications of $EuNi_{10}P_6$ [40]) and some recent synthetic attempts [41], our new compound, $EuNi_2P_4$, expands the P-rich region of the Eu – Ni – P system.

Crystal structure and its temperature dependence. A projection of the $EuNi_2P_4$ crystal structure is provided in **Figure 3.1.** It can be described similarly to $SrNi_2P_4$ as a Ni – P framework with the Eu^{2+} cations placed into its voids. Each Ni atom is surrounded by 4 phosphorus atoms at a distance of 2.20 – 2.22 Å, forming distorted tetrahedra. The NiP_4 tetrahedra share common edges forming infinite NiP_2 chains. These chains are linked by P – P bridges and form 24-vertex polyhedra that fill the whole space. In general, the details of the crystal structures of $SrNi_2P_4$ and $EuNi_2P_4$, including distances and angles, are very similar if not identical.

On decreasing the temperature the unit cell volume decreases, as it is shown in **Figure 3.3**, and so do the unit cell parameters as well as most of the interatomic distances (in SI). When comparing the cell parameters of $EuNi_2P_4$ (a = 5.175 Å, b = 9.456 Å, c = 18.975 Å, V = 928.5 Å^3 at 100 K) and $SrNi_2P_4$ (a = 5.193 Å, b = 9.560 Å, c = 18.958 Å, V = 941.1 Å^3 at 90 K), one can notice that the a, b parameters and cell volume follow the trend expected from ionic radii, while the c parameter behaves in an opposite way. Also, below 150 K both $EuNi_2P_4$ and $SrNi_2P_4$ [23] exhibit almost zero thermal expansion along the c-axis. Despite Eu being the heaviest atom in the structure, its room-temperature atomic displacements parameter (ADP) is substantially higher than for Ni and P. It also exhibits a pronounced anisotropy: the U_{33} is almost twice as high as U_{11}. Such an anomaly is attributed to the fact that the distances between the center of the cage (the ideal position of an Eu atom) and the atoms comprising the cage exceed 3 Å, while the cage itself is elongated along the c- direction, *i.e.,* the Eu^{2+} cation follows its shape.

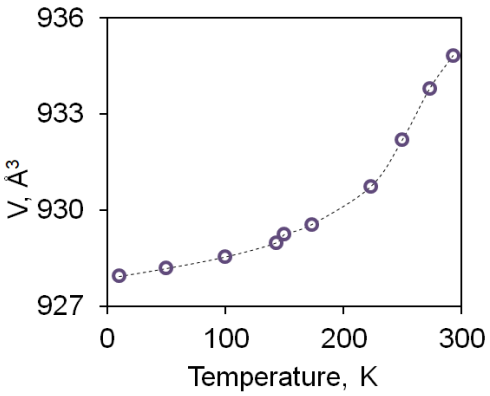

Figure 3.3 Temperature dependence of the unit cell volume of $EuNi_2P_4$. The graph combines both synchrotron and laboratory diffractometer data.

As the temperature decreases, the atomic displacement parameters also decrease (**Figure 3.4**). All presented ADP lines tend to low, though not zero, values, pointing to the fact that, some minor static disorder still persists [42]. ADPs on Eu atoms decrease much faster with temperature than on Ni and P atoms. At 100 K they are already comparable, while at 10 K the ADPs of Eu are twice smaller than those of Ni and P (in SI). Nevertheless, the anisotropy of Eu ADPs' still persists. For the data in the temperature region of 50 K – RT the temperature increments of ADP are $3.99 \cdot 10^{-5}$, $3.02 \cdot 10^{-5}$ and $9.24 \cdot 10^{-5}$ Å²/K for U_{11}, U_{22} and U_{33} of Eu respectively, and $1.15 \cdot 10^{-5}$, $1.99 \cdot 10^{-5}$ Å²/K for Ni and P respectively. Note that Ni and P were refined with isotropic ADPs. Deviations from the linearity of the atomic displacements parameters for the 10 K data (in SI) is already significant.

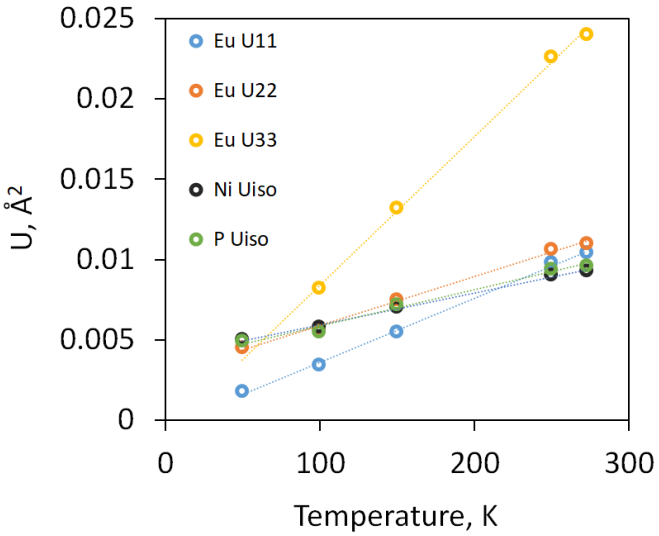

Figure 3.4 Temperature dependence of the isotropic ADPs of Ni and P, and of the anisotropic ADP tensor components (U_{11}, U_{22} and U_{33}) for Eu.

Assuming that Ni and P obey the Debye model, their slope of the *U(T)* functions can be expressed as:

$\frac{3h^2}{4\pi M\theta_D^2 k_B}$, where θ_D is a characteristic Debye temperature and *M* is the atomic mass [42].

The slope of the *U*(*T*) function for Eu yields the characteristic Einstein temperature θ_E of the quasi-free guest atom according to the expression:

$\frac{h^2}{8\pi^2 m\theta_E k_B}\coth(\frac{\theta_E}{2\pi})$, where *m* is the atomic mass of the oscillator (Eu^{2+}) [42].

Thus, the averaged Debye temperature from the data for Ni and P can be estimated as 475 K; the Einstein temperature from the U_{33} of Eu is 104 K (equivalent to 0.015 *eV* or 72 cm^{-1}) and the averaged Einstein temperature from U_{11} and U_{22} of Eu is 170 K.

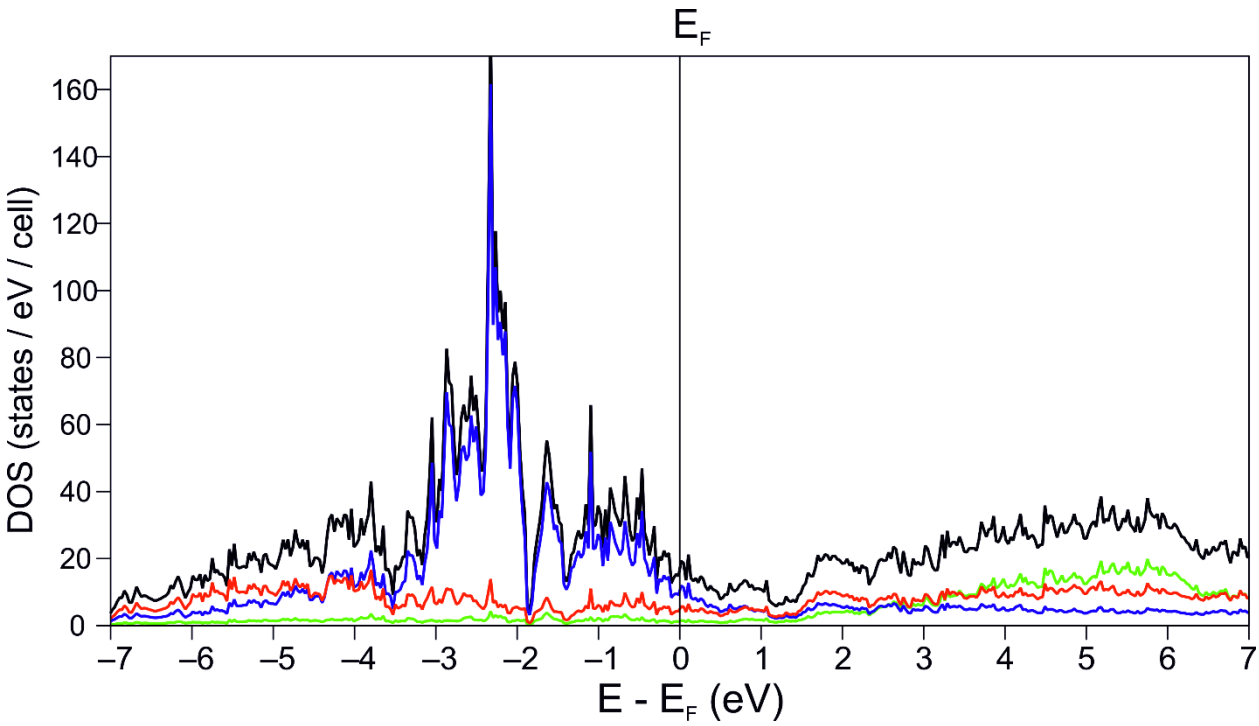

Figure 3.5 Total (TDOS) and projected (PDOS) density of states near the Fermi level for $EuNi_2P_4$: green – Eu PDOS, blue – Ni PDOS, P – red PDOS.

Electronic Structure. Calculated densities of states near the Fermi level for $EuNi_2P_4$ are shown in **Figure 3.5**. Non-zero density of states at the Fermi level indicates the metallic nature of this compound. Main contributions under the Fermi level are provided by the 3*d* states of Ni atoms, with 3*p* states of P also contributing at the Fermi level, albeit to a significantly lesser extent. Eu *d*-states mostly contribute to the region above the Fermi level, which is consistent with its supposedly cationic Eu^{2+} character (see magnetic data below).In general,

the DOS for $EuNi_2P_4$ is very similar to that of $SrNi_2P_4$ [10], complete with the pseudo-gap at *ca.* -1.9 eV. The mixing of the Ni and P states at the Fermi level may possibly imply a certain degree of covalency in the Ni – P bonds. This is confirmed by the calculated Bader atomic charges, which are: +1.4 (Eu), +0.1 (Ni), -0.4 (P). Low charges on the Ni and P atoms also indicate covalent bonding contributions between the nickel and phosphorus atoms.

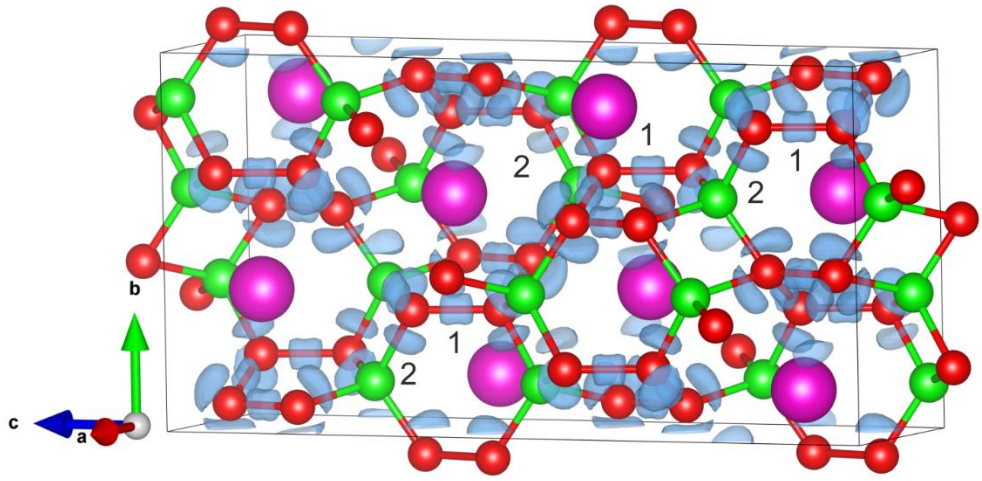

Figure 3.6 ELF isosurface (η = 0.80) for $EuNi_2P_4$: 1 – P – P bonds, 2 – Ni – P bonds. Ni atoms are shown in green, Eu in pink, P in red, ELF isosurface in blue.

To gain more insight into the bonding pattern in $EuNi_2P_4$, we performed a topological analysis of the Electron Localization Function (ELF), which allows to observe atomic shells, lone pairs, or bonds in direct space. For $EuNi_2P_4$ we clearly see two distinct kinds of the non-atomic ELF attractors presented in **Figure 3.6**: localization domains 1 and 2 corresponding to the pairwise P – P and Ni – P interactions. The P – P bond domains are completely symmetrical and apparently correspond to classical two-center non-polar covalent bonds. The Ni - P bond attractors are shifted towards phosphorus atoms, which means that the Ni - P bond has a degree of polarity (which agrees well with calculated atomic charges). The Ni - P bond localization domains also show asymmetry and are slightly shifted from the lines connecting Ni and P atoms towards the Eu cations in the voids. We have investigated the structuring of the phosphorus valence shell more closely, in order to see if additional type of attractor might be present that could influence the shape of the Ni – P bond domains, but found no extra ELF maxima (see SI). Thus, we can interpret the bonding in $EuNi_2P_4$ as europium cations embedded into the essentially covalent network of the Ni – P and P – P bonds.

Magnetic measurements. Temperature dependence of magnetic susceptibility in different fields as well as the Curie-Weiss fit are presented in **Figure 3.7**. Above 15 K, the sample behaves as a Curie –Weiss paramagnet with the derived magnetic moment of 7.93 μ_B per formula unit, consistent with divalent Eu, assuming that Ni and P are non-magnetic (the expected value for pure Eu^{2+} is 7.94 μ_B). The Curie-Weiss temperature $\theta_{CW} = -5.72$ K is negative, which points to the overall antiferromagnetic interactions in $EuNi_2P_4$.

A magnetic susceptibility curve taken at 0.005 T shows several anomalies below 15 K. From the dχ/dT plot (provided in SI) we infer the critical temperatures of 2.5 K, 4.1 K, 6.1 K, 7.8 K and 11.3 K. The 4.1 K and 7.8 K anomalies are already almost invisible in 0.025 T field and completely blurred in 0.1 T (**Figure 3.7**); they were not confirmed from heat capacity and resistivity measurements. Therefore, they are either extrinsic and caused by an impurity like $Eu_3(PO_4)_2$ that orders antiferromagnetically below 5 K [43], or arise from valence fluctuations (Eu^{2+}/Eu^{3+}) similar to $EuNi_2P_2$ at low temperature [22]. The low-temperature behaviour was further elucidated by combination of heat capacity measurements, temperature-dependent magnetic susceptibility and field-dependent magnetization data.

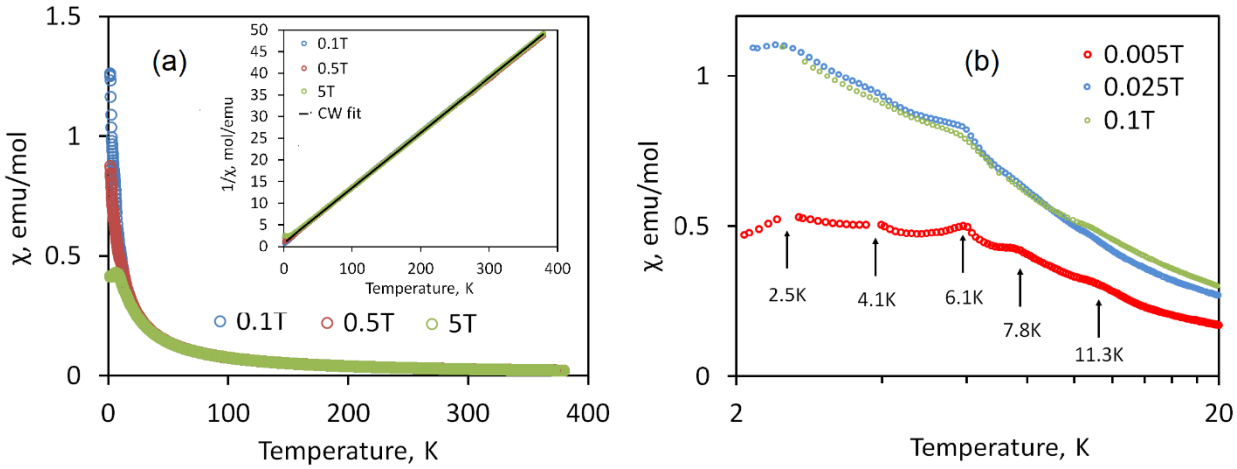

Figure 3.7 (a) Temperature dependence of the magnetic susceptibility ($\chi = M/H$) taken in the fields of 0.1 T, 0.5 T and 5 T, and the Curie-Weiss fit shown as insert. (b) Low-temperature part of the magnetic susceptibility curve measured in the 0.005 T, 0.025 T and 0.1 T applied fields. The positions of anomalies are identified from the first derivative (SI).

Magnetization curves taken at different temperatures are shown in **Figure 3.8.** Magnetization at 1.9 K increases with increasing field with one distinct inflection point at 5.2 T and several broad anomalies in lower fields. The positions of those anomalies were located from the dM/dH *vs.* T curve (provided in SI) and labeled on **Figure 3.8.** The 5.2 T anomaly does not exhibit hysteretic behaviour, while the positions of the low-field

anomalies (especially the one at ~1 T) substantially change upon switching the direction of the field. The strongly non-linear shape of the 1.9 K magnetization curve is consistent with the effects observed in the magnetic susceptibility data. Several anomalies are also observed in the 5 K magnetization curve, while the magnetization curve at 9 K and above is close to linear.

The curve measured at 1.9 K does not reach saturation even at 7 T; the highest magnetic moment is 5.4 μ_B/f.u., *i.e.,* 20 % less than the expected value of 7 μ_B for pure Eu^{2+}. This fact further confirms sizable antiferromagnetic interactions between the Eu^{2+} moments.

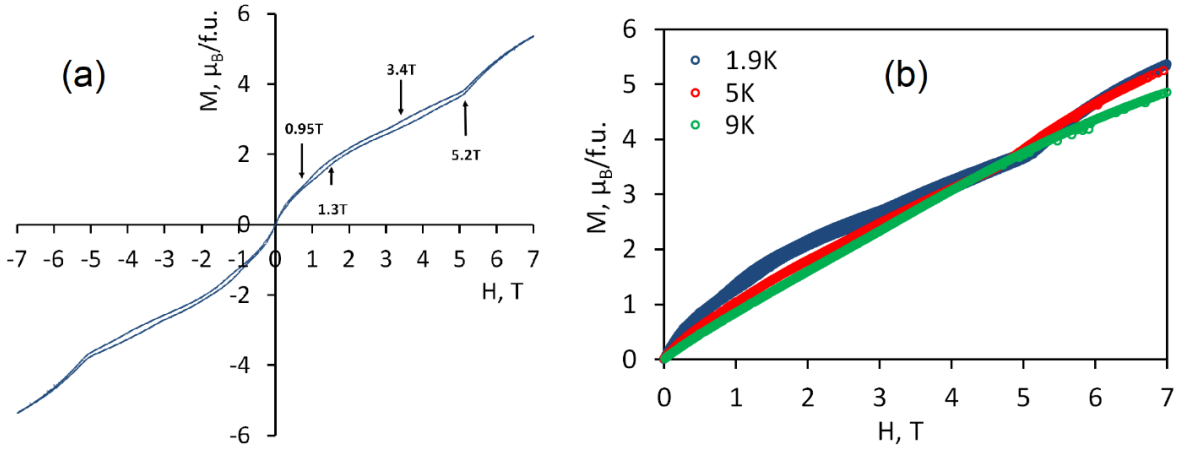

Figure 3.8 (a) Magnetization curve (magnetic moment *vs.* applied field) taken at 1.9 K. Three transitions at ~ 1 T, ~3.4 T, and 5.2 T are visible. The first two transitions exhibit a hysteresis. (b) Magnetization curves taken at 1.9 K, 5 K, and 9 K.

Heat capacity measurements. The heat capacity of $EuNi_2P_4$ also shows several anomalies (**Figure 3.9**). The large anomaly at 11.3 K signals a second-order magnetic transitions, while another pronounced anomaly at 2.5 K and a small anomaly around 6 K are first-order in nature. At low-temperatures, between 2 and 6 K, a broad hump, similar to that in $SrNi_2P_4$, is observed. Otherwise, the heat capacity curve below 15 K is smooth, suggesting that two other anomalies observed in the low-field susceptibility at 4.1 K and 7.8 K are likely extrinsic.

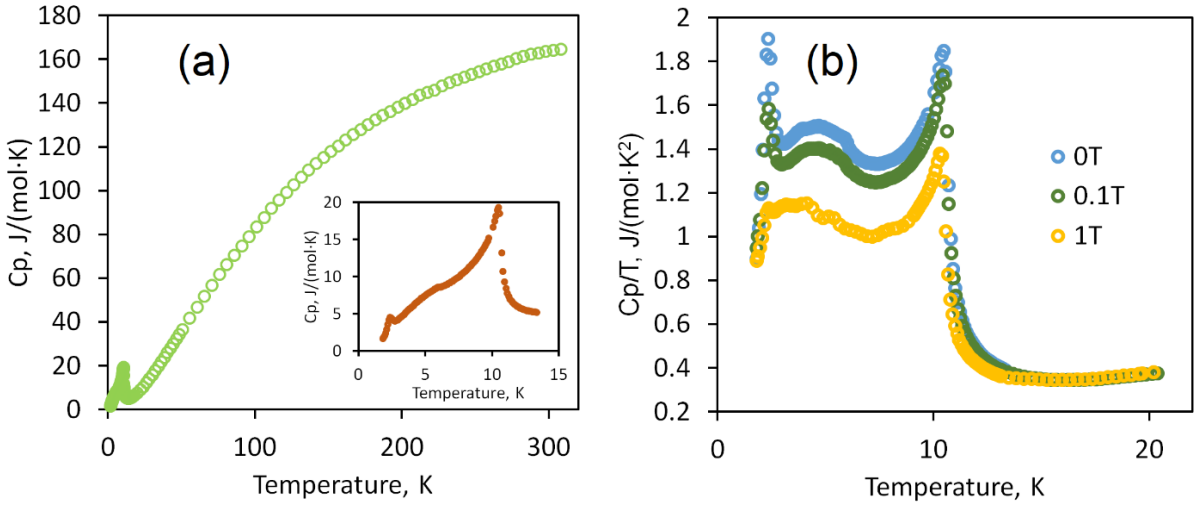

Figure 3.9 (a) Heat capacity measured from room temperature down to 2 K with the low-temperature part shown as insert. (b) Low-temperature part of the heat capacity measured in different fields plotted as C_p/T *vs.* T.

Above 15 K, the heat capacity curve is smooth, confirming the absence of phase transitions in this region. The heat capacity curve does not reach saturation at room temperature, while approaching the Dulong–Petit limit $C_p = N{\times}3R = 7{\cdot}3{\cdot}8.31 = 174.5$ J/(mol·K), where N is the number of atoms per formula unit. The C_p/T^3 *vs.* T^2 plot (in SI) intended to disclose a possible contribution from the Einstein modes caused by rattling is dominated by the magnetic transition at 11.3 K. Within the 15 K – 250 K temperature region, it is possible to fit the data with the following equation, similar to $SrNi_2P_4$ [23]:

$$C_V \approx C_P = a_D C_D\left(\frac{\theta_D}{T}\right) + a_{E1} C_E\left(\frac{\theta_{E1}}{T}\right) + a_{E2} C_E\left(\frac{\theta_{E2}}{T}\right)$$

We can argue that, similarly to $SrNi_2P_4$, the second Einstein term is due to a substantial anisotropy of the Eu^{2+} vibrations, which is evident from **Figure 3.4.** Indeed, our attempts to fit the heat capacity curve with the pure Debye model or with the Debye model supplied by a single Einstein mode were unsuccessful (see SI). In contrast, the model with two Einstein modes leads to a perfect fit up to 250 K, and the characteristic temperatures are $\theta_D = 521$ K, $\theta_{E1} = 73$ K, $\theta_{E2} = 159$ K.

Resistivity and thermoelectric properties. Temperature dependence of the resistivity (inverse electrical conductivity) and thermal conductivity measured on a pressed and sintered polycrystalline sample with ~85% density are shown in **Figure 3.10**. Whereas a contribution of grain boundaries cannot be excluded, we were nevertheless able to extract basic trends in transport properties. On increasing the temperature, the resistivity increases from 0.5 μΩ·m at 25 K to 3.5 μΩ·m at 300 K, confirming the metallic behaviour of $EuNi_2P_4$. Linear temperature dependence of the resistivity indicates electron-phonon interaction as the main scattering mechanism. The Seebeck coefficient is within the range of 0.6 – 0.9 μV/K at 10 – 300 K. The small but positive value of the Seebeck coefficient pinpoints the *p*-type conductivity in $EuNi_2P_4$. Above ~ 10K, thermal conductivity rapidly increases reaching ~4W/K·m at 100K. The electronic component of the thermal conductivity was calculated according to the Wiedemann–Franz law [10] and plotted together with the total thermal conductivity in **Figure 3.10**.

The low-temperature resistivity presented in **Figure 3.11** shows anomalies at 2.7 K and 11.3 K, which are consistent with the magnetic susceptibility and heat capacity data and confirm the intrinsic nature of the magnetic transitions.

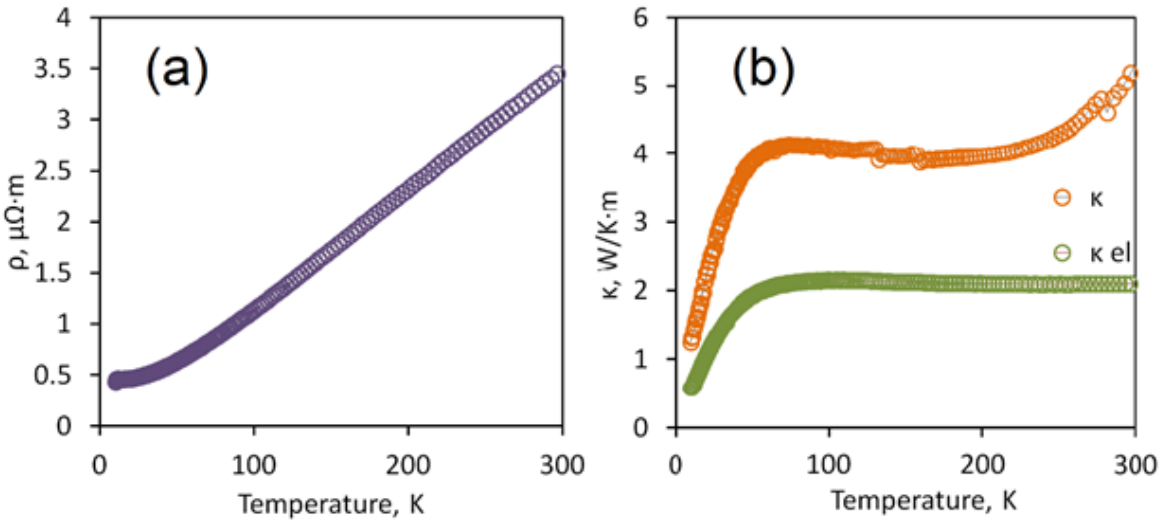

Figure 3.10 Temperature dependence of the resistivity (a), and thermal conductivity (b) in the 10 – 300K temperature range.

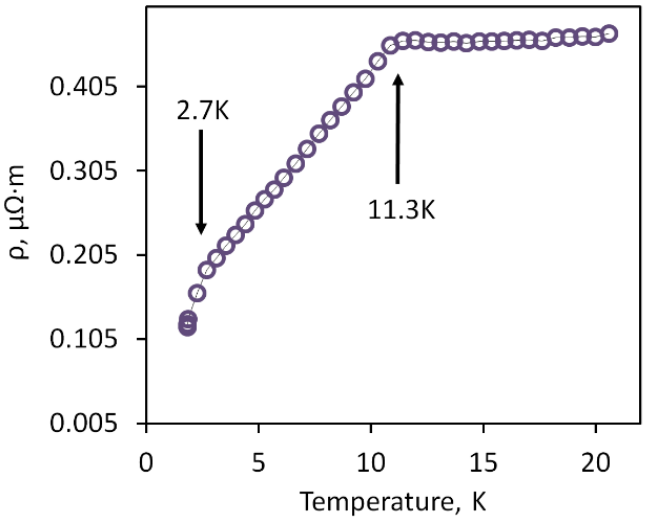

Figure 3.11 Low-temperature part of the electrical resistivity curve for $EuNi_2P_4$.

Raman spectroscopy data. Raman spectroscopy helps observing rattling modes in clathrates [44, 45]. The Raman spectrum of $EuNi_2P_4$ shown in **Figure 3.12** reveals a very strong vibration mode at 59 cm^{-1} that corresponds to a temperature of 85 K. The high-wavenumber region (also above 190 cm^{-1}) is featureless, which may signal that other modes are too weak to be distinguished over the background, given the strong absorption is caused by the metallic nature of the material.

The high Debye temperature of ~500 K suggests that the observed Raman mode does not belong to phonons of the host matrix. On the other hand, the mode frequency agrees very well with the characteristic values calculated from the slope of U_{33} of Eu (104 K) and with the low-energy contribution to the heat capacity (73 K). However, such a simplified consideration does not explain the absence of the second mode at a slightly higher energy, which would be expected from the anisotropic movements of Eu^{2+} inside the cage.

In order to get further insight into the Raman spectra, we calculated Raman-active vibrational modes in $EuNi_2P_4$. The obtained positions along with their relative intensities are the following: 65 cm^{-1} (100%), 71 cm^{-1} (1.5%), 92 cm^{-1} (0.6%), 94 cm^{-1} (0.4%), 367 cm^{-1} (4%), 401 cm^{-1} (7%), 409 cm^{-1} (3%). First of all, the only intense mode is at 65cm^{-1}, which is in a very good agreement with the observed one at 59cm^{-1}. The second point is that Γ-point phonons can be split into two parts well separated in energy.

The low-energy modes below 100 cm^{-1} are responsible for the Eu^{2+} rattling, whereas the high-energy modes are caused by vibrations of the host matrix. The presence of more than two calculated low-energy modes suggests that even the anisotropic harmonic model for the description of ADPs of the rattler is not fully adequate.

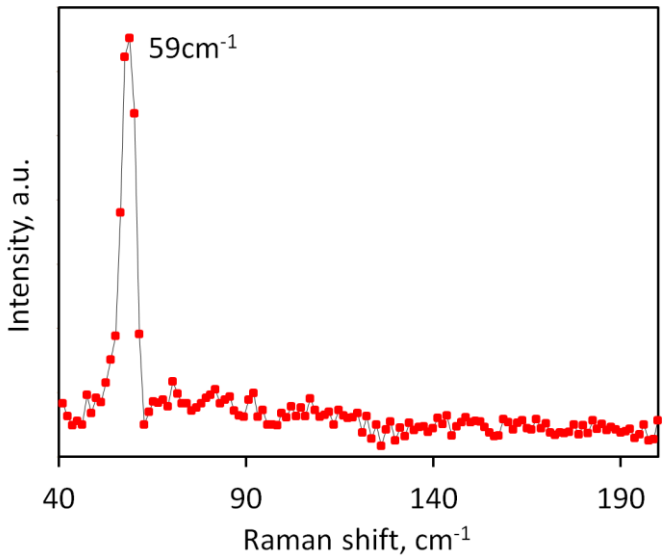

Figure 3.12 A room-temperature Raman spectrum of $EuNi_2P_4$ features a single intense mode at 59 cm^{-1}.

General overview and structure-properties relations. $EuNi_2P_4$ is the first representative of magnetic unconventional clathrates. Compared to $SrNi_2P_4$, the synthesis of the Eu analogue proved to be more difficult, given the size difference between Sr^{2+} and Eu^{2+}. Still the effect of the size mismatch between Eu^{2+} and the Ni – P framework in $EuNi_2P_4$ is somehow mitigated by re-assembling of the twisted Kelvin cell into a more symmetric ("less twisted") cage, as suggested by the trend in the unit cell dimensions of $SrNi_2P_4$ and $EuNi_2P_4$.

Unlike the majority of solids, clathrates cannot be described by the Debye lattice model. It is often assumed that phonon spectra of clathrates can be separated into two nearly independent parts. One of them corresponds to vibrations of the host matrix that occur at higher energies and can be described by the Debye model. As guest cations are located in the oversized cages, their movements are independent from the host matrix and can be described by pseudo-localized Einstein modes. The estimated Debye temperatures of $SrNi_2P_4$ and $EuNi_2P_4$ are comparable and lie around 500 K, as the frameworks of the two compounds are almost identical. The characteristic Einstein temperatures extracted from the heat capacity data for Eu^{2+} in $EuNi_2P_4$ (73K) and Sr^{2+} in $SrNi_2P_4$ (reported 71 K [23]) are also comparable.

This close similarity can be explained by two counteracting effects, because Eu^{2+} has a higher mass but a slightly smaller radius compared to Sr^{2+}.

According to the transport properties data, $EuNi_2P_4$ exhibits a behaviour similar to $SrNi_2P_4$, though its resistivity is slightly lower, while thermal conductivity is slightly higher. It is interesting that the thermal conductivity of $SrNi_2P_4$ almost exclusively arises from the electronic term, while in $EuNi_2P_4$ lattice and electronic contributions are comparable in magnitude. This could be explained by the presence of 4*f* electronic states near the Fermi level, as it has been outlined elsewhere [20]. However, the extracted magnetic moment of Eu suggests the absence of valence fluctuations and the full localization of 4*f* electrons on the Eu atoms.

Although Eu^{2+} magnetic cations are well separated in the crystal structure with the shortest Eu – Eu distance of 5.17 Å, sizable magnetic interactions occur. Our data reveal at least three phase transitions at ~2.5 K, ~6.1 K and ~11.3 K. According to the structural data, there are no structural transformations in $EuNi_2P_4$ down to 10K. The transition at 11.3 K is of second order and probably due to an antiferromagnetic ordering in the Eu sublattice, the transition at 6.1K is also of magnetic nature, while the one at ~2.5K is a first-order transition with a magnetic component.

The antiferromagnetic nature of $EuNi_2P_4$ is underpinned by the fact that the magnetization curve taken at 1.9 K shows a complex non-linear shape and does not reach saturation in a 7 T field. The negative Curie-Weiss temperature (θ_{CW} ~ – 5.7 K) reflects predominant antiferromagnetic interactions too, but its absolute value is twice smaller than the Neel temperature T_N = 11.3 K. The complex low-temperature behaviour observed in $EuNi_2P_4$ is rather unusual for magnetic clathrates. Magnetic interactions between the Eu^{2+} magnetic ions are mediated by conduction electrons through the RKKY mechanism and can be either ferro- or antiferromagnetic depending on the Eu – Eu distance. $EuNi_2P_4$ features several nearest-neighbor Eu – Eu distances that fall in the 5.17 – 5.42 Å range, and may thus combine ferro- and antiferromagnetic interactions, leading to a complex magnetic behaviour.

The low-temperature phase diagram of $EuNi_2P_4$ (**Figure 3.13**) reveals three distinct phases that transform into each other as a function of temperature and field. The outer phase boundary is typical for antiferromagnets, whereas the other phase boundaries may reflect additional magnetic or structural order. Our preliminary neutron diffraction measurements

confirm three low-temperature magnetically ordered phases; the derived magnetic structures will be communicated later.

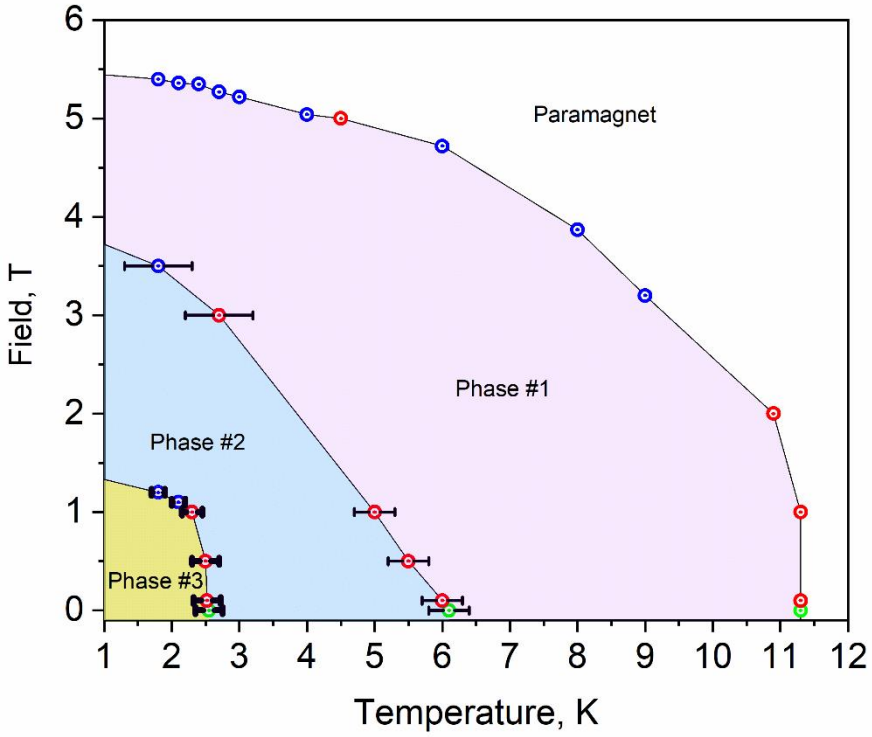

Figure 3.13 Field *vs.* temperature phase diagram of $EuNi_2P_4$. Blue points are taken from isothermal sections (magnetization *vs.* field), red – from constant field sections (magnetization *vs.* temperature), green – averaged zero-field data. The error bars are due to the hysteresis of first-order transitions.

Conclusions

$EuNi_2P_4$ is a new magnetic compound that extends the family of unconventional clathrates and provides the first example of a purely magnetic guest atom. This compound can be prepared by a combined mechanochemical and solid-state reaction. In its crystal structure, Eu^{2+} cations are encapsulated into 24-coordinated metallic twisted Kelvin cells formed by the Ni and P atoms. Pronounced rattling of the Eu^{2+} cation inside the oversized cage results in a strong Einstein contribution to the heat capacity, and is also evident from the Raman scattering and temperature-dependent diffraction data. Despite the large spatial separation between the Eu^{2+} magnetic centers, predominantly antiferromagnetic interactions occur. $EuNi_2P_4$ reveals complex magnetism with three phase transitions at 2.5 K, 6.1 K and 11.3 K in zero field. Metallic nature of $EuNi_2P_4$ leads to rather poor thermoelectric performance.

This chapter has been published in a peer-reviewed journal *Inorganic Chemistry Frontiers* of the publisher Royal Society of Chemistry (DOI 10.1039/C9QI01566C). The crystal structure of the title compound is deposited in ICSD under the reference number 1969248.

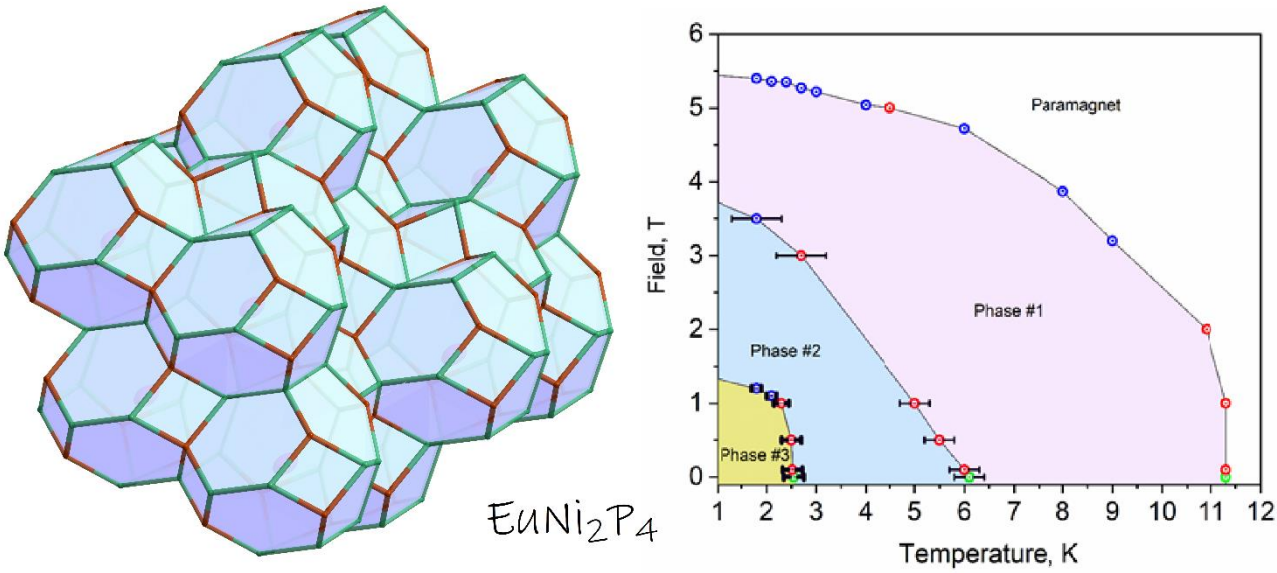

Figure 3.TOC Graphical abstract of the paper entitled "$EuNi_2P_4$, the first magnetic unconventional clathrate prepared *via* mechanochemically assisted route".

Several other people also contributed to this work

- Dr. Nazir Khan and Dr. Alexander A. Tsirlin performed physical properties measurements, low-temperature synchrotron diffraction, discussed the results and improved the manuscript.
- Dr. Alexey N. Kuznetsov and Dr. Dmitri O. Charkin performed DFT calculations, supported with discussion of crystallographic part and improved the manuscript.
- Prof. Andrei V. Shevelkov and Prof. Arno Pfitzner contributed to discussion of the work, provided the lab space and equipment for work and improved the manuscript.
- Prof. Alkwin Slenczka performed Raman measurements, but refused to be in the co-author list.
- Igor V. Plokhikh performed synthesis of the target compound, designed computations and measurements and wrote the draft of the paper.

Supporting Information

RAMAN SETUP

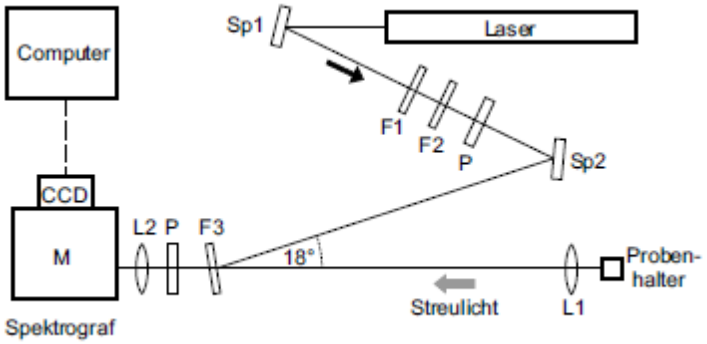

The Raman spectrometer is a homemade setup. It is equipped with a HeNe laser providing 35 mW at 632 nm. Signal detection is accomplished with a CCD camera attached to a grating spectrograph with 350 mm focal length and 1800/mm grating. The CCD-chip has a 1024x256 pixel active area and was operated in full vertical binning mode. Under these conditions and for the wavelength range dictated by the laser the CCD chip cover a spectral range of roughly 50 nm with 1024 data points. The laser is focused to the sample by a microscope objective (20x) (L1) and the signal is collected by the same objective in backward direction and finally focused by a lens (L2) to the entrance slit of the spectrograph. The collinear arrangement of laser beam and the spectrograph's optical axis is accomplished by a notch filter (F3) which at an incident angle of 9° reflects a spectral range of +/- 130 cm^{-1} centered to the laser frequency and transmits all other frequencies. The CCD camera is connected to a PC where spectra are digitally stored.

Two mirrors (Sp1, Sp2) for guiding the laser two filters (F1, F2) serve to eliminate other than the 632 nm laser line. (We have not been using a polarizer neither in the laser beam nor before the spectrograph).

The Raman shift was calibrated by means of an Ar-Ne lamp using the corresponding atomic lines as provided by NIST.

Table 3.S1 Details of synchrotron powder diffraction experiments for $EuNi_2P_4$ at different temperatures.

Phase	$EuNi_2P_4$					
Temperature in K	10	50	100	150	250	273
λ in Å	0.35456					
2θ range in deg	1 – 40					
d-spacing range in Å	0.5 – 20.3					
Space group	*Fddd (No. 70, origin choice 1)*					
Z	*8*					
Density in g/cm^3	5.630	5.628	5.626	5.621	5.598	5.594
Cell parameters						
a in Å	5.1737(1)	5.1742(1)	5.1749(1)	5.1762(1)	5.1841(1)	5.1852(1)
b in Å	9.4518(1)	9.4534(1)	9.4561(1)	9.4602(1)	9.4812(1)	9.4835(1)
c in Å	18.9754(2)	18.9758(2)	18.9752(2)	18.9765(2)	18.9864(2)	18.9894(2)
V in Å^3	927.93(2)	928.18(2)	928.54(2)	929.24(2)	932.20(2)	933.79(2)
Data points	26000	26000	26000	26000	26000	26000
Overall parameters	31	36	30	33	32	31
Reflections	881	881	881	884	887	887
Structural parameters	11	11	11	11	11	11
R values						
R_F in %	2.55	2.71	3.06	4.35	3.86	3.20
R_P in %	14.22	13.90	13.54	12.53	9.63	10.35
R_{wP} in %	18.80	18.35	18.10	16.90	13.92	14.80
χ^2	1.62	1.69	1.63	1.76	2.56	2.53

Table 3.S2 Refined atomic coordinates and atomic displacement parameters (in Å^2) in the crystal structure of $EuNi_2P_4$ at different temperatures.

At.	Site	10K	50K	100K	150	250	273
Eu	8*b* (0; 0; 0)						
	U_{eq}	0.0029(1)	0.0039(2)	0.0058(2)	0.0111(2)	0.0146(2)	0.0144(2)
	U_{11}	0.0013(2)	0.0018(2)	0.0034(3)	0.0055(3)	0.0098(3)	0.0104(3)
	U_{22}	0.0040(3)	0.0045(3)	0.0057(3)	0.0075(3)	0.0106(3)	0.0110(3)
	U_{33}	0.0036(3)	0.0055(3)	0.0082(2)	0.0132(3)	0.0226(4)	0.0240(3)
Ni	16*g* (0; 0, *z*)						
	z	0.11987(5)	0.11983(5)	0.11987(5)	0.12008(5)	0.11993(5)	0.11979(5)
	U_{iso}	0.0050(2)	0.0050(2)	0.0058(2)	0.0071(2)	0.0090(2)	0.0093(2)
P	32*h* (*x*; *y*; *z*)						
	x	0.3116(3)	0.3121(3)	0.3118(3)	0.3113(3)	0.3115(2)	0.3117(3)
	y	0.0568(1)	0.0572(1)	0.0571(1)	0.0569(1)	0.0570(1)	0.0570(1)
	z	0.19380(8)	0.19371(8)	0.19377(8)	0.19417(7)	0.19397(7)	0.19380(7)
	U_{iso}	0.0049(3)	0.0049(3)	0.0055(2)	0.0072(3)	0.094(3)	0.0096(3)

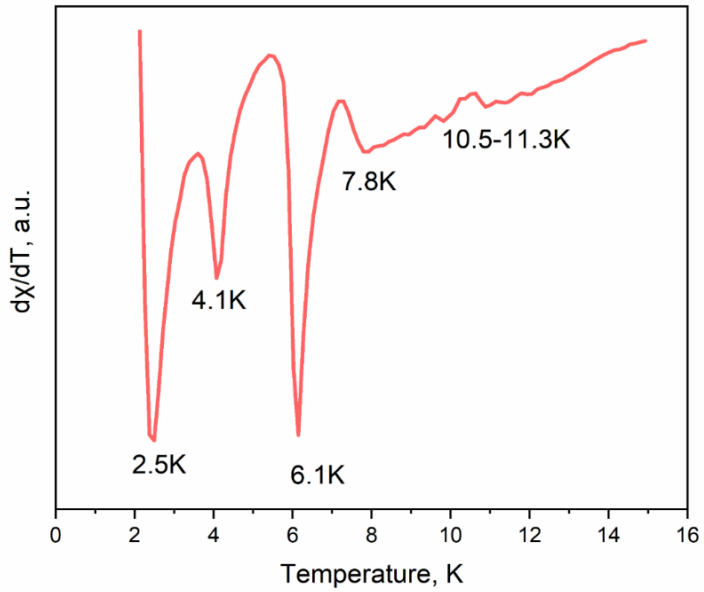

Figure 3.S1 The first derivative of the 0.005 T magnetic susceptibility curve for $EuNi_2P_4$. The anomalies are outlined.

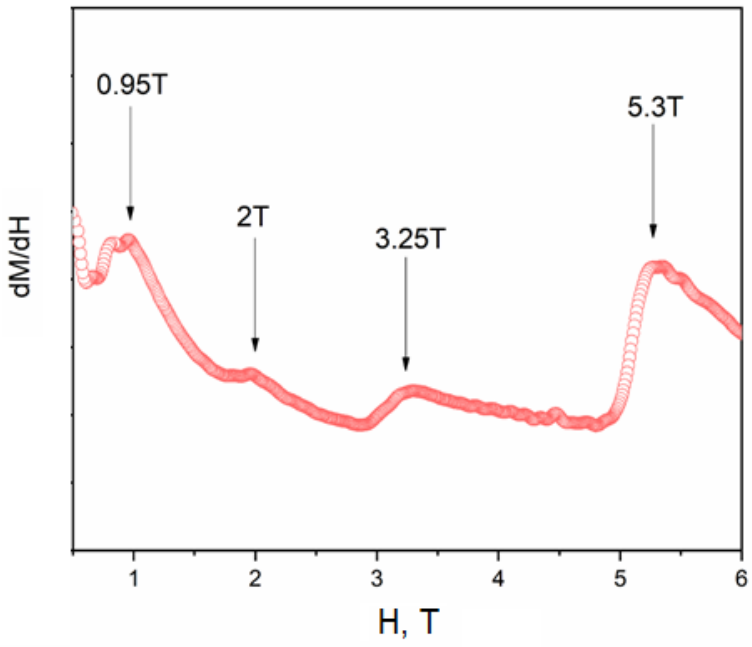

Figure 3.S2 The first derivative of the magnetization curve taken at 1.8 K for $EuNi_2P_4$. The anomalies are outlined.

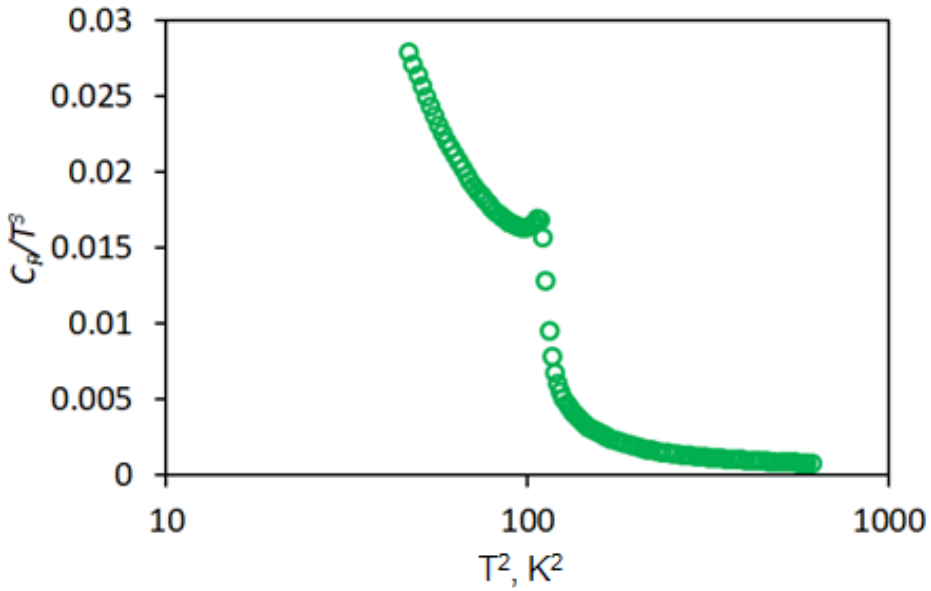

Figure 3.S3 C_P/T^3 *vs.* T^2 plot for $EuNi_2P_4$ intended to recover the contribution of the Einstein modes to heat capacity.

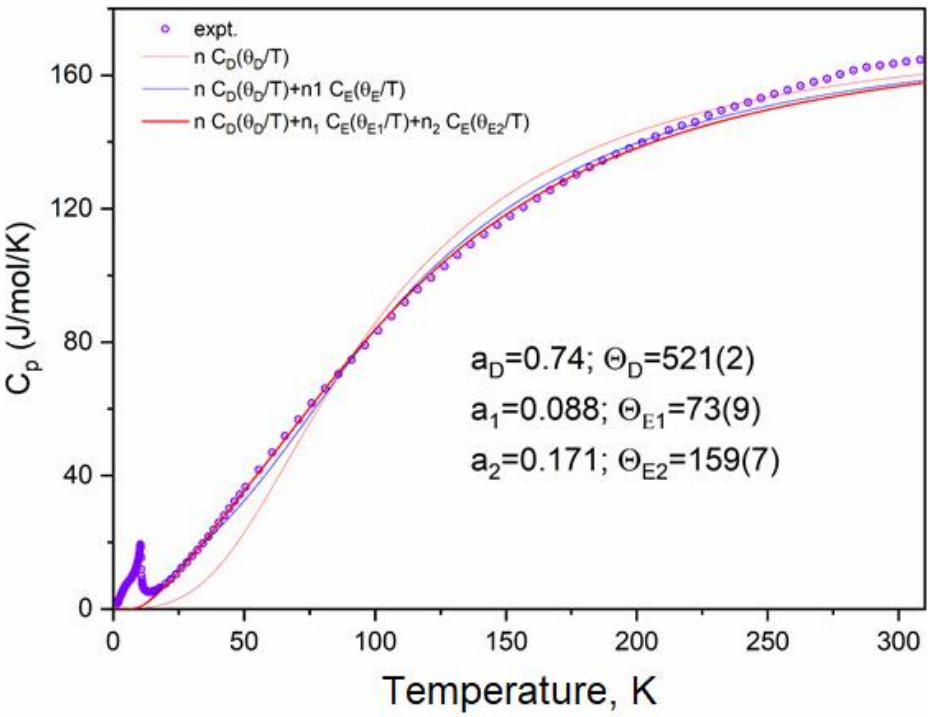

Figure 3.S4 Heat capacity *vs.* temperature plot and attempts to fit it with the Debye function, combination of the Debye function and one Einstein, combination of the Debye function and two Einstein. Fitting parameters for the last case are provided on the plot.

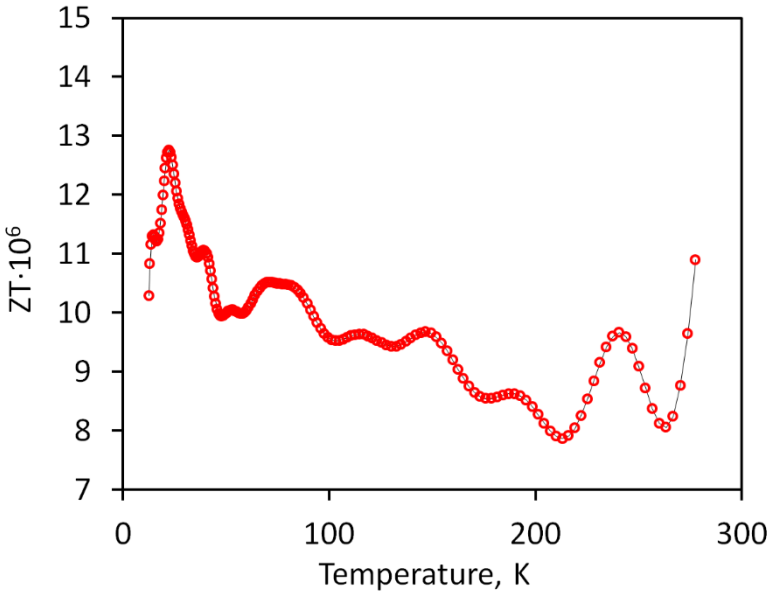

Figure 3.S5 ZT (thermoelectric figure-of-merit) *vs.* temperature plot for $EuNi_2P_4$.

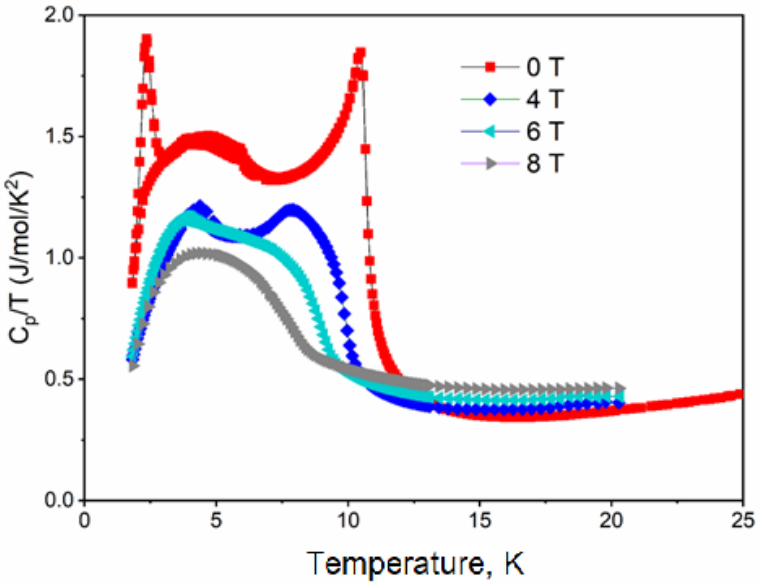

Figure 3.S6 *C_P/T vs. T* plot for $EuNi_2P_4$ in high fields.

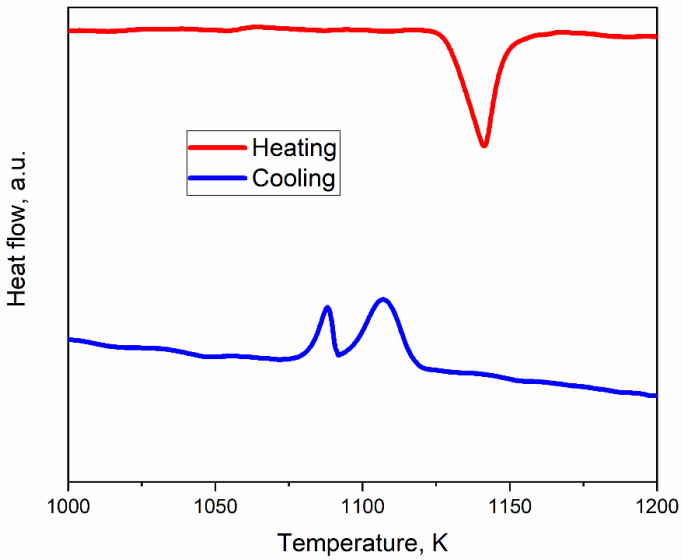

Figure 3.S7 Differential thermal analysis curve for $EuNi_2P_4$.

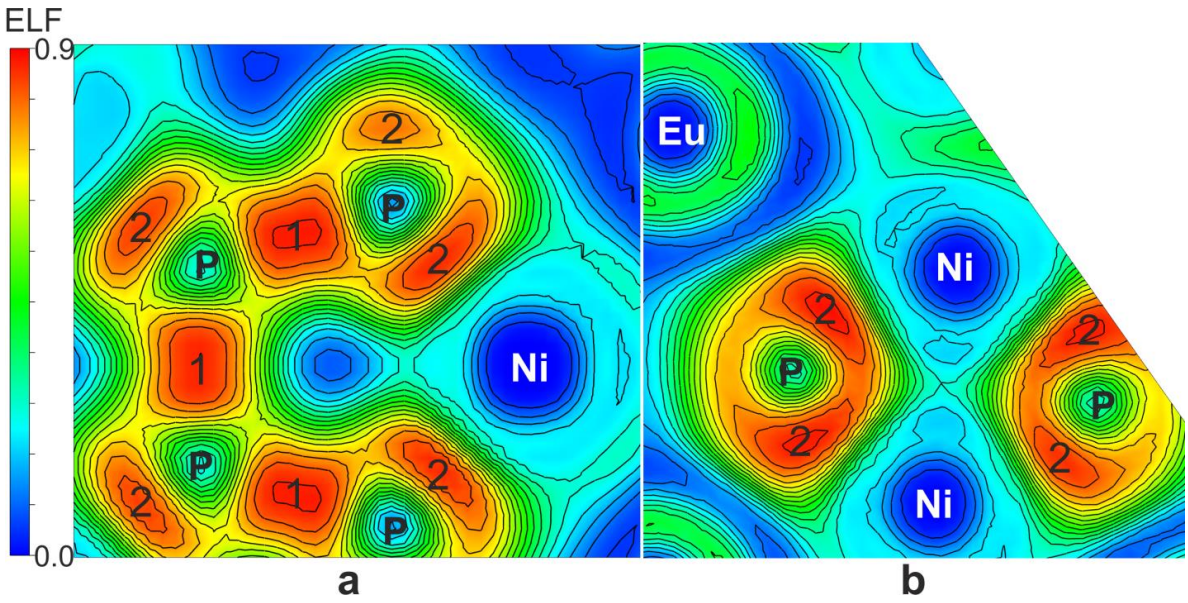

Figure 3.S8 ELF sections passing through a) P-P and P-Ni bonds, and b) P-Ni and P-Ni bonds. Localization domains corresponding to P-P bonds are labelled as 1, and P-Ni bonds as 2.

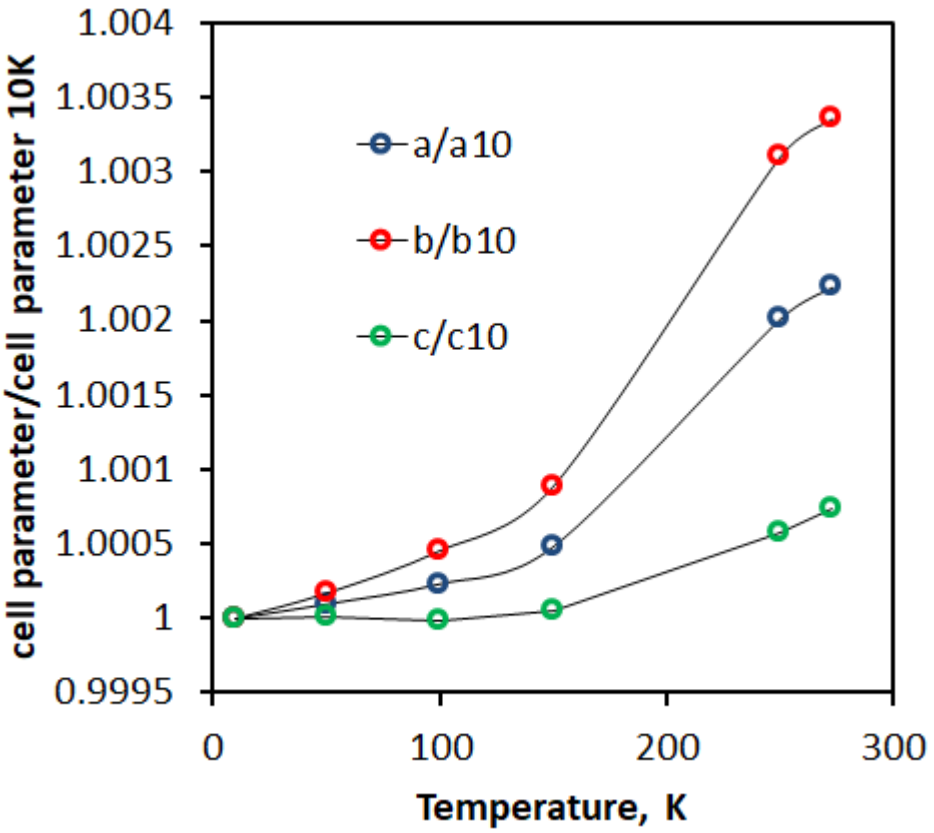

Figure 3.S9 Temperature dependence of *a*, *b* and *c* unit cell parameters.

Addendum

After the publication of the results presented in this chapter, several additional points raised up.

1. The oxygen-containing impurity, $Eu_3(PO_4)_2$, observed in the sample, is due to the extreme sensitivity of the intermediates to traces of oxygen and moisture in the synthetic environment (ball-mill surface, glove-box atmosphere, silica tubes). One approach to overcome this issue is to use bigger batches of the starting materials. For instance, nearly phase pure samples form, when 3 g mixture of precursors is taken. It is illustrated by the Rietveld plot provided in **Figure 3.A1**.

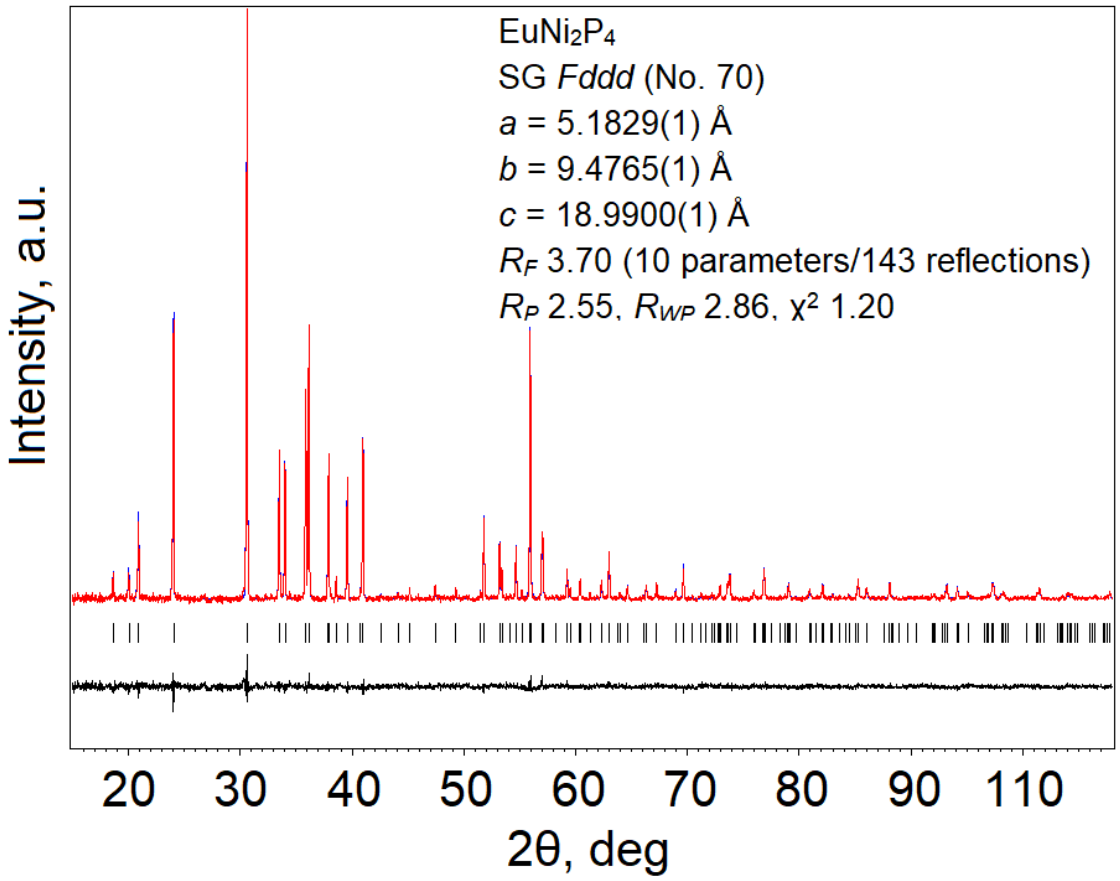

Figure 3.A1 Rietveld refinement plot for the 3g-load sample of the $EuNi_2P_4$.

2. Small single crystals of this compound form when a slightly lower annealing temperature is used (1113 K instead of 1123 K). This is useful, as studies of physical properties on single-crystals can give a more in-depth insight into its magnetic behaviour.

3. The first derivative of the magnetization curve at 2 K is more complicated than one can suggest from the phase diagram provided in the text. A bit more elaborated phase diagram (**Figure 3.A2**) has been constructed by our colleagues based on the magnetization data.

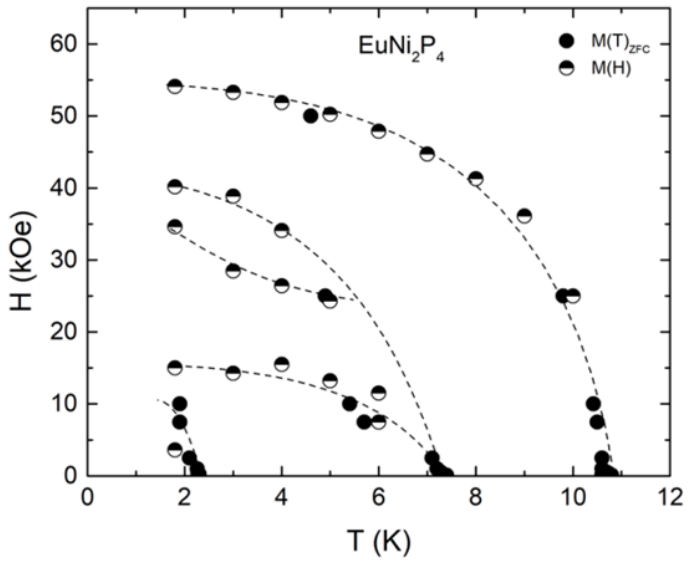

Figure 3.A2 Tentative H–T phase diagram constructed based on M(T) and M(H) data presented above. Dashed lines are guides for the eye. Taken from Novikov et al. *Phys. Chem. Chem. Phys.* 2020.

4. Raman spectroscopy was instrumental in observing the low-energetic vibration modes in clathrates. In the case of $EuNi_2P_4$, it was possible to trace the Raman active mode at ~ 60 cm^{-1}, despite the metallicity of the compound. The same belongs to the sibling of the $EuNi_2P_4$ – $SrNi_2P_4$, a Raman spectra of which has also been collected. The low-energetic Raman mode is visible at ~55 cm^{-1} (corresponds to 79 K), which is in a good agreement with 71 K, the Einstein contribution to heat capacity, which has been reported previously.

References

[1] G. A. Jeffrey. In: Hydrate Inclusion Compounds; Atwood, J.L., Davies, J.E., McNicol, D.D., Eds.; Academic Press: London, **1984**.

[2] A. V. Shevelkov, K. Kovnir. Zintl Clathrates. In: Fässler T. (ed) Zintl Phases. Structure and Bonding, vol 139. Springer, Berlin, Heidelberg, **2010**.

[3] K. A. Kovnir, A. V. Shevelkov. Semiconducting clathrates: synthesis, structure and properties. *Russ. Chem. Rev.* **2004**, *73*, 923 – 938.

[4] The Physics and Chemistry of Inorganic Clathrates; G. S. Nolas, Ed.; Springer: New York, **2014.**

[5] J.-A. Dolyniuk, B. Owens-Baird, J. Wang, J. V. Zaikina, K. Kovnir. Clathrate thermoelectrics. *Materials Science and Engineering: R: Reports,* **2016**, *108*, 1 – 46

[6] J. Wang, J.-A. Dolyniuk, K. Kovnir. Unconventional clathrates with transition metal–phosphorus frameworks, *Accounts of Chemical Research,* **2017**, *51*, 31 – 39.

[7] J.-A. Dolyniuk, P. S. Whitfield, K. Lee, O. I. Lebedev, K. Kovnir. Controlling superstructural ordering in the clathrate-I $Ba_8M_{16}P_{30}$ (*M* = Cu, Zn) through the formation of metal–metal bonds. *Chem. Sci.* **2017**, *8*, 3650 – 3659

[8] J.-A. Dolyniuk, J. V. Zaikina, D. C. Kaseman, S. Sen, K. Kovnir. Breaking the tetra-coordinated framework rule: new clathrate $Ba_8M_{24}P_{28+\delta}$ (M=Cu/Zn). *Angew. Chem.* **2017**, *56*, 2418 – 2422.

[9] D. O. Charkin, R. Demchyna, Yu. Prots, H. Borrmann, U. Burkhardt, U. Schwarz, W. Schnelle, I. V. Plokhikh, S. M. Kazakov, A. M. Abakumov, D. Batuk, V. Yu. Verchenko, A. A. Tsirlin, C. Curfs, Yu. Grin, A. V. Shevelkov. Two new arsenides, $Eu_7Cu_{44}As_{23}$ and $Sr_7Cu_{44}As_{23}$, with a new filled variety of the $BaHg_{11}$ structure. *Inorg. Chem.* **2017**, *53*, 11173 – 11184.

[10] J.-A. Dolyniuk, J. Wang, K. Lee, K. Kovnir. Twisted kelvin cells and truncated octahedral cages in the crystal structures of unconventional clathrates, AM_2P_4 (*A* = Sr, Ba; M = Cu, Ni). *Chem. Mater.* **2015**, *27*, 4476 – 4484.

[11] J. Dünner, A. Mewis, A. $BaCu_2P_4$-ein neues ternäres Polyphosphid. *J. Alloys Compd.*. **1990**, *167*, 127 – 134.

[12] V. Keimes, D. Johrendt, A. Mewis.$BaNi_2P_4$: Dimorphie durch Peierls-Verzerrung? Z. *Anorg. Allg. Chem.* **1995**, *621*, 925 – 930.

[13] N.-T. Suen, L. Huang, J. J. Meyers, S. Bobev. An unusual triple-decker variant of the tetragonal $BaAl_4$-structure type: synthesis, structural characterization, and chemical bonding of $Sr_3Cd_8Ge_4$ and $Eu_3Cd_8Ge_4$. *Inorg. Chem.* **2018**, *57*, 833 – 842.

[14] R. Zhang, M.-Y. Pan, M. Zhu, X.-T. Tao, S.-Q. Xia. Experimental and theoretical studies on the crystal structure of ternary copper arsenides $A_2Cu_3As_3$ (A = Sr, Eu). *Eur. J. Inorg. Chem.* **2016**, *23*, 3774 – 3780.

[15] D. O. Charkin, A. V. Urmanov, S. M. Kazakov, D. Batuk, A. M. Abakumov, S. Knoner, E. Gati, B. Wolf, M. Lang, A. V. Shevelkov, G. Van Tendeloo, E. V. Antipov. Synthesis, crystal structure, transport, and magnetic properties of novel ternary copper phosphides, $A_2Cu_6P_5$ (A = Sr, Eu) and $EuCu_4P_3$. *Inorg. Chem.* **2012**, *51*, 8948 – 8955.

[16] R. D. Shannon. Revised effective ionic radii and systematic studies of interatomic distances in halides and chalcogenides. *ActaCryst. A* **1976**, 32, 751 – 767.

[17] Y. Mudryk, P. Rogl, C. Paul, S. Berger, E. Bauer, G. Hilscher, C. Godart, H. Noël, A. Saccone, R. Ferro. Crystal chemistry and thermoelectric properties of clathrates with rare-earth substitution. *Physica B*, **2003**, *328*, 44 – 48.

[18] B. C. Sales, B. C. Chakoumakos, R. Jin, J. R. Thompson, D. Mandrus. Structural, magnetic, thermal, and transport properties of $X_8Ga_{16}Ge_{30}$ (*X* = Eu, Sr, Ba) single crystals. *Phys. Rev. B* **2011**, *63*, 245113.

[19] M. H. Phan, G. T. Woods, A. Chaturvedi, S. Stefanoski, G. S. Nolas, H. Srikanth. Long-range ferromagnetism and giant magnetocaloric effect in type VIII $Eu_8Ga_{16}Ge_{30}$ clathrates. *Appl. Phys. Lett*. **2008**, *93*, 252505.

[20] K. Kovnir, U. Stockert, S. Budnyk, Yu. Prots, M. Baitinger, S. Paschen, A. V. Shevelkov, Yu. Grin. Introducing a magnetic guest to a tetrel-free clathrate: Synthesis, structure, and properties of $Eu_xBa_{8-x}Cu_{16}P_{30}$ ($0 \le x \le 1.5$). *Inorg. Chem.* **2011**, *50*, 10387 – 10396.

[21] D. Johrendt, C. Felser, C. Huhnt, G. Michels, W. Schäfer, A. Mewis. Tuning the valence in ternary Eu-pnictides: the series $EuPd_{1-x}Ag_xP$ and $EuPd_{1-x}Au_xAs$. *J. Alloys Compd.* **1997**, *246,* 21 – 26.

[22] B. Perscheid, E. V. Sampathkumaran, G. Kaindl. Temperature and pressure dependence of the mean valence of Eu in $EuNi_2P_2$. *J. Magn. Magn. Mater.* **1985**, *47 – 48*, 410 – 412.

[23] V. Novikov, K. Pilipenko, A. Matovnikov, N. Mitroshenkov, I. Plokhikh, A. Tyablikov, A. Shevelkov. Structure-related thermal properties of type-VII clathrates $SrNi_2P_4$ and $BaNi_2P_4$ at low temperature. *Phys. Status Solidi*, **2018**, *255*, 1800067.

[24] STOE WinXPOW, Version 3.10, STOE &Cie GmbH, Darmstadt **2016**.

[25] V. Petricek, M. Dusek, L. Palatinus. Crystallographic computing system JANA2006: general features. *Z. Kristallogr.* **2014**, *229*, 345.

[26] G. Kresse, J. Furthmüller. Vienna Ab initio simulation package (VASP), v.5.3, http://www.vasp.at/.

[27] G. Kresse, D. Joubert. From ultrasoft pseudopotentials to the projector augmented-wave method. *Phys. Rev. B* **1999**, *59*, 1758 – 1775.

[28] H. J. Monckhorst, J. D. Pack. Special points for Brillouin-zone integrations. *Phys. Rev. B.* **1976**, *13*, 5188.

[29] J. P. Perdew, K. Burke, M. Ernzerhof. Generalized gradient approximation made simple. *Phys. Rev. Lett.* **1996**, *77*, 3865 – 3868.

[30] R. F. W. Bader. Atoms in Molecules: a Quantum Theory, Oxford University Press, Oxford, **1990**.

[31] M. Yu, D. R. Trinkle. Accurate and efficient algorithm for Bader charge integration, *J. Chem. Phys.* **2011**, *134*, 064111.

[32] B. Silvi, A. Savin. Classification of chemical bonds based on topological analysis of electron localization functions. *Nature.* **1994**, *371*, 683.

[33] A. Fonari, S. Stauffer. Vasp_raman.py, Python program to evaluate off-resonance Raman activity using VASP code, 2013. https://github.com/raman-sc/VASP/.

[34] S. I. Chykhrij, V. S. Babizhets'ky, S. V. Oryshchyn, Yu. B. Kuz'ma, L. G. Aksel'rud. Crystal structure of $Tb_{16}Ni_{36}P_{22}$ and isotypic lanthanoid nickel phosphides. *J. Alloys Compd.* **1997**, *259*, 186 – 190.

[35] V. S. Babizhets'ky, S. I. Chykhrij, S. V. Oryshchyn, Yu. B. Kuz'ma. Preparation of the new phosphides $Ln_9Ni_{26}P_{12}$ (Ln= Ce, Pr, Nd, Eu) and their crystal structure. *Russ. J. Inorg. Chem.* **1992**, *37*, 1372 – 1374.

[36] V. S. Babizhets'ky, S. I. Chykhrij, S. V. Oryshchyn, Yu. B. Kuz'ma. Synthesis and structure of some new phosphides of rare-earth metals and nickel. *Ukr. Khim. Zh. (Ukr. Ed.)*. **1993**, *59*, 240 – 242.

[37] J. V. Badding, A. M. Stacy. Synthesis and crystal structure of a new europium nickel phosphide phase, $EuNi_5P_3$. *J. Solid State Chem.* **1987**, *67*, 354 – 358.

[38] Yu. B. Kuz'ma, V. S. Babizhet'sky, S. I. Chykhrij, S. V. Oryshchyn, V. K. Pecharsky. Preparation and crystal structure of the $La_2Ni_{12}P_5$ and isotypic ternary lanthanoid-nickel phosphides. *Z. Anorg. Allg. Chem.* **1993**, *619*, 587 – 592.

[39] W. Jeitschko, B. Jaberg. Neue Verbindungen mit $Zr_2Fe_{12}P_7$-Struktur und Verfeinerung der Kristallstrukturen von $Er_2Co_{12}P_7$ und $Er_2Ni_{12}P_7$. Z. *Anorg. Allg. Chem.* **1980**, *467*, 95 – 104.

[40] V. Keimes, A. Hellmann, A. Mewis, C. Huhnt, N. Schütte. $SrNi_{10}P_6$, $EuNi_{10}P_6$ und $BaCo_{10}As_6$: Phasenumwandlungen und Kristallstrukturen. *Z. Anorg. Allg. Chem.* **2000**, *626*, 1653 – 1659.

[41] J.-A. Dolyniuk, J. Mark, S. Lee, N. Tran, K. Kovnir. Synthesis and characterization of K and Eu binary phosphides. *Materials.* **2019**, *12*, 251.

[42] B. C. Sales, D. G. Mandrus, B. C. Chakoumakos. Use of atomic displacement parameters in thermoelectric materials research *Semiconduct. Semimet.* **2001**, *70*, 1 – 36.

[43] I. Mayer, E. Fischbein, S. Cohen. Apatites of divalent europium *J. Solid State Chem.* **1975**, *14*, 307 – 312.

[44] G. S. Nolas, C. A. Kendziora. Raman scattering study of Ge and Sn compounds with type-I clathrate hydrate crystal structure. *Phys. Rev. B* **2000**, *62*, 7157.

[45] Y. Takasu, T. Hasegawa, N. Ogita, M. Udagawa, M. A. Avila, K. Suekuni, I. Ishii, T. Suzuki, T. Takabatake. Dynamical properties of guest ions in the type-I clathrate compounds $X_8Ga_{16}Ge_{30}$ (X = Eu, Sr, Ba) investigated by Raman scattering. *Phys. Rev. B* **2006**, *74*, 174303.

4 On the nature of the low-temperature phases in the first magnetic unconventional clathrate $EuNi_2P_4$

Abstract

Low-temperature magnetic structures of $EuNi_2P_4$, the first tetrel-free clathrate containing a magnetic guest, have been elucidated *via* neutron powder diffraction. In accordance with the previous report, $EuNi_2P_4$ undergoes three phase transitions at T_1 = 2.3 K, T_2 = 6 K and T_3 = 10.5 K. Below T_1 magnetic moments of Eu^{2+} are ordered antiferromagnetically and form a commensurate spin density wave with propagation vector k_1 = 0 ½ 0 and magnetic moments aligned along the *c*-axis. Above T_1 the magnetic propagation vector changes to k_2 = 0 ~0.55 0, which persists up to a transition at T_3, while still featuring a spin density wave, but an incommensurate one with a variable amplitude along *c*-axis. Between T_2 and T_3, there is an additional magnetic phase with propagation vector k_3 = 0 ~0.72 ~0.04 coexisting with the incommensurate spin density wave described by k_2. The origin of such behaviour is discussed based on a consideration of the arrangement of magnetic centers and the analysis of magnetic representations.

Introduction

Intermetallic clathrates are a fascinating class of materials, which feature separation of guest atoms from the host frameworks [1 – 4]. The interest in these compounds is ensured by their thermoelectric performance, which in turn originates from the possibility of almost independent optimization of electric and heat transport properties. Quasi-free guest ions located in the oversized cages introduce low-energetic phonons in the phonon spectra of the materials, which obstruct thermal transport. Another possibility arises from the placement of magnetic lanthanide cations as guest atoms. It has been proposed that mixing of 4*f* orbitals with valence states of the framework atoms can facilitate thermoelectric properties [5]. Additionally, when placing magnetic ions into clathrates, the originated cooperative magnetism can become of interest. Examples of magnetic cations of 4*f* elements introduced as guest atoms into clathrate frameworks are relatively rare. Among conventional intermetallic tetrel-based clathrates, $Eu_8Ga_{16}Ge_{30}$ is the only case [6 – 8]. In this compound ferromagnetic order evolves below T_C = 35 K, despite a pronounced disorder in the Eu^{2+} sublattice. The ferromagnetic ordering in this compound is accompanied by a substantial magnetocaloric effect. Attempts to introduce Eu^{2+} cations into frameworks of

the tetrel-free clathrate $Ba_8Cu_{16}P_{30}$ results in a small substitution range [5] and antiferromagnetic ordering at T_N = 3 K in the border solid-solution with the composition $Eu_{1.5}Ba_{6.5}Cu_{16}P_{30}$.

The recently reported compound $EuNi_2P_4$ is the first representative of unconventional (tetrel-free) clathrates, whose guest atom is a purely magnetic ion Eu^{2+} ($4f^7$) [9, 10]. Unlike its non-magnetic sibling, $SrNi_2P_4$ [11, 12], $EuNi_2P_4$ undergoes several phase transitions at low temperatures, as it has been proven from magnetic susceptibility, heat capacity and resistivity measurements. Evidently, such difference is majorly due to the presence of magnetic moments on the guest ions. Magnetic interactions between magnetic moments of Eu^{2+} take place through a conducting framework according to the RKKY mechanism; their amplitude and sign oscillate depending on a distance between magnetic centers [13] and can extend over the range exceeding just several nearest bonds. In $EuNi_2P_4$ the shortest Eu – Eu distances lie within a relatively broad range 5.18 – 5.46 Å and thus can ensure combined weak ferro- and antiferromagnetic interactions, which can result in a complex set of phase transitions and associated low-temperature magnetic structures. Our current neutron diffraction study confirms the low-temperature part of the phase diagram proposed previously and provide the first insight into the nature of the magnetically ordered phases evolving in $EuNi_2P_4$.

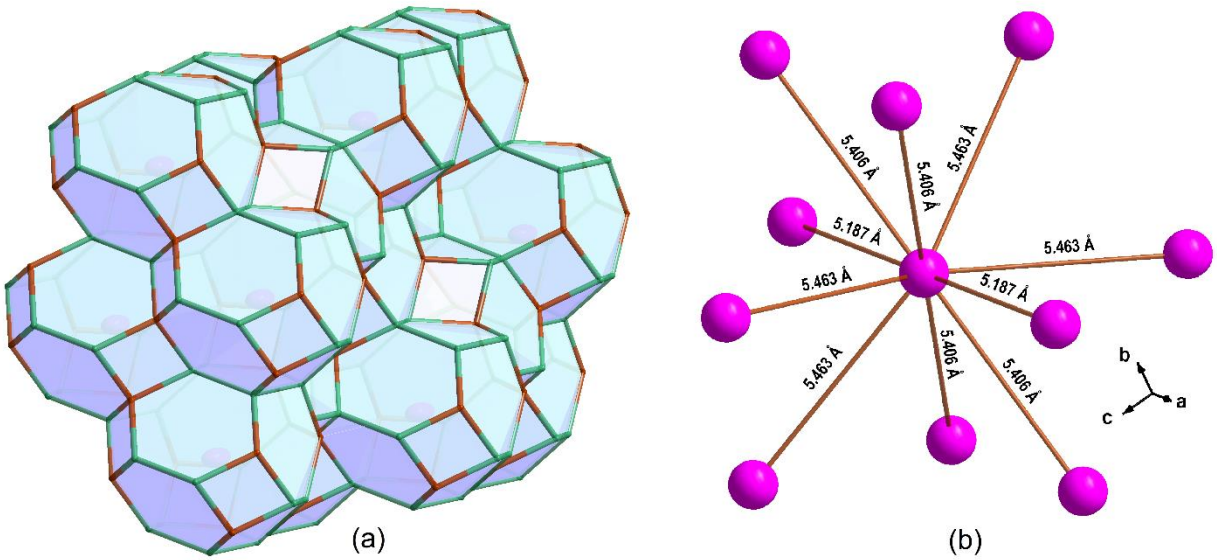

Figure 4.1 (a) Overview of crystal structure for $EuNi_2P_4$ and (b) plot showing the closest Eu – Eu contacts in the structure of $EuNi_2P_4$.

Experimental section

Powder samples of the $EuNi_2P_4$ have been prepared by a combined solid-state and mechanochemical approach, similar to the one described previously [9, 10]. The stoichiometric mixture pre-reacted at 873 K was treated in a ball mill at 600 r/min 10 times 5 min, each with intermediate cooling, pressed into pellets, and annealed at 1113 K for four weeks. X-ray powder diffraction performed using a STOE STADI P diffractometer ($MoK\alpha_1$ radiation, λ = 0.70930 Å, Ge (111) monochromator, Dectris Mythen 1K detector) indicate the formation of a phase-pure sample of $EuNi_2P_4$. The elemental composition and the homogeneity have been confirmed using a Zeiss EVO MA 15 scanning electron microscope equipped with a Bruker Quantax EDX system with an X Flash Detector 630 M.

Neutron diffraction measurements were performed using the WISH diffractometer at the TS2 of the ISIS spallation neutron source [14]. Eu is a strongly neutron-absorbing element; therefore, a thin 3 mm V container has been used as a sample holder, the same way it was done previously on WISH [15, 16]. The sample was placed in a 1.5 K He-cryostat. The data were collected at 1.5 K, 3.5 K, 5 K, 7 K, 9 K, and 15 K for 2 h per diffraction pattern. Magnetic reflections were indexed using the *k*-search code implemented in the FullProf software [17]. Single *k* magnetic structures were derived using magnetic group-subgroup relations implemented in JANA2006 [18]. The magnetic structure model for a double *k* case was derived using ISODISTORT [19, 20]. The further Rietveld refinement was processed in a straight forward manner using the standard mathematical apparatus implemented in JANA2006 [18]. The magnetic structures were drawn using VESTA software [21].

Results and discussions

Magnetic susceptibility and heat capacity data measured below 20 K are provided in **Figure 4.2**. Two strong anomalies in heat capacity at T_1 = 2.5 K and T_3 = 11 K found their counterparts as small effects in the magnetic susceptibility, while the most substantial effect in magnetic susceptibility data at T_2 = 6 K is accompanied by only a tiny kink in heat capacity. Based on a set of magnetization measurements, a magnetic phase diagram has been proposed [9, 10]. It outlines phase temperature-field boundaries of three magnetically ordered phases existing in this compound at low-temperature. The temperature evolution of the neutron diffraction pattern of $EuNi_2P_4$ is provided in **Figure 4.3**. The pattern at 15 K corresponds to a paramagnetic phase, and thus, as expected, contains only structural reflections, positions of which are consistent with the room-temperature crystal structure

except for the thermal expansion. The patterns at 9 K and below, besides structural reflections, also show several additional ones, presumably corresponding to magnetic ordering. The diffraction pattern at 1.5 K is qualitatively different from the diffraction patterns at 3.5 K and 5 K, which are also different from the data at 7 K and 9 K. This fact is in agreement with physical properties data and confirms the intrinsic nature of the transitions at T_1, T_2, and T_3. The room-temperature parameters are a = 5.1829(1) Å, b = 9.4765(1) Å, c = 18.9900(1) Å, the space group *Fddd* and atomic arrangement are in a good with reported ones [9]. This setting of the unit cell is further used for the discussion of *k*-vectors. No indications of perturbations in the structural motif at low temperatures were observed.

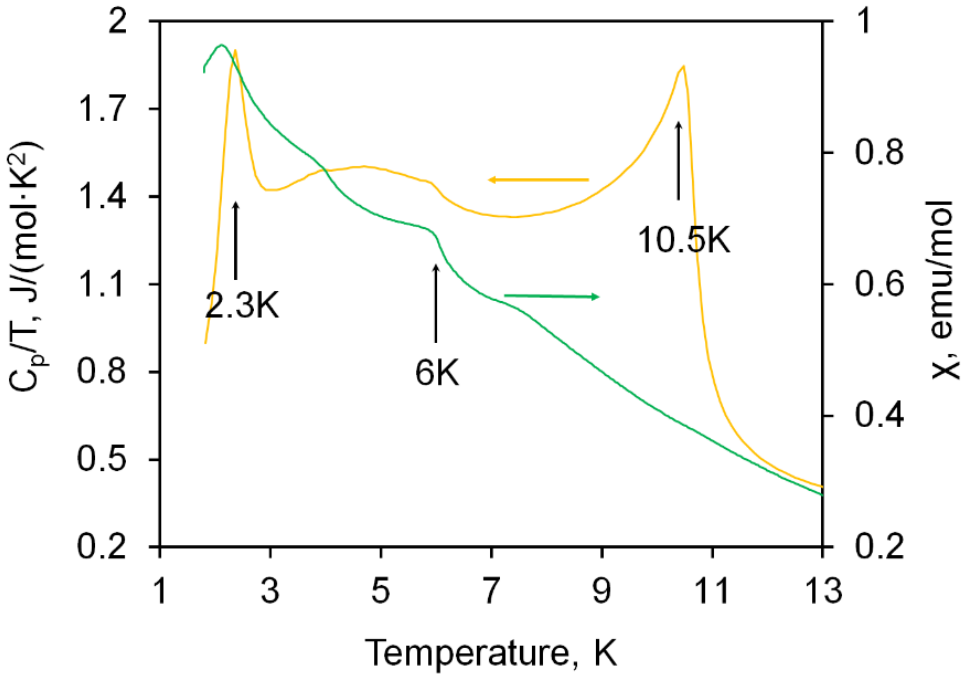

Figure 4.2 Summary of the physical properties data: heat capacity *vs.* temperature in zero field and magnetic susceptibility *vs.* temperature in 0.005 T field plots for $EuNi_2P_4$. Phase-transition temperatures are outlined.

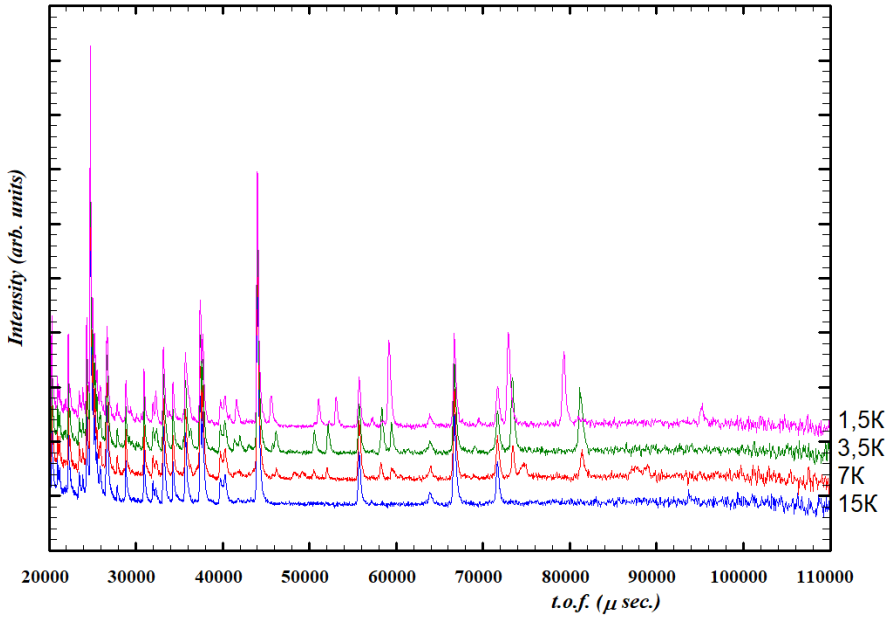

Figure 4.3 Comparison of raw neutron diffraction patterns (intensity *vs.* time-of-flight) for $EuNi_2P_4$ measured in the paramagnetic phase (15 K, blue), between T_2 and T_3 – at 7 K (red), between T_2 and T_1 – at 3.5 K (green), and below T_1 – at 1.5 K (magenta).

Magnetic reflections in the pattern at 1.5 K, *i.e.,* below T_1, can be indexed with the $k_1 = 0\ ^1/_2\ 0$ propagation vector, which corresponds to doubling of the orthorhombic *F*-centered cell along *b* direction. The high *d*-spacing bank indeed shows a magnetic reflection at ~18.8 Å (~2 *b*) (not shown), as it is expected from the cell metrics of $EuNi_2P_4$. Consequent representation analysis and refinement of the derived magnetic models results in the magnetic structure provided in **Figure 4.4.** The refined magnetic moment on Eu is 6.41(4) μ_B, which is just slightly lower than 7 μ_B, the theoretical value for pure Eu^{2+} ($4f^7$). This structure can be understood as two ferromagnetic (magnetic moments in the same direction along *c*-axis) blocks, stacked to each other in an antiferromagnetic manner along the *b*-axis.

A set of reflections at $d \sim 17.1$ Å, 5.38 Å, 4.86 Å, 3.94 Å, 3.86 Å, 3.45 Å, 3.44 Å and 3.05 Å is visible in the diffraction patterns between 3.5 K and 9 K. The intensities of these reflections decrease on increasing the temperature. They all can be indexed with an incommensurate propagation vector $k_2 = 0\ \sim 0.55\ 0$, close to k_1. k_2 exhibits a small temperature variation of the k_{2y} component – 0.55 – 0.56; the exact refined values at 3.5 K and 7 K are provided in **Figure 4.4.** From the representation analysis, the trivial solution is a spin-density wave propagating along the *b*-axis. The magnetic moments aligned along the *c*-axis are of a variable magnitude, as shown in **Figure 4.5.**

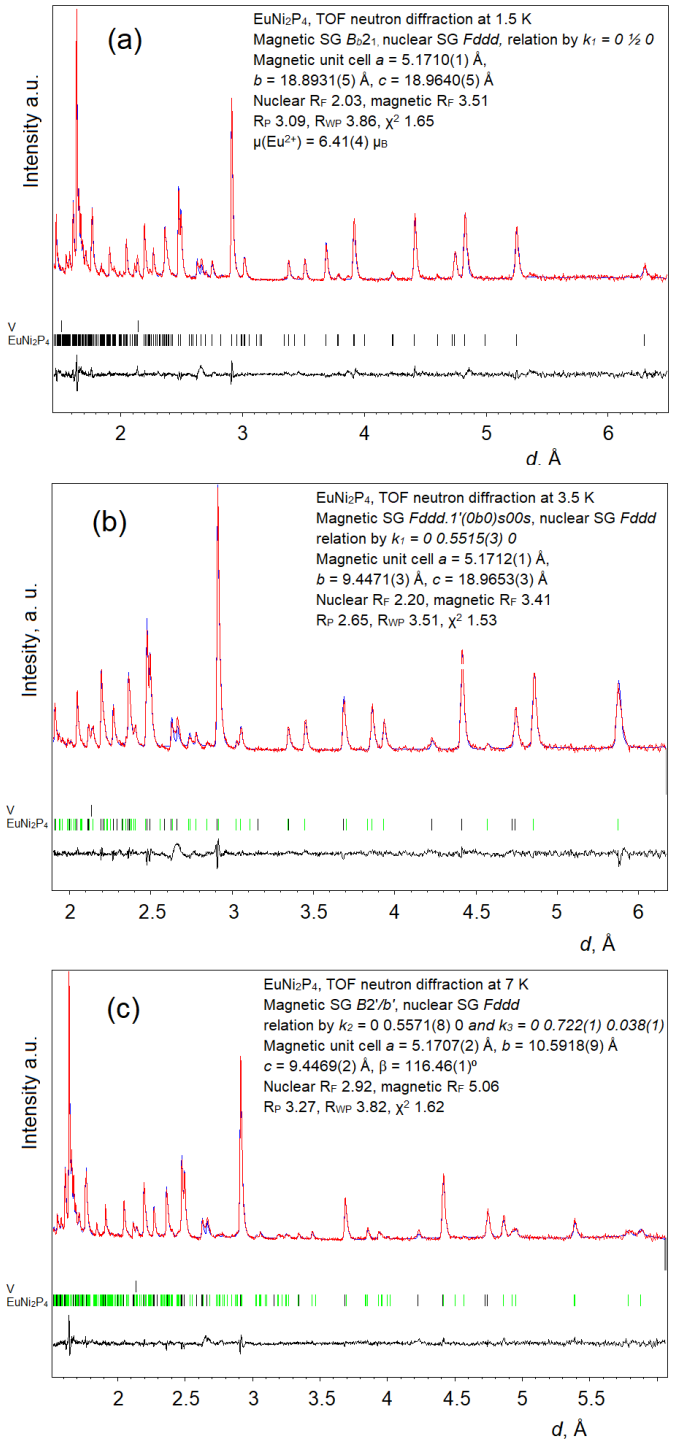

Figure 4.4 Rietveld refinement plots of magnetic structures for $EuNi_2P_4$ against TOF neutron diffraction data. (a) – at 1.5 K, (b) – at 3.5 K, (c) – at 7 K. Experimental points are red; calculated lines are blue; positions of reflections and difference curves are black; incommensurate satellites are green. V from the sample container is included in refinement. Technical details (cell parameters of the magnetic unit cells, magnetic space groups, and their relations to the nuclear ones) are provided on the graphs. Humps at ~ 2.7 Å originate from detector issues.

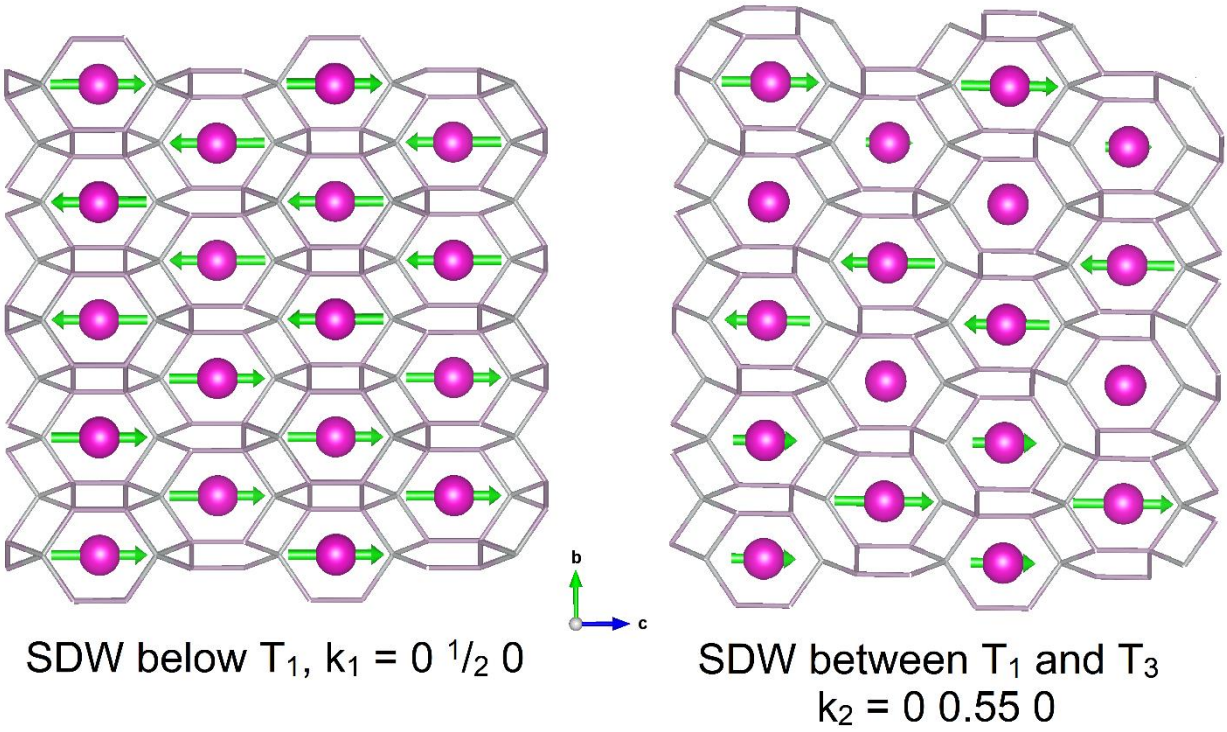

Figure 4.5 Comparison of a commensurate spin-density wave existing below T_1 and an incommensurate spin-density wave existing between T_1 and T_3. Eu atoms located inside the cages with their magnetic moments are shown. Ni and P atoms located at the vertices of the cages are omitted for clarity.

A comparison of the commensurate and incommensurate spin-density waves is provided in **Figure 4.5.** The neutron diffraction data revealed that the transition at T ~ 2.5 K in $EuNi_2P_4$ is associated with a change of the magnetic propagation vector from the incommensurate value k_2 = 0 0.55 0 in the high-temperature phase to the commensurate value k_1 = 0 ½ 0 in the ground state. The ground state propagation vector is not a special point of symmetry in the Brillion zone of the paramagnetic *Fddd1'* space group. It belongs to the Δ-line of symmetry, k = 0 k_y 0, and selection of the commensurate value k_y = 1/2 can be understood as a classical lock-in transition (see, for example [22]). The mechanism of this transition implies activation of a high order free energy invariant, which exists only for some particular value of the propagation vector components [23]. The lock-in term acts only on the propagation vector and is not expected to change the magnetic structure. This implies that similar to the ground state, the high-temperature incommensurate phase is also a spin-density wave with the moments polarized along the *c*-axis. Indeed this model provides a *uniquely* good refinement quality for the neutron diffraction data collected at 3.5 K. Attempts to construct magnetic structures with a constant magnetic moment failed.

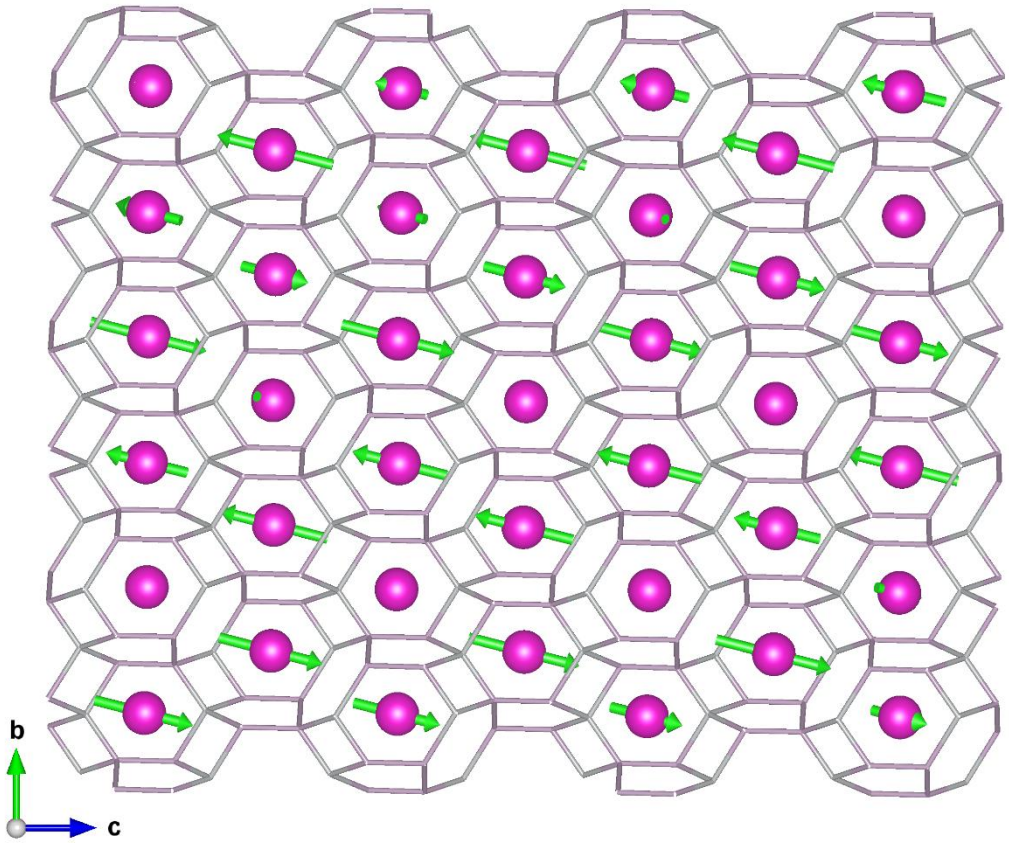

Figure 4.6 Double-*k* model of the magnetic structure of $EuNi_2P_4$ between T_2 and T_3. Eu atoms located inside the cages with their magnetic moments are shown. Ni and P atoms located at the vertices of the cages are omitted for clarity.

Between T_2 and T_3, besides the magnetic reflections corresponding to k_2, there are also small additional ones. It is possible to account for them with a single propagation vector k_3 = 0 ~0.73 ~0.04. With the help of ISODISTORT, a double-*k* magnetic structure has been constructed; its projection is shown in **Figure 4.6**. Due to the non-zero k_{3z} component, magnetic moments acquire additional components along *b* and *a*.

This study leaves two unresolved questions. The first one concerns the physical reasons why the highly-localized 4*f* electrons of Eu still form a spin-density wave with a variable amplitude of magnetic moment. The spin density wave magnetic structures found for the nominally isotropic Eu^{2+} ions are very surprising. Usually, this type of structure is stabilized in the systems with sufficiently strong magnetic anisotropy. The origin of the anisotropy in $EuNi_2P_4$ is not clear, and one candidate on this role can be magnetoelastic coupling, which is expected to be anisotropic in the orthorhombic crystal. The cases of incommensurate spin-density waves are reported for Eu compounds, for example, EuPdSn [24]. The second unusual thing is either a coexistence of two magnetic phases or a double-*k* structure. A very

similar case has been described for $EuCu_2Sb_2$, where it has been concluded that two magnetic phases belong to the same crystallographic one [25]. Still, it seems that such a complex behaviour observed in $EuNi_2P_4$ (with both lock-in and double-*k*) has not been studied in detail in any of the previous reports on Eu-compounds. From the structural point of view, the complexity of the low-temperature behaviour might be expected – the oscillating with distances RKKY interactions and the triangular arrangement of magnetic centers cause a bunch of magnetic frustrations. One option to resolve the named issues is to use polarized neutrons, which is, however, deemed to be impossible because the available fluxes of polarized neutrons are much smaller than those of unpolarized. Thus ^{151}Eu Mössbauer spectroscopy as a complementary technique [26] is proposed to be instrumental in the case of $EuNi_2P_4$.

Conclusions

Our neutron diffraction experiments confirmed three low-temperature magnetic phase transitions proposed previously from the physical properties measurements for $EuNi_2P_4$. The magnetic moments were found to be aligned along the *c*-direction of the orthorhombic unit cell and to form a commensurate, an incommensurate, and double-*k* spin-density waves depending on the temperature consequently. Additional ^{151}Eu Mössbauer measurements and single-crystal magnetization studies are necessary to address the nature of the low-temperature phases.

Several other people also contributed to this work:

1. Dr Dmitry Khalyavin (ISIS) performed neutron diffraction measurements and supported with interpretation of the results.
2. Dr. Alexander Tsirlin (Uni Augsburg) supported with interpretation of the results.

The raw-data files are available under DOI: 10.5286/ISIS.E.RB1920191.

References

[1] G. A. Jeffrey. In: Hydrate Inclusion Compounds, Eds.: J. L. Atwood, J. E. Davies, D. D. McNicol. *Academic Press, London,* **1984**.

[2] A. V. Shevelkov, K. Kovnir. In: Zintl Phases. Structure and Bonding. Ed.: T. Fässler, *Springer*. Berlin, Heidelberg, **2010**.

[3] K. A. Kovnir, A. V. Shevelkov. Semiconducting clathrates: synthesis, structure, and properties. *Russ. Chem. Rev.* **2004**, *73*, 923 – 938.

[4] The physics and chemistry of inorganic clathrates. Ed.: G. S. Nolas. *Springer*. New York, **2014.**

[5] K. Kovnir, U. Stockert, S. Budnyk, Y. Prots, M. Baitinger, S. Paschen, A. V. Shevelkov, Y. Grin. Introducing a magnetic guest to a tetrel-free clathrate: Synthesis, structure, and properties of $Eu_xBa_{8-x}Cu_{16}P_{30}$ ($0 \le x \le 1.5$). *Inorg. Chem.* **2011**, *50*, 10387 – 10396.

[6] B. C. Chakoumakos, B. C. Sales, D. G Mandrus. Structural disorder and magnetism of the semiconducting clathrate $Eu_8Ga_{16}Ge_{30}$. *J. Alloys Compd.* **2001**, *322*, 127 – 134.

[7] S. Leoni, W. Carrillo-Cabrera, Y. Grin. Modeling of the α (clathrate VIII) ⇌ β (clathrate I) phase transition in $Eu_8Ga_{16}Ge_{30}$. *J. Alloys Compd.* **2003**, *350*, 113 – 122.

[8] A. Biswas, S. Chandra, S. Stefanoski, J. S. Blázquez, J. J. Ipus, A. Conde, M. H. Phan, V. Franco, G. S. Nolas, H. Srikanth. Enhanced cryogenic magnetocaloric effect in $Eu_8Ga_{16}Ge_{30}$ clathrate nanocrystals. *J. Appl. Phys.* **2015**, *117*, 033903.

[9] I. V. Plokhikh, N. Khan, A. A. Tsirlin, A. N. Kuznetsov, D. O. Charkin, A. V. Shevelkov, A. Pfitzner. $EuNi_2P_4$, the first magnetic unconventional clathrate prepared *via* a mechanochemically assisted route. *Inorg. Chem. Front.* **2020**, *7*, 1115 – 1126.

[10] V. V. Novikov, S. L. Bud'ko, A. V. Matovnikov, N. V. Mitroshenkov, K. S. Pilipenko, N. A. Konoplin, I. V. Plokhikh, A. Pfitzner, A. V. Shevelkov. The specific features of phononic and magnetic subsystems of type-VII clathrate $EuNi_2P_4$. *Submitted*

[11] J.-A. Dolyniuk, J. Wang, K. Lee, K. Kovnir. Twisted kelvin cells and truncated octahedral cages in the crystal structures of unconventional clathrates, AM_2P_4 (*A* = Sr, Ba; *M* = Cu, Ni). *Chem. Mater.* **2015**, *27*, 4476 – 4484.

[12] V. Novikov, K. Pilipenko, A. Matovnikov, N. Mitroshenkov, I. Plokhikh, A. Tyablikov, A. Shevelkov. Structure-related thermal properties of type-VII clathrates $SrNi_2P_4$ and $BaNi_2P_4$ at low temperature. *Phys. Status Solidi* **2018**, *255*, 1800067.

[13] C. N. R. Rao. Modern aspects of solid state chemistry. *Springer Science & Business Media*, **2012**.

[14] L. C. Chapon, P. Manuel, P. G. Radaelli, C. Benson, L. Perrott, S. Ansell, N. J. Rhodes, D. Raspino, D. Duxbury, E. Spill, J. Norris. Wish: the new powder and single crystal magnetic diffractometer on the second target station. *Neutron News* **2011**, *22*, 22.

[15] R. Saha, A. Sundaresan, M. K. Sanyal, C. N. R. Rao, F. Orlandi, P. Manuel, and S. Langridge. Neutron scattering study of the crystallographic and spin structure in antiferromagnetic $EuZrO_3$. *Phys. Rev. B* **2016**, *93*, 014409.

[16] V. K. Anand, D. T. Adroja, A. Bhattacharyya, U. B. Paramanik, P. Manuel, A. D. Hillier, D. Khalyavin, Z. Hossain. *μ*SR and neutron diffraction investigations on reentrant ferromagnetic superconductor $Eu(Fe_{0.86}Ir_{0.14})_2As_2$. *Phys. Rev. B* **2015**, *91*, 094427

[17] J. Rodriguez-Carvajal. Recent advances in magnetic structure determination by neutron powder diffraction. *Physica B*, **1993**, *192*, 55 – 69.

[18] V. Petricek, M. Dusek, L. Palatinus. Crystallographic computing system JANA2006: general features. *Z. Kristallogr.* **2014**, 229(5), 345 – 352.

[19] H. T. Stokes, D. M. Hatch, and B. J. Campbell, ISODISTORT, ISOTROPY Software Suite, iso.byu.edu.

[20] B. J. Campbell, H. T. Stokes, D. E. Tanner, and D. M. Hatch. ISODISPLACE: an internet tool for exploring structural distortions. *J. Appl. Crystallogr.* **2006**, *39*, 607 – 614.

[21] K. Momma, F. Izumi. VESTA 3 for three-dimensional visualization of crystal, volumetric, and morphology data. *J. Appl. Crystallogr.* **2011**, *44*, 1272 – 1276.

[22] Y. A. Izumov and V. N. Syromyatnikov. Phase transitions and crystal symmetry. *Springer*. Dordrecht, Netherlands. **2011**.

[23] K. Ji, E. Solana-Madruga, A. M. Arevalo-Lopez, P. Manuel, C. Ritter, A. Senyshyn, J. P. Attfield. Lock-in spin structures and ferrimagnetism in polar $Ni_{2-x}Co_xScSbO_6$ oxides. *Chem. Commun.* **2018**, *54*, 12523 – 12526.

[24] P. Lemoine, J. M. Cadogan, D. H. Ryan, M. Giovannini. The magnetic structure of EuPdSn. *J. Phys.: Condens. Matter.* **2012**, *24*, 236004.

[25] W. N. Rowan-Weetaluktuk, D. H. Ryan, P. Lemoine, J. M. Cadogan. Thermal neutron diffraction determination of the magnetic structure of $EuCu_2Ge_2$. *J. Appl. Phys.* **2014**, *115*, 17E101.

[26] D. H. Ryan, J. M. Cadogan. ^{151}Eu hyperfine fields, isomer shifts and moments in Eu-based EuT_2X_2 intermetallic compounds. *Hyperfine Interactions* **2014**, *226*, 243 – 255.

Supporting Information

Proposal for neutron beamtime at the ISIS

1. Background and Context

Intermetallic clathrates are extensively studied as promising thermoelectric materials, since their structural features allow them to obey a phonon-glass-electron-crystal concept. The clathrates based on group IV elements (tetrels - Si, Ge, and Sn) are the most numerous. Tetrel atoms tend to have rather rigid coordination; the tetrel-based clathrates crystallize in a restricted number of structure types. Contrary to that, pnictide-based, so-called unconventional clathrates, are more structurally diverse, because the coordination of pnictogen atoms allows for more flexibility. Nonmagnetic alkali earth cations commonly serve as guest atoms; in many structures alkali earth cations can be substituted by magnetic Eu^{2+} ($4f^7$). However, magnetically unconventional clathrates were not yet reported.

The first magnetically unconventional clathrate $EuNi_2P_4$, the analog of $SrNi_2P_4$ [Chem. Mater., 2015, 27 (12), pp 4476–4484], has been prepared; it renders a complete characterization. From studies of the conventional clathrates it follows that their crystal structure can be separated into two parts – the host framework, which behaves as a conventional solid phase, and a quasi-free guest ion. Such separation has a strong impact on heat capacity, thermal expansion and temperature dependence of atomic displacements parameters. On the one hand, a quasi-free guest atom contributes to heat capacity as an Einstein oscillator, so that a total heat capacity can only be described as a combination of Einstein and Debye models [Phys. Status Solidi B, 2018, 255 (8), 1800067]. On the other hand, as the gust atom is quasi-free, the activation energy of its vibration is small, what makes the atomic displacement parameter growing with temperature much faster as compared to other atoms, comprising the clathrate framework. Another point is that, given the flexibility of the clathrate framework, once can expect structural transformations driven by magnetic interactions between Eu^{2+} magnetic centers.

2. Proposed experiment

The aim of the proposed study is to elucidate geometrical and magnetic influences of the cation with the high magnetic moment (Eu^{2+}, $4f^7$) on the framework of unconventional clathrates. By establishing the low temperature crystal and magnetic structures we should be able to explain the structural transformation evolving in $EuNi_2P_4$ on cooling and extract the effect of magnetic interactions between Eu^{2+} ions on the clathrate framework.

3. Summary of previous beamtime or characterization

Powder sample of $EuNi_2P_4$ can be prepared *via* conventional solid-state reaction. Its room temperature crystal structure, established from powder X-ray diffraction, is orthorhombic (*Fddd*, a = 5.1737(1) Å, b = 9.4518(1) Å, c = 18.9754(2) Å. Ni and P form a conducting clathrate framework, void of which are filled by magnetic Eu^{2+} cations. The distances between the centers of the voids

(ideal positions of Eu^{2+} cations) to the nearest P and Ni atoms are within 3.1 – 3.8 Å. Such spatial separation implies that Eu^{2+} cations are strongly under-bounded and can be considered as quasi-free. No neutron diffraction measurements were performed on the title compound yet. The compounds has been characterized by magnetization, resistivity and heat capacity measurements as well as low-temperature synchrotron diffraction. Down to 20K the sample behaves as paramagnet with high-temperature paramagnetic Curie-Weiss moment of 7.93 μ_B consistent with Eu in divalent state. From temperature dependence of atomic displacement parameters of Eu, Ni and P atoms, the characteristic temperatures of lattice dynamics of this compound were evaluated to be ~79K (the Einstein temperature, corresponding to vibrations of quasi-free Eu^{2+}) and ~450K (the Debye temperature of the framework). Low-energetic vibrational modes are also evident from Raman scattering.

The low-temperature (below 15K) behaviour of $EuNi_2P_4$ is strongly dissimilar to that of its nonmagnetic analog $SrNi_2P_4$. The later compound show no low-temperature anomalies. Contrary to that, magnetic susceptibility curves of $EuNi_2P_4$ show multiple anomalies between 2K and 12K, while heat capacity and resistivity measurements exhibit anomalies only at ~2.5K and 11.3K. Evidently, those effects are due to complete substitution of nonmagnetic Sr^{2+} with magnetic Eu^{2+}.

We can assume that at least the transitions at ~2.5K and 11.3K are intrinsic. Synchrotron diffraction measurements reveal that no structural transformation occur down to 10K, thus the phase transition at 11.3K is presumably of magnetic nature and most likely correspond to antiferromagnetic ordering in Eu^{2+} sublattice. Antiferromagnetic interactions are also evident from the fact that magnetization *vs.* field curves do not rich saturation even at 2K. Heat capacity measurements show that the transition at 2.5K is most likely of the first order and it is possible to assume that it is due to structural transformations at this temperature. The capabilities of synchrotron diffraction at such low temperatures are limited (strong heating of the sample), and we were not able to probe it. Nevertheless, it is expected to establish the nature of this transition by neutron diffraction.

4. Justification of beamtime request

We suggest measurements of our samples on the WISH diffractometer at several temperatures between 1.5K and 15K. Eu is a strong neutron absorber, however, $EuNi_2P_4$ contains just ~15at.%. Given our previous and successful experience with other Eu-containing compounds, as well as low Eu content, we assume, that 2 – 3 h per temperature point would yield sufficient statistics. Another facilitating fact is a high magnetic moment on Eu atoms (7μ_B); the intensities of magnetic reflections are expected to be comparable with the intensities of structural ones even if signal-to-noise ratio is low. Thus, for the whole experiment with 1 – 2K step (the steps will be smaller around the transitions at 2.5K and 11.3K) we need 2 days of beamtime.

5 Layered compounds BaFMg*Pn* (*Pn* = P, As, Sb and Bi), transition-metal-free representatives of the 1111 structure type

Abstract

Four new transition metal-free pnictide representatives of the LaOAgS structure type were predicted by DFT calculations and found in the BaFMg*Pn* (*Pn* = P, As, Sb and Bi) family. The compounds adopt the tetragonal space group *P4/nmm* with the unit cell parameters *a*/*c* 4.3097(1) Å / 9.5032(1) Å, 4.3855(1) Å / 9.5918(1) Å, 4.5733(1) Å / 9.8184(1) Å and 4.6359(1) Å / 9.8599(1) Å, respectively. According to the DFT calculations, these new compounds are semiconductors with band gaps steadily decreasing from *Pn* = P (*ca.* 2 eV) to *Pn* = Bi (*ca.* 1 eV). The corresponding strontium fluoride and rare-earth oxide analogs are unlikely to exist and have not been observed yet. The trends of the stability within 1111 and structurally and/or chemically related compounds based on a combined consideration of geometry and DFT calculations are discussed.

Introduction

The discovery of a new unconventional class of superconducting materials, the iron-based pnictide superconductors, in 2008 [1, 2] has renewed attention to compounds involving 2D anti-fluorite structural fragments, which can be termed layered anti-fluorites. Among the latter, two particularly widespread structure types have received the greatest attention, the $ThCr_2Si_2$ structure type (termed "122") [3] with the highest known number of representatives (exceeding 1000 by now)[4], and the LaOAgS structure type [5] where the highest superconducting transition temperature was observed [6]. The latter is sometimes distinguished from the related ZrCuSiAs structure type [7]. Both are generally summarized as "1111" (**Figure 5.1**) despite exhibiting different bonding schemes [8]. Besides superconductivity, the LaOAgS type comprises representatives exhibiting many other intriguing properties, *e.g.*, Ag^+-based ionic conductivity of the archetype [5], optical transparency *vs*. electric conductivity in doped Cu and Ag chalcogenides [9], colossal magnetoresistance (CMR) in doped Mn pnictides [10], or thermoelectricity in doped LaOZnSb [11].

The considerably high number of representatives (approaching 300 [12, 13]) can be explained by the relatively simple atomic arrangement best described as alternation of two very common motifs, the *type-anti-type* related fluorite (litharge, PbO) and anti-fluorite (mackinawite, FeS) type slabs (**Figure 5.1**). Based on the chemical composition of the litharge part, its representatives can be separated into several groups. Most numerous are oxide compounds containing $[M_2O_2]^{n+}$ (M = Th, U – Pu for n = 4, and Bi, La – Er for n = 2) slabs [14 – 17]; fluorides containing $[M'_2F_2]^{2+}$ fragments (M' = Ca, Sr, Ba, or Eu [18 – 26]) are less common mostly due to the smaller variety of the divalent cations; hydrides are the rarest [27], and there exists only one unique nitrogen-based compound, $ThN_{1-x}O_xFeAs$ [28].

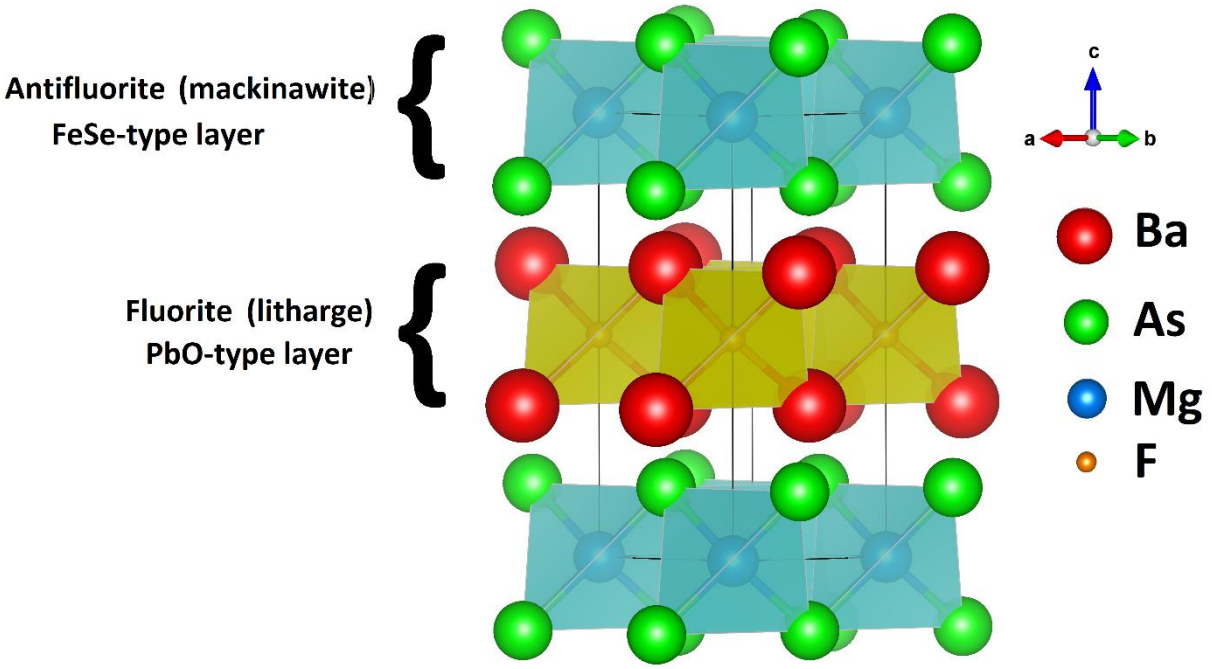

Figure 5.1 Crystal structure of BaFMgAs – a new representative of the 1111 family – comprising fluorite- and antifluorite-type layers of $[Ba_2F_2]^{2+}$ and $[Mg_2As_2]^{2-}$, respectively.

We note that the chemistry of PbO and FeSe slabs observed separately in related structures is essentially more diverse [17], and the number of their possible combinations into 1111 can be estimated as high as *ca*. 800, *e.g.*, just below the number of known $ThCr_2Si_2$-type compounds. The factors restricting their actual number are charge-balance, and chemical (mostly redox) and geometrical compatibility of the constituting layers. However, several groups of suggested combinations which seem not to violate any of the criteria listed above remain as yet unaddressed. Since most of the properties listed above are associated with mackinawite-type layers involving transition metals, the compounds of pre- and post-transition elements received very little attention.

Thus, a detailed knowledge on their existence is necessary for elucidation and exact formulation of compatibility criteria and selection rules to predict which new representatives are likely and unlikely to exist before undertaking the synthesis which commonly requires complicated synthetic procedures or expensive precursors. Our prediction and successful synthesis of two transition metal-free tetrelides, BaFAlSi and BaFAlGe [19], prompted us at investigation of some other valence isoelectronic systems, the most likely representatives being compounds involving $[Mg_2Pn_2]^{2-}$ (*Pn* = P – Bi) slabs observed in a series of ternary CeFeSi-type Group 1 – Group 2 pnictides. We also note that the Mg – *Pn* distances in structurally characterized NaMgAs, NaMnSb [29] and KMg*Pn* (*Pn* = P, As, Sb, and Bi [30]) are rather close to the Cd – *Pn* ones observed in BaFCd*Pn* [21, 26], suggesting the existence of BaFMg*Pn* compounds. The relatively large size of the mackinawite-type slabs makes the $[Ba_2F_2]^{2+}$ litharge-type slabs the best candidates for their counterparts; as in the previous cases, possible Sr – F and *Ln* – O analogs were also considered.

Experimental section

Synthesis and primary characterization. The starting compounds were elemental Mg, Ca, Sr, Ba, La, P, As, Sn, and Bi (purity > 99%), as well as SrF_2, BaF_2, and MgO (the latter calcined at 600°C overnight before use). New compounds were attempted *via* a high-temperature solid state route using La + MgO + *Pn* starting mixtures in ~1:1:1 or Ba (Sr) + BaF_2 (SrF_2) + Mg + *Pn* in ~1:1:2:2 ratios. All operations were performed in an Ar-filled glove-box (M'Braun). The barium compounds were prepared in the following way: metallic barium (Sigma Aldrich, 99.5%) was chopped in the glove-box right prior to the preparation; powdered BaF_2 (Chempur, 99.999%) was dried at 373K before use; cuttings of metallic Mg (99.5%) as well as red phosphorus (Chempur, > 99%), arsenic (Chempur, 99.9%), antimony (Chempur, 99.99%) and bismuth (purity) were used as purchased. The starting materials were mixed according to the 1111 composition (using 5 – 10 % excess of Ba metal, 2 – 3 % excess of BaF_2 and 2% excess of Mg), and then loaded in graphite crucibles which were flame-sealed in evacuated silica tubes. The samples were annealed for 48 – 72 h at 1223 K, 1173 K, 1073 K and 973 K (2 K/min heating rate) for BaFMgP, BaFMgAs, BaFMgSb, and BaFMgBi, respectively. Intermediate products were homogenized with 2 % excess of Mg metal, and annealed according to the same protocol for another100 h. The as-prepared samples are extremely oxygen and moisture sensitive black powders which decompose in air to mixtures of oxides (hydroxides) and fluorides within minutes.

They also readily react with water and acids releasing flammable gases. This behaviour reminds that of the tetrelides BaFAl*Tt* (*Tt* = Si, Ge) which are however essentially more stable in dry air or in contact with pure water [19].

Powder diffraction patterns for phase analysis as well as high-quality data sets for structure refinements were collected on a STOE STADI P diffractometer (Mo$K\alpha_1$ radiation, $\lambda = 0.70930$ Å, Ge (111) monochromator, DectrisMythen 1K detector). The powdered samples were loaded in quartz capillaries of 0.3 mm diameter and spun during the measurements. The temperature was controlled at 293K during the measurement. The WinXPOW software package from STOE &Ciewas used for data collection and processing [31]. Four new BaFMg*Pn* compounds were found to be present in the samples as majority phases. In all other cases, no signs of the target compounds were observed.

Elemental composition was confirmed using a Zeiss EVO MA 15 scanning electron microscope equipped with a Bruker Quantax EDX system with an X Flash Detector 630 M. Traces of oxygen were found to be present due to partial decomposition.

Structure refinement. Since no single-crystals of the target phases could be produced during the synthesis crystal structures were refined from high-resolution ($d_{min} < 0.8$ Å) X-ray powder diffraction data sets using the Rietveld method, implemented in the JANA2006 software package [32]. The crystal structures of previously reported analogs were used as starting models. A standard mathematical apparatus for the description of the peak profile (Pseudo-Voigt profile function, Legendre polynomials for background) was used. The refinements proceeded in a straight-forward manner. The relatively strong absorption of X-rays was corrected according to the model for Debye-Scherrer geometry to achieve realistic values of atomic displacement parameters. Further details of the powder diffraction experiments are collected in **Table 5.1**, refined atomic coordinates and displacement parameters are summarized in **Table 5.2**; selected interatomic distances are listed in **Table 5.3**, the final Rietveld refinement plots – in **Figure 5.2**. A projection of the BaFMgAs unit cell (**Figure 5.1**) is drawn by the VESTA software [33].

The thermal behaviour was studied *via* differential thermal analysis (DTA) utilizing a SETARAM TG-DTA 92 analyser. The samples were loaded in silica capillaries and subjected to 2 heating and cooling cycles. No obvious thermal effects are observed up to 1273K. However, container deterioration was observed, which suggests gradual release of magnesium vapour at elevated temperatures.

DFT calculations. Electronic structure calculations were performed at the Density Functional Theory (DFT) level using two approaches: i) the all-electron full-potential linearized augmented plane wave method (FP-LAPW) as implemented in the ELK code [34], and ii) the pseudopotential projector augmented wave method (PAW) as implemented in the Vienna *ab initio* Simulation Package (VASP) [35, 36].

Table 5.1 Details of the PXRD experiments for BaFMg*Pn* (*Pn* = P, As, Sb, Bi).

Compound	BaFMgP	BaFMgAs	BaFMgSb	BaFMgBi
Phase composition	Target phase + 4.7(1)% BaF_2	Target phase + 2.5(1)% BaF_2	Target phase +3.5(1)% BaF_2	Single phase
Space group	*P4/nmm (origin choice 2)*			
Cell parameters*				
a in Å	4.3097(1)	4.3855(1)	4.5733(1)	4.6359(1)
c in Å	9.5032(1)	9.5918(1)	9.8184(1)	9.8599(1)
V in $Å^3$	176.51(1)	184.48(1)	205.35(1)	211.91(1)
Density in g/cm^3	3.982	4.600	4.890	6.106
Radiation	Mo$K\alpha_1$			
2θ range in deg	3 – 55	2 – 55	3 – 63	3 – 63
Data points	3467	3543	4082	4082
Overall parameters	38	36	34	34
Reflections	153	159	243	261
Struct. parameters	8	10	9	9
R values:				
R_F *in %*	1.60	2.30	2.31	2.96
R_P *in %*	4.82	3.20	4.45	1.43
R_{wP} *in %*	6.64	4.38	6.58	1.93
χ^2	1.79	1.99	3.56	1.50

*In order to obtain more realistic standard deviations all the provided values should be multiplied by a factor of 3.

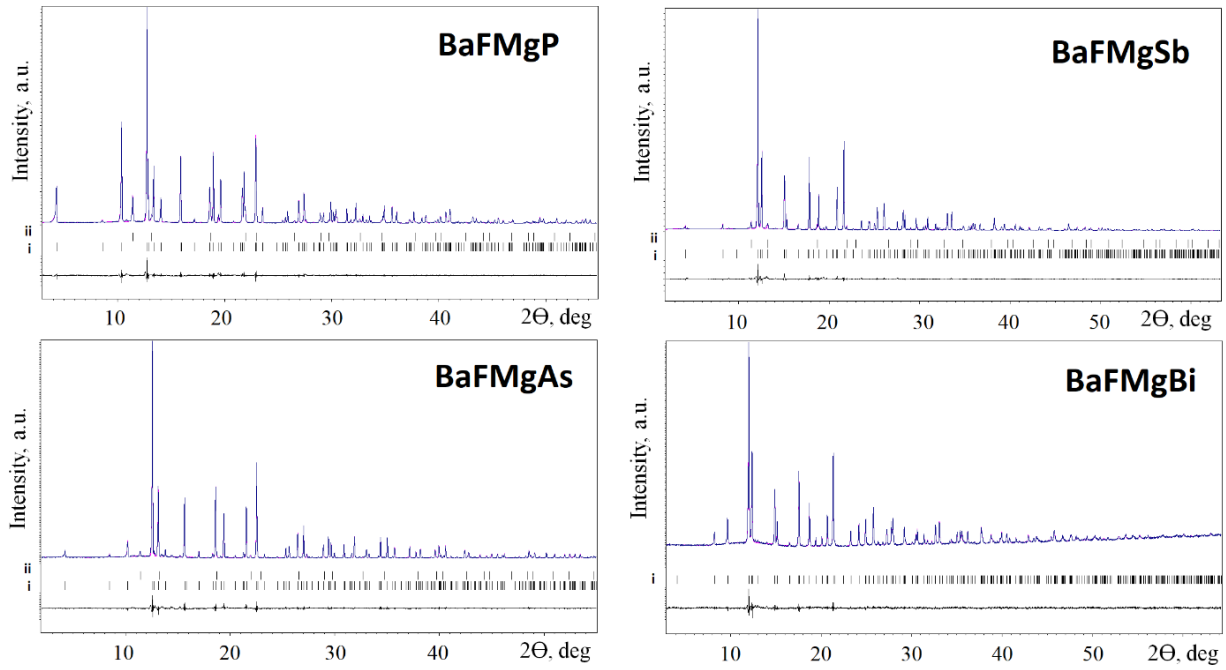

Figure 5.2 Experimental (blue), calculated (magenta) and difference plots (the Rietveld refinement plots) for BaFMg*Pn* (*Pn* = P, As, Sb and Bi) series. The reflections of the main phases are marked as **i**, traces of BaF_2 impurities are marked as **ii.**

In the first approach, which was used for energy calculations, the Perdew-Burke-Enzerhoff exchange-correlation functional revised for solids (PBESol) of the GGA-type was utilized [37]. The Brillouin zone sampling was performed using a 7 × 7 × 3 *k*-point grid, the muffin-tin sphere radii r_{MT} for the respective atoms were (Bohr): 2.80 (Ba, Bi), 2.60 (Sb), 2.40 (As), 2.20 (Mg, P), 2.00 (F), and the maximum moduli for the reciprocal vectors k_{max} were chosen so that $r_{MT}k_{max}$= 9.0.

In the second approach, which was used for both energy calculations and unit cell optimization, a Monckhorst-Pack [38] *k*-point mesh of 14 × 14 × 6 was employed, and the energy cutoff was set at 500 *eV*. The PBESol exchange-correlation functional of the GGA-type, and SCAN exchange-correlation functional of the meta-GGA-type [39], augmented with a non-local correlation part from the rVV10 van der Waals density functional, were used in the PAW-based calculations. The latter was used to take the potentially layered nature of the compounds into account, which would imply dispersive interactions between the layers. Unit cell optimization for the hypothetical LaOMg*Pn* (*Pn* = P, As, Sb and Bi) compounds and for SrFMgAs was performed using the PBESol functional. Starting models were taken from the respective barium-magnesium fluoropnictides. Unit cell metrics, its symmetry, and atomic coordinates were allowed to relax in each case. The convergence criterion for forces in ionic relaxation was set to 0.001 *eV*/Å.

Atomic charges were calculated in accordance with R. Bader's quantum theory of atoms in molecules (QTAIM) [40] using the DGrid4.6 package [41] and Bader code [42 – 44], utilizing ELK wave functions or VASP charge density, respectively, as inputs. The estimations of structure stabilities were made according to the approach established in ref. 26 by comparing calculated total energies of quaternary compounds and their precursors. The Electron localization function (ELF) [45] was calculated by the internal VASP routine.

Results and discussions

Synthesis. Compared to the previously reported cases [22 – 24, 26], the synthesis of BaFMg*Pn* type compounds is more complex due to high reactivity and volatility of magnesium above its melting point (~920K) and extreme air and moisture sensitivity of the target products. Although no thermal effects were observed for all four compounds up to 1273K, the synthesis temperature had to be decreased when passing from BaFMgP (1223K) to BaFMgBi (973K). This can be explained assuming lower reactivity of magnesium towards heavier pnictogens and competitive reactions of Ba and Mg vapors with the walls of the silica ampoules. The effects of the latter can be suppressed by introducing a slight (~2%) excess of metallic Mg and Ba; adding a slight excess of BaF_2 also favors the formation of the target compounds against ternary $BaMg_2Pn_2$ [46] compounds. Similar attempts to prepare LaOMgAs led to samples mostly consisting of MgO along with some poorly crystalline phases; annealed samples with nominal composition SrFMgAs consist mostly of SrF_2 and $SrMg_2As_2$ along with binary strontium and magnesium arsenides.

Crystal structures. As noted before, the structures of the new compounds represent regular commensurate sequences of $[Ba_2F_2]^{2+}$ (litharge-type) and $[Mg_2Pn_2]^{2-}$ (mackinawite-type) layers represented in **Figure 5.1.** These are formed by condensation (*via* edge sharing) of tetragonally distorted FBa_4 and $MgPn_4$ tetrahedra which flatten or stretch along the $\bar{4}$ axis to provide the commensurate overall structure. This results in splitting of six initially equal edges into groups of 2 (unshared, equal to the *a* cell parameter, corresponding angle α_2) and 4 (shared, α_4); the same is observed for the bond angles while the four center-to-vertex distances (corresponding to the Ba–F and Mg–*Pn* bonds) remain equal. The deviation of the bond angles from the ideal angle of 109.5° and the differences between them reflect the degree of the distortion.

As follows from **Table 5.3** and illustrated in **Figure 5.3**, BaFMgP features almost regular FBa_4 tetrahedra, while the MgP_4 moieties are slightly flattened. Following the trend in

atomic radii, the next representative, BaFMgAs, exhibits a longer distance *d*(Mg–*Pn*), which results in a slight flattening of the FBa_4 tetrahedra while the $MgAs_4$ counterparts are now almost regular. The heavier analogs, BaFMgSb and BaFMgBi, are characterized by increasingly flattened FBa_4 but elongated $MgSb_4$ and $MgBi_4$ tetrahedra since *d*(Mg–*Pn*) > *d*(Ba–F). The same trend is observed in the crystal structures of other BaF*TPn* (*T* = Zn, Mn and Cd) compounds [26]. The values of α_2 and α_4 of 119.8° and 104.6° in BaFMgBi are very close to those observed in the structure of BaFI [47]; however, they are probably rather close to the tolerance limit for the distortion of the FBa_4 tetrahedra. The BaFMgBi bismuthide exhibits the hitherto largest values of the *a* parameter and the cell volume among all 1111 type compounds. As in the isostructural series, along with the angular distortions of the tetrahedra, the distances *d*(Ba–F) elongate from 2.636 Å to 2.679 Å. The layered nature of BaFMg*Pn* implies that the atoms forming the interface between the layers, Ba and *Pn*, have asymmetric coordination, *i.e.*, they are surrounded by four F (Mg) at short distances (2.6 – 2.9 Å) from inside of the layer and by four *Pn* (Ba) at longer distances (3.5 – 3.7 Å) from the opposite side, as it is shown if **Figure 5.4**.

The unit cell metrics for the new compounds as well as for the related groups of BaFMn*Pn*, BaFZn*Pn* and BaFCd*Pn* are compared in **Table 5.4**. The unit cell parameters and volumes for BaFMg*Pn* are comparable to those of BaFCd*Pn* and slightly higher than for BaFZn*Pn* and BaFMn*Pn*. The *c/a* ratio, being slightly smaller than for BaFMn*Pn* and BaFZn*Pn*, also classifies BaFMg*Pn* into the same group as BaFCd*Pn*. The decreased *c/a* ratio implies a tendency for MgPn_4 and CdPn_4 tetrahedra to be more flattened along the 4-fold axis as compared to MnPn_4 and ZnPn_4, and thus, to dictate a higher *a* unit cell parameter. This in turn dictates the $[Mg_2Pn_2]^{2-}$ layer to be stretched, so that the intergrowths can exist only with the biggest fluorite layers like $[Ba_2F_2]^{2+}$. The expected distortions for the smaller $[Sr_2F_2]^{2+}$ and $[La_2O_2]^{2+}$ layers seem to be too large. Hence the desired intergrowths with $[Mg_2Pn_2]^{2-}$ counterparts were not observed experimentally, in agreement with the results of DFT calculations (*see below*).

Table 5.2 Atomic coordinates and displacement parameters (in Å^2).

Atom	Position	*x/a*	*y/b*	*z/c*	U_{iso}
BaFMgP					
Ba1	2*c*	¼	¼	0.15982(7)	0.0112(2)
P1	2*c*	¼	¼	0.6532(3)	0.0099(6)
Mg1	2*b*	¼	¾	½	0.0138(9)
F1	2*a*	¼	¾	0	0.010(1)
BaFMgAs					
Ba1	2*c*	¼	¼	0.1547(1)	0.0201(3)
As1	2*c*	¼	¼	0.6610(2)	0.0193(5)
Mg1	2*b*	¼	¾	½	0.019(2)
F	2*a*	¼	¾	0	0.021(3)
BaFMgSb					
Ba1	2*c*	¼	¼	0.14046(8)	0.0172(2)
Sb1	2*c*	¼	¼	0.67501(9)	0.0161(3)
Mg1	2*b*	¼	¾	½	0.007(1)
F1	2*a*	¼	¾	0	0.020(2)
BaFMgBi					
Ba1	2*c*	¼	¼	0.1363(1)	0.0165(5)
Bi1	2*c*	¼	¼	0.6819(1)	0.0137(3)
Mg1	2*b*	¼	¾	½	0.012(2)
F1	2*a*	¼	¾	0	0.018(4)

Table 5.3 Selected interatomic distances (in Å) and angles (in deg). α_2 and α_4 are defined in results and discussion section).

	BaFMgP	BaFMgAs	BaFMgSb	BaFMgBi
d(Ba – F)	2.6363(4)	2.6476(8)	2.6703(4)	2.6792(5)
d(Mg – *Pn*)	2.601(2)	2.682(2)	2.8603(5)	2.9308(6)
d(Ba – *Pn*)	3.528(2)	3.570(1)	3.7068(6)	3.7362(7)
d(Mg – Mg)	3.04740(4)	3.1010(1)	3.2338(1)	3.2781(1)
α_2(Ba – F – Ba)	109.65(1)	111.83(1)	117.81(1)	119.80(1)
α_4(Ba – F – Ba)	109.39(1)	108.31(1)	105.47(1)	104.57(1)
α_2(*Pn* – Mg – *Pn*)	111.91(1)	109.71(1)	106.15(1)	104.53(1)
α_4(*Pn* – Mg – *Pn*)	108.29(1)	109.35(1)	111.16(1)	112.00(1)

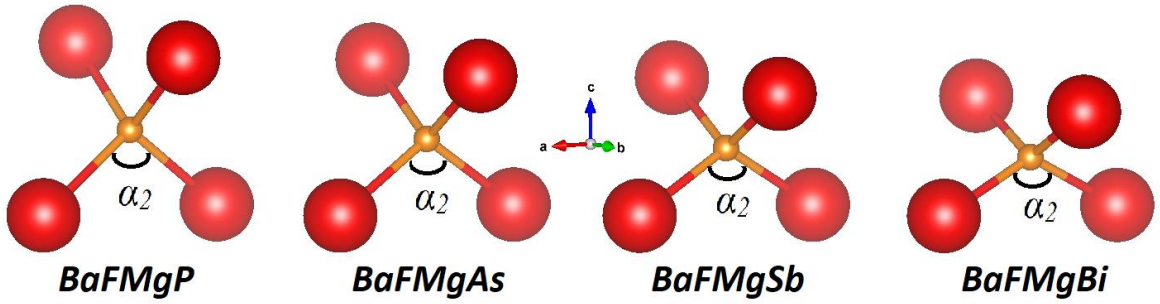

Figure 5.3 Evolution of FBa_4 tetrahedra in the BaFMg*Pn* series (*Pn* = P, As, Sb and Bi). The angle α_2 increases when passing to heavier pnictides, thus flattening the tetrahedra FBa_4. F atoms are yellow, Ba atoms are red. The distances between atoms are not drawn to the scale.

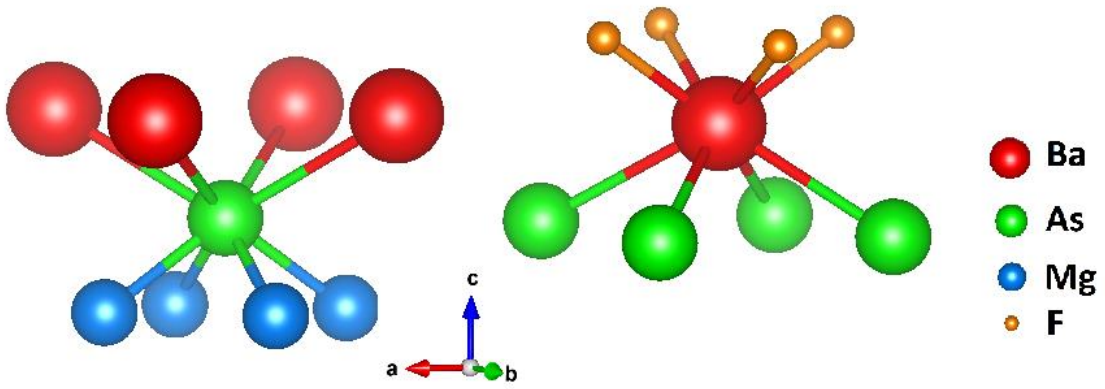

Figure 5.4 The first coordination spheres of Ba and As in the structure of BaFMgAs.

Table 5.4 Unit cell parameters for the compounds BaF*TPn* (*T* = Mg, Zn, Mn, Cd).

		BaFMg*Pn*	BaFZn*Pn*	BaFMn*Pn*	BaFCd*Pn*
Pn = P	*a* in Å	4.3097(1)	4.1563(1)	4.1793(2)	4.3300(1)
	c in Å	9.5032(1)	9.4574(3)	9.5040(5)	9.4933(2)
	c/a	2.205	2.275	2.274	2.192
	V in Å^3	176.51(1)	163.38(1)	166.00(2)	177.99(1)
Pn = As	*a* in Å	4.3855(1)	4.2383(1)	4.2739(1)	4.4008(1)
	c in Å	9.5918(1)	9.5260(2)	9.5875(2)	9.5466(2)
	c/a	2.187	2.247	2.243	2.169
	V in Å^3	184.48(1)	171.12(1)	175.13(1)	184.89(1)
Pn = Sb	*a* in Å	4.5733(1)	4.4384(2)	4.4791(1)	4.5792(9)
	c in Å	9.8184(1)	9.7789(6)	9.8297(2)	9.740(4)
	c/a	2.147	2.203	2.195	2.127
	V in Å^3	205.35(1)	192.64(2)	197.21(1)	204.24(9)
Pn = Bi	*a* in Å	4.6359(1)		4.5384(1)	
	c in Å	9.8599(1)		9.8929(2)	
	c/a	2.127		2.180	
	V in Å^3	211.91(1)		203.76(1)	

Electronic structure, stability and bonding analysis. Total (TDOS) and projected (PDOS) densities of states near the Fermi level for BaFMg*Pn* (*Pn* = P, As, Sb and Bi) are shown in **Figure 5.5**. According to the calculations, all these compounds are semiconductors, with band gaps decreasing from *Pn* = P to *Pn* = Bi. All methods used (FP-LAPW/PBESol, PAW/PBESol, PAW/SCAN) show this effect consistently, although numerical values of the calculated band gaps differ somewhat. For FP-LAPW/PBESol they are 1.69 eV (BaFMgP), 1.50 eV (BaFMgAs), 1.16 eV (BaFMgSb), and 0.96 eV (BaFMgBi). For VASP calculations that utilize PBESol we obtain bang gaps of 1.75 eV (BaFMgP), 1.58 eV (BaFMgAs), 1.25 eV (BaFMgSb), and 1.04 eV (BaFMgBi), while the respective band gaps calculated from SCAN-based results are *ca*. 0.4 - 0.5 eV wider. On the one hand, DFT is known to often underestimate band gaps of semiconductors, and thus wider gaps predicted by the more advanced SCAN functional could be at first glance considered an improvement. On the other hand, the results from PBESol-based calculations by both all-electron and pseudopotential approaches not only agree well with each other, but also are in much better agreement with the fact that all four compounds are black. Thus, in this particular

case, while both PBESol and SCAN produce qualitatively the same picture, the results obtained with the former are closer to the observed properties of the compounds. We have attempted to measure diffuse reflectance spectra for all compounds to obtain an experimental band gap values. Unfortunately, most of the data turned out to be unusable due to the severe air-instability of BaFMgPn. Probably the only spectrum that was possible to interpret was obtained in the case of BaFMgBi (see **Figure 5.S1** in the Supporting Information), which shows the band gap in BiFMgBi to be *ca.* 0.9 eV, which is in good agreement with calculated values.

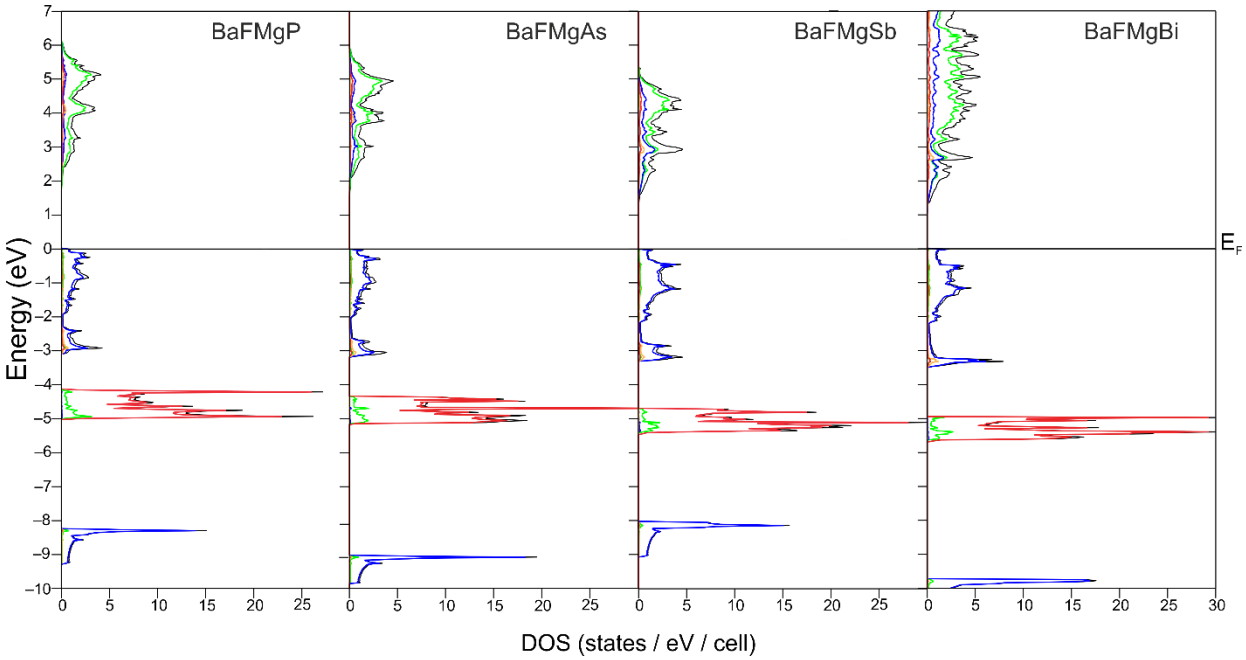

Figure 5.5 Total (TDOS) and projected (PDOS) densities of states for BaFMg*Pn* (*Pn* = P – Bi) calculated from VASP/PBESol data: TDOS – black line, Ba PDOS – green line, *Pn* PDOS – blue line, Mg PDOS – yellow line, F PDOS – red line.

In all four compounds, the top of the valence band is essentially formed by the *p*-states of pnictogen atoms (see **Figure 5.5**), while the bottom of the conduction band features strong contribution from barium *s*-states, along with smaller for *Pn* = P, but increasing from P to Bi to the extent of being almost equal, contribution from pnictogen *p*-states, and even smaller contribution from fluorine *p*-states and magnesium *s*-states. The zoomed DOS around the Fermi level for BaFMg*Pn* is given in **Figure 5.S2** in the *SI.* Thus, the band gap in this series is mostly formed by barium and pnictogen atoms, which is somewhat different from the previously investigated series of Ba and Eu *d*-metal fluoropnictides [23, 24, 26] where the cations in the fluorine-containing block provided relatively smaller contributions to the states in vicinity of the Fermi level. This reflects the key difference between the series

of *AFTPn* compounds, where *A* = Sr, Ba, Eu, *T*= transition metal, and the BaFMg*Pn* series under discussion, namely the change of the chemical nature of the metal in the metal-pnictogen block. With the change from *d*-metal to *s*-metal, the contributions near the Fermi level from the metal in the *M* – *Pn* block become comparable to the contribution from the metal in the *M* – F block.

Calculated QTAIM charges for the BaFMg*Pn* series are shown in **Table 5.5**.There is a very significant charge density transfer from barium and magnesium to fluorine and the pnictogens, making all structures essentially ionic. Barium and magnesium charges are the same in BaFMgP, and slightly diverge upon going towards *Pn* = Bi as the pnictogen atom electronegativity gradually decreases resulting in a slightly decreasing positive charge on magnesium. Nevertheless, effective atomic charges are still high and indicate a predominantly ionic nature even for BaFMgBi, which is expected to have the least ionicity in the magnesium-pnictogen structure blocks across the whole series. This might help to rationalize the results obtained with the SCAN functional, as the main idea behind its use here was to account for potential dispersion interactions, while the interatomic interactions turned out to be mostly of Coulomb type. Thus, it is possible that the highly ionic bonding nature of these compounds nullifies the benefits from using more advanced functionals in this case. Additional support to the ionic nature of bonding in these compounds is provided by the lack of non-atomic attractors in the topology of the electron localization function (ELF), even in the case of BaFMgBi (see **Figure 5.6**).

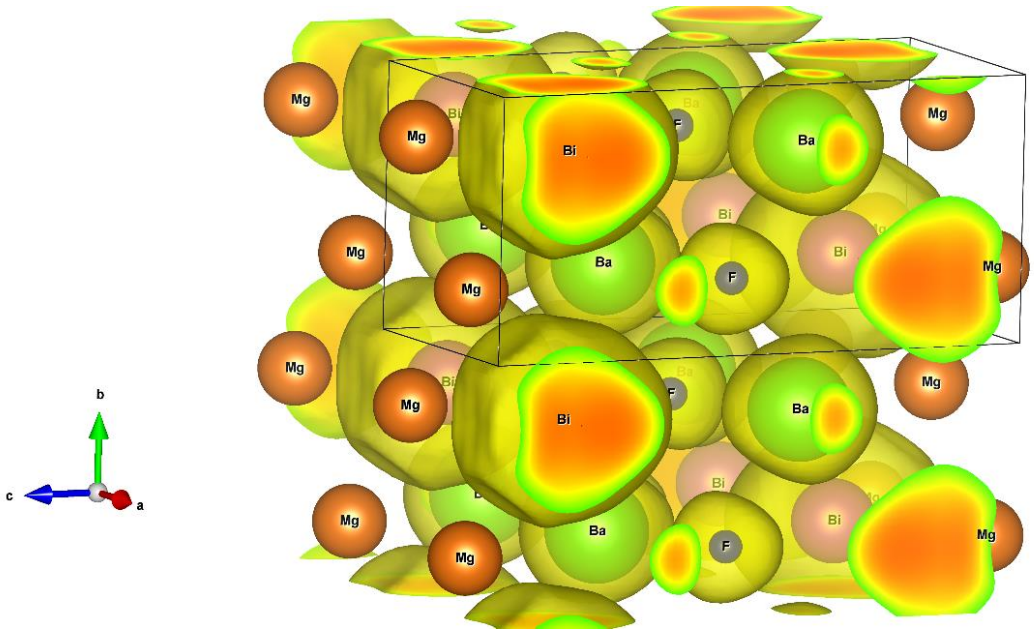

Figure 5.6 ELF isosurface (η=0.53) for BaFMgBi calculated from the VASP data.

Table 5.5 Calculated atomic charges for BaFMg*Pn* (*Pn* = P, As, Sb, and Bi) from ELK/Dgrid (E) and VASP/Bader (V) data.

Compound	Ba	F	Mg	*Pn*
BaFMgP (E)	+1.52	-0.84	+1.53	-2.21
BaFMgP (V)	+1.52	-0.83	+1.52	-2.21
BaFMgAs (E)	+1.52	-0.85	+1.51	-2.18
BaFMgAs (V)	+1.52	-0.84	+1.48	-2.16
BaFMgSb (E)	+1.51	-0.86	+1.47	-2.12
BaFMgSb (V)	+1.51	-0.85	+1.44	-2.10
BaFMgBi (E)	+1.50	-0.86	+1.42	-2.05
BaFMgBi (V)	+1.49	-0.86	+1.38	-2.01

The results of the investigation of the thermodynamic stabilities of BaFMg*Pn*, LaOMg*Pn* and SrFMgAs based on specific reactions are summarized in **Tables 5.6** and **5.7**. All BaFMg*Pn* compounds are found to be stable with respect to their likely precursors, with free enthalpies of the respective reactions (estimated at 0 K where entropy contribution is zero) being in the range of *ca*. -15 – -20 kJ/mol. This agrees with our observations during the syntheses, confirming that the compounds do not need to be quenched to avoid decomposition, and the main handling problem is their high reactivity rather than intrinsic instability. On the contrary, optimized structures of hypothetical oxygen-containing analogs of fluoropnictides (the LaOMg*Pn* series), as well as the strontium analogue of BaFMgAs, are found to be unstable with respect to their precursors (La*Pn* + MgO or SrF_2 + $SrMg_2As_2$, respectively). This explains why our synthetic attempts to produce these compounds were not successful. SrFMgAs has significantly less positive free enthalpy as compared to the LaOMg*Pn* series. Nevertheless, it is still deemed unfavorable, which agrees with the experimental observations. The compound was chosen since, in our experience and from the literature [25], arsenides of this structure type are always found even in the cases when the corresponding phosphide and/or antimonide analogs do not exist. The same probably applies to other SrFMg*Pn* compounds which are as unlike to exist (no synthetic attempts and calculations were made). The general pattern is the same as for the *Ae*FCd*Pn* compounds [21, 26] which is not surprising given the Mg – *Pn* distances being very close to Cd – *Pn*. It has to be noted that these predictions are only relevant to the 1111-type structures and reaction pathways specified in this paper; yet, our synthetic experience shows that when the target phase is not obtained, the precursors/decomposition products, AeF_2 + AeT_2Pn_2, in the respective reactions properly reflect phase compositions of the samples.

The new compound BaFMgBi is the second bismuthide representative of the 1111 structure type, the first being BaFMnBi [20]. Though the estimated distortions of the *T*Bi$_4$ tetrahedra in the hypothetical compounds BaFZnBi and BaFCdBi should be of the same order like those in BaFMgBi, all our attempts to prepare these compounds have not yet been successful [26]. In the meantime, such mackinawite-type slabs have been observed in the structures of intermetallic compounds (Sr,Ba)*T*Bi$_2$ [48, 49]. The reason is likely the same as we had suggested for non-existence of valence isoelectronic compounds BaFAlSn and BaFGa*Tt* (*Tt* = tetrel). In these cases, the mackinawite-type layers are expected to exhibit the largest degree of bond covalence while combinations of layers with essentially different bond nature (ionic/covalent or ionic/metallic) seem to be unfavorable. Evidently, studies in chemically related systems are necessary to verify our suggestions. Another interesting point is that the structures of our compounds contain two IIA group metals playing essentially different crystallographic roles. Similar patterns are observed in the structures of the CeFeSi-type compounds BaMg*Tt* [50] due to the very large size difference of Ba^{2+} and Mg^{2+} [51].

Table 5.6 Optimized structural parameters of hypothetical LaOMg*Pn* and SrFMgAs according to DFT/VASP calculations (tetragonal, *P*4/*nmm*).

	LaOMgP	LaOMgAs	LaOMgSb	LaOMgBi	SrFMgAs
a in Å	4.1219	4.1723	4.3071	4.3409	4.2111
c in Å	8.9002	9.0821	9.5120	9.7466	9.0268
z (La)*	0.1315	0.1265	0.1134	0.1096	0.1443
z (*Pn*)*	0.6721	0.6800	0.6940	0.6977	0.6790

*-atomic coordinate (¼;¼;*z*)

Table 5.7 Energy gain and free enthalpies of BaFMg*Pn*, SrFMgAs, and LaOMg*Pn* (*Pn* = P, As, Sb and Bi) formation according to specific reactions.

Reaction	*Pn* = P		*Pn* =As		*Pn* = Sb		*Pn* = Bi	
	-*ΔE* in eV	*ΔG* in kJ/mol	*ΔE* in eV	*ΔG* in kJ/mol	*ΔE* in eV	*ΔG* in kJ/mol	*ΔE* in eV	*ΔG* in kJ/mol
1*	0.155	-15.0	0.187	-18.1	0.208	-20.1	0.223	-21.5
2*	-	-	-0.025	2.4	-	-	-	-
3*	-0.405	39.1	-0.381	36.8	-0.501	48.3	-0.395	38.1

*1 – BaF_2 + $BaMg_2Pn_2$ = 2 BaFMg*Pn*

*2 – SrF_2 + $SrMg_2As_2$ = 2 SrFMgAs (estimations for a hypothetical compound)

*3 – La*Pn* + MgO = LaOMg*Pn* (estimations for hypothetical compounds)

Conclusions

Using solid state techniques, we successfully prepared a chemically novel family of 1111-type layered fluoropnictides *via* introducing a second non-transitional metal, magnesium, into the anti-fluorite part of the structure. According to DFT calculations, these compounds are semiconductors with calculated band gaps decreasing from *ca.* 2 eV (*Pn* = P) to *ca.* 1 eV (*Pn* = Bi). Bonding analysis shows predominantly ionic nature of chemical bonds in both Ba – F and Mg – *Pn* parts of the structures. Despite the fact that the compounds feature magnesium in the role more conventionally played by *p*- or *d*-block metals, main crystallographic features of this series fit the trends observed for the other members of the family, *e.g.*, gradual band gap decrease with increasing *Pn* atomic number, very well. The same holds for the trends in geometrical parameters of their crystal structures which are similar to the families of group 11 (Cu, Ag), 12 (Zn, Cd), and Mn-containing compounds.

This series, on the one hand, is a good example to show the flexibility of the LaOAgS structure type and to display its further perspectives with regard to even more exotic elemental compositions. On the other hand, very good agreement between theoretical predictions and experimental efforts in these systems encourages further use of theory in the search for new representatives of this structure type, as well as some closely related compounds.

This chapter has been published in a peer-reviewed journal *Inorganic Chemistry* of the publisher American Chemical Society (DOI 10.1021/acs.inorgchem.8b03554). The crystal structures of the title compounds are deposited in ICSD under the reference number 1881391, 1881383, 1881375 and 1881369.

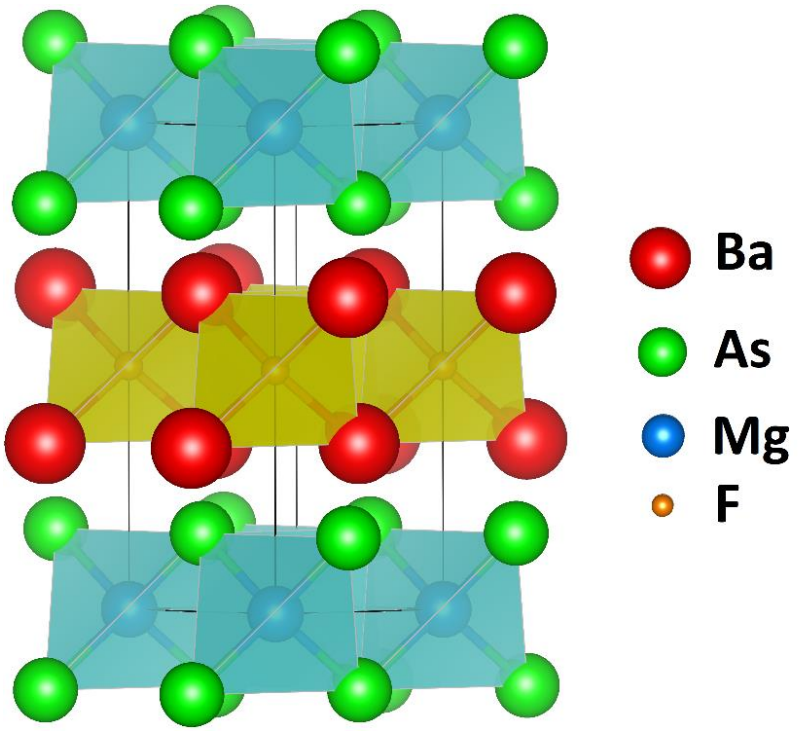

Figure 5.TOC Graphical abstract to the paper entitled "Layered compounds BaFMg*Pn* (*Pn* = P, As, Sb, and Bi), transition-metal-free representatives of the 1111 structure type".

Several other people also contributed to this work:

1. Alexey N. Kuznetsov and Dmitri O. Charkin performed calculations, discussed crystallographic part and improved the manuscript.
2. Andrei V. Shevelkov and Arno Pfitzner contributed to discussion of the results, provided the equipment and labspace and improved the manuscript.
3. Igor V. Plokhikh performed synthesis, designed calculations and wrote the draft of the manuscript.

Supporting Information

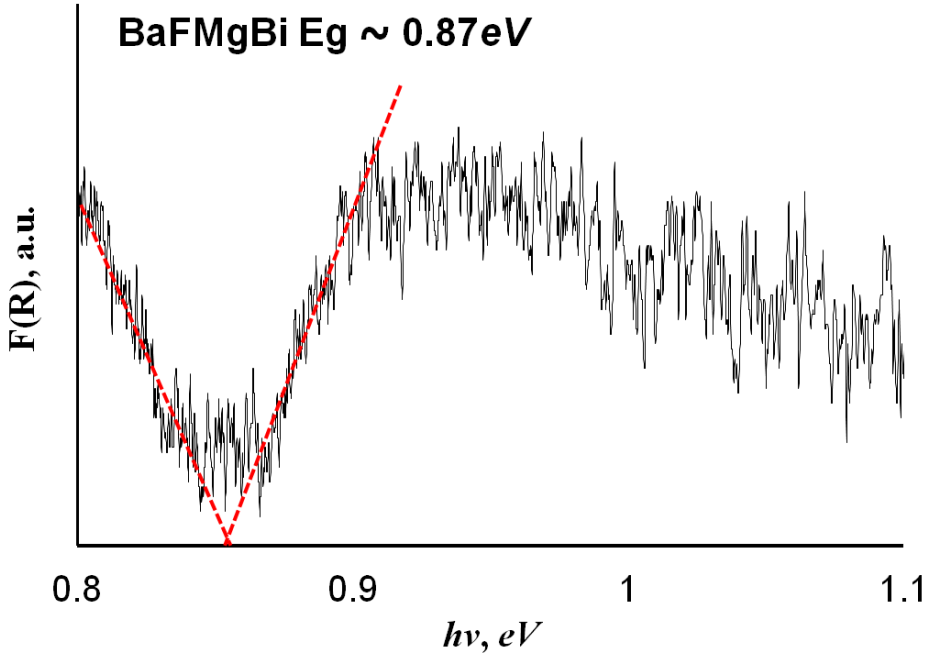

Figure 5.S1 Diffuse reflectance spectrum for BaFMgBi.

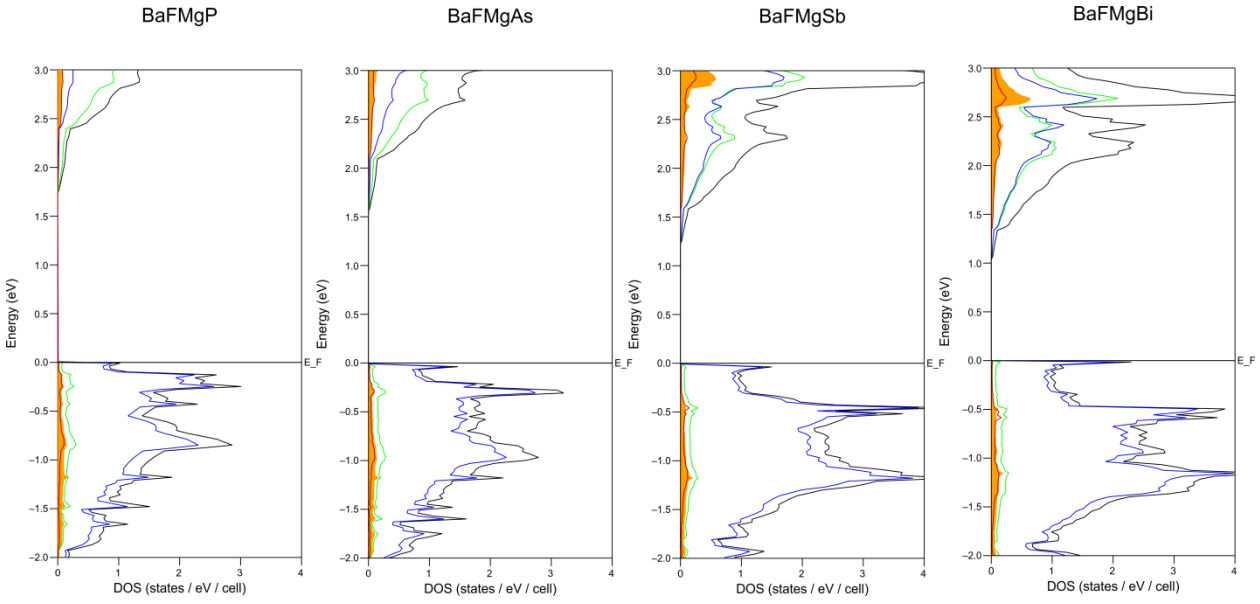

Figure 5.S2 Enlarged region of calculated (VASP/PBESol) total and projected DOS around the Fermi level for BaFMg*Pn* (*Pn* = P, As, Sb, Bi): TDOS – black line, Ba PDOS – green line, *Pn* PDOS – blue line, Mg PDOS – orange shading, F PDOS – red line.

Addendum

Table 5.4 features two gaps at the positions of two hypothetical bismuthides BaFZnBi and BaFCdBi, while analogous BaFMnBi and BaFMgBi were reported. The reason behind these gaps was unclear – is it due to thermodynamic issue (instability of these compounds because of geometrical mismatching) or kinetic (the starting materials are not reactive enough). One can propose a weak reactivity of Bi and Zn/Cd or evaporation of the precursors within the ampule. To resolve this issue, a ball-milling synthesis has been performed according to the following protocol. Stoichiometric mixtures of Ba, BaF_2, Bi, and Zn/Cd were milled at 600rpm ten times 5 min each with intermediate cooling for 5 min. Eventually, annealing of the resulting mixtures at 500 ^{0}C over 4 d results in the formation of the two missing compounds. Still, they are not observed in a phase-pure form. Their diffraction patterns (Rietveld plots) are provided in **Figure 5.A1**.

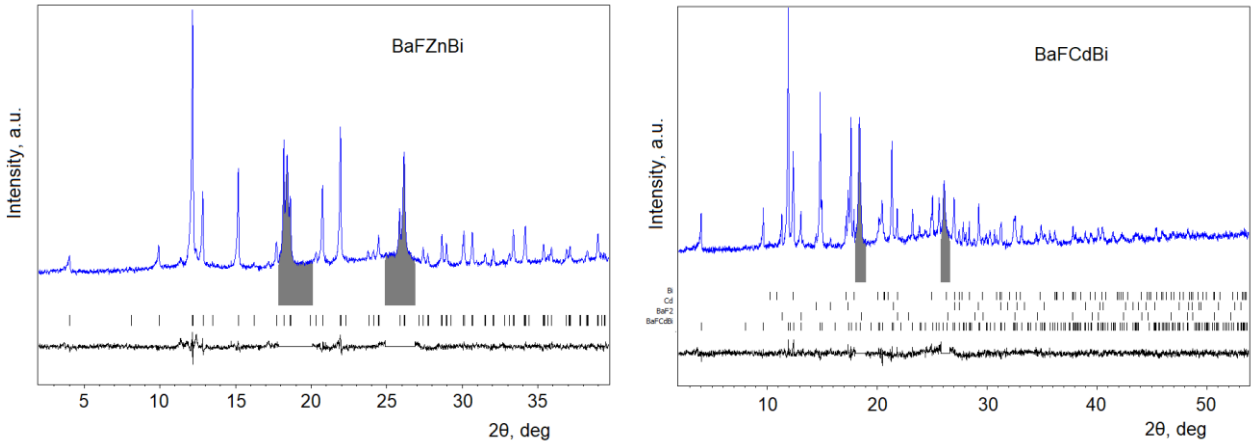

Figure 5.A1 Rietveld plots for BaFZnBi and BaFCdBi.

References

[1] Y. Kamihara, H. Hiramatsu, M. Hirano, R. Kawamura, H. Yanagi, T. Kamiya, H. Hosono, Iron-based layered superconductor: LaOFeP. *J. Am. Chem. Soc.* **2006**, *128*, 10012.

[2] Y. Kamihara, T. Watanabe, M. Hirano, H. Hosono, Iron-based layered superconductor $La[O_{1-x}F_x]FeAs$ (x = 0.05–0.12) with T_C = 26K. *J. Am. Chem. Soc.* **2008**, *130*, 3296.

[3] Z. Ban, M. Sikirica, The crystal structure of ternary silicides ThM_2Si_2 (M = Cr, Mn, Fe, Co, Ni and Cu). *Acta Crystallogr.* **1965**, *18*, 594.

[4] G. Just, P. Paufler, On the coordination of $ThCr_2Si_2$ ($BaAl_4$-type compounds within the field of free parameters. *J. Alloys Compd.* **1996**, *232*, 1.

[5] M. Palazzi, C. Carcaly, J. Flahaut, Un nouveau conducteur ionique (LaO)AgS. *J. Solid State Chem.* **1980**, *35*, 150.

[6] K. Ishida, Y. Nakai, H. Hosono. To what extent iron-pnictide new superconductors have been clarified: a progress report. *J. Phys. Soc. Jpn.* **2009**, *78*, 062001.

[7] V. Johnson, W. Jeitschko, ZrCuSiAs: a "filled" PbFCl type. *J. Solid State Chem.* **1974**, *11*, 161.

[8] D. O. Charkin, X. N. Zolotova, A crystallographic re-investigation of Cu_2Sb-related binary, ternary, and quaternary structures: how many structure types can exist upon the same topology of a unit cell? *Crystallogr. Rev.* **2007**, *13*, 201.

[9] K. Ueda, H. Hiramatsu, M. Hirano, T. Kamiya, H. Hosono, Wide-gap layered oxychalcogenide semiconductors: Materials, electronic structures and optoelectronic properties. *Thin Solid Films* **2006**, *496*, 8.

[10] E. J. Wildman, A.C. Mclaughlin, A variable temperature synchrotron X-ray diffraction study of colossal magnetoresistant $NdMnAsO_{0.95}F_{0.05}$. *Sci. Rep.* **2016**, *6*, 20705.

[11] T. Suzuki, M.S. Bahramy, R. Arita, Y. Taguchi, Y. Tokura. Doping control and thermoelectric properties in $R_{1-x}A_xZnSbO$ (R= La, Ce; A = Ca, Sr). *Phys. Rev. B* **2011**, *83*, 035204.

[12] R. Pöttgen, D. Johrendt, Materials with ZrCuSiAs-type structure. *Z. Naturforsch.* **2008**, *63*, 1135.

[13] D.Johrendt, R.Pöttgen, Pnictide oxides: a new class of high-T_C superconductors. *Angew. Chem.* **2008**, *47*, 4782.

[14] A. M. Kusainova, P. S. Berdonosov, L. G. Akselrud, L. N. Kholodkovskaya, V.A. Dolgikh, B.A. Popovkin. New layered compounds with the general composition (MO)(CuSe), where M = Bi, Nd, Gd, Dy, and BiOCuS: syntheses and crystal structure. *J. Solid State Chem.* **1994**, *112*, 189.

[15] S. Muir, M.A. Subramanian. ZrCuSiAs type layered oxypnictides: A bird's eye view of LnMPnO compositions. *Prog. Solid State Chem.* **2012**, *40*, 41.

[16] S. W. Park, H. Mizoguchi, K. Kodama, S.I. Shamoto, T. Otomo, S. Matsuishi, H. Hosono, Magnetic Structure and Electromagnetic Properties of LnCrAsO with a ZrCuSiAs-type Structure (Ln = La, Ce, Pr, and Nd). *Inorg. Chem.* **2013**, *52*, 13363.

[17] S. J. Clarke, P. Adamson, S. J. C. Herkelrath, O. J. Rutt, D. R. Parker, M. J. Pitcher, C. F. Smura, Structures, physical properties, and chemistry of layered oxychalcogenides and oxypnictides. *Inorg. Chem.* **2008**, *47*, 8473.

[18] H. Kabbour, L. Cario, F. Boucher. Rational design of new inorganic compounds with the ZrSiCuAs structure type using 2D building blocks. *J. Mater. Chem.* **2005**, *15*, 3525.

[19] D. O. Charkin, I. V. Plokhikh, A. N. Kuznetsov, S. M. Kazakov. BaFAlSi and BaFAlGe: First transition metal-free LaOAgS-type fluoride tetrelides. *J. Alloys Compd.* **2015**, *627*, 451.

[20] B. Saparov, D.J. Singh, V.O. Garlea, A. S. Sefat, Crystal, magnetic, and electronic structures, and properties of new BaMn*Pn*F (*Pn* = As, Sb, Bi). *Sci. Rep.* **2013**, *3*, 2154.

[21] B. Saparov, S. Bobev. Synthesis, crystal and electronic structures of the new quaternary phases $A_5Cd_2Sb_5F$ (*A* = Sr, Ba, Eu), and $Ba_5Cd_2Sb_5O_x$ ($0.5 < x < 0.7$). *Dalton Trans.* **2010**, *39*, 11335.

[22] D. O. Charkin, A. V. Urmanov, S. M. Kazakov. Preparation and crystal structures of novel LaOAgS-type copper and silver fluoride chalcogenides. *J. Alloys Compd.* **2012**, *516*, 134.

[23] I. V. Plokhikh, D. O. Charkin, V. Yu. Verchenko, A. N. Kuznetsov, S. M. Kazakov, A. A. Tsirlin, A. V. Shevelkov. Structural and thermodynamic stability of the "1111"structure type: a case study of the EuFZnPn series. *Inorg. Chem.* **2016**, *55*, 12409.

[24] I. V. Plokhikh, D. O. Charkin, V. Yu. Verchenko, A. N. Kuznetsov, S. M. Kazakov, A. A. Tsirlin, A. V. Shevelkov, Synthesis, crystal structure and physical properties of europium – manganese fluoride pnictides, EuMn*Pn*F (*Pn* = P, As, Sb). *J. Solid State Chem.* **2018**, *258*, 682.

[25] X. Zhu, F. Han, P. Cheng, G. Mu, B. Shen, L. Fang, H.-H. Wen, Superconductivity in fluoride-arsenide $Sr_{1-x}La_xFeAsF$ compounds. *Europhys. Lett*. **2009**, *85*, 4782.

[26] D. O. Charkin, A. V. Urmanov, I. V. Plokhikh, A. D. Korshunov, A. N. Kuznetsov, S. M. Kazakov. Synthesis and crystal structures of novel LaOAgS-type alkaline earth – zinc, manganese, and cadmium fluoride pnictides. *J. Alloys Compd.* **2014**, *585*, 644.

[27] S. Tencé, S.F. Matar, G. André, E. Gaudin, B. Chevalier, Hydrogenation inducing ferromagnetism in the ternary antiferromagnet NdCoSi. *Inorg. Chem.* **2010**, *49*, 4836.

[28] C. Wang, Z.-C. Wang, Y.-X. Mei, Y.-K. Li, L. Li, Z.-T. Tang, Y. Liu, P. Zhang, H.-F. Zhai, Z.-A. Xu, and G.-H. Cao, A new ZrCuSiAs-type superconductor: ThFeAsN. *J. Am. Chem. Soc.* **2016**, *138*, 2170.

[29] B. Krenkel, H.-U. Schuster, NaMgAs(Sb) - ternary compounds in a modified Cu_2Sb structure. *Z. Naturforsch., B: Chem. Sci.* **1978**, *33*, 1080.

[30] R. Vogel, H.-U. Schuster, Neue elektrovalente ternäre Verbindungen des Kaliums mit Magnesium und Elementen der 5. Hauptgruppe. *Z. Naturforsch.* **1979**, *34b*, 1719.

[31] STOE WinXPOW, Version 3.10, STOE &Cie GmbH, Darmstadt **2016**.

[32] V. Petricek, M. Dusek, L. Palatinus, Crystallographic computing system JANA2006: general features. *Z. Kristallogr.* **2014**, *229*, 345.

[33] K. Momma and F. Izumi, VESTA 3 for three-dimensional visualization of crystal, volumetric and morphology data. *J. Appl. Crystallogr.* **2011**, *44*, 1272.

[34] ELK, an all-electron full-potential linearized augmented-plane wave (FP-LAPW) code, ver. 3.1.12; http://elk.sourceforge.net.

[35] G. Kresse, D. Joubert. From ultrasoft pseudopotentials to the projector augmented-wave method. *Phys. Rev. B* **1999,** *59*, 1758.

[36] G. Kresse, J. Furthmüller, Vienna Ab-initio Simulation Package (VASP), v.5.4.4; http://vasp.at.

[37] J. P. Perdew, A. Ruzsinszky, G. I. Csonka, O. A. Vydrov, G. E. Scuseria, L. A. Constantin, X. Zhou, K. Burke, Restoring the density-gradient expansion for exchange in solids and surfaces. *Phys. Rev. Lett.* **2008**, *100*, 136406.

[38] H. J. Monckhorst, J. D. Pack, Special points for Brillouin-zone integrations. *Phys. Rev. B* **1976**, *13*, 5188.

[39] H. Peng, Z.-H. Yang, J.P. Perdew, J. Sun, Versatile van der Waals density functional based on a meta-generalized gradient approximation. *Phys. Rev. X* **2016**, *6*, 041005.

[40] R. F. W. Bader. Atoms in Molecules: A Quantum Theory. Oxford University Press: Oxford, U.K., **1990**.

[41] M. Kohout, DGrid, ver. 4.6; Radebeul, **2011**.

[42] G. Henkelman, A. Arnaldsson, and H. Jónsson. A fast and robust algorithm for Bader decomposition of charge density. *Comput. Mater. Sci.* **2006**, *36*, 354.

[43] E. Sanville, S. D. Kenny, R. Smith, and G. Henkelman. An improved grid-based algorithm for Bader charge allocation. *J. Comp. Chem.* **2007**, *28*, 899.

[44] M. Yu and D. R. Trinkle. Accurate and efficient algorithm for Bader charge integration. *J. Chem. Phys.* .**2011**, *134*, 064111.

[45] B. Silvi, A. Savin. Classification of chemical bonds based on topological analysis of electron localization functions. *Nature* **1994**, *371*, 683.

[46] P. Klüfers, A. Mewis, AB_2X_2-Verbindungen mit $CaAl_2Si_2$-Struktur. X. Zur Struktur neuer ternärer Erdalkaliphosphide und –arsenide. *Z. Kristallogr.* **1984**, *169*, 135.

[47] B. W. Liebich, D. Nicollin. Refinement of the PbFCl types BaFI, BaFBr and CaFCl. *Acta Crystallogr. B* **1977**, *33*, 2790.

[48] G. Cordier, B. Eisenmann, H. Schäfer. Darstellung und Kristallstruktur von $SrCu_2Sb_2$ und $SrZnBi_2$. *Z. Anorg. Allg. Chem.* **1976**, *426*, 205.

[49] E. Brechtel, G. Cordier, H. Schäfer. Neue ternäre Erdalkali-Übergangselement-Pnictide. *J. Less-Comm. Metals.* **1981**, *79*, 131.

[50] B. Eisenmann, H. Schäfer, A. Weiss. Der Übergang vom "geordneten" Anti-$PbCl_2$-Gitter zum anti-PbFCl-Gitter: ternäre Phasen ABX der Erdalkalimetalle mit Elementen der 4. Hauptgruppe (A = Ca, Sr, Ba; B = Mg; X = Si, Ge, Sn, Pb). *Z. Anorg. Allg. Chem.* **1972**, *391*, 241.

[51] R. D. Shannon. Revised effective ionic radii and systematic studies of interatomic distances in halides and chalcogenides. *Acta Cryst. A* **1976**, *32*, 751.

6 Synthesis, electronic structure and physical properties of two new layered compounds, EuFAgSe and $EuFAg_{1-\delta}Te$, featuring the active redox pair Eu^{2+}/Ag^{+}

Abstract

Systematic studies of the ZrCuSiAs (also LaOAgS or 1111) structure type resulted in the synthesis of two new fluoride chalcogenides, EuFAgSe and $EuFAg_{1-\delta}Te$, whereas their sulfide analog, EuFAgS, could not be obtained. Both new compounds are tetragonal, *P4/nmm,* with cell parameters a = 4.1542(1) Å, c = 9.2182(1) Å for the selenide and a = 4.3255(1) Å, c = 9.5486(1) Å for the telluride. Rietveld refinement reveals a significant silver deficiency in the telluride (δ = 0.05), while the selenide is nearly stoichiometric. Both compounds are semiconductors as shown by diffuse reflectance spectroscopy and confirmed by density-functional calculations of the band structure. Magnetism of both compounds is predominantly driven by Eu^{2+}, as indicated by magnetic susceptibility measurements and corroborated by ^{151}Eu Mössbauer spectroscopy. $EuFAg_{1-\delta}Te$ and EuFAgSe are paramagnetic down to 1.8 K.

Introduction

Among the layered inorganic structure types, that of ZrCuSiAs (commonly together with LaOAgS referred as 1111) has attracted significant attention over the last decade due to its diverse crystallography and a bunch of interesting physical properties (including superconductivity) exhibited by its representatives [1 – 5]. The structure is very simple and consists of two *anti*-isostructural litharge- and mackinawite-type layers (**Figure 6.1**). These layers are observed separately in many other related structure types [5 – 7]. The mackinawite layers $[T_2X_2]^{n-}$ formed by edge-sharing TX_4 tetrahedra (T = element of groups 6 – 13, X = element of groups 14 – 16) are believed to be mostly responsible for the physical properties. In contrast, the oxygen-containing litharge layers $[M_2O_2]^{n-}$ typically act as charge reservoirs. They are formed by the condensation of oxygen-centered OM_4 tetrahedra, where M is a trivalent (Bi, Y, *Ln*) or a tetravalent (Th and U) cation. Fluorine-centered tetrahedra FM'_4 are less common in the litharge part of the structure due to a small choice of divalent M'^{2+} cations available in this case (alkaline earth, Eu^{2+} or Sm^{2+}) [9 – 21]. The "compatibility criteria" arising from: i) charge balance; ii) size compatibility, and iii) redox compatibility of the layers, restrict the number of representatives.

The rather unusual oxidation state of +2 for Sm is known to be stable in some of the ZrCuSiAs-compounds, including the recently discovered and claimed to be a self-doped superconductor SmFFeAs [20] as well as in SmFCuSe [19]. The latter contains a redox-unstable pair of ions, Sm^{2+} and Cu^{+}, which nevertheless appears in this structure, probably due to the spatial separation of Sm and Cu. This suggests that the combination of Eu^{2+} and Ag^{+} could also be stable in certain crystal-chemical environments, as observed, for example, in the $EuAg_4Pn_2$ pnictides (*Pn* = As and Sb [22]). The close similarity of the ionic radii of Eu^{2+} and Sr^{2+} (1.17 Å *vs.* 1.18 Å [23]) and the existence of the SrFAg*Ch* type compounds for *Ch* = S, Se, and Te [16] suggest that their EuFAg*Ch* analogs can also be prepared. Following our previous successful experiments with Eu^{2+}-containing compounds [12, 13], we attempted to synthesize these compounds. Only two (*Ch* = Se and Te) of the three envisaged EuFAg*Ch* compounds were obtained, while attempts to prepare the respective sulfide have not yet been successful. Here, we report the crystal and electronic structures, as well as magnetic and optical properties of the two title compounds.

Experimental section

Synthesis and primary characterization. EuFAgSe and $EuFAg_{1-\delta}Te$ were prepared from the elements and europium fluoride by conventional solid-state reactions. All operations were performed in an argon-filled glovebox (oxygen and water vapor content below 2 ppm) due to the reactive properties of the precursors (Eu metal) and intermediates. The mixtures of freshly chopped europium metal (Novaelements, over 99.5%), EuF_3 (Chempur, 99.999%), silver (self-prepared by reduction of AgCl), and chalcogen powders (Se and Te, Chempur, 99.999%) were taken in the molar ratio 2 : 1 : 3 : 3, cold-pressed in pellets, placed in carbon-lined silica capsules, evacuated below 5 Pa, and flame sealed. Annealing was done at 850 K for EuFAgSe and at 920 K for EuFAgTe with several intermediate grindings. Attempts to prepare EuFAgS using various synthetic routes (using metallic silver or Ag_2S as starting compounds, transport reactions with I_2, high-pressure or mechanochemical treatment) were not successful.

Powder X-ray diffraction data acquired on a STOE STADI P diffractometer (STOE &Cie, Darmstadt, Germany) equipped with a Dectris Mythen 1K detector using Mo $K\alpha_1$ radiation (λ = 0.709300 Å) indicated that the as-prepared EuFAgSe and $EuFAg_{1-\delta}Te$ samples were nearly single-phase. The samples are orange (telluride) and yellowish-red (selenide) powders, stable against moisture and air over several months.

According to DTA measurements, performed with a SETARAM TG-DTA 92 analyzer, they decompose irreversibly at 880 K (selenide) and 1020 K (telluride).

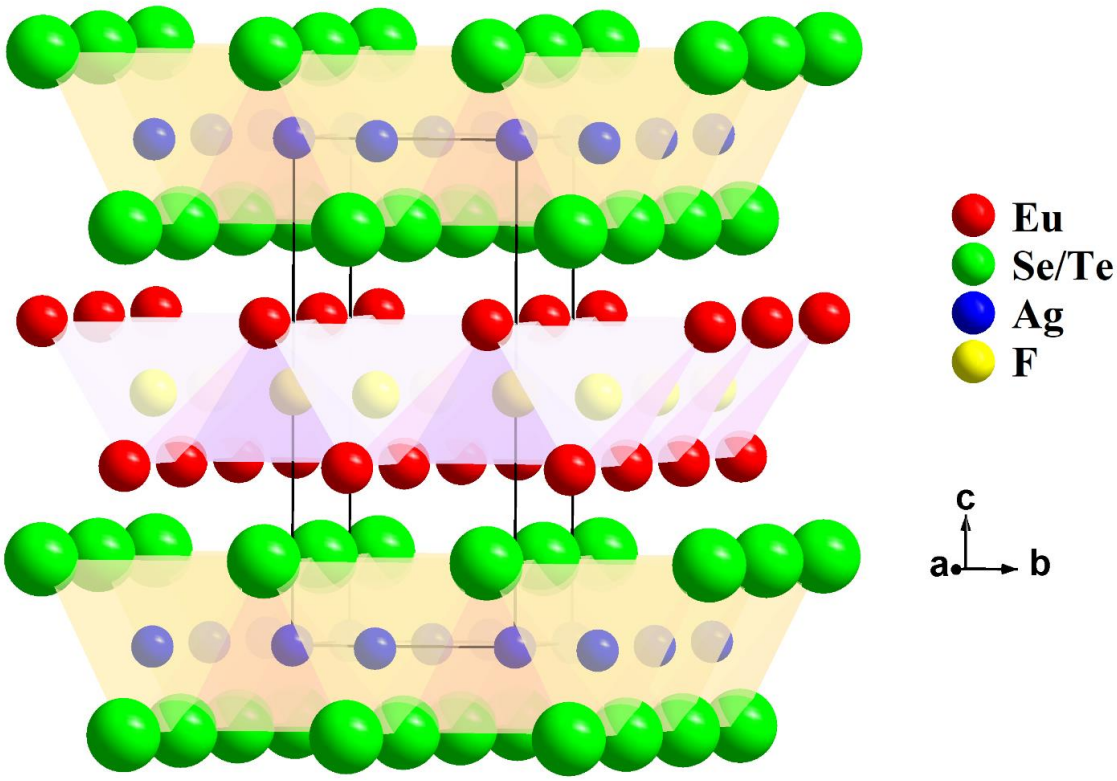

Figure 6.1 The crystal structure of the 1111-type compounds, as exemplified by EuFAg*Ch* (*Ch* = Se and Te). The litharge slabs $[Eu_2F_2]^{2+}$ are formed by the Eu^{2+} cations and F^- anions; the mackinawite blocks $[Ag_2Ch_2]^{2+}$ are formed by the chalcogen anions (*Ch*) and Ag^+ cations.

Crystal structure determination. As no single crystals could be obtained, the crystal structures of the new compounds were refined from room-temperature X-ray powder diffraction data collected on the same diffractometer. Rietveld refinements were performed in JANA2006 [24] using the structure of the archetype as a starting model and the standard mathematical apparatus for profile fitting (Pseudo-Voigt profile function; Legendre polynomials for background description). Traces of impurities were identified and included into the refinement, see **Table 6.1**. No evidence of substantial anisotropy of the atomic displacement parameters was found, therefore they were treated in isotropic approximation. During the refinement we noticed that full occupancy of the Ag site in EuFAgTe yields a substantially higher atomic displacement parameter as compared to the other sites (0.036 $Å^2$ *vs.* 0.005 - 0.016 $Å^2$) as well as a small negative difference Fourier peak at the position of Ag atom.

Therefore, the site occupancy was refined, resulting in an estimated vacancy content of ~ 5%. Therefore, we refer to this compound as $EuFAg_{1-\delta}Te$ throughout the paper. The occupancy of the Ag site in EuFAgSe deviates from unity, but the deviation remains within 3σ and is thus deemed insignificant. The difference Fourier maps are almost featureless, *i.e.*, they do not show structurally reasonable maxima. Final Rietveld refinement plots for $EuFAg_{1-\delta}Te$ and EuFAgSe are given in **Figure 6.2**; refinement results, together with some reference data, are listed in **Tables 6.1 – 6.3.**

UV/Vis spectroscopy. Diffuse reflectance measurements were performed with a Bruins Omega 20 UV/Vis spectrometer using $BaSO_4$ as a white standard (100% reflectance). The absorption spectrum was calculated using the Kubelka-Munk function.

Magnetic measurements. Temperature- and field-dependent magnetization of EuFAgSe and $EuFAg_{1-\delta}Te$ were measured with a SQUID-VSM magnetometer (MPMS 3) from Quantum Design in the temperature range 1.8 – 380 K and in fields up to 7 T. Molar magnetization has been calculated assuming that the content of the target phases in both samples is 97 % (due to the presence of impurities), and molar masses were corrected for the nonstoichiometry.

Mössbauer spectroscopy. The 21.53 keV transition of ^{151}Eu (65 MBq activity, 1% of the total source activity of the $^{151}Sm:EuF_3$ source) was used for the Mössbauer spectroscopic characterization of the $EuFAg_{1-\delta}Te$ sample. The measurements were performed at 78 K in transmission geometry using a continuous flow cryostat (Janis Research Co LLC). The source was kept at room temperature. The samples were filled in thin-walled PMMA containers and the optimized absorber thickness was calculated according to Long *et al*. [25]. The WinNormos for IGOR6 package [26] was used for fitting the spectra.

Table 6.1 Details of powder diffraction experiments

Target composition	EuFAgSe	EuFAgTe
Refined composition	EuFAgSe	$EuFAg_{1-\delta}Te$, $\delta = 0.051(4)$
Phase composition	Target phase + 2(1)%[1] EuOF + 1(1)%[1] EuSe	Target nonstoichiometric phase + 3(1)%[1] EuOF
Space group	*P4/nmm*, origin choice 1	
Z	2	
Cell parameters:		
a in Å	4.1542(1)	4.3255(1)
c in Å	9.2182(1)	9.5486(1)
V in Å^3	159.08(1)	178.65(1)
Calculated density in g/cm^3	7.42	7.45
Wavelength	$MoK\alpha_1$	
2θ range in deg	4 – 60	2 – 60
Data points / Overall parameters	3741/33	3820/37
Reflections / Structural parameters	176/7	193/8
R values:		
R_F	2.19	1.93
R_P	2.17	5.41
R_{wP}	3.40	7.22
χ^2	2.04	1.60
χ^2 (from Le Bail fit)	1.93	1.55

[1] Weight fraction

Table 6.2 Atomic coordinates and displacement parameters (in Å^2) in the structures of EuFAg*Ch* (*Ch* = Se, Te).

Atom	Position	*x/a*	*y/b*	*x/z*	U_{iso}
EuFAgSe					
Eu	2*c*	¼	¼	0.65242(8)	0.0089(2)
Se	2*c*	¼	¼	0.1968(1)	0.0163(4)
Ag	2*b*	¼	¾	½	0.0163(4)
F	2*a*	¼	¾	0	0.006(2)
$EuFAg_{1-\delta}Te$					
Eu	2*c*	¼	¼	0.63949(9)	0.0097(3)
Te	2*c*	¼	¼	0.1993(1)	0.0099(3)
Ag	2*b*	¼	¾	½	0.0168(6)
F	2*a*	¼	¾	0	0.027(3)

Computational details. Electronic structure calculations were performed on the Density Functional Theory (DFT) level using the pseudopotential projector augmented wave method (PAW) as implemented in the Vienna *ab initio* Simulation Package (VASP) [27, 28]. A Monckhorst-Pack *k*-point mesh of 16×16×8 was employed [29], and the energy cutoff was set at 500 *eV*. The energy convergence criterion for the calculations was set at 10^{-5} eV. The PBE exchange-correlation functional of the GGA-type was used in the PAW-based calculations [30]. In order to account for the *f*-orbitals of Eu^{2+}, a special potential for europium, supplied with the VASP package, was used, which places the localized *f*-orbitals into the core. This approach is well justified since the formal oxidation state of europium in the litharge slabs should closely match +2. The convergence of the total energy with respect to the *k*-point sets was checked. Experimental unit cell parameters and coordinates of atomic positions were taken as starting points for the calculations of Se- and Te-containing compounds (full Ag site occupancy was assumed for the latter), with atomic coordinates relaxed while retaining cell metrics. Atomic charges in the direct-space analysis were calculated according to Bader's QTAIM approach [31, 32]. The hypothetical structure of EuFAgS was obtained by unconstrained structure optimization using the VASP package and the unit cell parameters of SrFAgS (tetragonal, *P*4/*nmm*) as the starting model. The EuFAgS structure converged to values of a = 3.9905 Å, c = 8.7943 Å, z(Eu) = 0.1504, z(S) = 0.7035, which is, as expected, close to the respective values for SrFAgS, and the volume of the

optimized EuFAgS being only *ca.* 6% smaller than the experimentally determined value for its strontium analogue.

The Crystal Orbital Hamilton Population (COHP) analysis, based on the VASP calculations, was performed according to [33 – 35] using the Lobster 3.2.0 software package [36]. The COHP and DOS plots were done using the wxDragon package [37].

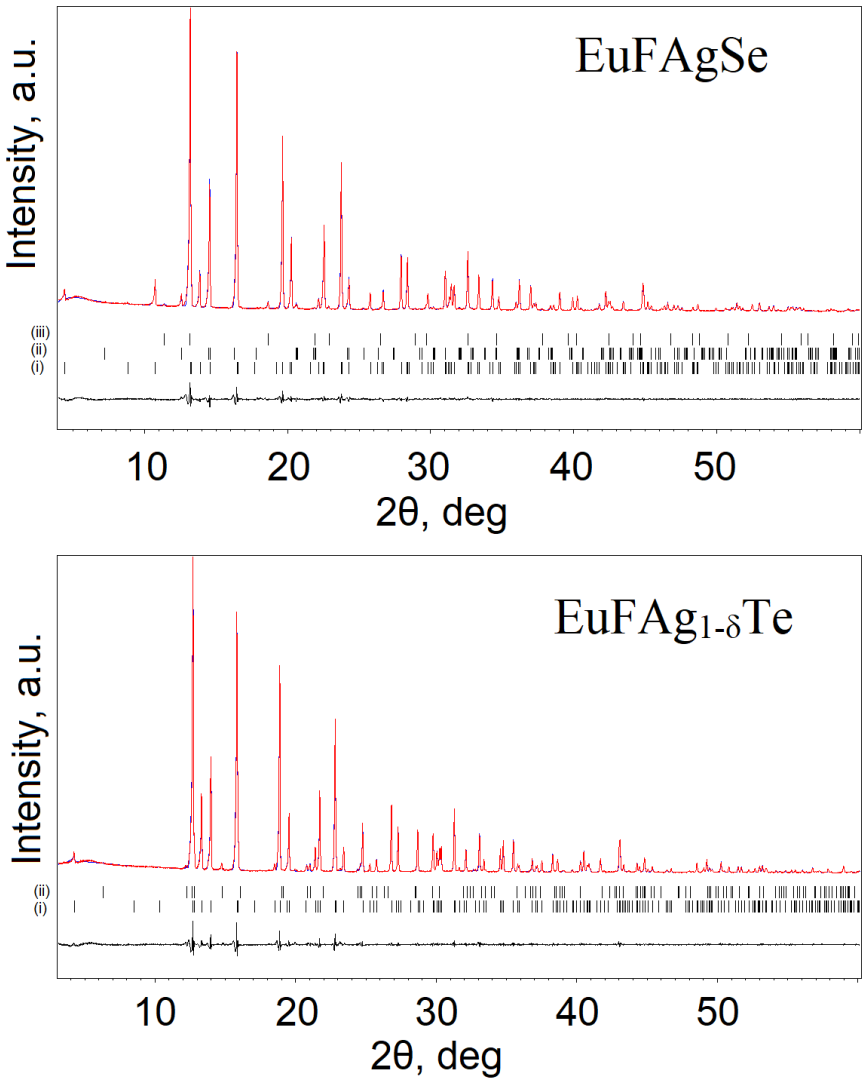

Figure 6.2 Final Rietveld refinement plots for EuFAgSe and $EuFAg_{1-\delta}Te$. i – the main phases, ii – EuOF, iii – EuSe.

Results and discussion

Synthesis. Assuming divalent europium the idealized formulas of both new compounds are $Eu^{2+}F^{-}Ag^{+}Ch^{2-}$. The use of EuF_3 as the fluorine source (by analogy to the preparation of other Eu^{2+} compounds [12, 13]) relies on the expected co-proportioning reaction between Eu^{III} and Eu^{0}, which is known to occur above ~ 870 K [38]. The effect of other constituents of the reaction mixture on this onset temperature is not known, but it is very close to the decomposition points of the target compound EuFAgSe at ~ 880 K. Hence, the temperature windows for a "one-pot" preparation are quite narrow (~ 850 – 880 K). For example, attempts to prepare EuFAgSe at 820 K yield mostly EuSe along with poorly crystalline by-products, while annealing just slightly above 880 K results in a mixture of the target phase with significant amounts of EuF_2, EuSe, and some other unidentified by-products. All attempts to synthesize EuFAgS have been unsuccessful so far. We could not fully avoid contamination of the samples with oxygen, similar to the previously reported EuFZn*Pn* (*Pn* = As and Sb) compounds [12], probably due to the extreme sensitivity of EuF_3 and intermediates to hydrolysis at elevated temperatures. For this reason, a multistep reaction is less preferred, as it can introduce additional impurities at each stage. Nevertheless, the fact that the synthetic environment for the EuFAg*Ch* (*Ch* = Se and Te) compounds is the same as for the EuFZn*Pn* [12] reassures that the oxygen content is low, with all oxygen confined to the minor EuOF impurity.

Crystal structures and stability. The crystal structures of the target compounds are very similar to those of the corresponding strontium fluoride chalcogenides, as is obvious from crystallographic data provided in SI and from the marginal difference between the ionic radii of Sr^{2+} and Eu^{2+}. Almost equal Ag – *Ch* distances among the Sr, Ba, and Eu compounds reflect very similar bonding patterns. As expected, the M – F distances elongate slightly and show rather similar increments upon replacing S by Se and Se by Te with an increasing mismatch between the FM_4 (*M* = Eu, Sr, or Ba) and TCh_4 tetrahedra (*T* = Cu or Ag). The pattern is nearly identical to those described for the isostructural Mg, Mn, Zn, and Cd pnictides [11 – 15]. The *M* – Ch distances are also transferable between the corresponding Cu and Ag compounds; in addition, the Eu – Te distances are very similar to those in the structurally related $Eu_{2/3}CuTe_2$ [39].

Table 6.3 Selected bond distances (in Å) and angles (in deg.) for the EuF*AgCh* (*Ch* = Se, Te) fluoride chalcogenides. α_2 and α_4 represent the two-fold and four-fold angles at the central atoms in tetrahedra.

	EuFAgSe	$EuFAg_{1-\delta}Te$
d(Eu – F)	2.508(1)	2.540(1)
d(Eu – Ch)	3.250(1)	3.424(1)
d(T – Ch)	2.758(1)	2.881(1)
α_2(EuFEu)	111.85(2)	115.87(1)
α_4(EuFEu)	108.29(1)	97.30(1)
α_2(ChTCh)	97.73(3)	105.96(1)
α_4(ChTCh)	115.64(2)	116.75(2)

Marginal size difference between Sr^{2+} and Eu^{2+} seems to be responsible for the instability of EuFAgS, whereas SrFAgS has been reported [17]. This pattern is also known for the valence-isoelectronic SrFZn*Pn* and EuFZn*Pn* compounds, where SrFZnP exists but its Eu analog does not [12], and experimental findings were corroborated by estimations of thermodynamic stability. EuFAgSe is less thermally stable than $EuFAg_{1-\delta}Te$. Thus, stability in this group of compounds decreases when going from heavier to lighter chalcogens. The active redox pair, $Eu^{2+}/Ag^{+} \leftrightarrow Eu^{3+}/Ag$, should also render Eu compounds less stable than their Sr analogs. Unfortunately, contrary to pnictides where the stability of *MFTPn* could be estimated against the MF_2 + MT_2Pn_2 "decomposition products", it is difficult to choose appropriate *existing* alternative products and provide realistic estimates of thermodynamic stability in the Eu case.

Similar to SmFCuSe [19], the new compounds EuFAgSe and $EuFAg_{1-\delta}Te$ give strong evidence that the ZrCuSiAs structure type can accommodate several redox-unstable pairs, provided that they are chemically and spatially separated. When incorporated into the anionic part of the structure, silver atoms bear only a small positive charge and should be less prone to oxidizing Eu.

Diffuse reflectance spectroscopy. As-prepared powders of EuFAgSe and $EuFAg_{1-\delta}Te$ are orange or yellowish, suggesting that these compounds are semiconductors with optical band gaps of 2 - 2.2 eV. Indeed, the diffuse reflectance spectra shown in **Figure 6.3** reveal optical band gaps of 2.11 eV and 2.26 eV. These values are also consistent with those reported for EuFCu*Ch*, SrFCu*Ch*, and LaOAg*Ch* [17], all of them having band gaps of 2 – 3 eV and red, orange, or yellow colors.

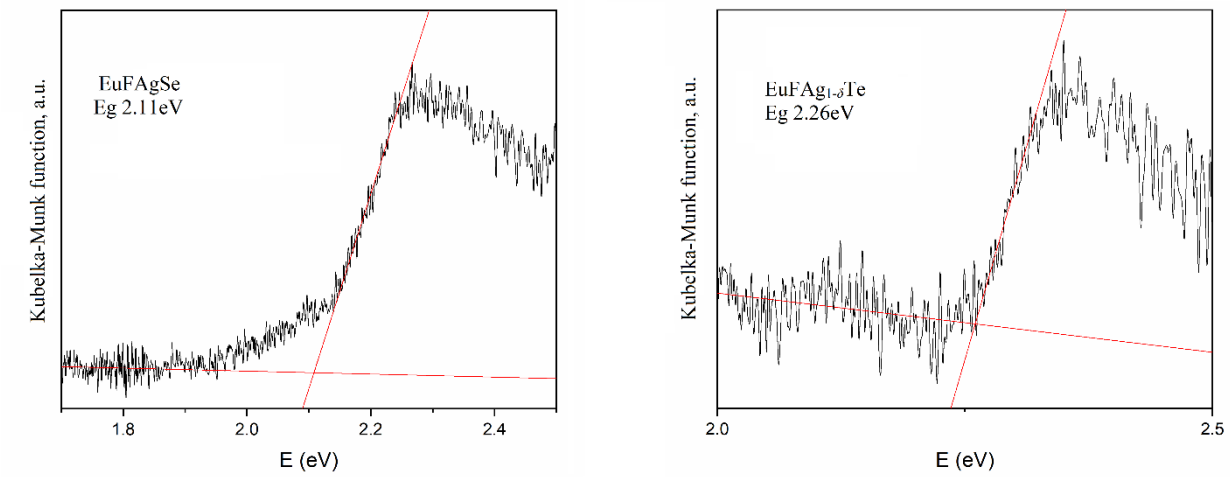

Figure 6.3 Diffuse reflectance spectrum of EuFAgSe (left) and $EuFAg_{1-\delta}Te$ (right).

Electronic structure. Total (TDOS) and projected (PDOS) densities of states near the Fermi level for the experimental EuFAgSe and EuFAgTe structures, as well as for the simulated EuFAgS structure, are shown in **Figure 6.4**. The calculations for EuFAgTe were performed assuming full occupancy of the Ag position.

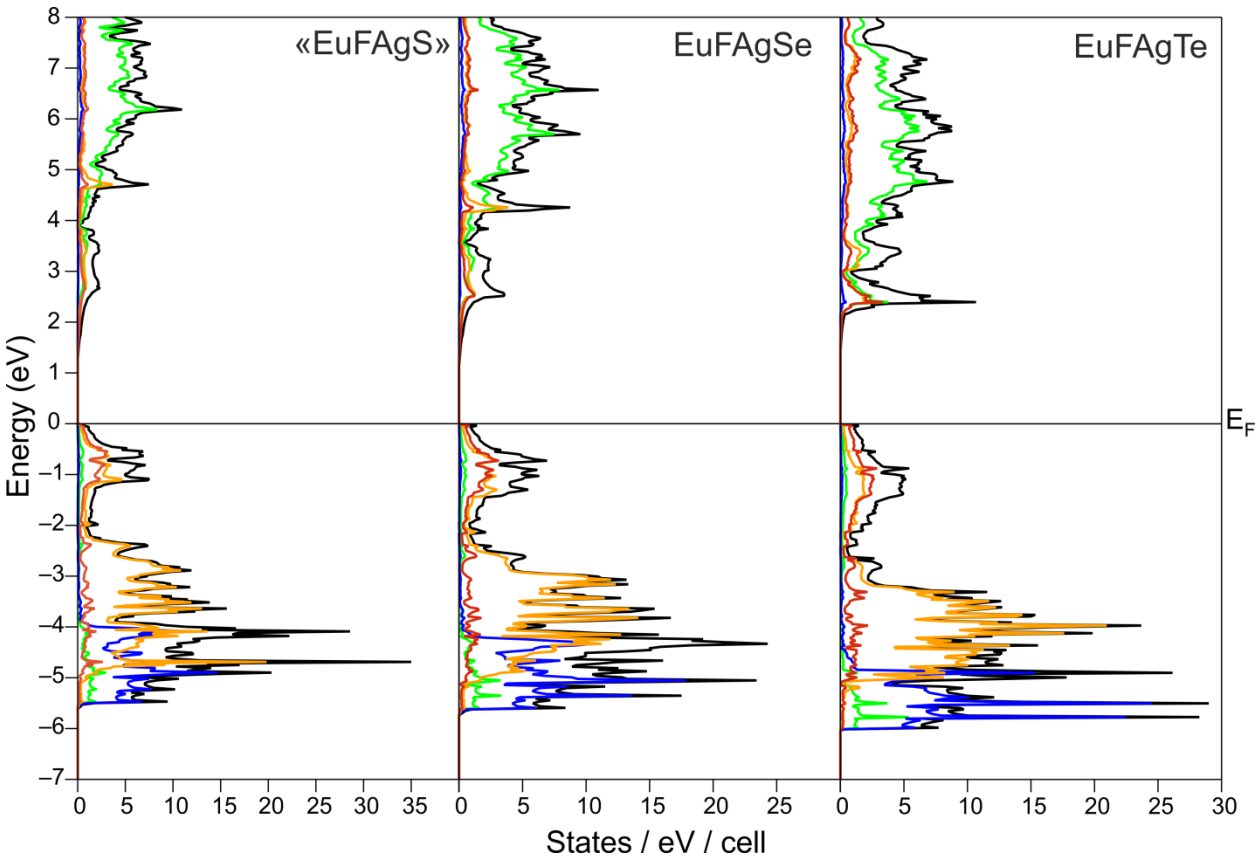

Figure 6.4 Total and projected DOS (black) for the EuFAgCh series, left to right: hypothetical EuFAgS, EuFAgSe, EuFAgTe. The green line denotes the Eu PDOS, blue – fluorine PDOS, orange – silver PDOS, and red – chalcogen PDOS.

As seen from the DOS plots, the electronic structures of the EuFAg*Ch* series are fully representative of the other compounds of this type, *e.g.*, the EuFZn*Pn* and EuFMn*Pn* series. All the compounds are semiconducting, with band gaps slightly below 2 eV. For the existing compounds, the calculated band gaps of 1.71 eV (EuFAgSe) and 1.95 eV ($EuFAg_{1-\delta}Te$) agree well with the experimentally determined values. Their slight underestimation (by 0.4 and 0.3 eV, respectively) is typical of the DFT approach in local approximations, but the trend of the increasing band gap between the selenide and telluride is reproduced correctly. The main contributions to the top of the valence band are from silver *d*-electrons and chalcogen *p*-electrons, while fluorine *p*-states are localized way down the energy scale. Small europium *d*-electron contributions are also seen near the top of the valence band, suggesting the possibility of weak covalent Eu – *Ch* interactions. The very bottom of the conduction band is mostly formed by silver and chalcogen *p*-states, with a small contribution from europium *d*-states. DOS plots for hypothetical EuFAgS are consistent with the ones observed for the experimentally found compounds and show no anomalies.

Atomic charges calculated according to the Bader's QTAIM approach are: Eu +1.60, F -0.85, Ag +0.28, S -1.03 (EuFAgS); Eu +1.57, F -0.85, Ag +0.20, Se -0.92 (EuFAgSe); Eu +1.55, F -0.86, Ag +0.16, Te -0.75 (EuFAgTe). As seen from the charges, the Eu – F bonds in the litharge-type fragments remain essentially ionic, while the Ag – *Ch* bonds become less polar upon going from S to Te. The slightly reduced positive charge on europium is, most likely, due to a partial electron transfer from the Ag – *Ch* fragments.

In order to get more insight into the bonding scheme and interactions, we calculated partial Crystal Orbital Hamilton Population (pCOHP) for Eu – F, Eu – *Ch*, and Ag – *Ch* interactions, as well as their integrals from -10 eV up to the Fermi level (IpCOHP), see **Figure 6.5** and **Table 6.4**. The trends are in agreement with the DOS and charge density analysis. The Ag – *Ch* contacts provide major contribution to the covalent bonding interactions below the Fermi level, while the Eu – F and Eu – *Ch* contacts are mostly non-bonding or weakly bonding/anti-bonding. The absence of anti-bonding states at the Fermi level or above indicates that the bonding scheme in all compounds has no inherent instabilities

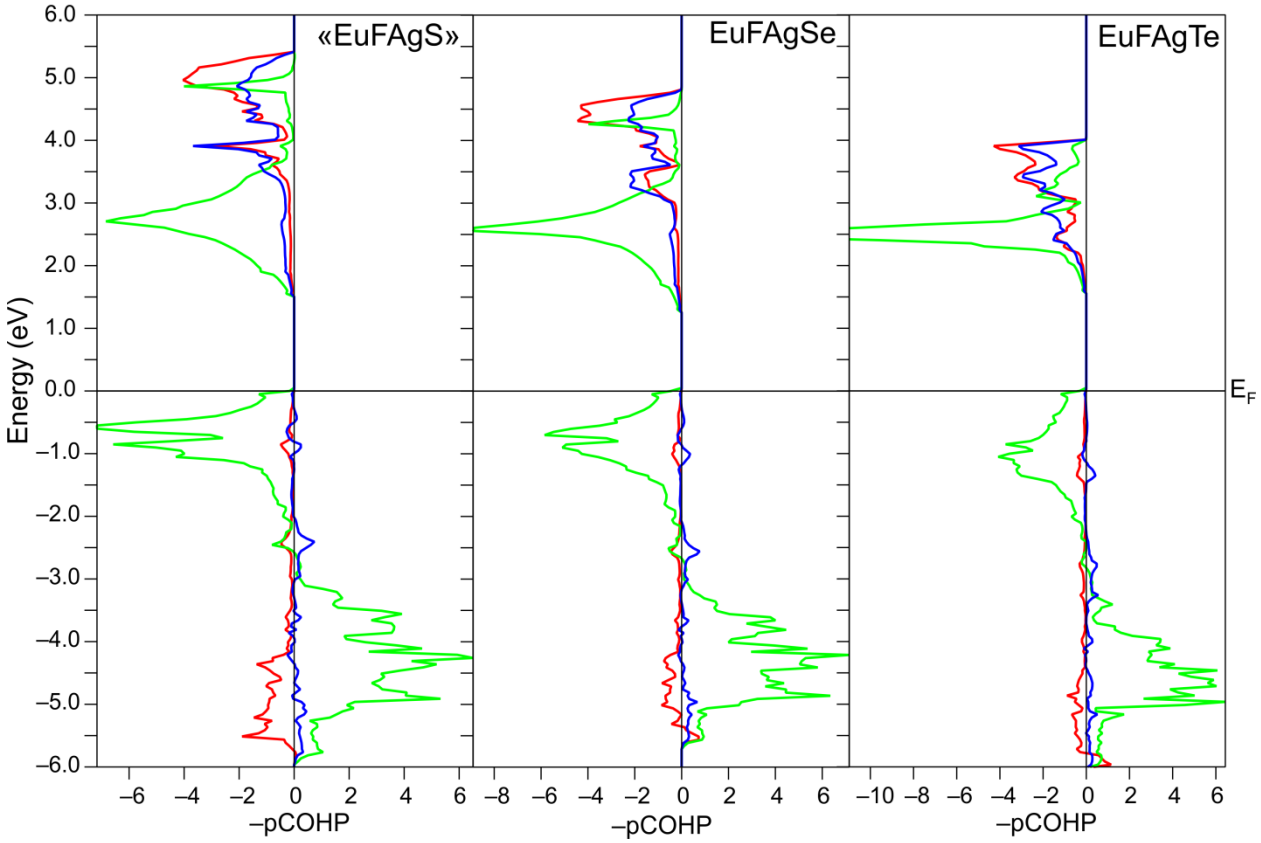

Figure 6.5 The plots of −pCOHP for EuFAg*Ch* (*Ch* = S (simulated), Se, Te). The Ag − *Ch* interactions are shown in green, Eu − *Ch* in blue, and Eu − F in red.

Table 6.4 Integrated partial COHP (-IpCOHP, eV/bond) in EuFAg*Ch* (*Ch* = S, Se, Te).

Bond	EuFAgS, Simulated	EuFAgSe	EuFAgTe
Eu − F	0.45	0.43	0.40
Eu − Ch	0.40	0.40	0.39
Ag − Ch	0.74	0.74	0.76

This is supported by the –IpCOHP data (see **Table 6.4**), which can be taken as an indication of a relative covalent bond strength. As seen from the **Table 6.4**, the strongest covalency is calculated for the Ag – *Ch* bond, which has its maximum for the Ag – Te interactions. The picture shows no drastic differences between hypothetical EuFAgS and synthesized EuFAg*Ch* (*Ch* = Se, Te). Yet, if we look closely at the anti-bonding Ag – *Ch* states below the Fermi level, we can see that in the case of *Ch* = S they are much more pronounced than in the two other compounds, being almost twice as large as for *Ch* = Te. This might be taken as an indication that the S-containing structure is the least stable of the three. The difference does not appear to be dramatic; however, when dealing with marginal stability, this might be enough.

Magnetic properties. The temperature dependence of the magnetic susceptibility for EuFAgSe and $EuFAg_{1-\delta}Te$ measured in different applied fields, as well as magnetization curves measured at a constant temperature, are shown in **Figures 6.6** and **6.7**. The high-temperature parts of the magnetic susceptibility for both EuFAgSe and $EuFAg_{1-\delta}Te$ can be approximated by a Curie-Weiss law, yielding μ_{eff} = 7.78 μ_B / θ_{CW} = -4.7 K and μ_{eff} = 7.45 μ_B / θ_{CW} = -7.8 K. In both cases, the Weiss temperatures are low, indicating rather weak interactions between the magnetic ions. Indeed, $EuFAg_{1-\delta}Te$ behaves as paramagnet down to the lowest measured temperature of 1.8 K, whereas EuFAgSe exhibits a small anomaly at ~ 5 K, which is nearly suppressed already at 0.1 T. Similar effects have been observed in the EuF*TPn* compounds [12, 13] and suggested to be extrinsic by heat-capacity data. Magnetization curves measured at 1.8 K reveal proximity to saturation in a 7 T field, yielding M_S = 6.59 μ_B/f.u. for EuFAgSe and M_S = 5.87 μ_B/f.u. for $EuFAg_{1-\delta}$ Te. The values of magnetic moments are reproducible for the samples from different batches of these compounds.

In both structures, only Eu^{2+} is expected to contribute to the paramagnetic response due to its non-zero magnetic moment in the ground-state $4f^7$ (J = 7/2) electronic configuration with the effective paramagnetic moment of 7.94 μ_B and saturated moment of 7 μ_B. In contrast, Eu^{3+} ($4f^6$, J = 0) would show pure van-Vleck paramagnetism and give only a small contribution compared to Eu^{2+} [40]. From the magnetization data, the Eu^{2+} fraction can be estimated as $(\frac{\mu_{eff}}{7.94})^2$. The effective paramagnetic moment of μ_{eff} = 7.78 μ_B in EuFAgSe corresponds to just 4% reduction and is in a good agreement with the values for the pure Eu^{2+} in other compounds [41, 42]. The magnetic moment obtained for $EuFAg_{1-\delta}Te$ is lower and clearly corresponds to the mixed-valence Eu^{2+}/Eu^{3+} state with ~ 12 % of Eu^{3+} in the $EuFAg_{1-\delta}Te$.

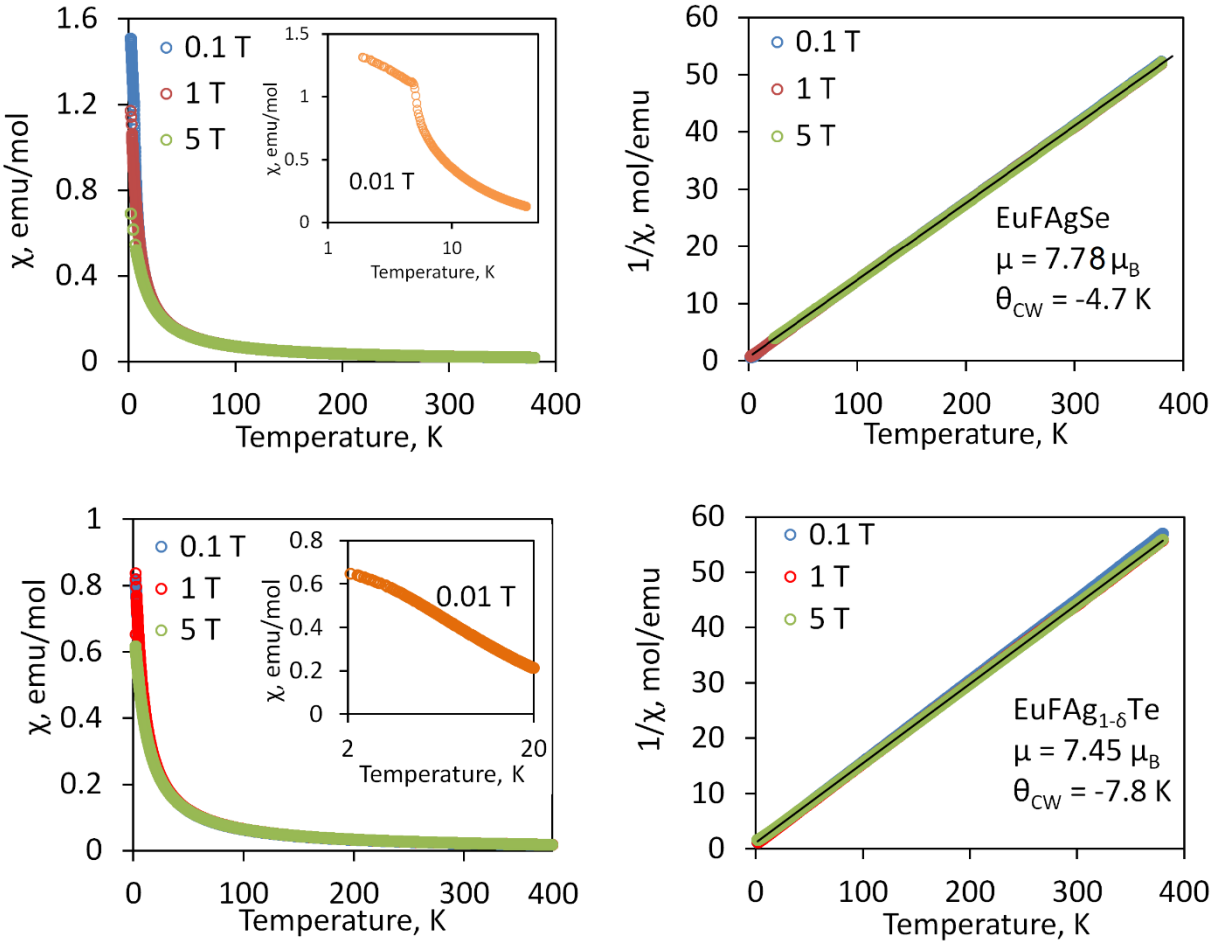

Figure 6.6 Temperature dependencies of the magnetic susceptibility (left) and inverse magnetic susceptibility (right) for EuFAgSe (top) and $EuFAg_{1-\delta}Te$ (bottom).

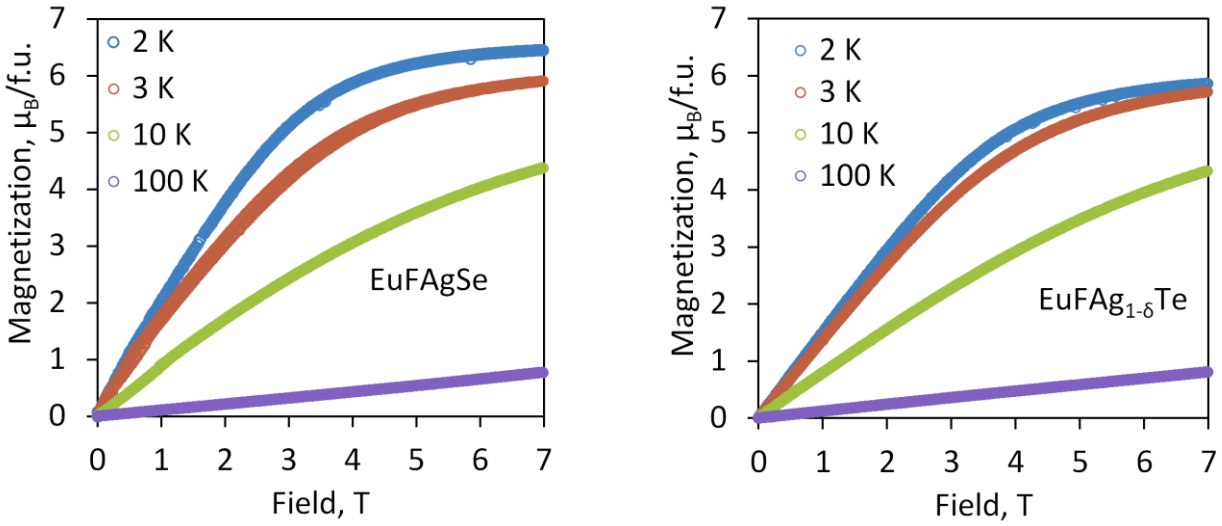

Figure 6.7 Magnetization *vs.* field curves for EuFAgSe and $EuFAg_{1-\delta}Te$.

The ^{151}Eu Mössbauer spectra for the $EuFAg_{1-\delta}Te$ is shown in **Figure 6.8** and summarized in **Table 6.5**. It is easily fit by a superposition of two signals, the stronger one resulting from Eu^{2+} (as the main component) and the weaker one from Eu^{3+}. $EuFAg_{1-\delta}Te$ exhibits quite negative isomer shift values manifesting the predominantly ionic bonding character in the $[Eu_2F_2]^{2+}$ layers. The isomer shift values of EuF_2 (–13.58 mm/s), EuSe (–12.06 mm/s), and EuTe (–12.28 mm/s) lie in a similar range [43, 44]. The quadrupole splitting parameters account for the non-cubic site symmetry (4*mm*) of the europium atoms.

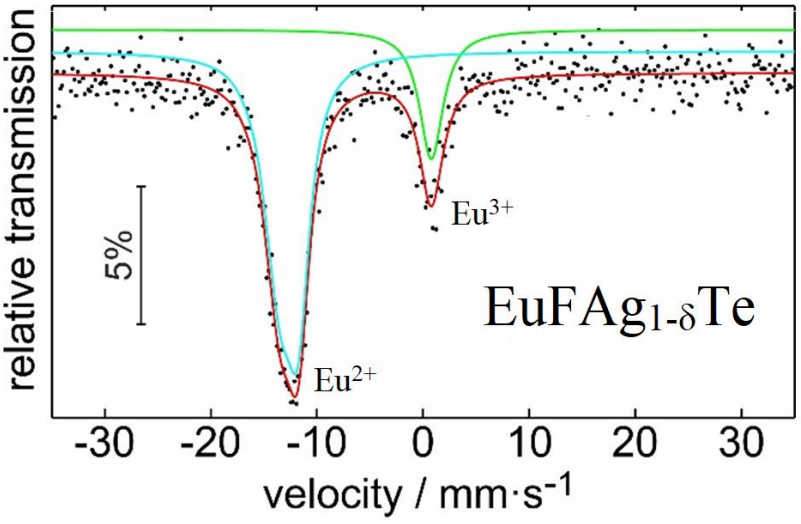

Figure 6.8 Experimental and simulated ^{151}Eu Mössbauer spectra of $EuFAg_{1-\delta}Te$ at 78 K. Experimental points are black, Eu^{2+} contribution is drawn in cyan, Eu^{3+} is green, and their sum is red.

Table 6.5 Fitting parameters of ^{151}Eu Mössbauer spectroscopic measurements of $EuFAg_{1-\delta}Te$ (78 K data). δ – isomer shift, ΔE_Q – electric quadrupole splitting, Γ – experimental line width. The isomer shifts are given relative to EuF_3.

Compound	Valence	δ(mm·s^{-1})	ΔE_Q (mm·s^{-1})	Γ(mm·s^{-1})	area (%)
$EuFAg_{1-\delta}Te$	2+	–12.74(4)	4.7(2)	2.6(1)	78(1)
	3+	0.77(7)	0*	2.7(2)	22(1)

* Parameters were kept fixed during the fitting procedure.

The non-stoichiometry and valence fluctuations rise a question on the mechanism of charge compensation in the semiconducting $EuFAg_{1-\delta}Te$ with just one crystallographic position of Eu. One might suggest an extrinsic origin of the Eu^{3+} contribution. A very similar pattern has been observed in the stoichiometric EuFCu*Ch* (*Ch* = S and Se; magnetic properties for *Ch* = Te were not reported), where paramagnetic effective moments are μ = 7.69 μ_B for *Ch* = S and μ = 7.42 μ_B for *Ch* = Se, *i.e.*, they also deviate from the theoretical values for pure Eu^{2+}, but the origin of this discrepancy has not been explored. The areas under the Mössbauer spectral lines are approximately proportional to the content of different valence forms. Part of the Eu^{3+} signal observed in the ^{151}Eu Mössbauer spectroscopic measurements should be ascribed to EuOF (~ 3 weight % corresponds to ~ 6 molar %), which together with 12 % from the magnetic measurements, gives 18 %. The latter value is in a fair agreement with 22 % from the Mössbauer data. Thus, there is clearly the Eu^{3+} contribution from the main phase, where a notable Ag-deficiency is also observed. Thus, we infer that the competitive red-ox process $Eu^{2+}/Ag^{+} \leftrightarrow Eu^{3+}/Ag$ should be partially responsible for the charge balance. On the other hand, charge compensation due to the coexistence of several types of defects has been proposed for Bi$O M_{1-\delta}Ch$ (*M* = Cu and Ag [45]), where non-stoichiometry occurs without a possibility of chemically plausible red-ox processes. $EuFAg_{1-\delta}Te$ prepared in our work may combine several mechanisms, and the same but to a lesser extent can belong to EuFAgSe. Detailed structural and magnetic studies using dedicated tools might be necessary to explain the observed effects, which is beyond the scope of the current work.

Conclusions

Despite a long history of the ZrCuSiAs structure type and more than 200 reported compounds, we succeeded in synthesizing two new representatives of this family. Our observation, along with the recently reported FeAs 1111 superconductors (ThNFeAs [46] and SmFFeAs [20]) as well as transition-metal-free representatives BaFMg*Pn* (*Pn* = P, As, Sb and Bi) [15], show that the full capacity of this structure type is not yet achieved. The crystal structures of the new compounds obey general structural and stability trends for this class. An interesting feature of the $EuFAg_{1-\delta}Te$ is that its Ag-site is partly vacant. Optical properties are determined by semiconducting $[Ag_2Ch_2]^{2-}$ layers, whereas the $[Eu_2F_2]^{2+}$ layers are predominantly ionic. According to magnetization measurements and ^{151}Eu Mössbauer spectroscopy data, europium in both cases is in a predominantly divalent form with a possibility of a mixed-valent state Eu^{2+}/Eu^{3+} in the $EuFAg_{1-\delta}Te$.

Supporting information

Table 6.S1. Selected bond distances (in Å) and angles (in deg.) for the M^{2+}F*TCh* (*T* = Cu, Ag; *Ch* = S, Se, Te) fluoride chalcogenides (taken from the literature).

	SrFCuS	**SrFCuSe**	**SrFCuTe**	**SrFAgS**	**SrFAgSe**	**SrFAgTe**
d(Sr – F)	2.445(1)	2.476(1)	2.515(1)	2.468(2)	2.503(1)	2.543(1)
d(Sr – Ch)	3.144(2)	3.239(2)	3.427(1)	3.190(3)	3.272(1)	3.456(1)
d(T – Ch)	2.430(2)	2.531(2)	2.671(1)	2.699(5)	2.761(1)	2.871(1)
α_2(SrFSr)	108.00(2)	110.26(4)	115.32(7)	108.88(5)	112.64(5)	117.1(1)
α_4(SrFSr)	110.21(2)	109.08(4)	106.63(3)	110.67(5)	107.91(2)	105.79(5)
α_2(ChTCh)	108.95(5)	106.75(5)	105.39(5)	97.50(1)	97.92(4)	98.19(5)
α_4(ChTCh)	109.73(5)	110.85(5)	111.55(3)	115.77(1)	115.54(2)	115.39(3)
	BaFCuS	**BaFCuSe**	**BaFCuTe**	**BaFAgS**	**BaFAgSe**	**BaFAgTe**
d(Ba – F)	2.607(1)	2.620(1)	2.652(1)	2.626(1)	2.642(1)	2.668(1)
d(Ba – Ch)	3.305(2)	3.387(1)	3.561(1)	3.337(2)	3.422(1)	3.586(1)
d(T – Ch)	2.464(3)	2.565(1)	2.694(1)	2.679(2)	2.753(1)	2.879(1)
α_2(BaFBa)	104.50(4)	108.01(3)	113.25(3)	107.69(2)	110.65(3)	116.15(1)
α_4(BaFBa)	112.01(2)	110.21(3)	107.61(3)	110.37(1)	108.88(1)	106.24(1)
α_2(ChTCh)	107.4(1)	111.44(3)	110.62(3)	104.65(8)	104.22(5)	103.69(1)
α_4(ChTCh)	113.6(2)	108.50(3)	108.90(3)	111.93(4)	112.16(2)	112.43(1)
	EuFCuS	**EuFCuSe**	**EuFCuTe**	**EuFAgS**	**EuFAgSe**	**EuFAg$_{1-\delta}$Te**
d(Eu – F)	2.465(2)	2.488(2)	2.520(1)	-	2.508(1)	2.540(1)
d(Eu – Ch)	3.134(2)	3.223(2)	3.393(1)	-	3.250(1)	3.424(1)
d(T – Ch)	2.434(1)	2.521(1)	2.666(1)	-	2.758(1)	2.881(1)
α_2(EuFEu)	106.44(5)	109.21(5)	114.40(1)	-	111.85(2)	115.87(1)
α_4(EuFEu)	111.01(5)	109.60(5)	107.06(1)	-	108.29(1)	97.30(1)
α_2(ChTCh)	108.46(2)	107.15(3)	105.27(1)	-	97.73(3)	105.96(1)
α_4(ChTCh)	109.98(2)	110.64(3)	111.61(1)	-	115.64(2)	116.75(2)

This chapter has been published in a peer-reviewed journal *Dalton Transaction* of the publisher The Royal Society of Chemistry (DOI 10.1039/D0DT01504K). The crystal structures of the title compounds are deposited in ICSD under reference number 1937807 and 1937849.

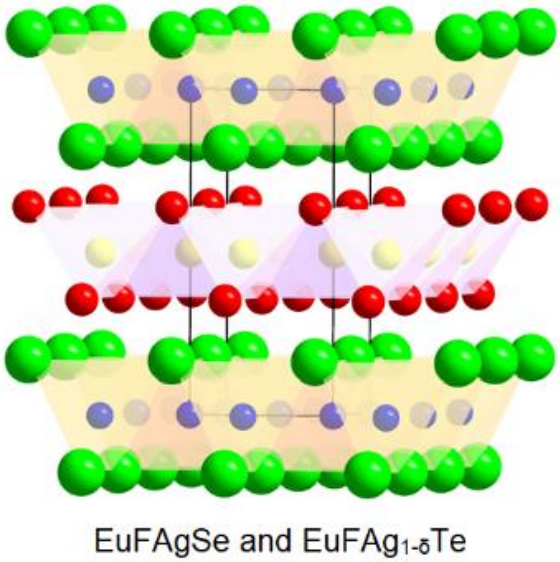

Figure 6.TOC Graphical abstract to the paper entitled "Synthesis, electronic structure and physical properties of two new layered compounds, EuFAgSe and $EuFAg_{1-\delta}Te$, featuring the active redox pair Eu^{2+}/Ag^{+}".

Several other people also contributed to this work:

1. Alexander A. Tsirlin, Lukas Heletta, Steffen Klenner, Rainer Pöttgen, performed magnetic and Mössbauer measurements, discussed the results, and improved the manuscript.
2. Dmitri O. Charkin and Alexey N. Kuznetsov performed calculations, contributed to the discussion of the crystallographic part, and improved the manuscript.
3. Andrei V. Shevelkov and Arno Pfitzner contributed to the discussion of the results, provided the equipment and lab space, and improved the manuscript.
4. Igor V. Plokhikh performed synthesis, designed calculations, and physical measurements, and wrote the draft of the manuscript.

References

[1] R. Pöttgen, D. Johrendt. Materials with ZrCuSiAs-type structure. *Z. Naturforsch.* **2008**, *63b*, 1135.

[2] D. Johrendt, R. Pöttgen. Pnictide oxides: a new class of high-T_C superconductors. *Angew. Chem.* **2008**, *47*, 4782.

[3] Y. Kamihara, H. Hiramatsu, M. Hirano, R. Kawamura, H. Yanagi, T. Kamiya, H. Hosono. Iron-based layered superconductor: LaOFeP. *J. Am. Chem. Soc.* **2006**, *128*, 10012.

[4] Y. Kamihara, T. Watanabe, M. Hirano, H. Hosono. Iron-based layered superconductor $La[O_{1-x}F_x]FeAs$ (x = 0.05–0.12) with T_C = 26 K. *J. Am. Chem. Soc.* **2008**, *130*, 3296.

[5] S. Muir, M.A. Subramanian, ZrCuSiAs type layered oxypnictides: A bird's eye view of LnM*Pn*O compositions. *Prog. Solid State Chem.* **2012**, *40*, 41.

[5] S. J. Clarke, P. Adamson, S. J. C. Herkelrath, O. J. Rutt, D. R. Parker, M. J. Pitcher, C. F. Smura. Structures, physical properties, and chemistry of layered oxychalcogenides and oxypnictides. *Inorg. Chem.* **2008**, *47*, 8473.

[6] G. Just, P. Paufler. On the coordination of $ThCr_2Si_2$ ($BaAl_4$-type compounds within the field of free parameters. *J. Alloys Compd.* **1996**, *232*, 1.

[7] D. O. Charkin, X. N. Zolotova. A crystallographic re-investigation of Cu_2Sb-related binary, ternary, and quaternary structures: how many structure types can exist upon the same topology of a unit cell? *Crystallogr. Rev.* **2007**, *13*, 201.

[8] H. Hosono, K. Tanabe, E. Takayama-Muromachi, H. Kageyama, S. Yamanaka, H. Kumakura, M. Nahara, H. Hiramatsu, S. Fujitsu. Exploration of new superconductors and functional materials and fabrication of superconducting tapes and wires of iron pnictides. *Sci. Technol. Adv. Mater.* **2015**, *16*, 033503-1-86.

[9] H. Kabbour, L. Cario, F. Boucher. Rational design of new inorganic compounds with the ZrSiCuAs structure type using 2D building blocks. *J. Mater. Chem.* **2005**, *15*, 3525.

[10] X. Zhu, F. Han, P. Cheng, G. Mu, B. Shen, B. Zeng, H. Wen. Parent phase and superconductors in the fluorine derivative family. Physica C **2009**, *469*, 381 – 384.

[11] D. O. Charkin, I. V. Plokhikh, A. N. Kuznetsov, S. M. Kazakov. BaFAlSi and BaFAlGe: First transition metal-free LaOAgS-type fluoride tetrelides. *J. Alloys Compd*. **2015**, *627*, 451.

[12] I. V. Plokhikh, D. O. Charkin, V. Yu. Verchenko, A. N. Kuznetsov, S. M. Kazakov, A. A. Tsirlin, A. V. Shevelkov. Structural and thermodynamic stability of the "1111"structure type: a case study of the EuFZn*Pn* series. *Inorg. Chem.* **2016**, *55*, 12409.

[13] I. V. Plokhikh, D. O. Charkin, V. Yu. Verchenko, A. N. Kuznetsov, S. M. Kazakov, A. A. Tsirlin, A. V. Shevelkov. Synthesis, crystal structure and physical properties of europium –

manganese fluoride pnictides, EuMn*Pn*F (*Pn* = P, As, Sb). *J. Solid State Chem.* **2018**, *258*, 682.

[14] D. O. Charkin, A. V. Urmanov, I. V. Plokhikh, A. D. Korshunov, A. N. Kuznetsov, S. M. Kazakov. Synthesis and crystal structures of novel LaOAgS-type alkaline earth – zinc, manganese, and cadmium fluoride pnictides. *J. Alloys Compd.* **2014**, *585*, 644.

[15] I. V. Plokhikh, A. N. Kuznetsov, D. O. Charkin, A. V. Shevelkov, A. Pfitzner. Layered Compounds BaFMg*Pn* (*Pn* = P, As, Sb, and Bi), Transition-Metal-Free Representatives of the 1111 Structure Type. *Inorg. Chem.* **2019**, *58*, 3435.

[16] D. O.Charkin, A. V. Urmanov, S. M. Kazakov. Preparation and crystal structures of novel LaOAgS-type copper and silver fluoride chalcogenides. *J. Alloys Compd.* **2012**, *516*, 134.

[17] E. Motomitsu, H. Yanagi, T. Kamiya, M. Hirano, H. Hosono. Synthesis, structure and physical properties of layered semiconductors *M*CuF*Ch* (*M* = Sr, Eu, *Ch* = S, Se). *J. Solid State Chem.* **2006**, *179*, 1668.

[18] B. Saparov, D. J. Singh, V. O. Garlea, A. S. Sefat. Crystal, magnetic, and electronic structures, and properties of new BaMn*Pn*F (*Pn*= As, Sb, Bi). *Sci. Rep.* **2013**, *3*, 2154.

[19] H. Grossholz, T. Schleid. CuSmFSe: Ein Kupfer(I)-Samarium(II)-Fluoridselenid mit aufgefüllter PbFCl-Struktur *Z. Anorg. Allg. Chem.* **2002**, *628*, 2169.

[20] D. Lin, H.-S. Xu, J. Luo, H. Huang, Y. Lu, K. Tang. A self-doped oxygen-free high-critical-temperature (High-Tc) superconductor: SmFFeAs. *Inorg. Chem.* **2019**, *58*, 15401.

[21] O. Janka, T. Schleid. CuEuFTe und AgBaFTe: Zwei neue Münzmetall(I)-Fluorid-Telluride mit unterschiedlichen M^{2+}-Kationen. *Z. Anorg. Allg. Chem.* **2008**, *634*, 2048.

[22] B. Gerke, C. Schwickert, S. S. Stoyko, M. Khatun, A. Mar, R. Pöttgen. Magnetic hyperfinefield splitting in $EuAg_4As_2$ and $EuAg_4Sb_2$. *Solid State Sci.* **2013**, *20*, 65.

[23] R. D. Shannon. Revised effective ionic radii and systematic studies of interatomic distances in halides and chalcogenides. *Acta Crystallogr.* **1976**, *A 32*, 751.

[24] V. Petricek, M. Dusek, L. Palatinus. Crystallographic computing system JANA2006: general features. *Z. Kristallogr.* **2014**, *229*, 345.

[25] G. J. Long, T. E. Cranshaw, G. Longworth. The ideal Mössbauer effect absorber thicknesses. *Moessbauer Eff. Ref. Data J.* **1983**, *6*, 42.

[26] R. A. Brand, WINNORMOS for IGOR6, version for IGOR 6.2 or above: 22.02.2017, Universität Duisburg, Duisburg, Germany, **2017**.

[27] G. Kresse, J. Furthmüller. Vienna Ab initio simulation package (VASP), v.5.4.4, http://www.vasp.at/.

[28] G. Kresse, D. Joubert. From ultrasoft pseudopotentials to the projector augmented-wave method. *Phys. Rev. B* **1999**, *59*, 1758 – 1775.

[29] H. J. Monckhorst, J. D. Pack. Special points for Brillouin-zone integrations. *Phys. Rev. B* **1976**, *13*, 5188.

[30] J. P. Perdew, K. Burke, M. Ernzerhof. Generalized gradient approximation made simple. *Phys. Rev. Lett.* **1996**, *77*, 3865 – 3868.

[31] R. F. W. Bader. Atoms in Molecules: a Quantum Theory, Oxford University Press, Oxford, **1990**.

[32] M. Yu, D. R. Trinkle. Accurate and efficient algorithm for Bader charge integration, *J. Chem. Phys.* **2011**, *134*, 064111.

[33] R. Dronskowski, P. E. Blöchl. Crystal orbital Hamilton populations (COHP): energy-resolved visualization of chemical bonding in solids based on density-functional calculations. *J. Chem. Phys.* **1993**, *97*, 8617.

[34] V. L. Deringer, A. L. Tchougreeff, R. Dronskowski. Crystal orbital Hamilton population (COHP) analysis as projected from plane-wave basis sets. *J. Phys. Chem. A,* **2011,** *115*, 5461.

[35] S. Maintz, V.L. Deringer, A.L. Tchougreeff, R. Dronskowski. Analytic projection from plane-wave and PAW wavefunctions and application to chemical-bonding analysis in solids. *J. Comput. Chem.* **2013**, *34*, 2557.

[36] S. Maintz, V.L. Deringer, A.L. Tchougréeff, R. Dronskowski. LOBSTER: A tool to extract chemical bonding from plane-wave based DFT. *J. Comput. Chem.* **2016**, *37*, 1030.

[37] *wxDragon* 2.1.7. http://www.wxdragon.de.

[38] O. Greis. Über neue Verbindungen in den Systemen EuF_2–EuF_3 und SrF_2–EuF_3. *Z. Anorg. Allg. Chem.* **1978**, *441*, 39.

[39] R. Patschke, P. Brazis, C. R. Kannewurf and M. G. Kanatzidis. $Cu_{0.66}EuTe_2$, KCu_2EuTe_4 and $Na_{0.2}Ag_{2.8}EuTe_4$: compounds with modulated square Te nets. *J. Mater. Chem.* **1999**, *9*, 2293.

[40] H. Lueken, Magnetochemie, Teubner Studienbücher Chemie, Leipzig, **1999**.

[41] D. H. Ryan, J. M. Cadogan. ^{151}Eu hyperfine fields, isomer shifts and moments in Eu-based EuT_2X_2 intermetallic compounds. *Hyperfine Interact.* **2014**, *226*, 243.

[42] S. Klenner, Z. Zhang, R. Pöttgen, L. Li. Magnetic and magnetocaloric properties of the equiatomic europium intermetallics EuAgZn, EuAgCd, EuPtZn and EuAuCd. *Intermetallics,* **2020**, *120*, 106765.

[43] G. Gerth, P. Kienle, K. Luchner. Chemical effects on the isomer shift in ^{151}Eu. *Phys. Lett. A* **1968**, *27*, 557.

[44] G. K. Shenoy, F. E. Wagner (Eds.). Mössbauer Isomer Shifts, North Holland Publishing, Amsterdam, **1978**.

[45] J. Gamon, D. Giaume, G. Wallez, J.-B. Labégorre, O. I. Lebedev, R. Al Rahal, Al Orabi, S. Haller, T. Le Mercier, E. Guilmeau, A. Maignan, P. Barboux. Substituting copper with silver in the Bi*MOCh* layered compounds (*M* = Cu or Ag; *Ch* = S, Se, or Te): crystal, electronic structure, and optoelectronic properties. *Chem. Mater.* **2018**, *30*, 549.

[46] C. Wang, Z.-C. Wang, Y.-X. Mei, Y.-K. Li, L. Li, Z.-T. Tang, Y. Liu, P. Zhang, H.-F. Zhai, Z.-A. Xu, and G.-H. Cao. A new ZrCuSiAs-type superconductor: ThFeAsN. *J. Am. Chem. Soc.* **2016**, *138*, 2170.

7 Magnetic structure of Eu*T*AsF (*T* = Zn, Mn and Fe) *via* neutron powder diffraction

Abstract

We report a neutron powder diffraction study of Eu^{2+} ($4f^7$) magnetic structures in three compounds (Eu*T*AsF, *T* = Zn, Mn, and Fe) belonging to the 1111 structure type. They all undergo an antiferromagnetic ordering in the Eu^{2+} sublattice at 2 – 4 K, as follows from physical properties measurements reported previously. EuZnAsF contains a single magnetic ion Eu^{2+} and has T_N = 2.6 K. Magnetic reflections can be described by a propagation vector *k* = ½ ½ 0, and the ordering pattern is orthorhombic (P_cmab magnetic space group) with magnetic moments forming ferromagnetic stripes stacked to each other in an antiferromagnetic manner. Up to high temperatures, magnetic moments of Mn^{2+} in EuMn*Pn*F (*Pn* = P and As) are ordered antiferromagnetically. Corresponding magnetic reflections obey propagation vector *k* = 0 0 ½; the derived magnetic structure is *G*-type antiferromagnetic order (P_c4_2/ncm magnetic space group) with Mn^{2+} magnetic moments aligned along the *c*-direction in a staggered manner. Below T_N = 2.8 K in EuMnAsF, both Eu^{2+} and Mn^{2+} magnetic moments are ordered independently, following the superposition of two independent patterns for Eu^{2+} and Mn^{2+}. EuFeAsF being the typical representative of iron-based superconductors undergoes a tetragonal-to-orthorhombic transition presumably coupled with antiferromagnetic ordering in the Fe sublattice at 153 K. Below T_N = 3.4 K the neutron diffraction reveals magnetic reflections which can be indexed using an incommensurate propagation vector *k* = 0 0.961(1) ½ (*a* = 5.5917(2) Å, *b* = 5.6344(2) Å and *c* = 8.8821(3) Å). The derived magnetic structure is a cycloid in the *bc*-plane; magnetic moments of Eu^{2+} at 1.5 K are refined to 5.64(3) μ_B.

Introduction

The interplay between magnetism and superconductivity in the family of iron-based superconductors is of the particular interest as iron itself, and many of its compounds are ferromagnets, *i.e.,* exhibit properties that are detrimental for superconductivity [1]. The general structural feature of iron-based superconductors is the negatively charged antifluorite 2D layers $[Fe_2E_2]^{n-}$ (*E* – pnictides or chalcogenides, but in most of the cases As) which are separated by positively charged counter-layers [2 – 5]. In the majority of compounds, the latter act as charge reservoirs only and affect the behaviour of the functional Fe-layers only in an indirect manner, *i.e.,* by adjusting geometry or charge carriers

sign and concentration. They are usually ionic and hence do not contribute to the electronic structure at the vicinity of the Fermi level. A wide choice of positively charged layers leads to crystallographic diversity of iron-based superconductors – more than ten structure types were reported to the moment [6].

Examples of FeAs-based superconductors containing magnetically active ions in a supplementary layer are sparse. Still, the existing cases induce extended discussions in the literature ([7] and references therein are an illustrative example). The simplest possibility arises from the placing of magnetically active Eu^{2+} ($4f^7$) cations solely between FeAs layers. It results in the 122-type compound, $EuFe_2As_2$ [8]. Electron/hole doping by substituting in Eu and Fe positions and chemical pressure via As-by-P substitution lead to the development of superconductivity with critical temperatures of superconducting transitions up to 29 K, *i.e.,* the compound behaves like a typical member of this family without any apparent influence of Eu^{2+} magnetism [9]. A fascinating difference, however, is that detwinning of magnetic domains below the tetragonal-to-orthorhombic distortion temperature can be achieved without mechanical straining, but through applying a magnetic field [10]. It has been proposed that such behaviour is due to a biquadratic coupling between Fe and Eu spins [11]. Also, several variants of doping stabilize the ground state exhibiting coexistence of superconductivity and ferromagnetism [12], also observed in $RbEuFe_4As_4$, featuring a decorated variant of the 122 structure [13].

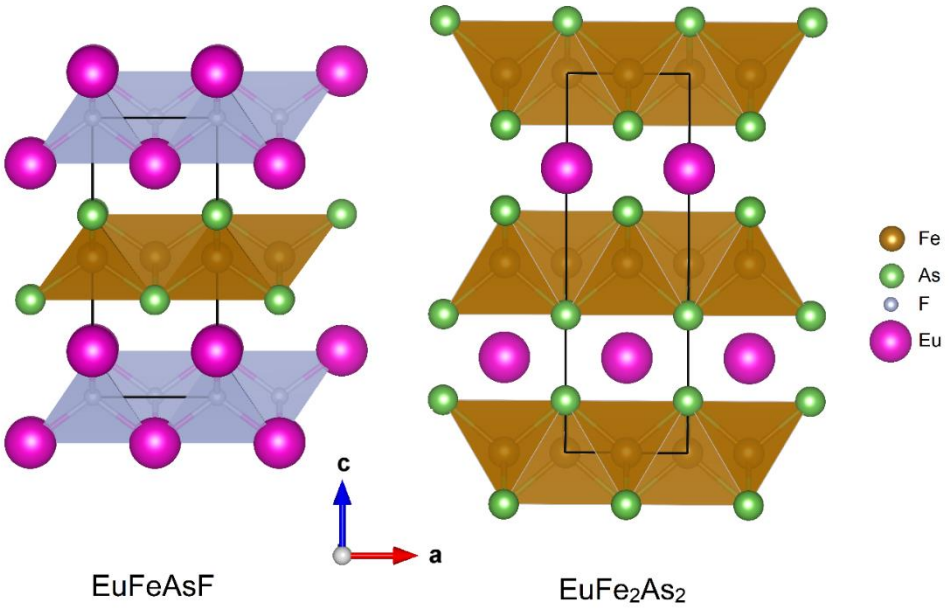

Figure 7.1 Comparison of crystal structures of $EuFe_2As_2$ and EuFeAsF.

Placing of a fluorite layer $[Eu_2F_2]^{2+}$ instead of the single tetragonal net of Eu^{2+} cations leads to another compound, EuFeAsF, the representative of the 1111 (also known as LaOAgS or ZrCuSiAs) structure type [14, 15]. **Figure 7.1** provides a comparison of the 122 and 1111structures. EuFeAsF, a non-superconducting undoped parent phase of iron-based superconductors, is in the focus of the current study. Despite extended analyses of $EuFe_2As_2$, its sibling EuFeAsF has been only poorly described and discussed in literature, mainly as a supplement to other 1111-type compounds, SrFeAsF and CaFeAsF. From resistivity measurements, EuFeAsF has been reported to undergo a transition at 153 K, which, similar to its non-magnetic sibling SrFeAsF [16] and other 1111-type compounds, has been ascribed to an orthorhombic distortion coupled with an antiferromagnetic ordering in the Fe-sublattice. Contrary, neither in the case of $EuFe_2As_2$ nor in the case of Eu*TPn*F (*T* = Zn, Mn; *Pn* = As, Sb) compounds [17, 18], anomalies due to ordering of Eu^{2+} magnetic moments were reported. Motivated by chemical and structural similarities of EuFeAsF and $EuFe_2As_2$, we undertook a study of its low-temperature behaviour using neutron diffraction. To extract the effect of magnetic fluorite layers $[Eu_2F_2]^{2+}$ on antifluorite layers, we also investigate other structurally and chemically related materials containing both non-magnetic $[Zn_2As_2]^{2-}$ (Zn^{2+}, $3d^{10}$) and magnetic $[Mn_2As_2]^{2-}$ (Mn^{2+}, $3d^5$) species, thus framing the whole interval of possible effects.

Although numerous Eu^{2+}-based materials attract attention due to their complex magnetic behaviour or sophisticated implications of magnetism on the structure and physical properties, detailed studies of their magnetic structures using neutron diffraction are relatively sparse. The reason is that the isotope ^{151}Eu has an absorption crossection of 9100 barn [19], and thus Eu is considered as a black element for neutrons. Therefore it is mostly assumed that it is impossible to perform routine neutron scattering experiments with compounds containing natural Eu. However, as the effectiveness of the modern neutron diffractometers grows, it is getting possible to perform such experiments routinely with natural europium and ordinary diffractometer setups, but with just slightly longer counting time.

In the current study, we report magnetic structures for the title compounds, determined from neutron powder diffraction. The data were collected at the WISH (TS2 ISIS, UK) diffractometer in its ordinary setup; europium metal used for these experiments contains the natural isotope mixture.

Experimental section

Synthesis and primary characterization. Large samples of EuZnAsF, EuMnAsF, and EuFeAsF were produced through a standard ampoule technique, similar to the one described in refs. [14, 15, 17, 18]. Elemental Eu (Chempur, 99.5%), EuF_3 (Chempur, 99.999%), Zn, Mn, As, and Sb were used as starting materials. Stoichiometric mixtures were annealed at 1173 K in evacuated silica tubes several times until homogenous black powders are obtained. This synthetic procedure leads to nearly phase pure samples without using binary precursors as it has been described in [17, 18]. Their phase composition was checked using a STOE STADI P diffractometer (STOE & Cie, Darmstadt, Germany) equipped with a Dectris Mythen 1K detector with $CuK\alpha_1$ radiation (λ = 1.5406 Å). According to the DTA data, EuFeAsF decomposes at ~ 1225 K, while EuZnAsF and EuMnAsF are stable up to at least ~ 1275 K.

Neutron diffraction. Neutron powder diffraction data were collected at the ISIS pulsed neutron and muon facility of the Rutherford Appleton Laboratory (UK) on the WISH diffractometer located at the second target station (TS2) [20]. The samples of EuZnAsF, EuMnAsF, and EuFeAsF (~ 1g each) were loaded into a thin cylindrical 3 mm-diameter vanadium can and measured in a temperature range of 1.5 – 300 K. Crystal and magnetic structures solution and refinement were performed in the JANA2006 [21] and FullProf [22] software using magnetic space group-subgroup relations and representation analysis. Double-*k* magnetic models were constructed using ISODISTORT [23, 24].

Results and discussion

Magnetic and transport properties, as well as heat capacity data for EuZnAsF, EuMnAsF, and EuMnPF, were reported previously [17, 18], while magnetization data for EuFeAsF were measured in the current study and are provided in **Figure 7.2**. Concerning magnetization data, all compounds are qualitatively similar; they exhibit anomalies at 2.5 – 4 K, presumably due to antiferromagnetic ordering in the Eu^{2+} sublattice, nearly zero high-temperature paramagnetic Weiss constants and paramagnetic moments very close to 7.94 μ_B as expected for pure Eu^{2+}. This behaviour is reasonable for EuZnAsF, which contains a single magnetic ion Eu^{2+}. Mn^{2+} ($3d^5$) ions in EuMnAsF are expected to contribute to the paramagnetic response along with Eu^{2+}, but they do not because their magnetic moments are presumably coupled by strong antiferromagnetic interactions. Very similar behaviour has been described for a series of isostructural compounds BaMn*Pn*F (*Pn* = P, As, Sb, and Bi), where T_Ns are above 270 K as confirmed from neutron diffraction data [25, 26].

Although the magnetic susceptibility curve for EuFeAsF is featureless below RT, the previously reported resistivity data indicate an anomaly at 153 K. Similar to other FeAs compounds, in particular, SrFeAsF, this anomaly has been ascribed to a tetragonal-to-orthorhombic distortion coupled with antiferromagnetic ordering in the Fe sublattice. Antiferromagnetic ordering in the Eu^{2+} sublattice in this compound is manifested by a sharp susceptibility maximum at T_N = 3.4 K.

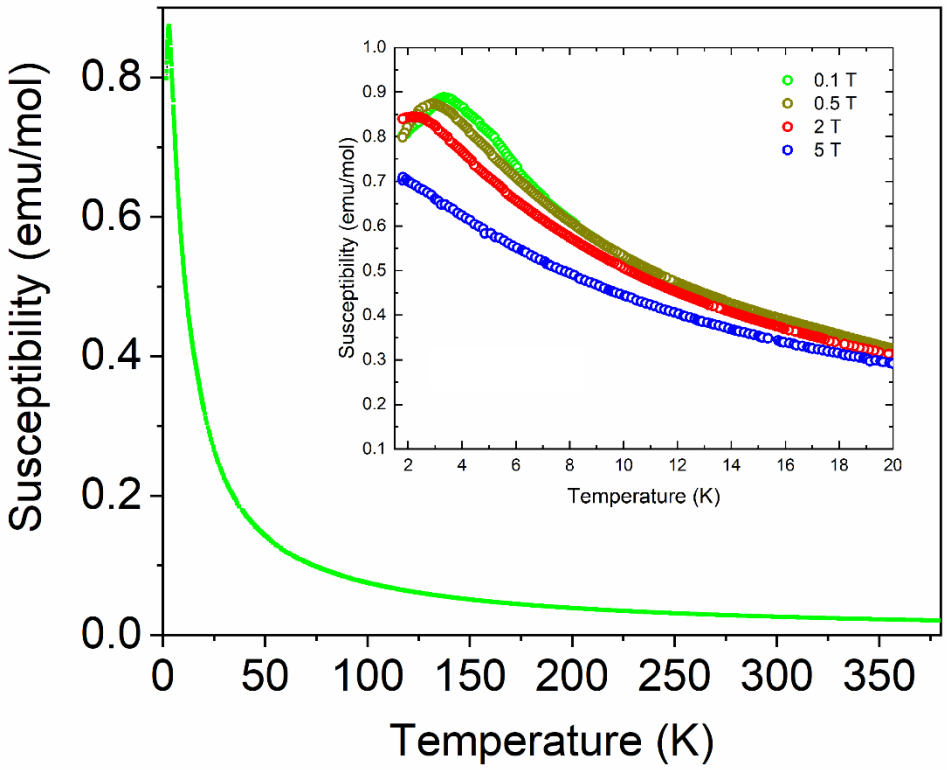

Figure 7.2 Magnetic susceptibility curve for EuFeAsF measured in the 0.1 T field. On the insert – low-temperature part of the magnetic susceptibility curves measured in different fields. The bulk magnetization data are also representative of EuZnAsF and EuMnAsF described in this chapter.

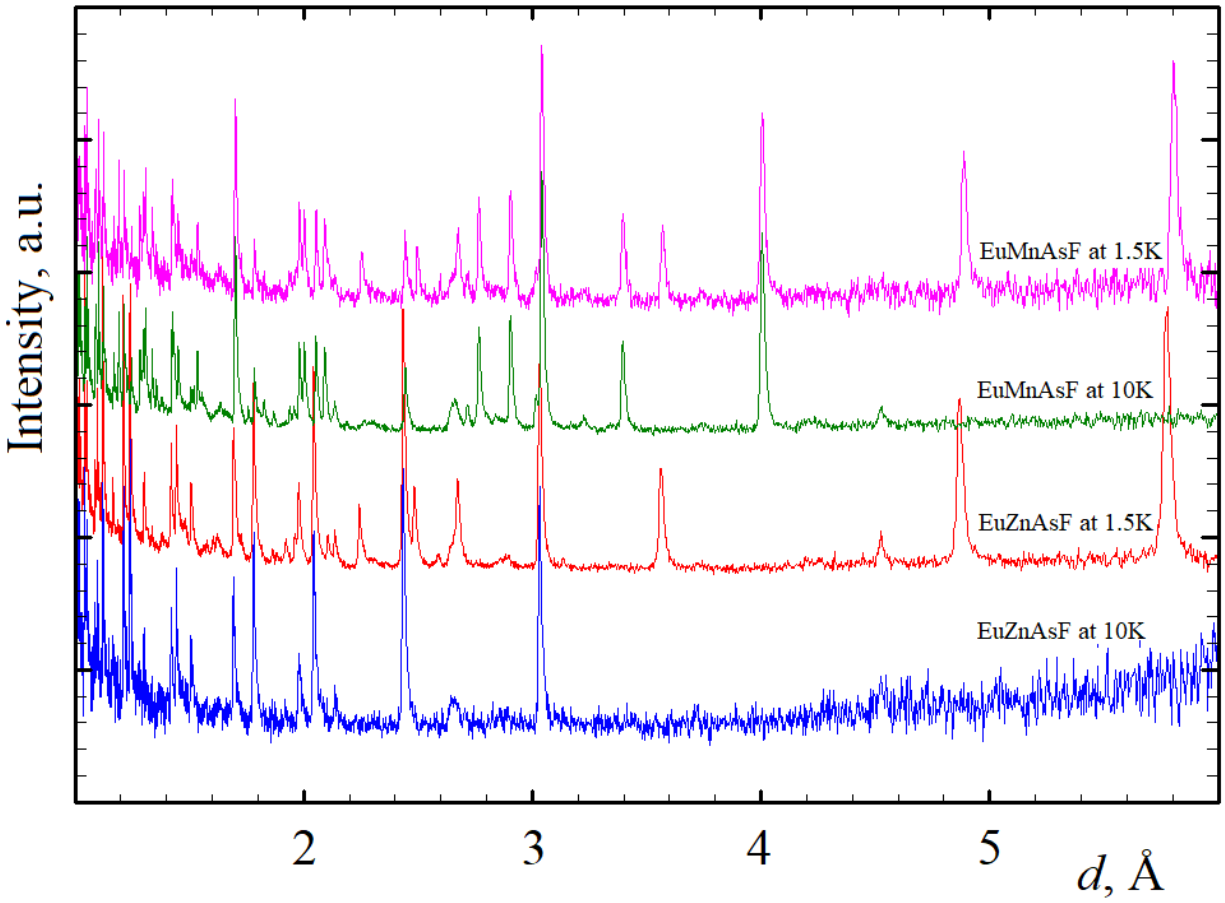

Figure 7.3 Comparison of TOF neutron diffraction patterns of (from the bottom to the top) EuZnAsF at 10 K in paramagnetic state, EuZnAsF at 1.5 K with antiferromagnetic ordering in Eu^{2+} sublattice, EuMnAsF at 10 K with antiferromagnetic ordering in Mn^{2+} sublattice and EuMnAsF at 1.5 K exhibiting antiferromagnetic ordering in both Mn^{2+} and Eu^{2+}.

The trial neutron diffraction measurements show that the employed setups provide the data sets of a quality sufficient for structure refinement, despite a strong neutron absorption. A comparison of the normalized diffraction patterns of Eu*T*AsF (*T* = Zn and Mn) at 1.5 K and 10 K measured within 2 – 3 h each is provided in **Figure 7.3**. EuZnAsF at 10 K exhibits only nuclear reflections consistent with those expected from the room-temperature X-ray diffraction data except for thermal expansion. Still, above 4 Å, increasing background intensity, characteristic for paramagnetic compounds at the temperatures just slightly above magnetic phase transition, is visible. It indicates the incipient magnetic correlations. Additional reflections appear upon cooling of this sample down to 1.5 K. They can be indexed using a commensurate propagation vector k_1 = ½ ½ 0. EuMnAsF exhibits reflections already above 4 K, which cannot be explained using a structural model obtained from the room-temperature X-ray data. They all can be indexed using a propagation vector k_2 = 0 0 ½. Further cooling of EuMnAsF down to 1.5 K leads to the development of

additional reflections, which do not overlap with those provided by k_2, but very close to those provided by k_1. Thus, the magnetic model, in this case, is a superposition of two, without any mutual influence.

The models of magnetic structures have been derived by testing all magnetic superspace groups compatible with the crystallographic symmetry; they are schematically drawn in **Figure 7.4**. Magnetic moments of Eu^{2+} in the EuZnAsF, located at the vertexes of tetrahedra, are aligned along *a*-direction of the magnetic unit cell ($\sqrt{2}a \times \sqrt{2}a \times c$ supercell of the crystallographic one), thus breaking the tetragonal symmetry. Two out of four Eu^{2+} magnetic moments, located at the vertices of tetrahedra, are coupled ferromagnetically and together with magnetic moments from the neighboring layer form a ferromagnetic ribbon, propagating along *c*-direction. The magnetic unit cell contains two of those ferromagnetic ribbons stacked to each other in an antiferromagnetic manner along *b*-direction, yielding a global antiferromagnetic order consistent with magnetization data. No orthorhombic stains of crystal structure associated with magnetic ordering are observed.

The magnetic structure of EuMnAsF above 4 K is a close match with the previously reported BaMn*Pn*F as well as other Mn-containing 1111 materials. Magnetic moments of Mn^{2+} cations centering the $MnAs_4$ tetrahedra are aligned along *c*-direction. Each magnetic moment of a Mn^{2+} cation is coupled antiferromagnetically with its nearest neighbor forming a checkerboard layer. Theses layers stuck in an antiferromagnetic manner on top of each other along *c*-direction. The refined magnetic moment at 10 K is 3.4 μ_B. It is lower than the expected value of 5 μ_B for isolated Mn^{2+} ($3d^5$) cations, but it is in a good agreement with other 1111 compounds, where refined moments are in the range between 3 and 3.9 μ_B. The deviation is attributed to the freezing of Mn 3*d* orbital moments.

In agreement with the separation of k_1 and k_2 magnetic reflections, the magnetic structure of EuMnAsF at 1.5 K features independent ordering of Eu^{2+} and Mn^{2+} in a $\sqrt{2}a \times \sqrt{2}a \times 2c$ magnetic supercell according to the pattern described above. Also, several diffraction patterns measured between 4 K and RT show no changes of the propagation vector, which along with the bulk properties data, rules out a spin-reorientation scenario in the Mn sublattice contrary to the case described for CeMnAsO [27, 28] or ThMnAsN [29].

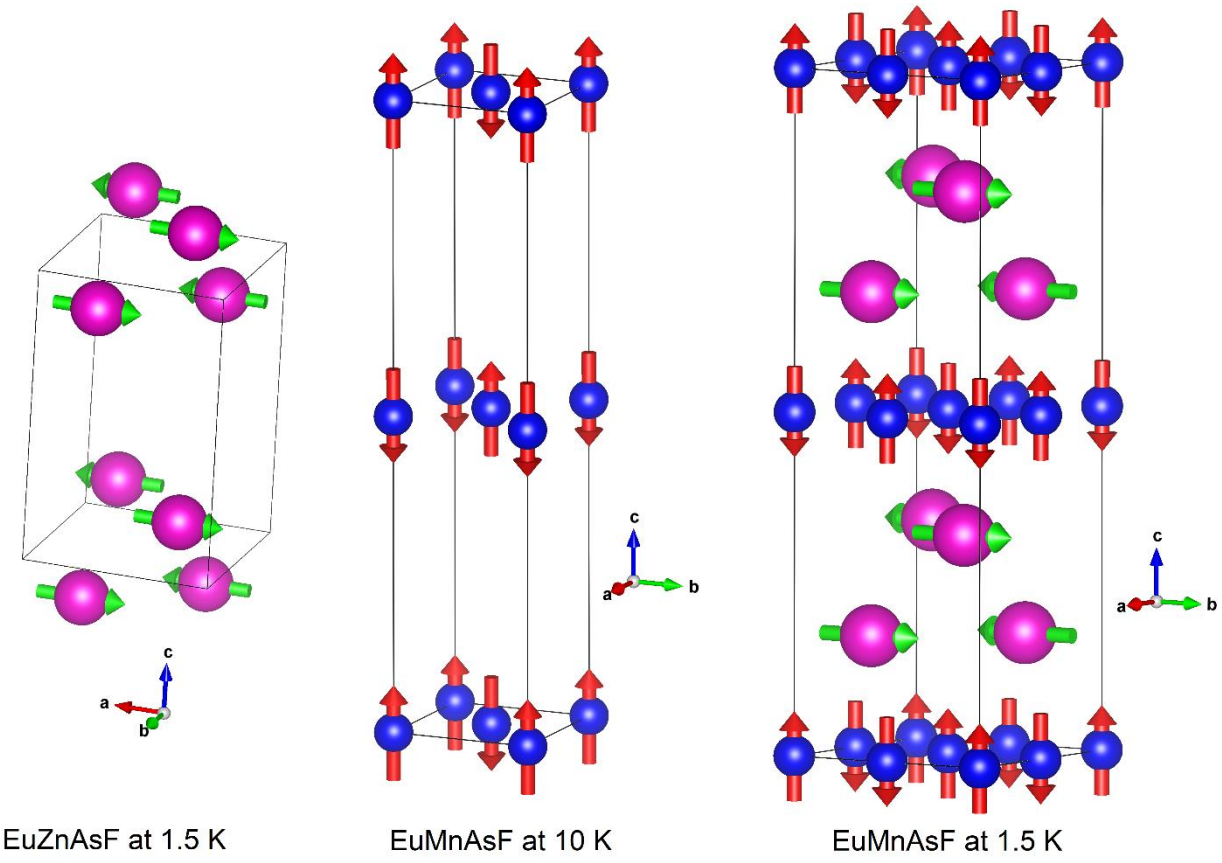

Figure 7.4 Magnetic structure of (from left to right) EuZnAsF at 1.5 K, EuMnAsF at 10 K, and EuMnAsF at 1.5 K. Magnetic unit cells are outlined. Only magnetic atoms (Mn – blue, Eu – pink) with their ordered magnetic moments (red and green, respectively) are shown for clarity.

Table 7.1 Details of neutron powder diffraction experiments.

	EuZnAsF	EuMnAsF	EuMnAsF	EuFeAsF
Temperature	1.5 K	10 K	1.5 K	1.5 K
Nuclear space group	*P4/nmm*			*Cmme*
Cell parameters				
a in Å	4.0852(2)	4.1075(2)	4.1059(2)	5.5923(2)
b in Å	= *a*	= *a*		5.6335(2)
c in Å	9.0462(3)	9.0486(3)	9.0447(5)	8.8812(3)
k-vector				
k_1	½ ½ 0		½ ½ 0	0 0.961(1) ½
k_2		0 0 ½	0 0 ½	
Magnetic space group	P_Cmab[1]	P_C4_2/ncm	P_Ibcm	*Cmm*2(0*b*1/2)*s*00
d-spacing range in Å	0.75 – 5.85	0.8 – 4.8	0.96 – 6.1	1.15 – 5.70
Reflections	443/230[2]	453/123[2]	464/346[2]	339/127[2]
Structural parameters	7/1[1]	6/1	9/2	7/1
R values				
R_P in %	3.19	3.10	5.52	3.84
R_{wP} in %	2.83	3.42	5.80	4.72
χ^2	1.28	1.77	1.07	1.36
R_F in %	4.41/3.90/6.23[3]	2.07/1.63/3.23[3]	5.47/4.88/7.17[3]	5.55/4.55/7.32[3]
Refined magnetic moment in μ_B	5.47(2)/Eu^{2+}	3.39(2)/Mn^{2+}	4.59(6)/Eu^{2+} 3.56(5)/Mn^{2+}	5.64(3) μ_B/Eu^{2+}
μ_{CW} in μ_B	7.93	7.67		7.92
M_S at 2K in μ_B	7.00	6.84		6.75

[1] The non-standard setting is chosen to preserve the relation to initial paramagnetic phase

[2] Overall/magnetic

[3] On all reflections/ structural reflections/magnetic reflections

The diffraction patterns of the EuFeAsF measured above (at 10 K) and below (at 1.5 K) phase transition at 3 K are provided in **Figure 7.5**. Several very strong magnetic reflections are observed, including those whose intensities are stronger than intensities of structural reflections. The triplet of magnetic reflections at 5.19 Å, 5.33 Å, and 5.57 Å at *d*-spacing comparable though not coinciding with *a* and *b* cell parameters is an indication of an incommensurate magnetic order pattern. Indeed, these reflections, as well as those at lower *d*-spacing, can be indexed with an incommensurate vector $k = 0\ 0.961(1)\ ½$ (assuming the following setting of the unit cell: $a = 5.5917(2)$ Å, $b = 5.6344(2)$ Å and $c = 8.8821(3)$ Å). Representation analysis yields four maximal magnetic superspace groups of the initial nuclear group *Cmme*, which allow non-zero magnetic moments on Eu atoms: *Cmme*.1'(0$b^{1}/_{2}$)000*s*, *Cmme.*1'(0$b^{1}/_{2}$)*s*0*ss*, *Cmme*.1'(0$b^{1}/_{2}$)*s*00*s*, *Cmme.*1'(0$b^{1}/_{2}$)00*ss*. Attempts to refine the magnetic structures using symmetry restrictions imposed by these superspace groups result in the third one, *Cmme.*1'(0$b^{1}/_{2}$)*s*00*s*, to give an acceptable description of all magnetic reflections. A trivial solution is an incommensurate spin density wave. Magnetic moments are aligned along *b*-direction, *i.e.,* the direction of propagation; their amplitude changes as a sin-wave from 7.36 μ_B to zero. The magnetic moment in maximum is higher than theoretically expected (7 μ_B), which indicates that the proposed model is not physically realistic. Also, an incommensurate spin density wave is highly unlikely to be a ground state structure as it does not allow all localized magnetic moments of Eu^{2+} to be saturated at their maximum allowed value. Therefore we attempted to search for more physical constant-moment models among subgroups of the initial superspace group.

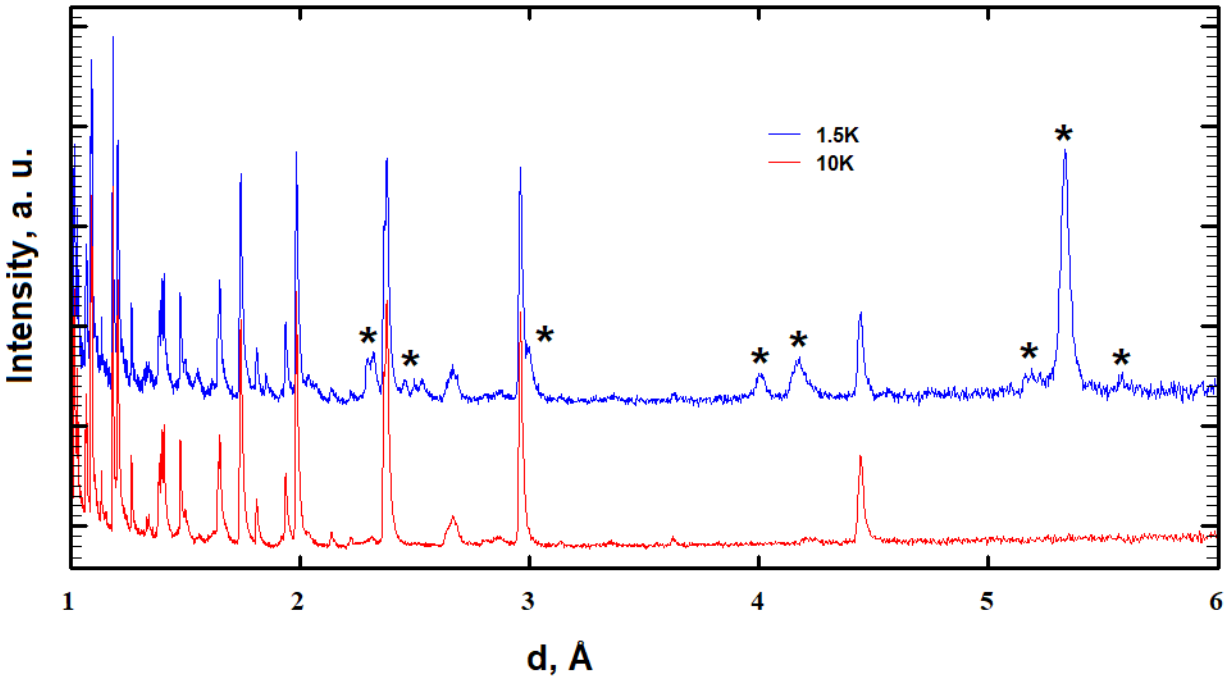

Figure 7.5 Comparison of TOF neutron diffraction patterns of EuFeAsF at 1.5 K (below magnetic ordering in Eu^{2+} sublattice) and 10 K. The strongest magnetic reflections or their groups are outlined by asterisks.

Removing the 1' symmetry element results in a set of magnetic space groups which differ from each other by permutation of space group generators (*m* and *m'*, m and *m'*, *b* and *b'* along *a*, *b* and *c* direction), but allow to stay in the same crystallographic space group *Cmme*, *i.e.,* without splitting of atomic positions. Unfortunately, none of these eight groups results in a model essentially different from the one provided by the *Cmme*.1'(0*b*½)*s*00*s*. Therefore we attempted to lower symmetry by removing one of the planes, *i.e.*, transform from *mmm* crystallographic point symmetry to *mm*2. The group *Cmm*2(0*b*½)*s*00 splits the position of the Eu atom into two and allows the magnetic moment to have a refinable component along *c*-direction. By forcing the amplitude of magnetic moments to be equal for both atomic positions and have the same amplitude throughout the whole structure, we obtain the final solution, details of which are provided in **Table 7.1**. Consequent refinement (**Figure 7.6**) yields a magnetic moment on Eu^{2+} cations of 5.64(3) μ_B, which is only slightly lower than the expected value of 7 μ_B. The deviation is probably because the sample's temperature is not low enough to ensure full saturation of magnetic moments. Similar to the above mentioned commensurate case, the *b*-component of magnetic moments forms two stripes per unit cell, that are coupled to each other in an antiferromagnetic manner. Overall, the magnetic moments rotate by 14^0 when passing from one Eu^{2+} ion to another along *b*-direction (**Figure 7.7**).

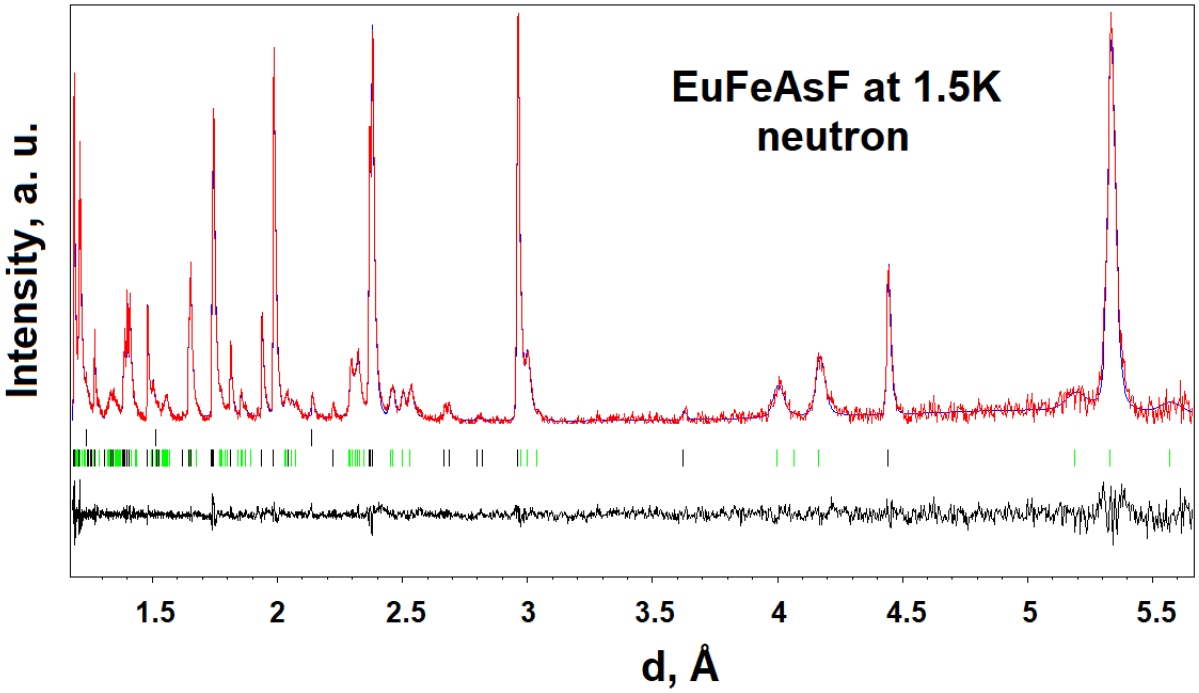

Figure 7.6 Refinement of the nuclear and magnetic structures of EuFeAsF against TOF neutron diffraction data at 1.5 K. Measured points are red, the calculated curve is blue, positions of structural reflections and difference curve are black, and positions of magnetic reflections are green. Reflections from the V container (black) were included in the refinement.

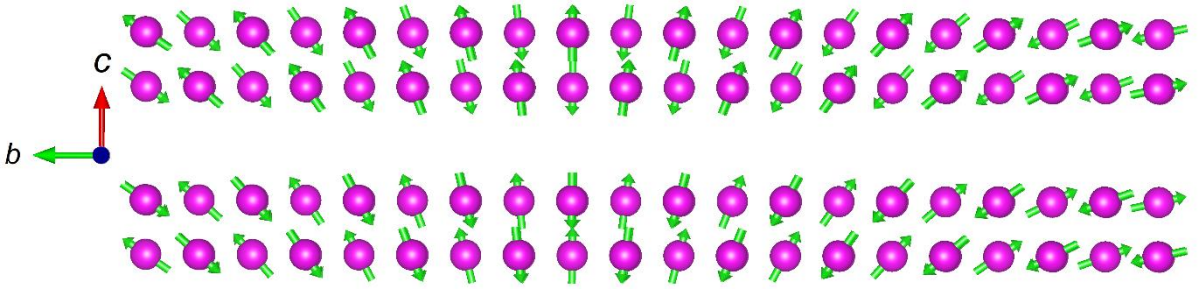

Figure 7.7 *a* × 9*b* × 2*c* supercell of EuFeAsF. Only Eu atoms with their magnetic moments are shown for clarity.

The diffraction pattern at 10 K does not feature magnetic reflections, which are characteristic for magnetic ordering in the Fe sublattice in other undoped 1111 compounds. Based on diffraction data only, it is impossible to judge if Fe is in a magnetically ordered state or not, because the intensities of magnetic reflections might be too low, given the low magnetic moment of Fe in similar compounds (5 – 7 μ_B on Eu^{2+} cations *vs.* 0.6 μ_B on Fe atom in SrFeAsF [30, 31]). Still, several types of behaviour of iron have been observed in

other FeAs materials containing magnetically active atoms – from the absence of ordering in $EuFe_2P_2$ [32] to spin reorientation in *Ln*FeAsO (*Ln* = Ce and Pr) [33 – 35]. Diffraction data of a higher quality or other dedicated local tools (like ^{57}Fe Mössbauer spectroscopy) might be necessary to elucidate this question.

Conclusions

Our neutron diffraction studies have confirmed antiferromagnetism of EuZnAsF, EuMnAsF, and EuFeAsF and established the magnetic ordering pattern of Eu^{2+} ($4f^7$) magnetic moments below T_Ns ~ 3K. The magnetism of Mn^{2+} ($3d^5$) is indeed hidden by the strong antiferromagnetic interactions, which persist up to room temperature at least. Magnetic structures of semiconducting EuZnAsF and EuMnAsF are commensurate and nearly identical, which rules out the influence of Mn^{2+} on the magnetic behaviour of Eu-containing layers. On the other hand, the magnetic structure of metallic EuFeAsF is a complex incommensurate cycloid. These results imply that the sheer amplitude of magnetic moments on the atoms in the complementary layer has a lower influence on the magnetic behaviour of $[Eu_2F_2]^{2+}$ as compared to the electronic structure.

Several other people also contributed to this work:

1. Dr Dmitry Khalyavin (ISIS) performed neutron diffraction data and supported with interperation of the results.
2. Dr. Alexander Tsirlin (Uni Augsburg) supported with interpretation of the results.

References

[1] J. Wen, G. Xu, G. Gu, J M Tranquada, R. J. Birgeneau. Interplay between magnetism and superconductivity in iron-chalcogenide superconductors: crystal growth and characterizations. *Rep. Prog. Phys.* **2011**, *74*, 124503.

[2] A. A. Kordyuk. Iron-based superconductors: magnetism, superconductivity, and electronic structure. *Low Temp. Phys.* **2012**, *38*, 888.

[3] J. Hao, S. Yun-Lei, X. Zhu-An, C. Guang-Han. Crystal chemistry and structural design of ironbased superconductors. *Chinese Phys. B* **2013**, *22*, 087410.

[4] P. M. Aswathy, J. B. Anooja, P. M. Sarun, U. Syamaprasad. An overview on iron based superconductors. *Supercond. Sci. Technol.* **2010**, *23*, 073001.

[5] D. Johrendt, R. Pöttgen. Pnictide oxides: a new class of high-T_C superconductors. *Angew. Chem.* **2008**, *47*, 4782.

[6] S.J. Clarke, P. Adamson, S.J.C. Herkelrath, O.J. Rutt, D.R. Parker, M.J. Pitcher, C.F. Smura. Structures, physical properties, and chemistry of layered oxychalcogenides and oxypnictides. *Inorg. Chem.* **2008**, *47*, 8473.

[7] M. A Albedah, F. Nejadsattari, Z. M. Stadnik, Y. Liu, G.-H. Cao. Magnetism of the 35 K superconductor $CsEuFe_4As_4$. *J. Phys.: Condens. Matter* **2018**, *30*, 155803.

[8] M. Tegel, M. Rotter, V. Weiß, F. M Schappacher, R. Pöttgen and D. Johrendt. Structural and magnetic phase transitions in the ternary iron arsenides $SrFe_2As_2$ and $EuFe_2As_2$. *J. Phys.: Condens. Matter* **2008**, *20*, 452201.

[9] Z. Ren, Q. Tao, S. Jiang, C. Feng, C. Wang, J. Dai, G. Cao, Z. Xu. Superconductivity induced by phosphorus doping and its coexistence with ferromagnetism in $EuFe_2(As_{0.7}P_{0.3})_2$. *Phys. Rev. Lett.* **2009**, *102*, 137002.

[10] S. Zapf, C. Stingl, K. W. Post, J. Maiwald, N. Bach, I. Pietsch, D. Neubauer, A. Löhle, C. Clauss, S. Jiang, H. S. Jeevan, D. N. Basov, P. Gegenwart, M. Dressel. Persistent detwinning of iron-pnictide $EuFe_2As_2$ crystals by small external magnetic fields. *Phys. Rev. Lett.* **2014**, *113*, 227001.

[11] J. Maiwald, P. Gegenwart. Interplay of 4*f* and 3*d* moments in $EuFe_2As_2$ iron pnictides. *Phys. Rev. X.* **2017**, *254*, 1600150.

[12] S. Nandi, W. T. Jin, Y. Xiao, Y. Su, S. Price, D. K. Shukla, J. Strempfer, H. S. Jeevan, P. Gegenwart, Th. Brückel. Coexistence of superconductivity and ferromagnetism in P-doped $EuFe_2As_2$. *Phys. Rev. B*, **2014**, *89*, 014512.

[13] J.-K. Bao, K. Willa, M. P. Smylie, H. Chen, U. Welp, D. Y. Chung, M. G. Kanatzidis. Single crystal growth and study of the ferromagnetic superconductor $RbEuFe_4As_4$. *Cryst. Growth Des.* **2018**, *18*, 3517 - 3523.

[14] X. Zhu, F. Han, P. Cheng, G. Mu, B. Shen, B. Zeng, H. Wen. Parent phase and superconductors in the fluorine derivative family. Physica C **2009**, *469*, 381-384.

[15] X. Zhu, F. Han, P. Cheng, G. Mu, B. Shen, L. Fang and H.-H. Wen Superconductivity in fluoride-arsenide $Sr_{1-x}La_xFeAsF$ compounds. *EPL*, **2009**, *85*, 17011.

[16] M. Tegel, S. Johansson, V. Weiß, I. Schellenberg, W. Hermes, R. Pöttgen and D. Johrendt. Synthesis, crystal structure and spin-density-wave anomaly of the iron arsenide-fluoride SrFeAsF. *EPL* **2008**, *84*, 67007.

[17] I.V. Plokhikh, D.O. Charkin, V. Yu. Verchenko, A.N. Kuznetsov, S.M. Kazakov, A.A. Tsirlin, A.V. Shevelkov, Structural and thermodynamic stability of the "1111"structure type: a case study of the EuFZn*Pn* series. *Inorg. Chem.* **2016**, *55*, 12409.

[18] I.V. Plokhikh, D.O. Charkin, V. Yu. Verchenko, A.N. Kuznetsov, S.M. Kazakov, A.A. Tsirlin, A.V. Shevelkov. Synthesis, crystal structure and physical properties of europium – manganese fluoride pnictides, EuMn*Pn*F (*Pn* = P, As, Sb). *J. Solid State Chem.* **2018**, *258*, 682.

[19] https://www.ncnr.nist.gov/resources/n-lengths/elements/eu.html

[20] L. C. Chapon, P. Manuel, P. G. Radaelli, C. Benson, L. Perrott, S. Ansell, N. J. Rhodes, D. Raspino, D. Duxbury, E. Spill, J. Norris. Wish: the new powder and single crystal magnetic diffractometer on the second target station. *Neutron News* **2011**, *22*, 22.

[21] V. Petricek, M. Dusek, L. Palatinus. Crystallographic computing system JANA2006: general features. *Z. Kristallogr.* **2014**, 229(5), 345-352.

[22] J. Rodríguez-Carvajal. Recent advances in magnetic structure determination by neutron powder diffraction. *Physica B.* **1993**, *192*, 55.

[23] H. T. Stokes, D. M. Hatch, and B. J. Campbell, ISODISTORT, ISOTROPY Software Suite, iso.byu.edu.

[24] B. J. Campbell, H. T. Stokes, D. E. Tanner, and D. M. Hatch. ISODISPLACE: an internet tool for exploring structural distortions. *J. Appl. Cryst.* ***2006***, *39*, 607 - 614.

[25] B. Saparov, D. J. Singh, V. O. Garlea A. S. Sefat. Crystal, magnetic and electronic structures and properties of new BaMnPnF (Pn = As, Sb, Bi). *Sci. Rep.* **2013**, *3*, 2154.

[26] F. Islam, E. Gordon, P. Das, Y. Liu, L. Ke, D. L. Abernathy, R. J. McQueeney, D. Vaknin. Spin dynamics in the antiferromagnetic oxy- and fluoro- pnictides: LaMnAsO, LaMnSbO, and BaMnAsF. *Phys. Rev. B* **2020**, *101*, 155119.

[27] A. Marcinkova, T.C. Hansen, C. Curfs, S. Margadonna, J.W.G. Bos. Nd-induced Mn spin-reorientation transition in NdMnAsO. *Phys. Rev. B* **2010**, 82. 174438.

[28] Q. Zhang, W. Tian, S. G. Peterson, K. W. Dennis, D. Vaknin. Spin reorientation and Ce-Mn coupling in antiferromagnetic oxypnictide CeMnAsO. *Phys. Rev. B* **2015**, *91*, 064418.

[29] F. Zhang, B. Li, Q. Ren, H. Mao, Y. Xia, B. Hu, Z. Liu, Z. Wang, Y. Shao, Z. Feng, S. Tan, Y. Sun, Zhi Ren, Q. Jing, B. Liu, H. Luo, J. Ma, Y. Mei**,** C. Wang**,** G.-H. Cao. ThMnPnN (Pn = P, As): synthesis, structure, and chemical pressure effects. *Inorg. Chem.* **2020**, *59*, 2937 – 2944.

[30] Y. Xiao, Y. Su, R. Mittal, T. Chatterji, T. Hansen, S. Price, C. M. N. Kumar, J. Persson, S. Matsuishi, Y. Inoue, H. Hosono, and Th. Brueckel. Neutron diffraction study of phase transitions and thermal expansion of SrFeAsF. *Phys. Rev. B* **2010**, *81*, 094523.

[31] Y. Xiao, Y. Su, R. Mittal, T. Chatterji, T. Hansen, C. M. N. Kumar, S. Matsuishi, H. Hosono, and Th. Brueckel. Magnetic order in the $CaFe_{1-x}Co_xAsF$ (x = 0.00, 0.06, 0.12) superconducting compounds. *Phys. Rev. B* **2009**, *79*, 060504.

[32] B. Ni, M. M. Abd-Elmeguid, H. Micklitz, J. P. Sanchez, P. Vulliet, D. Johrendt. Interplay between structural, electronic, and magnetic instabilities in EuT_2P_2 (T = Fe, Co) under high pressure. *Phys. Rev. B* **2001**, *63*, 100102.

[33] W. Tian, W. Ratcliff, II, M. G. Kim, J.-Q. Yan, P. A. Kienzle, Q. Huang, B. Jensen, K. W. Dennis, R. W. McCallum, T. A. Lograsso, R. J. McQueeney, A. I. Goldman, J. W. Lynn, and A. Kreyssig. Interplay of Fe and Nd magnetism in NdFeAsO single crystals. *Phys. Rev. B* **2010** *82*, 060514.

[34] J. Zhao, Q. Huang, C. de la Cruz, J. W. Lynn, M. D. Lumsden, Z. A. Ren, Jie Yang, X. Shen, X. Dong, Z. Zhao, P. Dai. Lattice and magnetic structures of PrFeAsO, $PrFeAsO_{0.85}F_{0.15}$, and $PrFeAsO_{0.85}$. *Phys. Rev. B* **2008**, *78*, 132504.

[35] M. A McGuire, R. P Hermann, A. S Sefat, B. C Sales, R. Jin, D. Mandrus, F. Grandjean, G. J Long. Influence of the rare-earth element on the effects of the structural and magnetic phase transitions in CeFeAsO, PrFeAsO and NdFeAsO. *New J. Phys.* **2009**, *11*, 025011.

8 Neutron powder diffraction study of the low-temperature magnetic phase transitions in the ternary europium-copper phosphides, $EuCu_2P_2$, $EuCu_4P_3$, and $Eu_2Cu_6P_5$

Abstract

Low-temperature magnetic structures of three europium copper phosphides, $EuCu_2P_2$, $EuCu_4P_3$, and their intergrowth $Eu_2Cu_6P_5$, have been established *via* the neutron powder diffraction. The neutrons used in these experiments are monochromatic (λ = 1.5482 Å) from the reactor source; the sample holder is a double-wall cylinder dedicated to mitigating Eu absorption. $EuCu_2P_2$ and $Eu_2Cu_6P_5$ are simple ferromagnets below 44 K and 34 K respectively with propagation vector k = 0 0 0, and magnetic moments aligned along the *c*-axes of the tetragonal unit cells. The amplitudes of magnetic moments are 6.8(1) μ_B for $EuCu_2P_2$ and 6.50(8) μ_B for $Eu_2Cu_6P_5$ at the base temperature of 3.5 K. Below the antiferromagnetic transition at 70 K, $EuCu_4P_3$ is a cycloidal structure obeying the propagation vector k = 0.098(1) 0.098(1) 0. The magnetic moments of amplitude 7.0(2) μ_B lie within the *a*-*b*-plane of the tetragonal unit cell and gradually rotate from one unit cell to another with approximately 10 unit cells period along *a* and *b* directions. The cycloidal phase persists from 70 K down to the base temperature.

Introduction

Layered compounds belonging to the $ThCr_2Si_2$ structure type caused tremendous interest in the physical community after the discovery of superconductivity in iron pnictides and chalcogenides [1 – 4]. Structural simplicity and a huge number of currently known representatives (over 700 unique and over 2500 including different substitutional possibilities) make these compounds to be called “perovskites among intermetallics” [5]. The structure is simple and consists of alternating antifluorite layers and tetragonal grids of cations. Anionic antifluorite layers are usually considered as physical properties carriers, which depending on the composition, can predispose superconductivity (including heavy-fermion) [6], unusual magnetic [7] and thermoelectric [8] properties. On the other hand, tetragonal grids are believed to affect the properties dictated by the antifluorite layers only in an indirect manner, *i.e.*, by adjusting the geometry or concentration of the charge carriers. The effect of a lanthanide ion with a high magnetic moment on the physical behaviour of the anifluorite layers has been probably well-understood only in the case of $EuFe_2As_2$, a non-superconducting parent phase of iron-based superconductors [9]. Here the

detwinning of single-crystals upon a tetragonal-orthorhombic transition can be achieved without mechanical stressing, but by applying a moderate magnetic field, due to the sophisticated mechanism proposed in ref. [10].

Here we shall elaborate the magnetic structures of one of the $ThCr_2Si_2$-type compounds, $EuCu_2P_2$, as well as its siblings, $EuCu_4P_3$ and $Eu_2Cu_6P_5$. $EuCu_2P_2$ is a non-stoichiometric compound, whose compositions can be more correctly expressed as $EuCu_{1-x}P_2$ ($\sim 0.1 < x < 0.25$). However, for the sake of simplicity, we use the stoichiometric formula throughout the text. These three compounds were reported previously, including their physical properties [11 – 14]. They represent an interesting case of "building block game" – three compounds are constructed from just three structural units, namely Eu^{2+} square nets, single $[Cu_2P_2]^{2-}$ and double $[Cu_4P_3]^{2-}$ fluorite layers. $EuCu_2P_2$ and $EuCu_4P_3$ are formed by Eu sheets separated by single and double fluorite layers respectively, while $Eu_2Cu_6P_5$ features both kinds of layers placed on top of each other in an ordered manner as shown in **Figure 8.1**. It results in *a*-cell parameters of the tetragonal unit cells being nearly equal and *c*-cell parameters being additive. From the physical point of view, $EuCu_2P_2$ and $Eu_2Cu_6P_5$ are rather simple – bulk properties measurements indicate a single ferromagnetic transition at 44 K and 34 K, respectively. Magnetic and resistivity curves reported for $EuCu_4P_3$ are surprisingly complex with at least three zero-field transitions at 18 K, 43 K, and 70 K. It is particularly interesting that such complexity is demonstrated by the compound exhibiting a rather simple structure with just one single, symmetrically independent magnetic ion Eu^{2+}.

A strong neutron absorption precludes routine studies of Eu compounds [15]. Still, for almost all Eu-containing $ThCr_2Si_2$ compounds, the magnetic structures were established [16], including short-wavelength single-crystal studies for $EuCr_2As_2$ [17] and a bunch of various reports on $EuFe_2As_2$ [18, 19]. Yet, for $EuCu_2P_2$, this kind of data is missing. In the current study, we elaborate the nature of low-temperature phases existing in $EuCu_2P_2$, $EuCu_4P_3$, and $Eu_2Cu_6P_5$. Ferromagnetic ordering of Eu^{2+} magnetic moments with a trivial propagation vector k = 0 0 0 is observed in the first and the third compound, while a complex cycloidal incommensurate structure persists in $EuCu_4P_3$ below 70K. Neutron data do not allow distinguishing between magnetically ordered phases existing in this compound below 70 K.

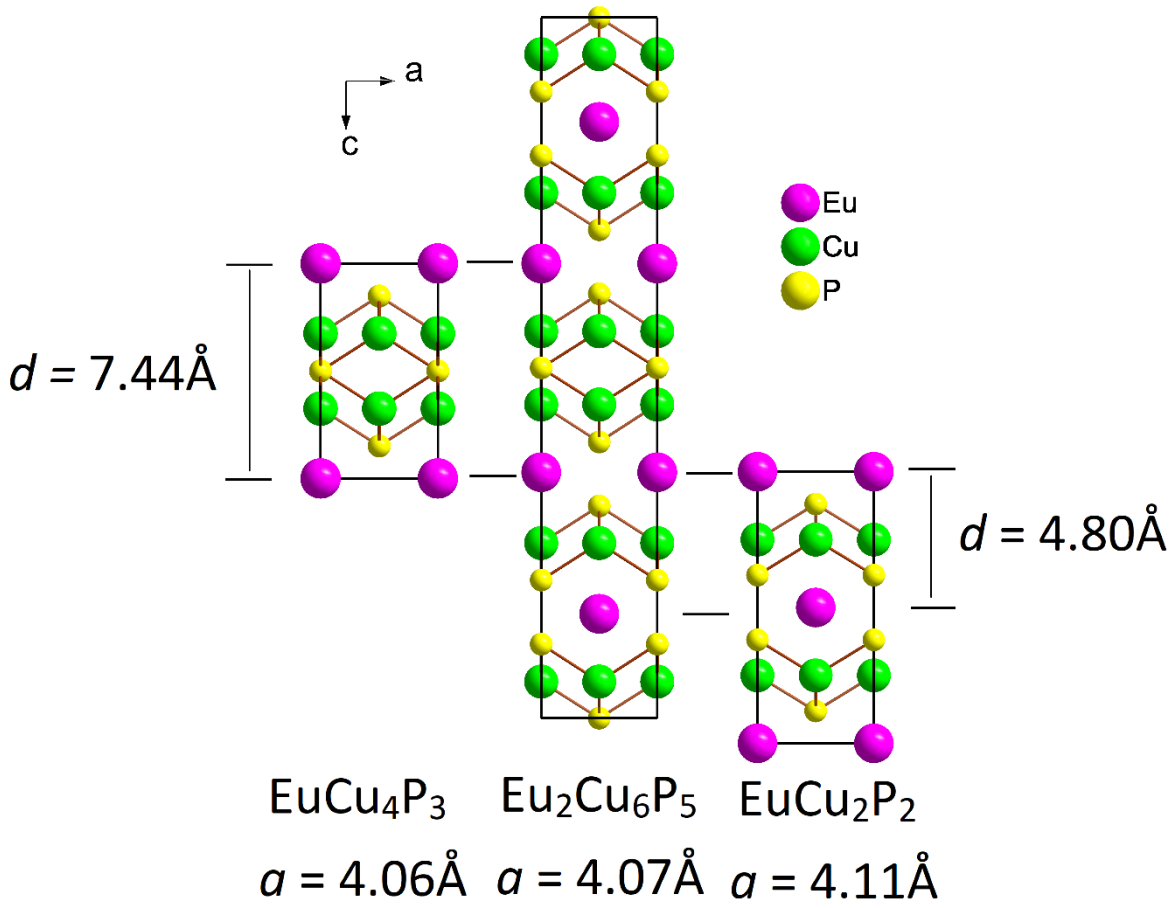

Figure 8.1 Relations between crystal structures of $EuCu_4P_3$, $EuCu_2P_2$ and their intergrowth $Eu_2Cu_6P_5$.

Experimental section

Phase-pure large (up to 4 g each) powder samples of the title compounds ($EuCu_2P_2$, $EuCu_4P_3$, and $Eu_2Cu_6P_5$) have been prepared from the elements *via* a conventional solid-state reaction. All operations were performed in Ar-filled glow-box (M'Braun, O_2, and H_2O less than 2 ppm). Copper was purified from surface oxides by heating in hydrogen flow at 873 K; europium was chopped right before the synthesis. Stoichiometric mixtures were loaded in graphite crucibles, flame-sealed in silica ampules, and slowly (0.2 K/min) heated up to 873 K. Intermediate mixtures were thoroughly re-grinded, pressed into pellets and annealed several more times at 1123 K until homogeneous crystalline black powders were obtained. Phase purity was checked using a STOE STADI P diffractometer ($CuK_{\alpha 1}$ radiation).

Elastic coherent neutron scattering experiments were performed in zero field on the high-resolution structure powder diffractometer (SPODI) at the research reactor FRM-II (Garching, Germany) with monochromatic neutrons of 1.54812 Å wavelength [20]. Measurements were performed in Debye–Scherrer geometry. The powder samples (*ca.* 3 –

3.5 g, 0.8 cm^3 in volume) were filled into a double-wall thin vanadium can of 22 mm diameter with a 0.5 mm gap between the walls to mitigate the effects of Eu neutron absorption [21]. The sample holders were mounted in a top-loading closed-cycle cryostat, which was cooled down from room to 3.5 K (base temperature). Powder diffraction data were collected between 3.5 and 80 K and then corrected for geometrical aberrations and the curvature of the Debye–Scherrer rings. The collecting time for a typical diffraction pattern was 12 h.

Magnetic structure refinements have been processed using the magnetic option implemented in the JANA 2006 software package [22]. *k*-search code implemented in the FullProf software package [23] has been used for indexing of magnetic reflections. Magnetic structures have been plotted using the Vesta software package [24].

Results and discussions

Details of the neutron powder diffraction experiments for $EuCu_2P_2$ and $Eu_2Cu_6P_5$ are provided in **Figures 8.2** and **8.3**, respectively. Above 44 K for the $EuCu_2P_2$ and 34 K for the $Eu_2Cu_6P_5$, the neutron diffraction patterns feature only nuclear reflections, which are, except for thermal expansion, consistent with the crystal structure obtained from the room-temperature X-ray diffraction data. Several strong magnetic reflections evolve upon cooling below T_Cs in both cases. The magnetic intensities grow on top of some nuclear reflections. In particular, the strongest magnet reflections (101 for $EuCu_2P_2$ and 103 for $Eu_2Cu_6P_5$) have zero intensity in paramagnetic phases. Hence, the magnetic ordering process in both cases can be described as a removal of the time inversion symmetry from the paramagnetic space group *I*4/*mmm*1′. The magnetic Shubnikov space groups generated thereof differ from each other by permutation of mirror planes *m* and mirror planes combined with time inversion *m′*. According to the representation analysis, out of eight generated magnetic space groups, only *I*4/*mm′m′* allows for a non-zero *z*-component of magnetic moment on the Eu atoms. Consequent refinements of the 3.5 K data results in good residuals and magnetic structures provided in **Figures 8.2** and **8.3**. At 3.5 K, magnetic moments on Eu atoms are 6.8(1) μ_B for $EuCu_2P_2$ and 6.50(8) μ_B for $Eu_2Cu_6P_5$. They are in a good agreement with 7 μB, the magnetic moment expected for Eu in a divalent form, and consistent with other Eu^{2+} materials studied by neutron diffraction [16, 17]. Note that a small deviation can be ascribed to the effects of absorption, which cannot be accounted for entirely.

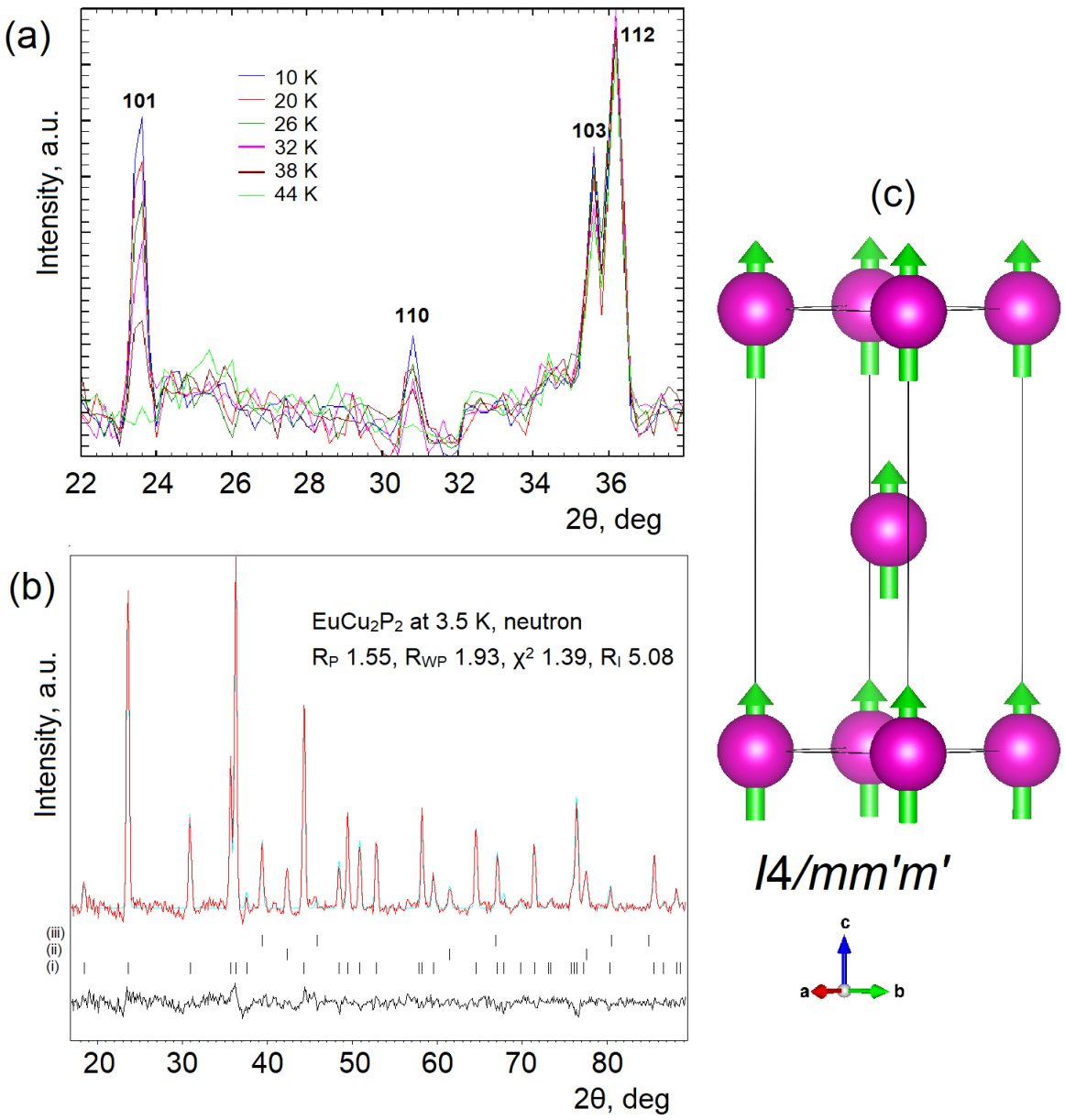

Figure 8.2 (a) Temperature dependence of neutron diffraction pattern (each measured within 2h). (b) Final Rietveld refinement plot at 3.5 K with details of the 12h experiment and residuals Along with the main phase (i), contributions of V (ii), and Al (iii) from the sample holder are included in refinement. (c) Magnetic structure of $EuCu_2P_2$ and magnetic space group. Only Eu atoms (pink) with their magnetic moments (green) are shown for clarity.

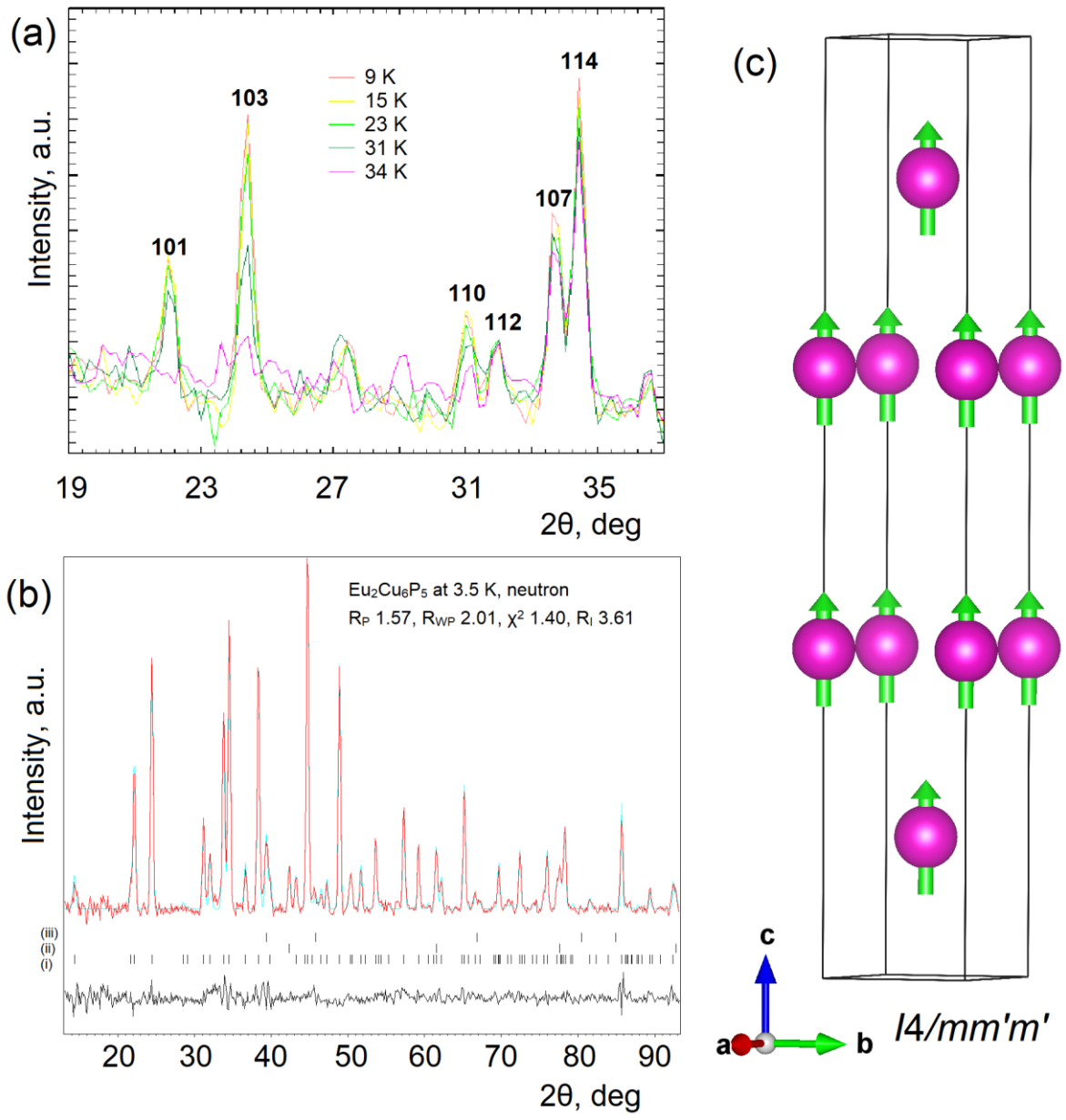

Figure 8.3 (a) Temperature dependence of neutron diffraction pattern (each measured within ~2 h). (b) Final Rietveld refinement plot at 3.5 K with details of the 12 h experiment and residuals. Along with the main phase (i), contributions of V (ii) and Al (iii) from the sample holder are included in refinement (c) Magnetic structure of $Eu_2Cu_6P_5$ and magnetic space group. Only Eu atoms (pink) with their magnetic moments (green) are shown for clarity.

Magnetization *vs.* field and temperature curves for $EuCu_4P_3$ are provided in **Figure 8.4**, the temperature dependence of heat capacity in **Figure 8.5** Both curves feature three distinct anomalies at ~ 20 K, 38 K, and 70 K. Magnetization curve taken at 2 K also reveals a strong non-linear behaviour with at least two metamagnetic transitions. Overall, the positions of these anomalies are consistent with those reported previously [12]. When discussing in

more detail, one can notice that the transitions at 70 K and 38 K are of second-order and most likely correspond to the processes taking place in the magnetic subsystem. The transition at 20 K is of first order (features latent heat and hysteresis).

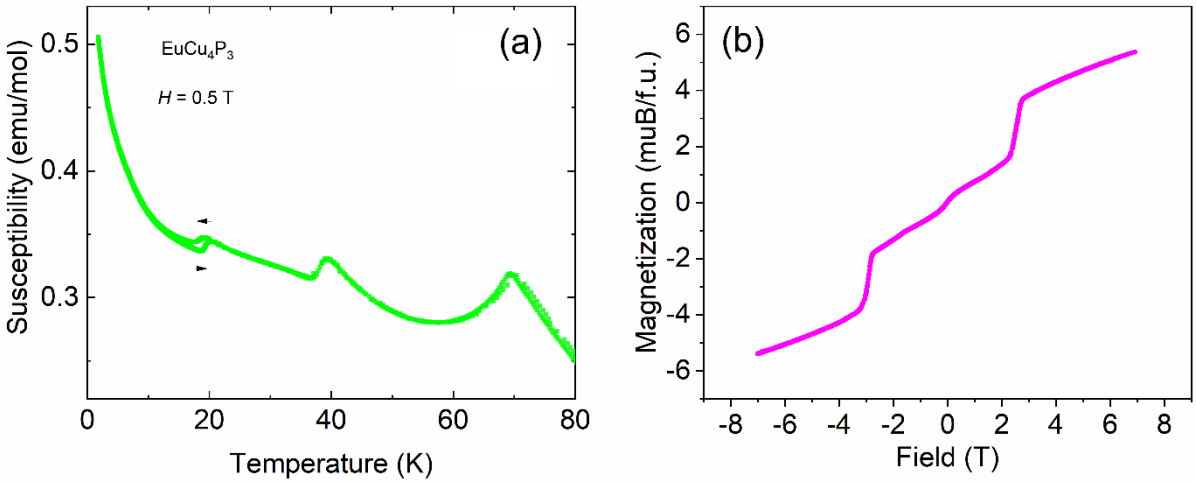

Figure 8.4 Summary of magnetic properties for $EuCu_4P_3$. (a) Magnetic susceptibility *vs.* temperature plot measured in 0.5 T field. The hysteretic behaviour of the transition at 20 K is marked with arrows. (b) Magnetization *vs.* field curves measured at 2 K.

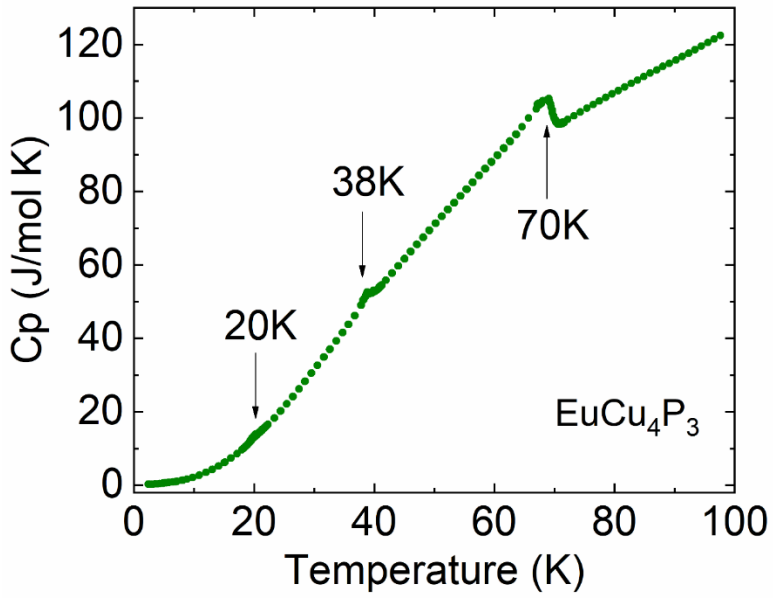

Figure 8.5 Heat capacity *vs.* temperature plot for $EuCu_4P_3$. Phase transition temperatures are outlined.

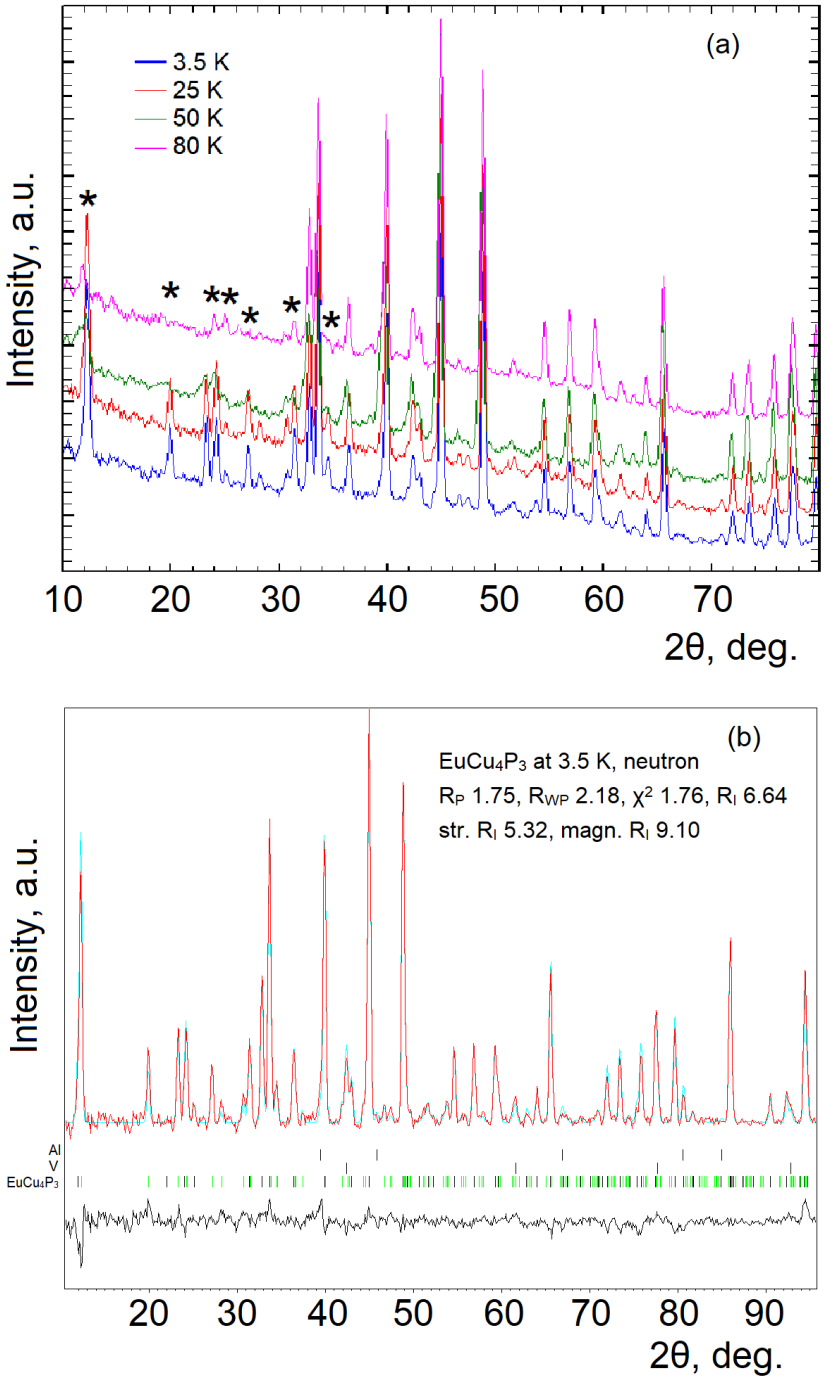

Figure 8.6 Details of the neutron diffraction experiment for $EuCu_4P_3$: (a) comparison of the neutron diffraction pattern measured at 3.5 K, 25 K, 50 K, and 80 K. The strongest magnetic reflections are marked with asterisks. (b) Final Rietveld refinement plot for 3.5 K data. Positions of structural reflections are marked in black, magnetic in green.

Long neutron diffraction measurements (*ca.* 12 h each) have been performed below the magnetic ordering temperature of 70 K, in between the magnetic phase transitions – at 3.5 K, 25 K, and 50 K. The neutron diffraction pattern measured at 80 K, *i.e.*, in the paramagnetic state, exhibits only reflections consistent with the room-temperature crystal

structure. The base-temperature diffraction pattern, besides nuclear reflections, exhibits multiple additional reflections, most likely of a magnetic origin. The strongest of them at $2\theta \sim 12^{\circ}$ is very close to the structural reflection 001, which made us propose a $k = 0\ 0\ 0$ at first. The Le Bail fitting of the diffraction pattern exhibits a strong discrepancy between calculated and measured positions of reflections, which rules out the trivial vector. Supposed magnetic reflections were attempted to be indexed through a random search of *k*-vector using *k*-search code. The latter indicate $k = 0.1\ 0.1\ 0$ as the most probable solution, which after the full profile refinement becomes $k = 0.098(1)\ 0.098(1)\ 0$. Note that the tetragonal symmetry of the unit cell constrains *x* and *y* components of the *k*-vector to be equal. Consequent representation analysis and testing the magnetic models result in a model with the Eu^{2+} magnetic moment lying within the *a*-*b* plain. Eu^{2+} is expected to exhibit localized magnetism; thus, a constant-moment magnetic structure was constructed by constraining the real and imaginary components of the magnetic moment to be equal.

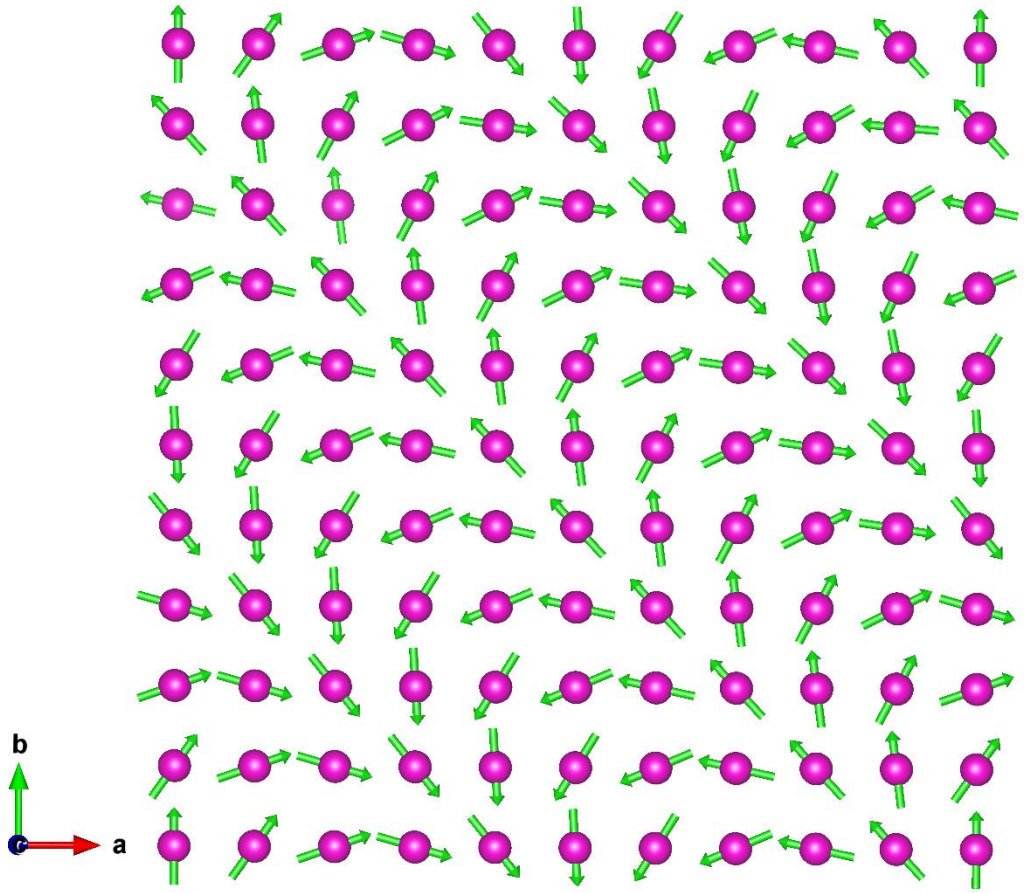

Figure 8.7 *a*-*b*-projection of the magnetic structure of $EuCu_4P_3$ (10 *a* × 10 *b* supercell). Only Eu atoms with their magnetic moments are shown for clarity.

The top projection (*i.e.,* along the *c*-axis) of the derived structure is provided in **Figure 8.7**. The magnetic moments gradually rotate from one unit cell to another, making the whole turn within approximately 10 unit cells both along *a* and *b* directions. Thus, the angle between magnetic moments in two neighboring unit cells is *ca.* 36^0.

Despite the structural and chemical similarities, the three title compounds behave significantly different. They are metallic as reported in refs. [12, 13], and thus, interactions between the magnetic moments of the highly-localized 4*f* electrons of Eu take place through the RKKY (Ruderman–Kittel–Kasuya–Yosida) mechanism. As follows from theory, amplitude and sign of the RKKY interactions changes depending on the distance between magnetic centers in a particular structure [24] and can extend over relatively long distances. The interactions are strongly ferromagnetic at short distances, oscillate from ferro- to antiferromagnetic at intermediate separations and are vanishingly small at longer distances. The shortest distances in the structures of the three title compounds are between Eu atoms separated by a cell parameter (~ 4.1 Å) along the *a* and *b* axes. Therese short distances presumably ensure dominant ferromagnetic interaction. The second nearest distances in the structures of the $EuCu_2P_2$ and $Eu_2Cu_6P_5$ are the diagonal ones within *a*-*b* tetragonal grinds as well as between neighboring staggered grids along the *c*-axis, which are both ~ 5.7 – 5.8 Å. It seems that such combination ensures overall a 3D ferromagnetic configuration, consistent with the neutron data. $Eu_2Cu_6P_5$ possesses twice less of the interlayer contacts (see **Figure 8.1**), and thus exhibits a slightly lower Curie temperature as compared to the $EuCu_2P_2$. On the other hand, the separation between the tetragonal grids of Eu in the $EuCu_4P_3$ is equal to the *c*-cell parameter of ~ 7.4 Å, *i.e.,* there are no short contacts between the layers, which could ensure relatively strong out of plane interactions. The theoretical consideration of the frustrated tetragonal nets is provided in [26], with the nearest and the diagonal contacts considered. Through the Monte-Carlo simulations, it has been demonstrated that the 2D spiral with $k = x$; x can be one of the ground state magnetic structures in tetragonal atomic arrangement. Thus, the cycloidal structure observed in $EuCu_4P_3$ has a theoretical basis.

The intermediate-temperature measurements (at 25 K and 50 K, *i.e.,* in between the transitions at 20 K, 38 K, and 70 K) for the $EuCu_4P_3$ are qualitatively very similar to the one at 3.5 K, with the only difference being the intensities of the magnetic reflection, which gradually decrease upon increasing the temperature. Also, no evidence of structural distortions, like the splitting of the nuclear reflections or changes in their relative intensities,

is observed. Unfortunately, neutron data on their own do not allow for distinguishing between the magnetically ordered phases existing below 70 K. It is clear that the transition at 70 K represents the global ordering of Eu^{2+} magnetic moments since the heat capacity data reveal the strongest entropy in this anomaly. One can propose that the first-order phase transition at 20 K is associated with a minor structural deformation, which might be inaccessible by a relatively low-resolution instrument like SPODI. Another possibility is that, similar to the case of the $EuNi_2P_4$, it represents a lock-in transition. The components of the propagation vector are very close to 0.1 and have just minute variations with temperature. Thus, this propagation vector can change from incommensurate to commensurate predisposing the transformation. Concerning the intermediate transition, one can propose a transformation from an intermediate-temperature spin-density wave to a cycloidal constant moment structure that is shown in **Figure 8.7**. Two of these models are indistinguishable from the unpolarized neutron data. Overall, additional low-temperature high-resolution synchrotron and polarized neutron studies are highly desirable in order further to address the nature of the low-temperature phases in $EuCu_4P_3$.

Conclusions

This work was intended to uncover the microscopic nature of three phase transitions in the $EuCu_4P_3$ and to attempt to explain this complexity by comparison with two other related phases $EuCu_2P_2$ and $Eu_2Cu_6P_5$. As follows from the neutron data, phase transitions at 44 K and 34 K in $EuCu_2P_2$ and $Eu_2Cu_6P_5$ respectively are due to the ferromagnetic ordering of Eu^{2+} magnetic moments with a trivial propagation vector k = 0 0 0. They are aligned along the *c*-direction of the tetragonal unit cells and, at 3.5 K, recover almost full amplitude expected for Eu^{2+}. The persistence of ferromagnetic ordering in these two compounds is most likely due to strong interlayer interactions. Contrary to that, Eu^{2+} tetragonal nets in $EuCu_4P_3$ are separated by more than 7 Å, precluding frustrating interactions between the layers. The tetragonal plane topology of Eu atoms predisposes a complex cycloidal structure within the *a*-*b*-plane, which persists from T_N = 70 K down to the lowest temperature.

Several other people also contributed to this work:

1. Dr Anatoliy Senyshyn (FRM II) performed neutron diffraction measurements and supported with interperation of the results.
2. Dr. Alexander Tsirlin (Uni Augsburg) supported with interpretation of the results.

Supporting information

Proposal for neutron beamtime 1 ($EuCu_4P_3$)

Introduction and state of science

Layered antifluorites are extensively studied due to superconductivity and magnetic phenomena in transition-metal-based layers. Another interesting possibility arises from placing magnetic ions such as Eu^{2+} between the antifluorite slabs, because magnetic fields generated thereof may have strong influence on the physics. For example, Eu^{2+} magnetism reinforces superconductivity of FeAs layers resulting in the remarkably high zero-field T_c of 37 K in $RbEuFe_4As_4$ [Phys. Rev. B 98, 104503 (2018)]. Here, square planes of the Eu^{2+} ions are well separated along the *c* direction. This raises a general question of how the Eu^{2+} moments interact at such high distances, and how these moments affect the transition-metal slabs.

Here, we shall elaborate on this problem by studying crystal and magnetic structures of $EuCu_4P_3$ [Inorg. Chem. 51 (2012) 8948–8955]. An interesting feature of this material is the presence of double-antifluorite layers leading to the interplane Eu^{2+} separations of more than 7 Å. Remarkably, these large separations render the magnetism very different and arguably more complicated than in compounds like $EuFe_2As_2$ with the single antifluorite layer.

Previous results

The powder sample of $EuCu_4P_3$ can be prepared from elements *via* a solid-state reaction. The crystal structure comprises the double-antifluorite layers $[Cu_4P_3]^{2-}$ that separate the square planes of the Eu^{2+} ions, as shown in **Figure 8.S1**. The nearest-neighbor in-plane distance of 4.06 Å between the Eu^{2+} ions is notably shorter than the interplane distance of 7.44 Å.

The compound was characterized by the magnetic susceptibility and resistivity measurements between 2K and 290K. The compound exhibits metallic behaviour over the whole measured temperature range and demonstrates three consecutive phase transitions at 70, 43, and 18K visible in both magnetic susceptibility and resistivity. A substantially positive Curie-Weiss temperature of θ_{CW} = 45 K indicates that magnetic interactions between the Eu^{2+} magnetic centers are predominantly ferromagnetic, while the high-temperature Curie-Weiss paramagnetic moment is consistent with the divalent state of Eu ($4f^7$) as well as the non-magnetic monovalent Cu^+ ($3d^{10}$). We believe that at least some of the observed transitions are of the magnetic nature, but structural components may be present as well, so neutron diffraction is the most suitable tool for unraveling the nature of the observed phase transitions. Low-temperature synchrotron x-ray powder diffraction experiments will also be performed, thus facilitating the interpretation of the neutron data.

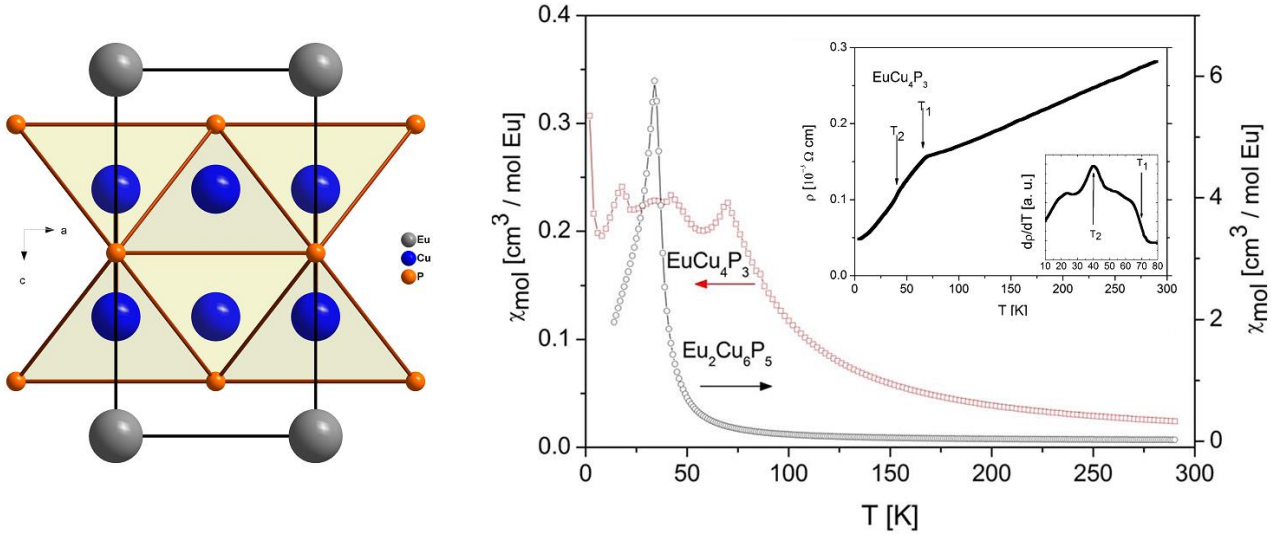

Figure 8.S1 (Left) crystal structure of $EuCu_4P_3$; (right) magnetic susceptibility *vs.* temperature plots for $EuCu_4P_3$ and $Eu_2Cu_6P_5$; (insert) resistivity *vs.* temperature plot for $EuCu_4P_3$. Taken from Inorg. Chem. 51 (2012) 8948–8955.

Aim of proposed work

In the proposed experiment we seek to extend our knowledge about the influence of atoms with a high magnetic moment on metallic antifluorite layers. This study is aiming to uncover the microscopic nature of phase transitions occurring in $EuCu_4P_3$ by establishing the evolution of crystal and magnetic structures upon cooling.

Proposed experiments

We suggest powder diffraction measurements for $EuCu_4P_3$ on the SPODI diffractometer at several temperatures. As Eu is a highly absorbing nucleus, the longer counting time is required, and thus we have to refrain from the full temperature scan. We envisage data collection at 5K (below the lowest transition), at 30K and at 55K (between the three phase transitions), at 90K, and at room temperature. Each measurement will take 12h, thus yielding 2.5 days in total. We suggest measurements in double wall cylinder geometry with a suitably chosen sample thickness to mitigate the effect of absorption.

Although Eu-containing samples are not very commonly studied by neutrons, there are still few examples known from the literature. Eu^{2+} exhibits high magnetic moments. Therefore, we expect the magnetic reflections to be detectable even if the signal to noise ratio is higher than usual. Another positive factor is the structural simplicity of our compound, its unit cell is tetragonal with the volume of 120 $Å^3$ only. The experimental strategy is the same as for the already approved 14435 experiment (Magnetic structure of EuMnSbF and EuZnSbF *via* neutron diffraction at different temperatures).

Proposal for neutron beamtime 2 ($EuCu_2P_2$ and $Eu_2Cu_6P_5$)

Introduction and state of science

The layered antifluorites are extensively studied due to superconductivity and magnetic phenomena. Antifluorite layers are usually considered as physical properties carriers. Their counterparts (the remaining structural units) are believed to affect their behavioru in an indirect manner (geometry tuning, electron/hole doping). While geometrical and electronic effects on the antifluorite layers seem to be studied rather comprehensively, the effects, originated from the ions bearing high magnetic moments (like lanthanides, in particular, Eu^{2+}, $4f^7$, $7\mu_B$) are yet sparsely studied. Probably, the only well-understood example is $EuFe_2As_2$, where by virtue of a special biquadratic coupling, Eu^{2+} facilitates magnetic detwinning [Maiwald et al, Phys. Rev. X 8 (2018) 011011]. Magnetic interactions between localized magnetic moments of Eu^{2+} ($4f^7$) take place through metallic conducting frameworks according to RKKY mechanism; their magnitude and sign are distance-dependent. The ternary compounds EuT_2P_2 (T = Fe, Co, Ni and Cu) are: canted antiferromagnet $EuFe_2P_2$, helical antiferromagnetic $EuCo_2P_2$, mixed-valent nearly paramagnetic $EuNi_2P_2$ and ferromagnetic $EuCu_2P_2$. Nevertheless, comparison of the members of this group does not allow to clearly de-convolute geometrical and electronic effects. Contrary to that, a ternary system Eu-Cu-P contains three chemically and structurally related layered compounds, $EuCu_4P_3$, $EuCu_2P_2$ (more correctly, $EuCu_{2-x}P_2$, $x \sim 0.25$) and $Eu_2Cu_6P_5$. They can serve as a good example for understanding the effects of ions with high magnetic moments on the metallic antifluorite layers depending on a distance between magnetic centers.

Previous results

The powder samples of $EuCu_4P_3$, $EuCu_{2-x}P_2$, and $Eu_2Cu_6P_5$ can be prepared from the elements by solid-state reaction. Synthesis and properties of $EuCu_4P_3$ and $Eu_2Cu_6P_5$ were first described in [Inorg. Chem. 51 (2012) 8948–8955], while $EuCu_{2-x}P_2$ has been investigated before [J. Phys.: Conf. Ser. 263 (2011) 012014]. The neutron diffraction experiment on the SPODI diffractometer for $EuCu_4P_3$ has already been approved under reference number 15324. The compounds have been reproduced and their documented physical properties were confirmed for our samples.

The structures of the titled phases can be described as tetragonal Eu-grids separated by double-antifluorite layers in $EuCu_4P_3$, by single antifluorite layer in $EuCu_2P_2$ and by both types of layers in $Eu_2Cu_6P_5$, as it is shown in **Figure 8.S2**. In general, the crystal structure of $Eu_2Cu_6P_5$ is an intergrowth between $EuCu_2P_2$ and $EuCu_4P_3$ structures. Thus, the distances between Eu^{2+} magnetic centers inside the tetragonal grids are equal to *a*-cell parameters, *i.e.*, ~4.1 Å in all cases, while the separations between grids are defined by the size of the corresponding antifluorite layers. In case of $EuCu_2P_2$, the Eu^{2+} grids are separated by 4.8 Å and shifted by (½;½;0) relative to each other, in $EuCu_4P_3$ – by 7.44 Å and strictly on top of each other, in $Eu_2Cu_6P_5$ alternate both types of arrangement. Eu in a

divalent form predetermines magnetism of these compounds. $Eu_2Cu_6P_5$ and $EuCu_2P_2$ are ferromagnets below 34K and 51K, while low-temperature magnetic behavior of $EuCu_4P_3$ represents a delicate interplay between ferro- and antiferromagnetism what results in three consequent phase transitions at 18, 43 and 70K.

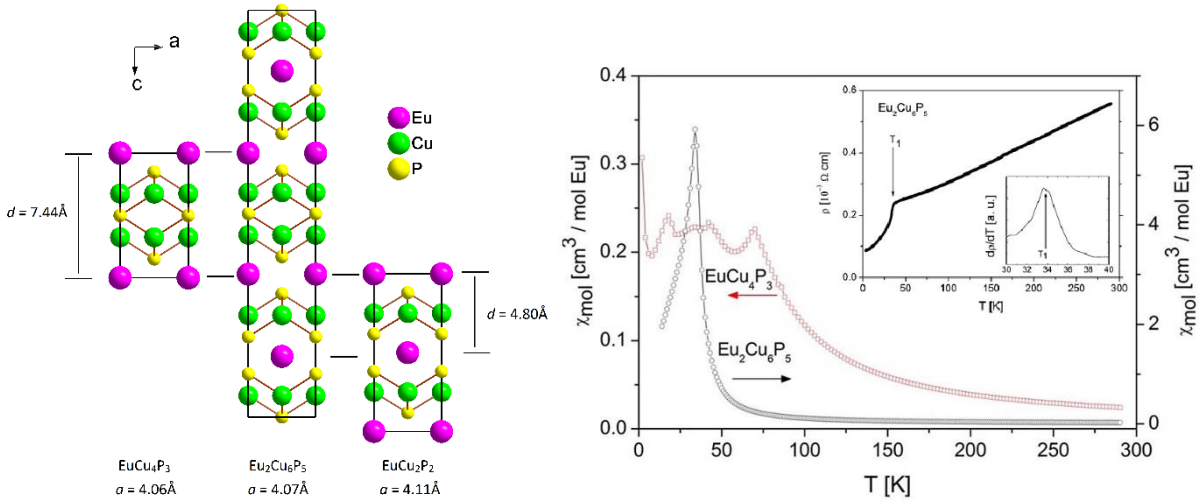

Figure 8.S2 (left) Relations between crystal structures of $EuCu_4P_3$, $EuCu_2P_2$ and their intergrowths, $Eu_2Cu_6P_5$. (right) Magnetic susceptibility in 0.05T field for $EuCu_4P_3$ and $Eu_2Cu_6P_5$ and resistivity (insert) data for $Eu_2Cu_6P_5$.

Aim of proposed work

In the proposed experiment, we seek to extend our knowledge about the influence of atoms with a high magnetic moment on metallic antifluorite layers depending on the distances between magnetic centers. This study is aiming to uncover the microscopic nature of phase transitions occurring in $EuCu_{2-x}P_2$ and $Eu_2Cu_6P_5$ by establishing their crystal and magnetic structures evolving on cooling.

Proposed experiments

We suggest measurements for our sample on the SPODI diffractometer at several temperatures. As Eu is highly absorbing element, the longer counting time is required, and thus we refuse the whole temperature scan. We propose measurement at the lowest available temperature (ideally 1.5K), slightly below and slightly above T_C for both compounds. Each measurement will take 12h; 3 days in total. We suggest measurements in double-wall cylinder geometry with a suitably chosen sample thickness. Although Eu-containing samples are not very commonly studied by neutrons, there are still few examples known from the literature. Eu^{2+} exhibits high magnetic moments; therefore, we expect the magnetic reflections to be detectable even if a signal to noise ratio is lower than usual. Both compounds crystallize in rather small and symmetric unit cells and exhibit only single ferromagnetic transition each. The experimental strategy is the same as for approved 14435 and 15324 experiments.

References

[1] A. Mewis. Ternary phosphides with the $ThCr_2Si_2$ structure. *Z. Naturforsch.* **1980**, *35 b*, 141 – 145.

[2] S. J. Clarke, P. Adamson, S. J. Herkelrath, O. J. Rutt, D. R. Parker, M. J. Pitcher, C. F. Smura. Structures, physical properties, and chemistry of layered oxychalcogenides and oxypnictides. *Inorg. Chem.* **2008**, *47*, 8473 – 8486.

[3] M. Rotter, M. Tegel, D. Johrendt. Superconductivity at 38 K in the iron arsenide $(Ba_{1-x}K_x)Fe_2As_2$. *Phys. Rev. Lett.* **2008**, *101*, 107006.

[4] A. K. Ganguli, J. Prakash. Iron-based superconductors with extended FeX_4 (X = As and Se) tetrahedral. *Eur. J. Inorg. Chem.* **2011**, *26*, 3868 – 3876.

[5] M. Shatruk. $ThCr_2Si_2$ structure type: The "perovskite" of intermetallics. *J. Solid State Chem.* 2019, *272*, 198 – 209.

[6] P. C. Canfield, Sergey L. Bud'ko. FeAs-based superconductivity: a case study of the effects of transition metal doping on $BaFe_2As_2$. *Annu. Rev. Condens. Matter Phys.* **2010**, *1.1*, 27 – 50.

[7] X. Tan, Z. P. ZTener, and M. Shatruk. Correlating itinerant magnetism in RCo_2Pn_2 pnictides (R = La, Ce, Pr, Nd, Eu, Ca; Pn = P, As) to their crystal and electronic structures. *Acc. Chem. Res.* **2018**, *51*, 230 – 239.

[8] W. Peng, S. Chanakiana, A. Zevalkink. Crystal chemistry and thermoelectric transport of layered AM_2X_2 compounds. *Inorg. Chem. Front.*, **2018**, *5*, 1744-1759

[9] M. Tegel, M. Rotter, V. Weiß, F. M Schappacher, R. Pöttgen, D. Johrendt. Structural and magnetic phase transitions in the ternary iron arsenides $SrFe_2As_2$ and $EuFe_2As_2$. *J. Physics: Cond. Matter* **2008**, *20*, 45.

[10] J. Maiwald, I. I. Mazin, P. Gegenwart. Microscopic theory of magnetic detwinning in iron-based superconductors with large-spin rare earths. *Phys. Rev. X* **2018**, *8*, 011011.

[11] D. Huo, J. Lin, G. Tang, L. Li, Z. Qian, T. Takabatake. Ferromagnetic ordering in $EuCu_2P_2$. *J. Phys.: Conf. Ser.* **2011**, *263*, 012014.

[12] D.O. Charkin, A.V. Urmanov, S. M. Kazakov, D. Batuk, A.M. Abakumov, S. Knoner, E. Gati, B. Wolf, M. Lang, A.V. Shevelkov, G. Van Tendeloo, E. V. Antipov, Synthesis, crystal structure, transport, and magnetic properties of novel ternary copper phosphides, $A_2Cu_6P_5$ (A = Sr, Eu) and $EuCu_4P_3$. *Inorg. Chem.* **2012**, *51*, 8948 – 8955.

[13] R. M. Bornick, A. M. Stacy, R. D. Taylor, G. H. Kwei. An investigation of the europium valence in $EuCu_{1.75}P_2$ by Eu Mössbauer and Eu L_{III}-edge X-Ray absorption spectroscopy. *J. Solid State Chem.* **1999**, *144*, 252 – 254.

[14] V. V. Novikov, A. V. Matovnikov, N. V. Mitroshenkov, A. V. Morozov, K. S. Pilipenko, I. V. Plokhikh, A. Pfitzner, A.V. Shevelkov. Ferromagnetic phase transition and anomalies of thermodynamic characteristics of copper-deficient $EuCu_2P_2$ at low temperatures. *J. Alloys Compd.* **2020**. 156150.

[15] https://www.ncnr.nist.gov/resources/n-lengths/elements/eu.html.

[16] D. H. Ryan, J. M. Cadogan. ^{151}Eu hyperfine fields, isomer shifts and moments in Eu-based EuT_2X_2 intermetallic compounds. *Hyperfine Interactions* **2014**, *226*, 243 – 255.

[17] S. Nandi, Y. Xiao, N. Qureshi, U. B. Paramanik, W. T. Jin, Y. Su, B. Ouladdiaf, Z. Hossain, Th. Brückel. Magnetic structures of the Eu and Cr moments in $EuCr_2As_2$: neutron diffraction study. *Phys. Rev. B* **2016**, *94*, 094411.

[18] Y. Xiao, Y. Su, M. Meven, R. Mittal, C. M. N. Kumar, T. Chatterji, S. Price, J. Persson, N. Kumar, S. K. Dhar, A. Thamizhavel, Th. Brueckel. Magnetic structure of $EuFe_2As_2$ determined by single-crystal neutron diffraction. *Phys. Rev. B* **2009**, *80*, 174424.

[19] J. Koo, J. Park, S. K. Cho, K. D. Kim, S.-Y. Park, Y. H. Jeong, Y. J. Park, T. Y. Koo, K.-P. Hong, C.-H. Lee, J.-Y. Kim, B.-K. Cho, K. B. Lee, H.-J. Kim. Magnetic and structural phase transitions of $EuFe_2As_2$ studied *via* neutron and resonant X-ray scattering. *J. Phys. Soc. Jpn.* **2010**, *79*, 114708.

[20] M. Hoelzel, A. Senyshyn, N. Juenke, H. Boysen, W. Schmahl, H. Fuess. High-resolution neutron powder diffractometer SPODI at research reactor FRM II. *Nucl. Instr. A*, **2012**, *667*, 32 – 37.

[21] D. Schmitt and B. Ouladdiaf. Absorption correction for annular cylindrical samples in powder neutron diffraction. *J. Appl. Cryst.* **1998**, *31*, 620 – 624.

[22] V. Petricek, M. Dusek, L Palatinus, L. Crystallographic computing system JANA2006: general features. *Z. Kristallogr.* **2014**, *229*, 345.

[23] J. Rodriguez-Carvajal. Recent advances in magnetic structure determination neutron powder diffraction. *Physica B*, **1993**, *192*, 55 – 69.

[24] K. Momma, F. Izumi. VESTA 3 for three-dimensional visualization of crystal, volumetric and morphology data. *J. Appl. Crystallogr.* **2011**, *44*, 1272 – 1276.

[25] C. N. R. Rao. Modern aspects of solid state chemistry. *Springer Science & Business Media*, **2012**.

[26] L. Seabra, P. Sindzingre, T. Momoi, N. Shannon. Novel phases in a square-lattice frustrated ferromagnet: 13 -magnetization plateau, helicoidal spin liquid, and vortex crystal. *Phys. Rev. B.* **2016**, *93*, 085132.

9 Conclusions and outlook

Modern solid-state chemistry pursues the design of new functional materials, utilizing the cumulated knowledge about structure-property relations in inorganic compounds. The goal of this thesis was both to predict and synthesize new magnetic Eu-containing materials and at least try to refine the rules for new predictions. Peculiarities of its crystal chemistry have dictated the choice of the element – it is one of the lanthanides, but crystallographically behaves more similar to alkaline-earth metals. For this reason, one could expect the formation of magnetic analogs of the already known non-magnetic compounds, which was indeed observed in the current work. The thesis consists of two logical parts. The first one is a classical synthetic work accompanied by the determination of physical properties. Several structural classes of inorganic materials were considered – analogs of the Sr – Pt – P superconductors which are more close to intermetallic compounds, 1111 layered compounds which in one structure combine ionic and covalent parts, and finally, inclusion compounds – clathrates, which feature separation of the guest ions inside the cages with large coordination number. It has been proved that magnetic ground states can be different depending on the type of structural environment – from simple paramagnetism to very complex behavior with several transitions. One should mention here that a fascinating case has been found on the way to this goal – BaFMg*Pn*, the rare transition-metal-free representatives of the 1111 structure type.

The second part can be entitled "neutron diffraction study of magnetic structures of Eu-containing materials". Neutrons are the most straightforward probe capable of assessing magnetically ordered states in any kind of magnetic material. Still, in the case of Eu, the major obstacle is strong neutron absorption of the natural isotope mixture, which blacked this element against any neutron scattering studies. A spiral development of science is particularly visible in this part. We managed to perform several experiments on the WISH diffractometer at ISIS (chapters 4 and 7), which has been commissioned only in 2011 and reached full power just a few years later. On the one hand, it means that the experiments performed in this thesis would not be possible even ten years ago. On the other hand, our results open further perspectives for neutron scattering studies of Eu compounds. Such studies can add more to the understanding of the effects of ions with high magnetic moment on the physical behavior of the matrices, where it is located.

The first tetrel-free clathrate, which contains a purely magnetic guest, $EuNi_2P_4$, was probably the most challenging part of this work. It was easy to propose its existence, given the

already known $SrNi_2P_4$, but experimental feasibility has appeared to be much more difficult. Several different synthetic techniques have been tried, but only one – a mechanochemically assisted route – was valid, because this ternary system already contains many thermodynamically stable compounds. Ones the compounds were prepared, it was interesting to study their physical behavior – thermal and electron transport properties as well as magnetism, which could originate from placing a magnetically active ion in the oversized cage. Rattling, the quasi localized vibrations of Eu^{2+}, is evident from three independent techniques (Raman scattering, heat capacity, and temperature dependence of ADPs) and predisposes low thermal conductivity, which is suitable for thermoelectric properties. The particular topology of magnetic centers in $EuNi_2P_4$ leads to a set of three magnetic phase transitions, which have been proved to be intrinsic using neutron scattering.

Overall, this study resulted in the successful preparation of twelve new compounds, including transition-metal-free representatives of the 1111 structure type along with the very first unconventional tetrel-free clathrate with a purely magnetic guest. Several more compounds previously described in the literature have been reproduced to perform physical measurements and neutron diffraction for establishing their magnetic structures. Neutron diffraction experiments for the first time have been done for seven compounds, which comprises a significant supplement to the set of Eu materials studied with neutrons in literature.

While contributing new knowledge, this work also brings some perspectives for further use of the title compounds as materials, as well as leaves questions that should be addressed later. Neutron diffraction data on their own provided in most of the cases significant information. Still, some fine details of magnetic and nuclear structures are needed to be refined using complementary techniques like Mössbauer spectroscopy, X-ray absorption spectroscopy, or DFT calculations. Overall, the results of this work can be interesting to both solid-state chemistry and physics communities.